DOKUZ EYLÜL UNIVERSITY
GRADUATE SCHOOL OF NATURAL AND APPLIED SCIENCES

CHARACTERIZATION AND DETERMINATION OF ELECTROACTIVE PROPERTIES OF NANOPARTICLE- REINFORCED CELLULOSE ACTUATORS

by
Emine ALTINKAYA

September, 2016
İZMİR

CHARACTERIZATION AND DETERMINATION OF ELECTROACTIVE PROPERTIES OF NANOPARTICLE- REINFORCED CELLULOSE ACTUATORS

A Thesis Submitted to the
Graduate School of Natural and Applied Sciences of Dokuz Eylül University
In Partial Fulfillment of the Requirements for the Degree of Doctor of Philosophy in Chemistry

by

Emine ALTINKAYA

September, 2016
İZMİR

Ph.D. THESIS EXAMINATION RESULT FORM

We have read the thesis entitled **"CHARACTERIZATION AND DETERMINATION OF ELECTROACTIVE PROPERTIES OF NANOPARTICLE- REINFORCED CELLULOSE ACTUATORS"** completed by **EMİNE ALTINKAYA** under supervision of **Prof. Dr. YOLDAŞ SEKİ** and we certify that in our opinion it is fully adequate, in scope and in quality, as a thesis for the degree of Doctor of Philosophy.

Prof. Dr. Yoldaş SEKİ

Supervisor

Prof. Dr. Kadir YURDAKOÇ

Thesis Committee Member

Assist. Prof. Dr. Mehmet SARIKANAT

Thesis Committee Member

Balcan

Prof.Dr. Mehmet BALCAN

Examining Committee Member

Prof. Dr. Hasan YILDIZ

Examining Committee Member

Prof. Dr. Ayşe OKUR

Director

Graduate School of Natural and Applied Sciences

ACKNOWLEDGMENTS

I would like to thank my supervisor, Prof. Dr. Yoldaş SEKİ, for his help, excellent guidance and continuous encouragement throughout my student life at Dokuz Eylül University.

I want to acknowledge my thesis committee members, Prof. Dr. Kadir YURDAKOÇ, and Assist. Prof. Dr. Mehmet SARIKANAT due to their helpful comments and encouragements. Also I acknowleged to my friends.

And also I thank to Assist. Prof. Dr. Levent ÇETİN, Özgün Cem YILMAZ, Okan ÖZDEMİR, İbrahim ŞEN, Barış Oğuz GÜRSES, and Assoc. Prof. Dr. Kutlay SEVER for their help.

This thesis is financially supported by The Scientific and Technological Research Council of Turkey (TÜBİTAK) under grant number 111M643.

Finally, I would like to thank my family for their invaluable support. And also I would like to thank my husband Cihan ALTINKAYA for his invaluable support.

Emine ALTINKAYA

CHARACTERIZATION AND DETERMINATION OF ELECTROACTIVE PROPERTIES OF NANOPARTICLE- REINFORCED CELLULOSE ACTUATORS

ABSTRACT

The aim of this thesis is to determine the electroactive properties of nanoparticle – reinforced cellulose and chitosan based actuators. The thesis can be divided into three parts. In the first part of the thesis, multilayer graphene-reinforced cellulose composites were synthesized by dissolution of cellulose in 1-ethyl-3-methylimidazolium diethylphosphonate and loading graphene at different ratios (0.2, 0.4, and 0.6 percent). The effect of graphene loading on thermal stability, crystallographic properties, chemical functional groups, morphological and mechanical properties of cellulose based films were investigated by characterization tests such as thermogravimetric analysis, X-ray diffraction, Fourier transform infrared spectroscopy, scanning electron microscopy, and tensile test, respectively. Electroactive behaviour of samples was investigated under excitation voltages of 1, 3, 5, and 7 voltages. The max tip displacement was exhibited by Cel-PO$_4$-Gr0.2.

In the second part of the thesis chitosan based actuators were synthesized. The chitosan was crosslinked with N, N'-Methylenebisacrylamide through free radical polymerization. The crosslinker was used in three different concentrations to determine the effect of crosslinker concentration on actuation performance. The samples were anlyzed using characterization tests mentioned above. Besides, the actuation performance of samples was investigated. It can be noted that crosslinker concentration affected the electroactive properties chitosan actuator.

In the third part of the thesis chitosan based actuators including different amounts of poly(diallyldimethylammonium chloride) were sythesized. The samples were examined by characterization tests. The greatest tip displacement values were obtained with ChiPM-50.

Keywords: Cellulose, chitosan, electroactive, ionic liquids, graphene.

NANO PARÇACIK TAKVİYELİ SELULOZ AKTÜATÖRLERİN ELEKTROAKTİF ÖZELLİKLERİNİN BELİRLENMESİ VE KARAKTERİZASYONU

ÖZ

Bu tezin amacı, selüloz ve kitosan tabanlı aktüatorlerin elektroaktif özelliklerinin belirlenmesidir. Tez üç kısma ayrılmıştır. Tezin birinci kısmında selülozun 1-etil-3-metilimidazolyum dietilfosfat içinde çözünmesi ve farklı oranlarda grafen (yüzde 0,2 0,4 ve 0,6) eklenmesiyle çok katmanlı grafen ile güçlendirilmiş selüloz kompozitler üretildi. Grafen yüklenmesinin selüloz tabanlı filmlerin termal dayanımı, kristolografik özellikleri, kimyasal fonksiyonel grupları, morfolojik ve mekaniksel özellikleri üzerine olan etkisi sırasıyla termogravimetrik analiz, X ışınları kırınım difraktometrisi, Fourier Dönüşümlü Kızılötesi Spektroskopisi, taramalı elektron mikroskobu, ve çekme testi ile belirlendi. Örneklerin elektroaktif davranışları DC voltaj (1, 3, 5 ve 7 volt) altında incelendi. Maksimum yer değiştirme Cel-PO_4-Gr0.2 tarafından sergilendi.

Tezin ikinci kısmında kitosan tabanlı aktüatorler üretildi. Kitosan N, N'-Metilenbisakrilamid ile serbest radikal polimerizasyonu yoluyla çapraz bağlandı. Çapraz bağlayıcı konsanrasyonunun aktüasyon performansı üzerine olan etkisinin incelenmesi için çapraz bağlayıcı üç farklı konsantrasyonda kullanıldı. Örnekler yukarıda bahsedilen karakterizasyon testleri kullanılarak analiz edildi. Bunun yanısıra, hareket performansları değerlendirildi. Çapraz bağlayıcı miktarının chitosanın elektroaktiflik performansını etkilediği görülmüştür.

Tezin üçüncü kısmında farklı oranlarda poli(dialildimetilamonyum klorür) içeren kitosan tabanlı aktüatorler üretildi. Örnekler karakterizasyon testleri ile incelendi. En büyük uç yerdeğiştirme ChiPM-50 ile elde edilmiştir.

Anahtar kelimeler: Selüloz, kitosan, elektroaktif, iyonik sıvı, grafen.

CONTENTS

Pages

CHAPTER TWO - MATERIALS AND METHODS... 27

CHAPTER THREE - RESULTS AND DISCUSSION 31

LIST OF FIGURES

Pages

LIST OF TABLES

Pages

CHAPTER ONE
INTRODUCTION

1.1 Active Polymers

In recent decades, researches on polymer were increased. The polymers take part in many technological field such as aerospace, electronics, automobiles, and household goods. Having attractive properties made it indispensable part of life. Polymers are inexpensive, pliable, easily processed and manufactured, lightweight, and fracture tolerant (Gurunathan, Murugan, Marimuthu, Mulik, & Amalnerkar, 1999; Bar-Cohen, 2000).

Polymers react to external stimuli such as pH, light, a magnetic field, and electrical field by changing shape or size (Shahinpoor, Bar-Cohen, Simpson, & Smith, 1998; Antony and De, 2001; Rousseau and Mather, 2003; Zhou and Li, 2003; Bar-Cohen, 2000; Colombani et al., 2007). The stimuli responsive polymers are known as active polymers. In recent decades, many studies were carried out about active polymers (Kim and Tadokoro, 2007). Biomimetic studies were the significant applications of active polymers. Biomimetic movements of active polymers is shaped like fish, bird, snake, arm etc. (Ayre, 2003).

According to type of actuation active polymers were broadly classified as electroactive polymers (EAPs) and nonelectroactive polymers (actuated by nonelectric stimuli such as temperature, pH, light, etc.). The electroactive polymers activated with electrical stimuli categorized depending on actuation mechanism as electronic (EAPs) and ionic (EAPs). Electronic EAPs are actuated by coulomb forces or electric field. Ionic EAPs are actuated by diffusion or mobility of the ions and conjugated substance in polymer. The actuations of the nonelectroactive polymers take place chemically. They can be classified as thermally activated gels, inflatable structures, light-activated polymers, magnetically activated polymers shape-memory polymers (Bar-Cohen, 2000).

1.1.1 *Nonelectroactive Polymers*

1.1.1.1 Chemically Activated Polymers

A polymer can change in shape or dimension by external chemical stimuli's. Artificial muscle was the indispensable topic in active polymers and there are many studies about it. The first artificial muscle developed in 1950 was a chemically activated polymer (pH activated). The activated polymeric gels developed can respond to stimuli such as solvent, temperature, light, and pH (Kim and Tadokoro, 2007).

Physical cross-linking occurs in pH stimuli polymers due to the ionic interactions. The physical cross-linking was shown schematically in Figure 1.1. The physical cross-linking provides a viscoelastic response. The ionic interactions affect the mechanical properties of polymer and help to improve compatibility of polymers in blends (Ahn, Kasi, Kim, Sharma, & Zhou, 2008).

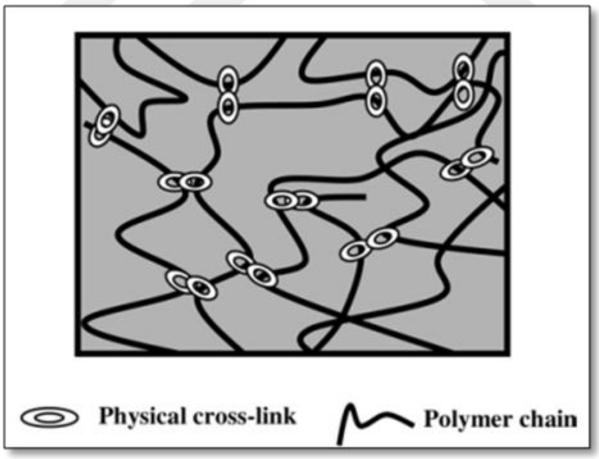

Figure 1.1 Physically cross-linked gel (Ahn, Kasi, Kim, Sharma, & Zhou, 2008).

In medicine pH stimuli polymers are indispensable and there are many studies about it. These polymers can be used in the body using the pH variance of body. The certain tissues and cellular compartments have specific pH values (Schmaljohann, 2006). The pH values of tissues and cellular compartments are given in Table 1.1.

The variance of pH the swelling and deswelling mechanism was used in medicine studies (Markland, Zhang, Amidon, & Yang, 1999; Kwon, Osada, & Gong, 2006; Yoshida et al., 2009).

Table 1.1 pH in tissues and cellular compartments (Grabe and Oster, 2001; Watson, Jones, & Stephens, 2005; Schmaljohann, 2006; Florence and Attwood, 2011)

Tissue/cellular compartment	**pH**
Blood	7.35-7.45
Stomach	1.0-3.0
Duodenum	4.8-8.2
Colon	7.0-7.5
Early endosome	6.0-6.5
Late endosome	5.0-6.0
Lysosome	4.5-5.0
Golgi	6.4
Tumour-extracellular	7.2-6.5

1.1.1.2 Light Activated Polymers

Light activated polymers respond mechanically when exposed to the light at particular wavelengths (Long, Scott, Qi, Bowman, & Dunn, 2009). The dimensional changes in polyelectrolyte gels, resulted from the chemically induced ionization, are expressed by mechanochemistry. The dimensional changes due to the light induced ionization were explained by mechanophotochemicaleffect (Aviram, 1978; Kim and Tadokoro, 2007).

Most of the photo activated polymers work based on the following mechanism (Meng and Hu, 2010):

1. Photodeformability induced by photoisomerization (Finkelmann, Kim, Munoz, Palffy-Muhoray, & Taheri, 2001; Warner and Terentjev, 2003; Yu, Nakano, & Ikeda, 2004),

2. Photodeformability induced by photoreactive Molecules (Andreopoulos, Deible, Stauffer, Weber, Wagner, Beckman et al., 1996; Thomsen, Keller, Naciri, Pink, Jeon, Shenoy, et al., 2001; Ikeda, Nakano, Yu, Tsutsumi, & Kanazawa, 2003; Yu and Ikeda, 2005; Jiang, Kelch, & Lendlein, 2006),
3. Reversible photoinduced ionic dissociation.

1.1.1.2 1. Photodeformability Induced by Photoisomerization. Photodeformability of the polymer such as azobenzenes induced by photoisomerization. Azobenzenes exhibit the reversible cis-trans isomerization (Finkelmann, Kim, Munoz, Palffy-Muhoray, & Taheri, 2001; Meng and Hu, 2010). The angle between the aromatic rings of azobenzenes changed and the distance between the rings decreased from 9Å (trans) to 5.5Å (cis) due to the trans-cis isomerization (Meng and Hu, 2010). The photo induced trans-cis isomerization of azobenzene was exhibited in Figure 1.2.

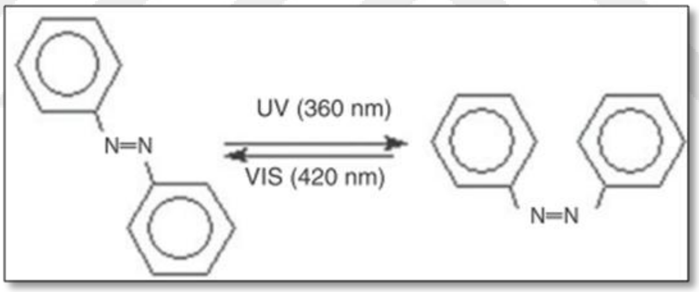

Figure 1.2 Photoisomerization of azobenzene (Meng and Hu, 2010).

1.1.1.2.2 Photodeformability Induced by Photoreactive Molecules. The photoreactive molecules have capability to form photoreversible covalent cross-link in polymer (Meng and Hu, 2010). This phenomena (photodimerization) was exhibited in Figure 1.3 for cinnamic acid (Yu and Ikeda, 2005). Lendlein et al. fabricated the photo active grafted polymers with the cinnamic acid as the terminal groups by using the reversible photo cross-linking reaction (Lendlein, Jiang, Jünger, & Langer, 2005; Meng and Hu, 2010).

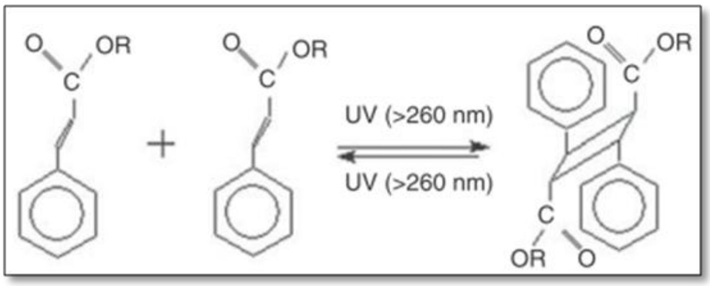

Figure 1.3 Photodimerization of cinnamic acid (Yu and Ikeda, 2005; Meng and Hu, 2010).

1.1.1.2.3 Reversible Photoinduced Ionic Dissociation. Derivatives of triphenylmethane leuco dissociated into ion pairs with the exposure to UV light. The recombination of the ion pairs happen thermally in the dark (Meng and Hu, 2010). The mechanism was shown in Figure 1.4.

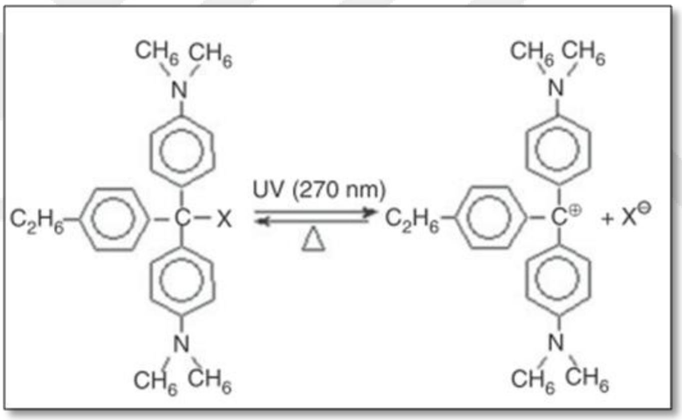

Figure 1.4 Dissociation and recombining of ion pairs of triphenylmethane leuco derivatives (Meng and Hu, 2010).

1.1.1.3 Magnetically Activated Polymers

Magnetically activated polymers called ferrogels show strain result of the changes in the magnetic field. The magnetic field has a role as driving force on ferrogels. Magnetically controlled medium can be a swollen network loaded with specific type of filler (ferrofluid). The ferrogels are chemically cross-linked polymer. Magnetic particles were attached to the ferrogel chains with strong adhesive forces in these gels (Zrínyi, Barsi, & Büki, 1996; Kim and Tadokoro, 2007; Meng and Hu, 2010).

The forces in ferrogels occur under the different magnetic fields, any forces were not observed under uniform magnetic field. The change can be seen on Einstein-de Haas effect which led to differences in the magnetic field vector.

The shape deformation ad movement of polymer gel with complex fluid was obtained under the magnetic and electric field. Poly(vinyl alcohol) and poly(N-isopropylacrylamide) gel beads, which include magnetic particles, were fabricated. The changes were observed due to the magnetophoteric force under the non-uniform field while any changes under the uniform field were not observed. The changes of the magnetic gels in shape are quick and controllable so they can be used in artificial muscles (Zrinyi, 2000; Kim and Tadokoro, 2007). These polymer gels allow to fabrication of reliable and quick actuators.

1.1.1.4 Thermally Activated Polymers

Thermally active polymers exhibit the volume change under the temperature changes ranging from 20 to 40 °C. The thermally active polymers display a contractile force of 100 kPa in the response time 20-90 seconds (Bar-Cohen, 2000; Kim and Tadokoro, 2007). The prevalent property of these polymers is having both hydrophilic (e.g., carboxyl, amide) and hydrophobic (e.g., methyl, ethyl, propyl) groups in one network. The thermally active polymers change the properties hydrophilic to hydrophobic structure under the lower critical solution temperature (LCST) (Meng and Hu, 2010). The hydrogen bonding which exists between the hydrophilic segments increased the solubility of polymer in water at lower temperature. The hydrophobic interaction increased at higher temperature while hydrogen bonding becomes weaker (Tanaka, 1978; Hirokawa and Tanaka, 1984; Amiya, Hirokawa, Hirose, Li, & Tanaka, 1987; Yoshida et al., 1995; Kopeček, 2003; Meng and Hu, 2010; Qiu and Park, 2012).

The most studied polymers as thermally activated are N-substituted polyacrylamide derivatives. The first volume phase transition of poly(N-isopropylacrylamide) (PNIPAAm) gel was reported in 1984 by Hirokawa and

Tanaka (Hirokawa and Tanaka, 1984). Poly (vinyl methyl ether) (PVME) is one of the widely used thermally active polymer. Phase transition of the PVME is 38 ^{o}C, under this temperature PVME completely dissolve in water (Kim and Tadokoro, 2007).

1.1.1.5 Shape-Memory Polymers

Shape-memory polymers (SMPs) change into the temporary shape under the external stimuli and return to the fixed shape when the stimuli were removed. The phenomenon was explained with schema in Figure 1.5. These polymers have shape-memory effect (Behl and Lendlein, 2007; Dietsch and Tong, 2007; Liu, Lv, Lan, Leng, & Du, 2009). The thermally activated shape memory effect was used widely (Meng and Hu, 2009). The thermally shape memory effect was expressed in Figure 1.6. The thermal sensitive shape memory polymer have crystalline/amorphous hard phase, chemical cross-linking structure, physical cross-linking structure, and a low temperature transition of crystalline, liquid–crystal or amorphous phase as a switch (Meng and Hu, 2009).

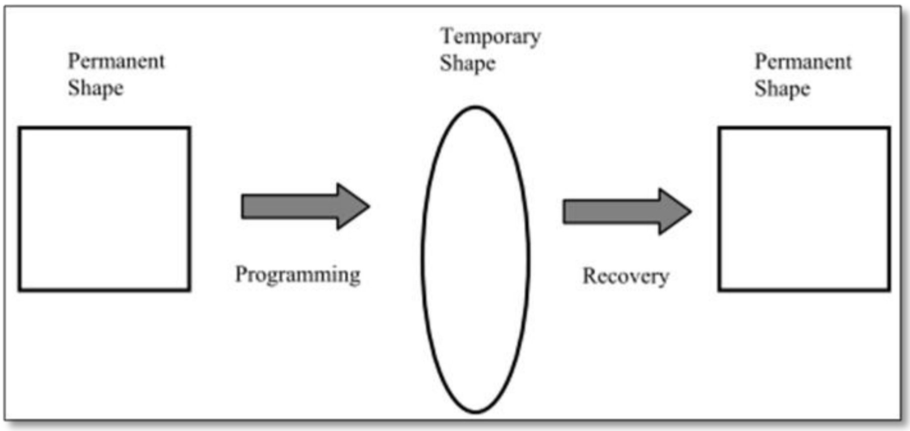

Figure 1.5 Schematic expression of Shape-memory polymers (Kim and Tadokoro, 2007).

SMPs have wide application areas such as intelligent medical devices (Lendlein and Langer, 2002; Metcalfe et al., 2003; Wache, Tartakowska, Hentrich, & Wagner, 2003), sensor and actuators (Lan et al., 2008; Leng, Lu, Liu, & Du, 2008), applications in smart textiles and apparels (Meng, Hu, & Yeung, 2007; Meng, Hu, Zhu, Lu, & Liu. 2007), self-deployable structures in space-craft (Mahoney, 1967; Kim, Lee, & Xu, 1996; Grim, Iglesias, Speakes, Campos, & Pelote, 1999; Jin, Pramoda, Xu, & Goh, 2001; Jin-lian, Xue-mei, Xiao-ming, & Jian-ming, 2002; Meng et al.,2007), high performance water–vapor permeability materials (Mondal and Hu, 2006; Mondal, Hu, & Yong, 2006), micro-systems (Gall, et al., 2002) in the formats of solution, emulsion (Russel, Hayashi, & Yamada 1999; Jin-lian, et al., 2002; Fan, Hu, & Ji, 2004), foam (Lendlein and Langer, 2004; Tobushi, Matsui, Hayashi, & Shimada, 2004; Tobushi, Hayashi Hoshio, & Miwa, 2006), film (Russel et al., 1999), or bulk (Hayashi, Tasaka, Hayashi, & Akita, 2004), heat shrinkable packages for electronics (Meng and Hu, 2009; Charlesby, 2013).

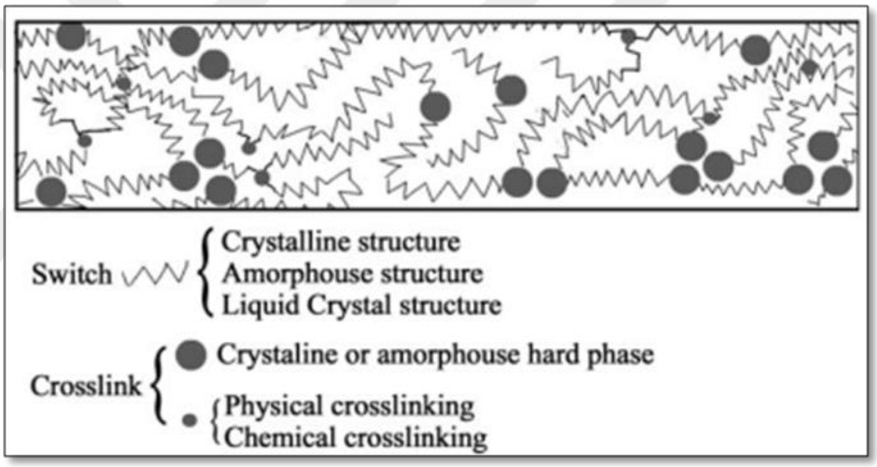

Figure 1.6 The mechanism of thermal shape memory effect (Meng and Hu, 2009).

1.1.2 Electroactive Polymer

Electroactive polymers that exhibit shape change, actuation, etc. under the electrical stimulation. Elecroactive polymers can be classified into two groups (Bar-Cohen, 2000):

1. Ionic Electroactive Polymer
2. Electronic Electroactive Polymer

The ionic electroactive polymers are driven by mobility or diffusion of ions under the electric field while electronic electroactive polymers are driven by Coulomb forces or electric field (Bar-Cohen, 2000).

The electroactive polymers exhibit similar responses like natural muscles. The similarity allows to potential applications such as biomimetic engineering for biomimetic robots and biomedical devices (Lu, Kim, Lee, & Oh, 2008; Jeon, Kang, Lee, & Oh, 2009; Jeon and Oh, 2009; Jung, Vadahanambi, & Oh, 2010; Rajagopalan and Oh, 2011; Hong, Ki, Jeon, Che, Park, Kee, & Oh, 2013).

1.1.2.1 Ionic Electroactive Polymer

1.1.2.1.1 Ionic Polymer Gels. The response of these polymer gels occurs via chemical reactions. The chemical reactions give rise to changes in ionic polymer gel such as swollen and shrinking. The pH activated polymers are indispensible for actuator technology. However, the gels were damaged during the pH changes. The interaction between acid solution and basic solution give rise to formation of salts. The salts may be accumulated on polymer surface and affecting the response time (Kim and Tadokoro, 2007).

The development in electro activated polymer system makes the ionic gels potential material for robotic applications. It is easy to control the electrically driven system. The actuation under the electrical stimuli was first studied by Tanaka (Tanaka, Nishio, Sun, & Ueno-Nishio, 1982; Kim and Tadokoro, 2007). The study was about the polyacrylic acid gels. The size and shape of the polyacrylic acid gel was changed when placed between electrodes in aqueous solution. In another study acrylic acid-acrylamide copolymer gel was fabricated and it was exhibited a bending when placed between electrode in aqueous solution (Shiga and Kurauchi, 1990; Kim and Tadokoro, 2007).

1.1.2.1.2 Ionic Polymer-Metal Composite (IPMC). The ionic polymer metal composites (IPMC) are kind of electroactive polymer. They have invaluable properties and offer some advantages. IPMCs; requiring low driving voltage (<5 V), soft and flexible, have an ability to operate in aqueous environments. Recent scientific studies show that IPMCs have many application areas such as various biomedical systems (Biddiss and Chau, 2006; Lee, Jung, Lee, Mun, & Moon, 2006; Chen, Shen, Xi, & Tan, 2007; Yoon, Reinhall, & Seibel, 2007), underwater robotics (Kim, Yim, Paquette, & Kim, 2007; Yim, Lee & Kim, 2007; Aureli, Kopman, & Porfiri, 2010; Chen, Shatara, & Tan, 2010), energy harvesting (Brufau-Penella, Puig-Vidal, Giannone, Graziani, & Strazzeri, 2008; Tiwari, Kim, & Kim, 2008; Aureli et al., 2010; Palmre et al., 2013).

Ionomeric Polymer-Metal Composites (ImPMC) are desirable type of electroactive polymer actuation materials because of their characteristics of mechanical flexibility, large electrically induced bending, low density, low excitation voltage, and ease of produce. Bending of material can be explained by diffusion of ions between the electrodes (Bao, Bar-Cohen, & Lih, 2002). EAPs have attractive properties for artificial muscles, biomimetic sensors, robotic actuators, and medical devices (O’Halloran, O’Malley, & McHugh, 2008). IPMCs are incomparable electroactive polymers for soft actuation bending with low driving voltages (Shahinpoor and Kim, 2001; Pugal, Jung, Aabloo, & Kim, 2010).

An ionic polymer which comprises of strong ionic groups such as carboxylic and sulfuric acid attached to the backbone of polymer. The strong ionic groups create highly ionic clusters that give rise to the transport of the mobile ions across the backbone of polymer. The transportation of mobile ions results under the small electrical field. Electrical field is created by two thin metal electrodes on the both surface of polymer (Shahinpoor, 2003; Bahramzadeh and Shahinpoor, 2014).

The bending displacement is resulted from solvent transport and ion migration (Grodzinsky and Shoenfeld, 1977). When the voltage is applied, the bending of IPMC will be toward to the anode due to moving of hydrophilic positive or cations to the cathode. Under an applied voltage, displacement of tip and blocked force are used for quantification of actuator performance (Newbury and Leo, 2002;

Bahramzadeh and Shahinpoor, 2014).

The properties of mobile ions, ion diameter, charge number, hydrated ion diameter and ion mobility, affect the actuation of IPMC. The mobile cations in the polymer membrane can be exchanged with appropriate ion via dipping in a salt solution. Alkly metal ions (K^+, Na^+, Li^+, Ru^+, Cs^+) can be loaded by immersing in suitable salt solution such as NaCl, KCl, and LiCl. Alkyl ammonium ions (TBA^+, TMA^+) can be loaded by dipping in tetrabutylammonium and tetramethylammonium solutions. Li^+ ion gives rise to largest displacement among the alkyl metal ions. Alkali metal ions lead to rapid displacement comparing to alkyl ammonium ions but pumping efficiency or charge-specific displacement is small. Rapid displacement property of alkly metal ions can be related with the small radius of hydrated ion relative to hydrophilic radius channel of polymer membrane. Pumping efficiency or charge-specific displacement of alkly ammonium ions is increased while rate decreases related with molecular size (Abe et al., 1998). As a result it can be said that hydrated volume of ion has an important role in achieving the highest force (Shahinpoor and Kim, 2000; Bahramzadeh and Shahinpoor, 2014).

The electrode of IPMC has an important role in actuation performance. Several methods have been used to create conductive electrode on polymer surface. Electroless deposition depends on chemical reduction of metal nanoparticles. Physical plating by heat-pressing is a method to form electrode by hot-pressing metal powder. Physical vapor deposition also can be used by the condensation of a vaporized form of the metal on polymer surface. In another study polyaniline nanorods were used to form electrode on Nafion surface (Kim, Oh, & Choi, 2010). Silver nano powder, which is mixed with Nafion solution, was cast on Nafion surface and conductive surface was obtained (Chung et al., 2006; Bahramzadeh and Shahinpoor, 2014).

Nonmetalic particles were also used to create conductive polymer surface. Non metallic particles which used for electrode on ionic polymer surface are MWCT, CNT, carbon aerogels and graphene (Bahramzadeh and Shahinpoor, 2014). Some of examples of different electrode method were shown in Figure 1.7.

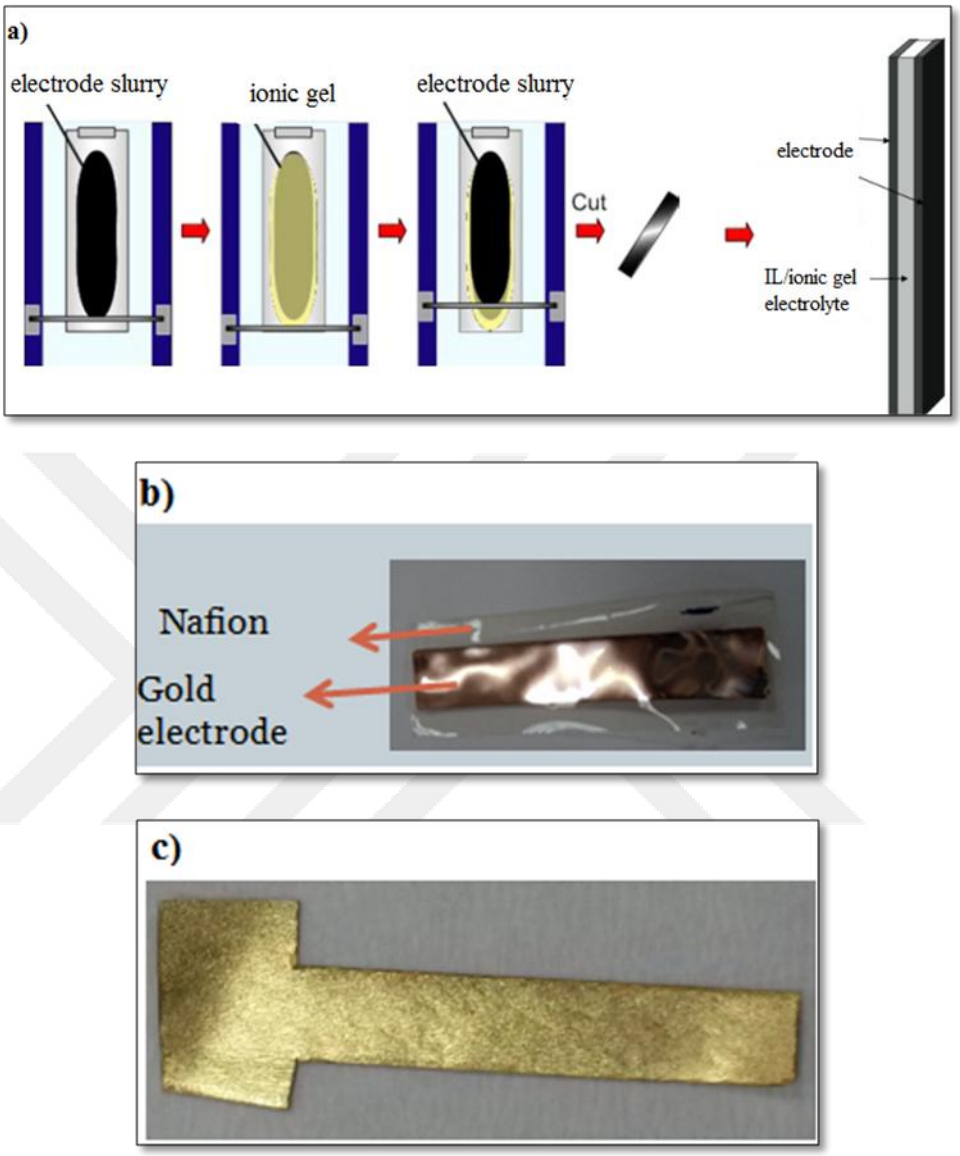

Figure 1.7 a) ionic gel was coated with nonmetallic particles (Asaka, Mukai, Sugino, & Kiyohara, 2013; Imaizumi, Ohtsuki, Yasuda, Kokubo, & Watanabe, 2013), b) Gold coated Nafion by vapor evaporation method (Altınkaya et al., 2016), c) Gold coated ionic gel by using gold leaf (Altınkaya et al., 2016).

1.1.2.1.3 Conducting Polymers. Conducting polymers are electronically conducting organic polymers. The demands for conducting polymers were provided with loading conducting powders such as gold, silver and graphene to the polymer. However loading of conducting powder into polymer brought some disadvantages such as deterioration in polymers that affect the other properties and high cost. The known conducting polymers polypyrole (PPy), polyaniline, and polythiophene have been used in studies due to having good environmental stability, high electrical conductivity (Ansari, 2006). However, conducting polymers have disadvantages such as low cycle life and energy conversion efficiency, and the need of electrodes for actuation.

PPy has important position among the conducting polymers due to high conductivity, stability, flexibility, and good mechanical properties. It has potential important application areas such as counter electrode in electrolytic capacitors (Krings, Havinga, Donkers, & Vork, 1993), chromatographic stationary phases (Ge, Teasdale, & Wallace, 1991), electronic and electrochromic devices (Talaie et al., 2000; Rowley and Mortimer, 2002; Ansari, 2006), sensors (Slater and Watt, 1989; Adeloju, Shaw, & Wallace, 1993; Sukeerthi and Contractor, 1994), light-weight batteries (Mermilliod, Tanguy, & Petiot, 1986), membrane separation (Mirmohseni, Price, Wallace, & Zhao, 1993; Ansari, 2006).

Polyaniline has application areas such as organic light emitting diodes (OLEDs) (Burn, Lo, & Samuel et al., 2007), field-effect transistors (OFETs) (Nam et al., 2011), corrosion (De Souza, 2007), and solar cells (Alet et al., 2006).

The conducting polymers have higher work densities per cycle, lower power densities, and slightly lower force generation according to the piezoelectric materials. The conducting polymers are indispensible for medical actuator applications such as micro actuators and catheters due to the need of low actuation voltages (Baughman, 1996). These polymers may be used in biosensor applications (Gerard, Chaubey, & Malhotra, 2002).

1.1.2.1.4 Carbon Nanotube Actuators. Carbon Nanotubes brought new advantages such as mechanical and electrical properties to the electroactive actuators. Single walled carbon nanotubes (SWCNTs) was discovered by Iijima in 1991 (Iijima, 1991; Iijima and Ichihashi, 1993). Since then conducting carbon materials such as graphene (Xie et al., 2010), carbon nanotube (Baughman et al., 1999;

Fennimore et al.,2003; Aliev et al., 2009; Chen et al., 2011), and other carbon materials attracted great interest in studies due to high conductivity, unique mechanical & electrical properties, large surface area, and their light weight. Baughman et al. reported that SWCNTs have a capability for actuation in an electrolyte solution and also above mentioned properties could enhance the electromechanical process (Baughman, 1996; Kong and Chen, 2014).

SWCNT actuators were exhibited higher strain and stress than high-modulus ferroelectrics and natural muscle, respectively. The actuators do not need dopant intercalation. The electronic charge was injected into the SWCNT electrode by changing the applied voltages (Baughman et al., 1999).

1.1.2.2 Electronic Electroactive Polymer

1.1.2.2.1 Ferroelectric Polymers. Polymers show three distinct mechanism of electric polarization (Figure 1.8); ferroelectricity, metastable electret orientation, and nonuniform space-charge (Fukada, 1989; Eberle, Schmidt, & Eisenmenger, 1996; Poulsen and Ducharme, 2010).

Ferroelectric may be divided into two categories; organic (liquid crystals, molecular crystals, and polymers) and inorganic (oxides and non-oxides). The inorganic type consists of many oxides and non-oxides in the form of ceramics. The organic type includes a few polymer such as some VDF-containing fluorinated copolymers, poly(vinylidene difluoride) (PVDF), certain odd-numbered polyamides such as Nylon 7 and Nylon 11 (Nalwa, 1991; Takase, Lee, & Newman, 1991; Su, Ma, Scheinbeim, & Newman, 1995; Setter and Waser, 2000; Li and Shimizu, 2008; Guo, Zeng, & Dkhil, 2014).

The ferroelectric polymer in polar phase’s β and Ɣ show ferroelectric behaviour. Organic ferroelectrics exhibit low Curie temperature (phase transition temperature), low spontaneous polarization, and low dielectric constant according to the inorganic ferroelectrics. Ferroelectric polymers have many specific application areas due to having invaluable properties such as light weight, flexibility, ease of processing, high electric breakdown field (Guo et al., 2014).

The ferroelectric polymers, like ferromagnets, have dipoles which can be aligned. The dipoles lose their permanent polarization above the Curie point. The ferroelectric polymer actuators have high work density and exhibit fast response like inorganic piezo- and ferroelectrics (Bar-Cohen, 2000; Mirfakhrai, Madden, & Baughman, 2007).

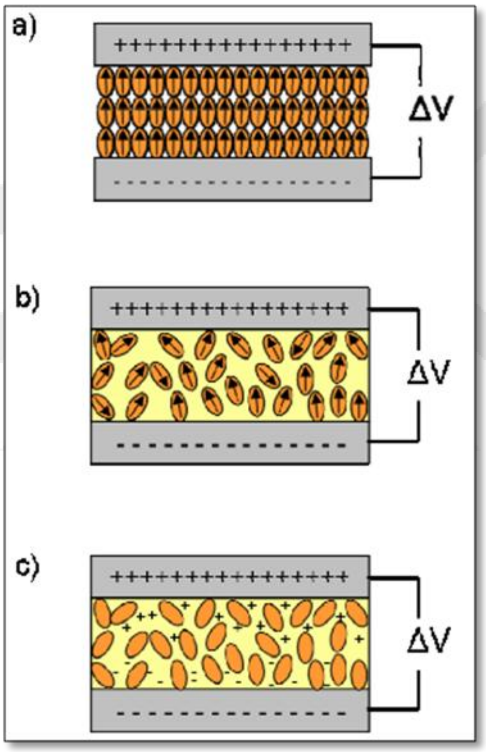

Figure 1.8 Polarization in a) ferroelectricity, b) metastable electret orientation, and c) nonuniform space-charge (Poulsen and Ducharme, 2010).

1.1.2.2.2 Dielectric Elastomers. The charged particles move under the applied voltage as a result of response. The charged particles move relative to one another by small distances. The polarization and deformation in dielectric are inherently coupled. All dielectrics exhibit electroactive properties and so they are electroactive (Suo, 2010).

The dielectric elastomer actuators were composed of highly deformable and incompressible dielectric medium. Under the electric field a stress was generated by coulombic forces between the charges, as a result of the stress causing the electrodes to move closer. The stress was called as Maxwell stress. The mechanism of dielectric elastomer was shown in Figure 1.9 (Kim and Tadokoro, 2007).

The dielectric elastomers have desirable properties such as no noise, low cost, fast response, and light weight (Suo, 2010).

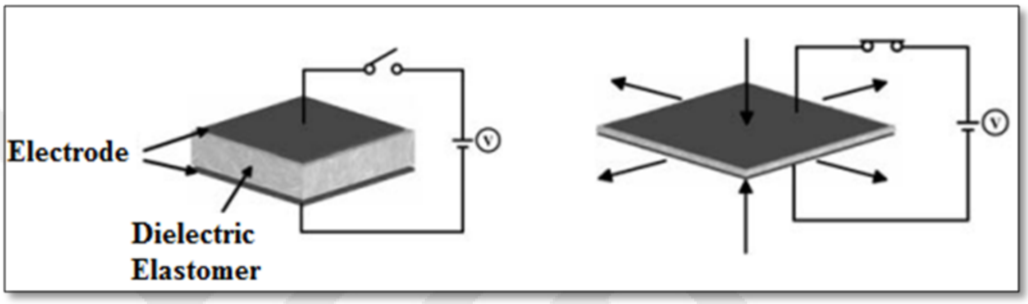

Figure 1.9 The mechanism of dielectric elastomer (Kim and Tadokoro, 2007).

Choi et al. used the dielectric elastomers in musclelike and microrobots applications developed for biomimetic actuators (Choi et al., 2005; Kim and Tadokoro, 2007). The design and control are required for developing in application of dilectric elastomer. These reseaches require multiphysics including mechanical, electrostatic, and material (Hackl, Tang, Lorenz, Turng, & Schröder, 2004; Kim and Tadokoro, 2007).

1.1.2.2.3 Electrostrictive Graft Elastomers. The graft elastomers have flexible backbone chains, and also there are polar groups which were attached to the flexible backbones as side chains. The polar groups come together to create polar crystalline regions. The structure of graft elastomer was depicted in Figure 1.10 (Wang, Sun, Zhou, & Su, 2004; Mirfakhrai et al., 2007) .

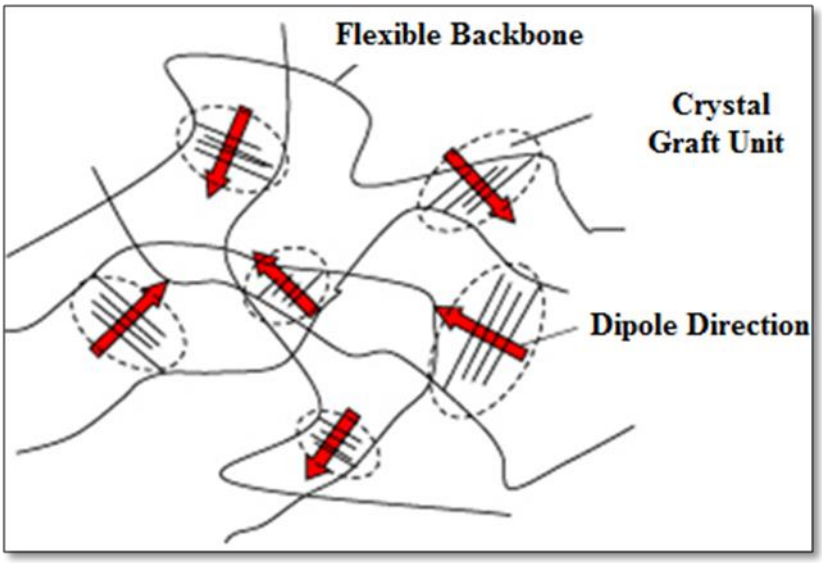

Figure 1.10 Structure of graft elastomer (Wang et al., 2004).

The deformation of elastomers under the electric field can be classified into two groups; backbone chain reorientation and crystal unit rotation. The deformation groups can be seen in Figure 1.11 (Wang et al., 2004).

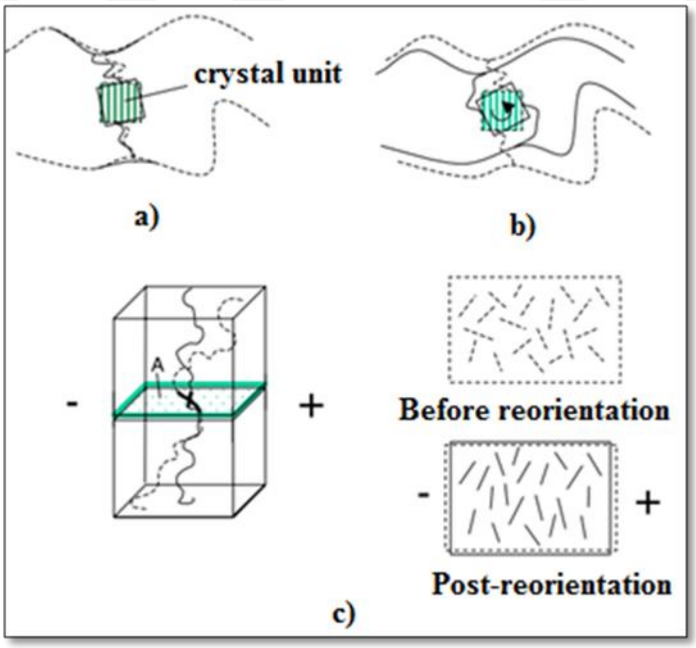

Figure 1.11 The deformation mechanism a) Local elastic deformation, b) Crystal unit rotation, and c) Local reorientation of backbones (Wang et al., 2004).

1.1.2.2.4 Liquid Crystal Elastomers. Liquid crystal polymers are divided into the two groups; side-chain and main-chain types (Sherrington, 1989; Freidzon and Shibaev, 1993). The side-chain liquid crystalline polymers can be synthesized by polymerization or molecular reaction of mesogenic vinyl monomers (Finkelmann and Rehage, 1980) while the main-chain liquid crystalline polymers synthesized with bifunctional monomers. The segments in the liquid crystalline polymer can move freely above the glass transition temperature (Tg) because of the micro-Brownian movement and orientation of decoupled mesogens. The network polymers are created via cross-linking of polymer chains. While the cross-linking of the polymer affects the macro Brownian movement, it does affect the micro Brownian movement. The liquid crystalline polymers can be cross-linked to create the elastomers. The schematic exhibition of liquid crystalline elastomers formed via cross-linking was given in Figure 1.12.

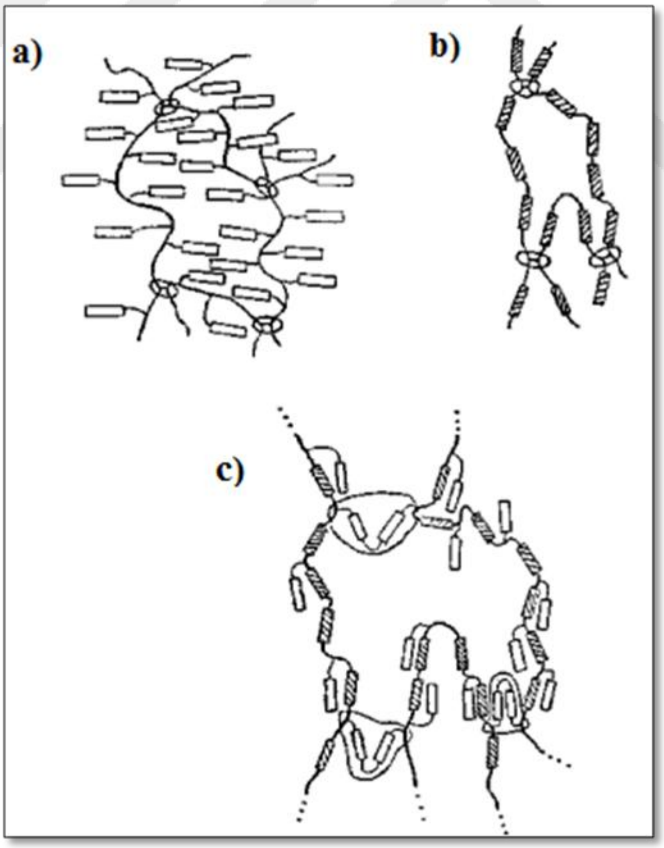

Figure 1.12 Different type of liquid crystalline elastomers; a) side-chain, b) main-chain, and c) combined (main-chain/side-chain), the cross-linked points were circled (Finkelmann and Rehage, 1980).

For the last decade this research field has potential application areas; smart material for turning optical or electrical energy into mechanical energy such as electrically switchable color-tunable reflectors, electro- or photo-controllable nano- or micro-machinery, artificial muscles, light scattering electro-optical switches, etc.

1.2 Natural Electroactive Polymers

The most abundant natural polymers on the earth are cellulose, chitin, and starch. The natural polymers are renewable and eco-friendly. And also these natural polymers exhibit electroactive properties (Finkenstadt, 2005). Biopolymers have many application areas like as energetic applications, environmentally sensitive membranes, controlled release devices, electroactive polymers and mimic materials (Finkenstadt and Willett, 2005).

1.2.1 Cellulose

Cellulose (Cel) is a linear polymer that is formed by β-(1-4)-glycosidic linkages. Molecular structure of cellulose was indicated in Figure 1.13. It can be produced with different way such as isolating from plant, biosynthesis with different microorganisms, the chemosynthesis from glucose and enzymatic in vitro synthesis starting from cellobiosyl fluoride (Tsuchida and Yoshinaga, 1997; Eichhorn et al., 2001; Cai, Hou, & Yang, 2012).

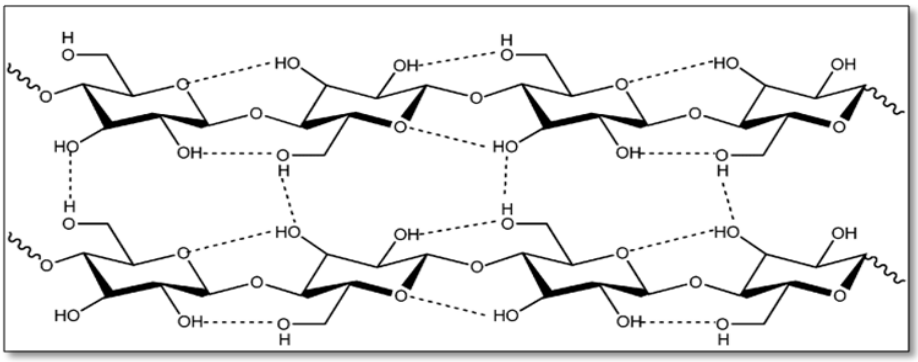

Figure 1.13 Molecular structure of cellulose with intermolecular and intramolecular hydrogen bonds (Wang, Gurau, & Rogers, 2012).

It provides many advantages to industrial applications such as renewability and being abundant (Klemm, Heublein, Fink, & Bohn, 2005). It is also biocompatible and biodegradable. Because of having these invaluable advantages make it valuable in many applications in polymer industries, filter membrane, pharmaceutics, in paper (Swatloski, Spear, Holbrey, & Rogers, 2002). In spite of these valuable properties handling of cellulose is difficult due to dissolving problems because of the hydrogen bondings and crystalline structure (Cao et al., 2009). There are few dissolving methods for cellulose. Conventional methods for dissolving cellulose include the cuprammonium and xanthenes processes and require the use of unusual solvents, typically with high ionic strength and use relatively harsh conditions. They were also expensive and inaduquate for dissolution of cellulose (Heinze and Liebert, 2001; Swatloski et al., 2002; Wu et al., 2004; Zhang, Wu, Zhang, & He, 2005; Zhu et al., 2006). In addition to these disadvantages they give serious hazards to environment (Zhang et al., 2005).

Dissolving system known for cellulose are LiCl/1,3-dimethyl-2-imidazolidinone (DMI), (LiCl)/ N,N-dimethylacetamide (DMAc), LiCl/N-methyl-2-pyrrolidine, DMSO/paraformaldehyde, dimethylsulfoxide (DMSO)/tetrabutylammonium fluoridetrihydrate, aqueous solutions of NaOH, some aqueous solutions of metal complexes, some molten salt hydrates such as $LiClO_4.3H_2O$, and $LiSCN.2H_2O$ (Heinze and Liebert, 2001), N-methylmorpholine oxide (NMMO) (Wang et al., 2012; Finkelmann et al., 2001), and N,N-dimethylformamide/nitrous tetroxide (DMF/N_2O_4) (Wang et al., 2012). Molecular structure of solvents for cellulose dissolution was given in Figure 1.14. Some of these dissolution solvents are toxic, unstable during cellulose processing, volatile, and difficult for recovery (Cao, Wu, Zhang, Li, Zhang, & He, 2009).These problems required the new "green" cellulose dissolving method.

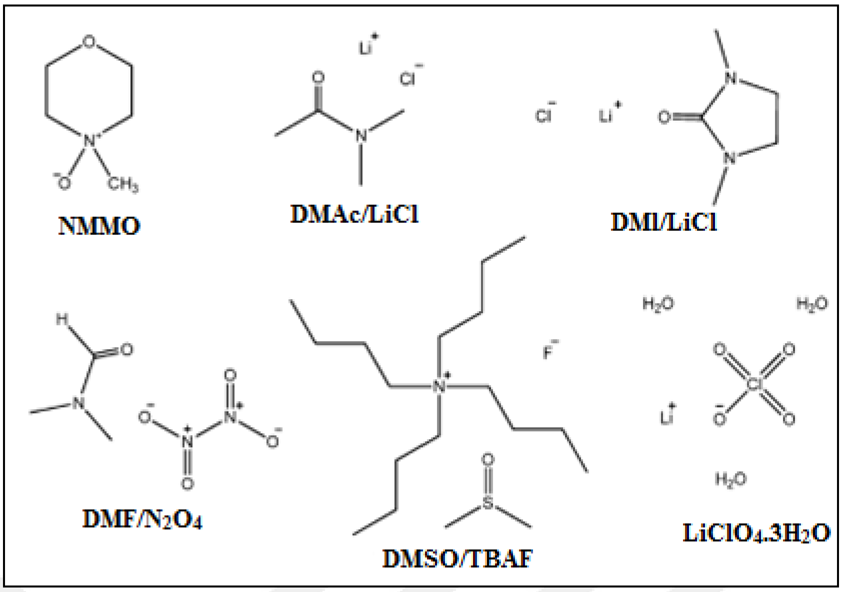

Figure 1.14 Molecular structure of solvents for cellulose dissolution (Wang et al., 2012).

Ionic liquids (ILs) are salts that fluid below or around 100°C (Seddon, 1997; Rogers and Seddon, 2003). Most of the ILs has wide electrochemical window, low vapor pressure, high thermal stability, wide liquid range and high solvation ability to solve kindly inorganic and organic substances (Welton, 1999; Dupont, de Souza & Suarez, 2002; Kosmulski, Gustafsson, & Rosenholm, 2004).

Cellulose can be dissolve in IL without any addition such as water, ethanol, methanol, acetone, acetonitrile etc. (Swatloski et al., 2002; Zhang et al., 2005; Mäki-Arvela, Anugwom, Virtanen, Sjöholm, & Mikkola, 2010; Xu, Wang, & Wang, 2010; Wang et al., 2012).

1-ethyl-3-methylimidazolium diethylphosphonate ([EMIM]DEP) is a room temperature ionic liquid. [EMIM]DEP is a suitable solvent for cellulose dissolution (Zhao et al., 2012).

1.2.1.1 Ionic Liquids

The ionic liquids (ILs) are used as greener organic solvent due to negligible vapor pressures, high chemical and thermal stability, excellent dissolution capability, nonflammability, and broad liquid range (Dias et al., 2013). The ILs have wide application areas such as polymer chemistry (Zhang, Li, Feng, Zhou, & Nie, 2014), electrochemistry (Galiński, Lewandowski, & Stępniak, 2006; Sasi, Rao, & Devaki, 2014), drug delivery (Dias et al., 2013), and many applications. ILs are often classified as green solvent (Deetlefs and Seddon, 2006; Tundo, Perosa, & Zecchini, 2007).

The ILs which is liquid at room temperature is called as room temperature ionic liquids (RTILs). The physicochemical properties are the same as other high temperature ILs. The RTILs are usually quaternary ammonium salts like tetraalkylammonium $[R_4N]^+$, or cyclic amines, aromatic (pyridiniumi imidazolium), saturated (piperidinium, pyrrolidinium). ILs are shown in Figure 1.15 (Galiński et al., 2006).

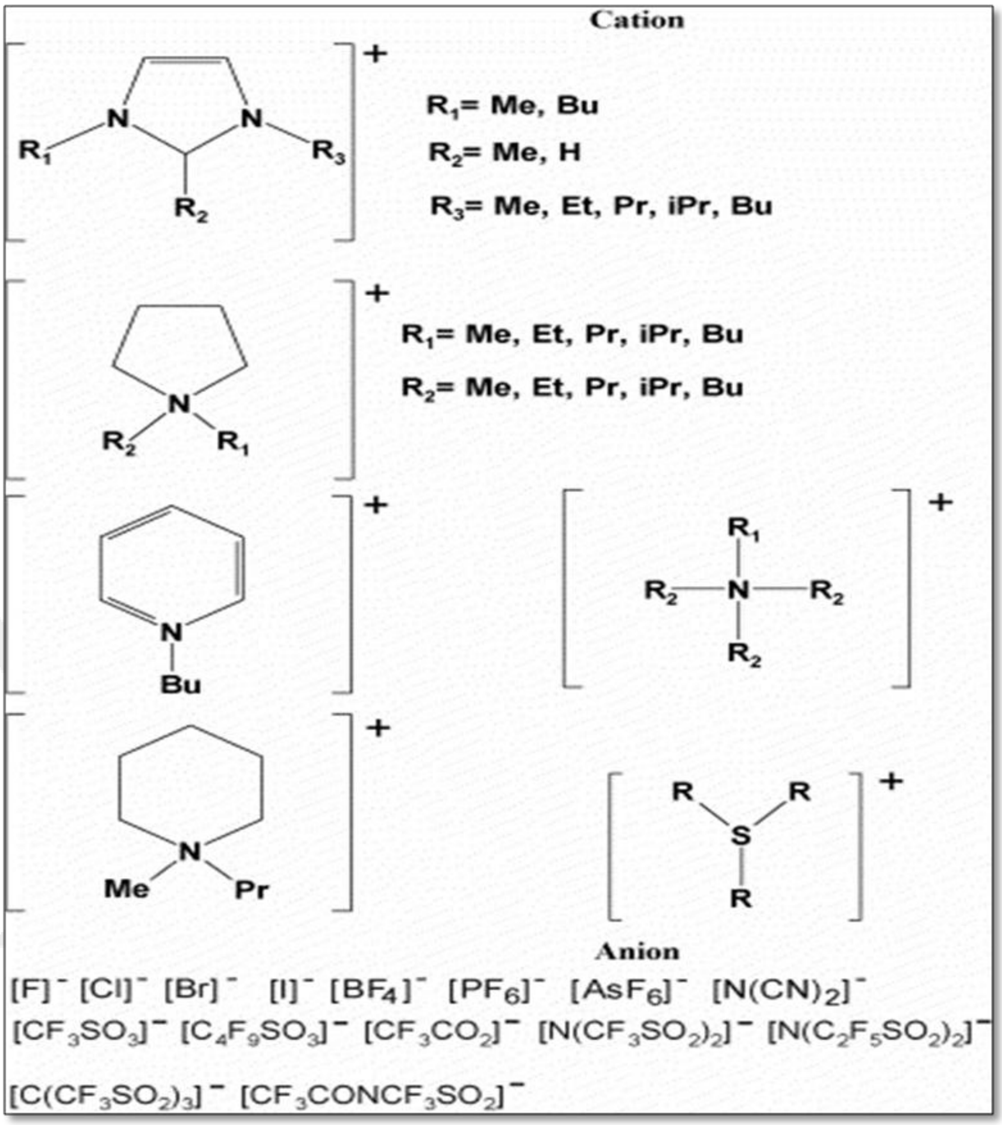

Figure 1.15 Ionic liquids (Galiński et al., 2006).

2.2.2 Chitosan

Chitosan (Chi) is a biopolymer obtained by deacetylation of chitin. The chitin is the most abundant biopolymer after the cellulose. The chitosan is biodegradable, biocompatible, and abundant natural cationic polyelectrolyte (Koev et al., 2010). The chemical structure of chitin and chitosan was exhibited in Figure 1.16.

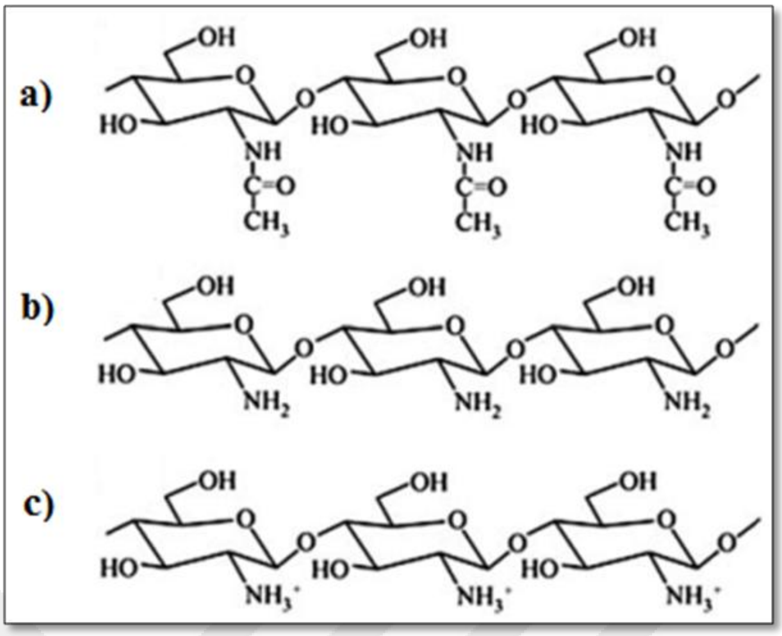

Figure 1.16 Chemical structure of a) chitin, b) chitosan, and c) protonated chitosan (Koev et al., 2010).

The amine groups of chitosan are protonated and so become soluble below the pH 6.5 and the amine groups are deprotonated above this pH value (Koev et al., 2010). The amino and hydroxyl groups on backbone of chitosan make chitosan hydrophilic and polycationic (Wang, Chen, & Kim, 2007). Chitosan has many application areas including electroactive polymers (Siqueira et al., 2006; Cai and Kim, 2008; Shang, Shao, & Chen, 2008; Jang, Kim, Zhijiang, & Kim, 2009) due to having functional groups like amides, alcohols, and free amine groups (Jeon, Cheedarala, Kee, & Oh, 2013).

Wang et al. (Wang et al., 2007) prepared an electroactive paper based on chitosan and cellulose. They investigated the effect of acetic acid concentration which is used for dissolution of chitosan. And also the effect of frequency, humidity, voltage, and time were investigated in this study. The results show that actuation performance increased with the increasing humidity and voltage (Wang et al., 2007).

Lu and Chen (Lu and Chen, 2010) fabricated composite ionic actuator. The fabrication of ionic actuator was summarized in Figure 1.17. Multi walled carbon nanotubes were wrapped by chitosan and so the conductive electrode was fabricated. The electrolyte was fabricated using the mixture of chitosan, glycerol, and ionic liquid. The results show that the composite ionic actuator exhibited the considerable actuation performance under the low actuation voltages (Lu and Chen, 2010).

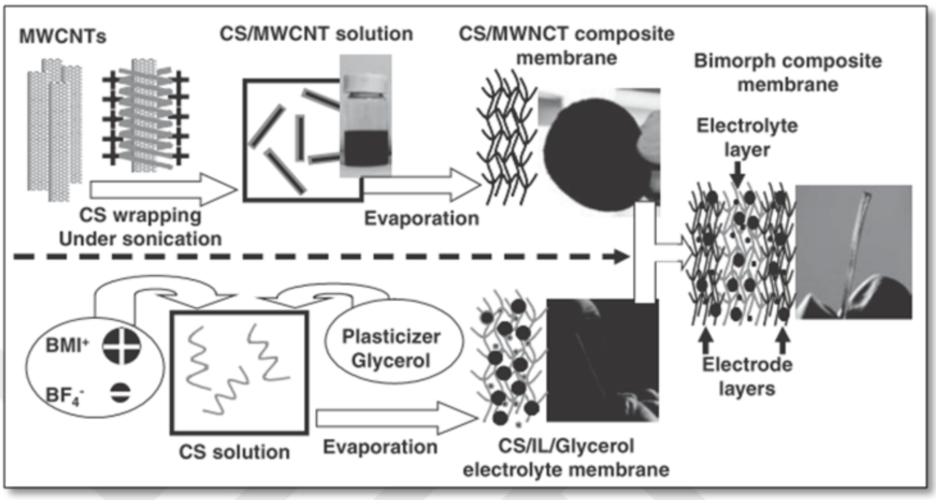

Figure 1.17 Fabrication of composite ionic actuator (Lu and Chen, 2010).

Kim et al. prepared an electroactive paper actuator based on cellulose-chitosan laminated film. The film was coated with gold. SEM micrograph of electroactive paper was shown in Figure 1.18. The effect of free ions Cl^-, NO_3^-, and CF_3COO^- was investigated. The results showed that type of free ions affected the actuation. The best actuation was obtained for Cl^- free ion (Kim, Wang, & Chen, 2007).

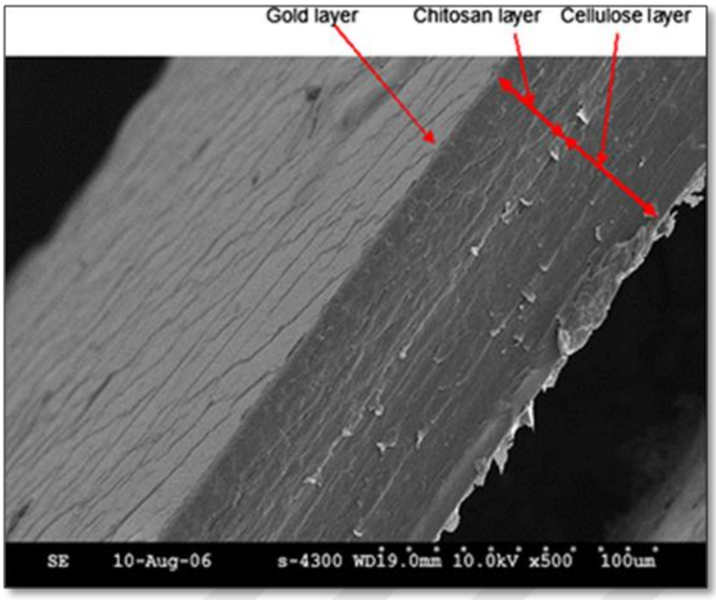

Figure 1.18 SEM photograph of cellulose-chitosan laminated electroactive paper (Kim et al., 2007).

CHAPTER TWO

MATERIALS AND METHODS

2.1 Materials

Cellulose, 1-ethyl-3-methylimidazolium diethylphosphonate ([EMIM]DEP) and N, N dimethyle acetamid (DMAc) were purchased from Sigma-Aldrich. Graphene (Gr), with an average particle diameter of 5–10 µm, was purchased from Grafen Kimya Sanayi A.Ş. Gold leaf which has a thickness of 10µm was obtained from L.A. Gold leaf (Akar et al., 2015; Altınkaya et al., 2016). Chitosan (low-viscousity, 50494), acetic acid (≥99.85%), N, N'-methylenebisacrylamide (146072-100G), N,N,N′,N′-tetramethylethylenediamine (T22500) (TEMED), ammonium persulfate (248614) (APS), poly(diallyldimethylammonium chloride) [pDADMAC] [20 wt. % in H_2O], and polyethylene glycol (PEG) with average molecular weight of 1450 g/mol were purchased from Sigma-Aldrich (Akar et al., 2015; Altınkaya et al., 2016).

2.2 Fabrication of Cellulose and Chitosan-Based Films and Actuators

2.2.1 Fabrication of Cel-Based IPMC Actuators

0.39 g cellulose was dissolved in 5.58 g [EMIM]DEP in water bath at about 100 °C. 3 mL DMAc as a plasticizer was added to clear solution and mixed for 1 hour. Different ratios of Gr with 0.2, 0.4, and 0.6 wt% of total mass material were added the solution and well dispersed by ultrasonic processer (20 amplitude (A) with 1 cycle for 1min. and 50A with 1 cycle for 2 min). Then the wet film was obtained using film maker, thickness of the films was set as 1.0 mm. The wet film was dried at room temperature for 18 hours and thus film was obtained. Two sides of the film were wrapped with gold leaves to fabricate ionic polymer metal composites (IPMC).

2.2.2 Fabrication of Chi-Based IPMC Actuators

For the preparation of 2.3% (w/v) chitosan solution; chitosan was dissolved in 2% (v/v) acetic acid and stirred overnight at room temperature. Appropriate amounts of PEG and pDADMAC were added to the 2.3% (w/v) chitosan solution. On the other hand, 0.0123g of MBA was dissolved in 1.87 mL distilled water, and 0.230 mL of 4.34% (v/v) TEMED and 0.15 mL of 0.876 M APS solutions were added to the MBA solution (Akar et al., 2015; Altınkaya et al., 2016). The mixture was soaked in water bath at 100 °C for 20 min. Then it was added to the chitosan solution and stirred for 24 h at room temperature. The mixture was poured into the petri dish and dried in vacuum oven at 80 °C for 16 h.

The above mentioned method was carried out again by using 0.032g and 0.1 g of MBA as crosslinker. The samples including 0.0123 g, 0.032 g, and 0.1 g of MBA were called as ChiPM-1, ChiPM-2, and ChiPM-3, respectively. Two side of the films were wrapped with gold leaf to create fabricate chitosan-based actuators (Altınkaya et al., 2016).

2.2.3 Fabrication of Chi-Based IPMC Actuators Including Different Amount of pDADMAc

For the preparation of 2.3% (w/v) chitosan solution; chitosan was dissolved in 2% (v/v) acetic acid and stirred overnight at room temperature. Afterwards, appropriate amounts of PEG, pDADMAC, and 0.25 μL [EMIM]DEP were added to 65 mL to the 2.3% (w/v) chitosan solution. On the other hand, 0.032g of MBA was dissolved in 1.87 mL distilled water, and 0.230 mL of 4.34% (v/v) TEMED and 0.15 mL of 0.876 M APS solutions were added to the MBA solution. The mixture was soaked in water bath at 100 °C for 20 min, and then added to the chitosan solution. Afterwards, the mixture was stirred for 24 h at room temperature and poured into petri dish, and dried in vacuum oven at 80 °C for 16 h (Altınkaya et al., 2016).

The fabricated samples including 0.25, 0.50, and 0.75 mL pDADMAC were called as ChiPM-25, ChiPM-50, and ChiPM-75 (Altınkaya et al., 2016). The samples were wrapped with gold leaves to fabricate IPMC (Akar et al., 2015; Altınkaya et al., 2016).

2.3 Fourier Transform Infrared Spectroscopy (FTIR) Analysis

FTIR spectra of cellulose membrane were analyzed by using FTIR (Perkin Elmer Spectrum BX-II) The spectra were recorded with the sum of 25 scans at a resolution of 4 cm^{-1} in the range of 4000–400 cm^{-1} (Akar et al., 2015; Altınkaya et al., 2016).

2.4. X-Ray Diffraction Analysis (XRD)

The XRD instrument was set to operate in continuous PSD fast scan mode. A Cu-Kα a radiation (λ=1.54 Å) generated at a 30 kV voltage and the films were scanned from 0° to 70° (2θ). The scan step size is 0.012º and duration were set is 14.4 s, respectively. The crystallinity values were investigated by the DIFFRAC.EVA V3.0 software (Akar et al., 2015; Altınkaya et al., 2016).

2.5. Thermogravimetric Analysis (TGA)

Thermal behavior of cellulose membrane was examined by using TGA (Shimadzu, TGA 50). Thermogravimetric analysis (TGA) was performed at a heating rate of 10 ^{0}C/min range from 30 to 600 ^{0}C under nitrogen atmosphere with a flow rate of 1.0 mL/min (Akar et al., 2015; Altınkaya et al., 2016).

2.6 Scanning Electron Microscopy (SEM)

SEM analysis and cross-sections of samples were conducted by using Quanta FEG 250 scanning electron microscope at an accelerating voltage of 5 kV (Akar et al., 2015; Altınkaya et al., 2016).

2.7. Mechanical Properties

The tensile strength and tensile modulus were determined by a Shimadzu universal testing machine with a 100N load cell at a crosshead speed of 0.1 mm/min (Akar et al., 2015; Altınkaya et al., 2016). Four samples, with size of 10x40 mm, were cut from gold leaf coated samples.

2.8 Dynamic Mechanic Analysis (DMA)

DMA Analyses of the films were evaluated by using TA Instrument Q800 Dynamic Mechanical Analyzer. Specimens (13 mm x 6.40 mm x 0.10 mm) were measured in film tension mode at a frequency of 1 Hz. The films were heated from 20 to 200 °C at a heating rate of 10 °C/min (Akar et al., 2015; Altınkaya et al., 2016).

2.9 Actuator Characterization

For electroactive capabilities such as moving and generating force of samples were investigated. Movement of the actuator films were observed by machine vision system, which includes a camera (Basler acA2040-180km camera) and a frame grabber (NI PXIe-1435) running on industrial PC (Computer M0814-MP - 8mm – F1.4 lens) (Akar et al., 2015; Altınkaya et al., 2016). The blocking force of the actuator was measured via a precision balance (Precisa 225SM-DR). For both blocking force and tip displacement tests, the input signals were generated via analog output card (NIPXIe-9133pc) and amplified with a buffer (TDA2040). All the input/output and control codes were developed by ourselves. The vision data were analyzed using Kinovea. All tip displacement and blocking force experiments were carried out in air at room temperature (Akar et al., 2015; Altınkaya et al., 2016).

CHAPTER THREE
RESULTS AND DISCUSSION

3.1 Cel-based IPMC actuators

3.1.1 Fourier Transform Infrared Spectroscopy (FTIR) Analysis

Figure 3.1 shows the FTIR spectra of Cel, Cel-PO_4-Gr0.2, Cel-PO_4-Gr0.4, and Cel-PO_4-Gr0.6. In the FTIR spectra of cellulose, a broad band between 3600-3200 cm^{-1} indicates the -OH stretching vibrations. The sharp peak at 3342 cm^{-1} can be related with the -OH stretching vibrations due to the intramolecular hydrogen bonds (Li and Renneckar, 2011; Khan et al., 2012). The absorption bands between 3000-2800 cm^{-1} and 1500-1250 cm^{-1} are attributed to the C-H and C-H_2 stretching vibration, respectively (Nikonenko, Buslov, Sushko, & Zhbankov, 2000; Wang and Roman, 2011; Khan et al., 2012). The absorption band around the 1630 cm^{-1} is caused by the presence of water (Naboka, Sanz-Velasco, Lundgren, Enoksson, & Gatenholm, 2012). The band at around the 1160 cm^{-1} is originated from C-O-C stretching vibration. The band at 1042 cm^{-1} is related to C-O stretching vibration (Kondo, 1997; Nikonenko et al. 2000; Nikonenko, Buslov, Sushko, & Zhbankov, 2005; Khan et al., 2012). For [EMIM]DEP, the absorption band between 1505 and 1590 cm^{-1} at around 1570 cm^{-1} is due to stretching vibration of phosphate group $(PO_4)^{3-}$ (Trchová, Šeděnková, Morávková, & Stejskal, 2014). The P-O stretching vibration is observed between 1200-900 cm^{-1} (Abdu, Hull, Fayek, & Hawthorne, 2011; Pisarski, Żur, & Pisarska, 2011). The band between 1200-1250 cm^{-1} is assigned to asymmetric stretching vibration of P=O (Pisarski et al., 2011; Akar et al., 2015; Altınkaya et al., 2016).

Addition of [EMIM]DEP, graphene and DMAc led to some changes in FTIR spectrum of cellulose. The formation of new absorption bands were observed at 1570, 1216, 944 and 794 cm^{-1}. It was observed that the bands at 1436, 1366, 1164 and 1042 cm^{-1} shifted to the bands at around 1450, 1390, 1169 and 1056 cm^{-1}, respectively. And also it can be seen that there are some changes in the spectra of samples after the addition of graphene. The intensity of the absorption bands at around 3400 and 1366 cm^{-1} decreased depending on graphene concentration. The strong vibration band at 1042 cm^{-1}, which is assigned to C-O stretching in cellulose, shifted to 1056, 1047 and 1052 cm^{-1} after graphene loadings of 0.2, 0.4, and 0.6 wt.%, respectively (Akar et al., 2015; Altınkaya et al., 2016).

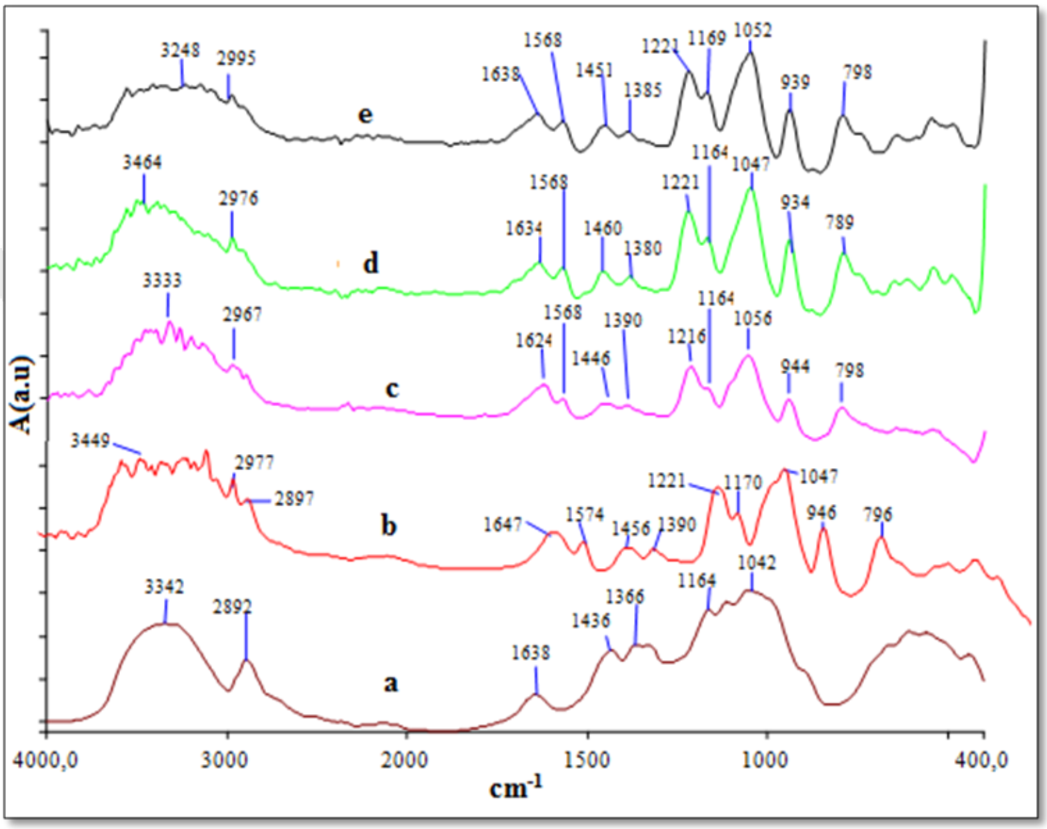

Figure 3.1 FTIR spectra of samples (a) Cel, b) Cel-PO$_4$, c) Cel-PO4-Gr0.2, d) Cel-PO4-Gr0.4, and e) Cel-PO4-Gr0.6 (Akar et al., 2015).

3.1.2 X-Ray Diffraction Analysis (XRD)

The XRD patterns of the samples were shown in Figure 3.2, 3.3, and 3.4. The main 2θ degrees of the samples are 22.5°, 23.5°, 23°, 24.45° and 24.5° for Cel, Cel-PO$_4$, Cel-PO$_4$-Gr0.2, Cel-PO$_4$-Gr0.4, and Cel-PO$_4$-Gr0.6, respectively. Cellulose has two main peaks in XRD pattern while other samples have only one. The main peaks of cellulose were seen at 2θ=22.5° and 2θ=14.5° (Kim et al., 2010). The small mean peak at 2θ=14.5° was disappeared after the treatment with ionic liquid and graphene, and the mean peak at 2θ=22.5° shifted to 23.5°, 23°, 24.45°, and 24.5° for Cel-PO_4, Cel-PO_4-Gr0.2, Cel-PO_4-Gr0.4, and Cel-PO_4-Gr0.6, respectively. Addition of ionic liquid and graphene increased the 2θ degree of the cellulose (Akar et al., 2015).

The crystallinity (%) of the cellulose was calculated by using XRD peak height method with the following equation (Terinte, Ibbett,& Schuster, 2011):

$$C = 100 * (I_{200} - I_{non-cr})/I_{200} \tag{3.1}$$

C indicates the apparent crystallinity (%), I_{200} indicates the maximum intensity of peak, I_{non-cr} gives the intensity of non crystalline component. Figure 3.2 explains the XRD peak height method schematically (Akar et al., 2015).

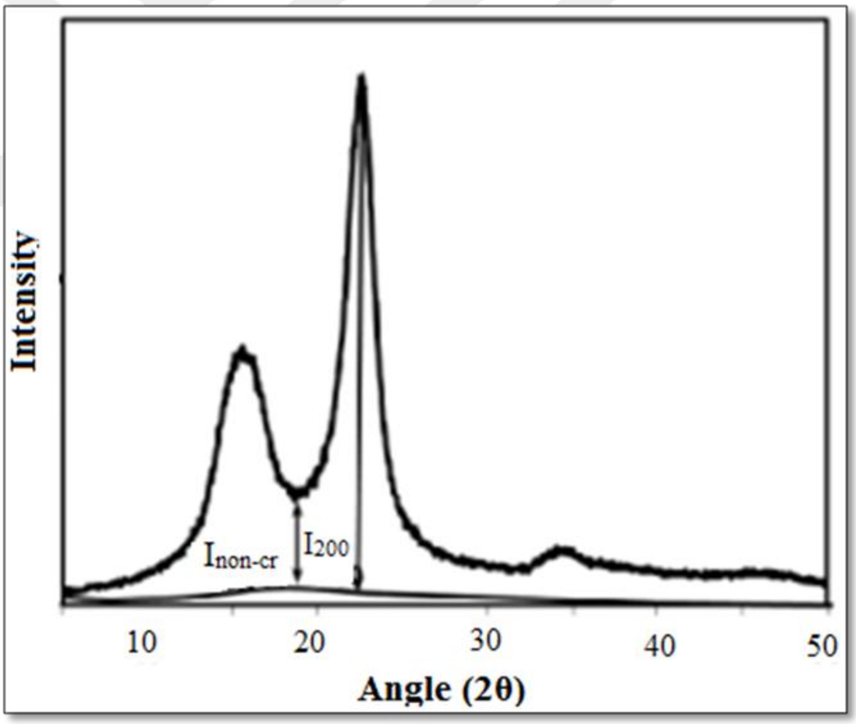

Figure 3.2 The explaining of XRD peak height method for calculation of crystallinity index (Terinte et al., 2011).

Table 3.1 The XRD values of Cel based samples

Samples	**2θ**		**CI %**
Cel	22.5	14.5	83
Cel-PO_4	23.5		23
Cel-PO_4-Gr0.2	23		17
Cel-PO_4-Gr0.4	24.5		34
Cel-PO_4-Gr0.6	24.5		38

The considerable decrease in crystallinity index of cellulose was observed after film formation. The % crystallinity index of cellulose was calculated as % 82.71. Sen et al. found the similar result for cellulose (Sen et al., 2015). Addition of ionic liquid decreased the % crystallinity index of cellulose. Addition of 0.2 wt.% graphene into Cel-PO_4 sample decreased the crystallinity of the Cel-PO_4. However, when 0.4 and 0.6 wt.% of graphene were loaded into cellulose the increasing in % CI were observed (Akar et al., 2015).

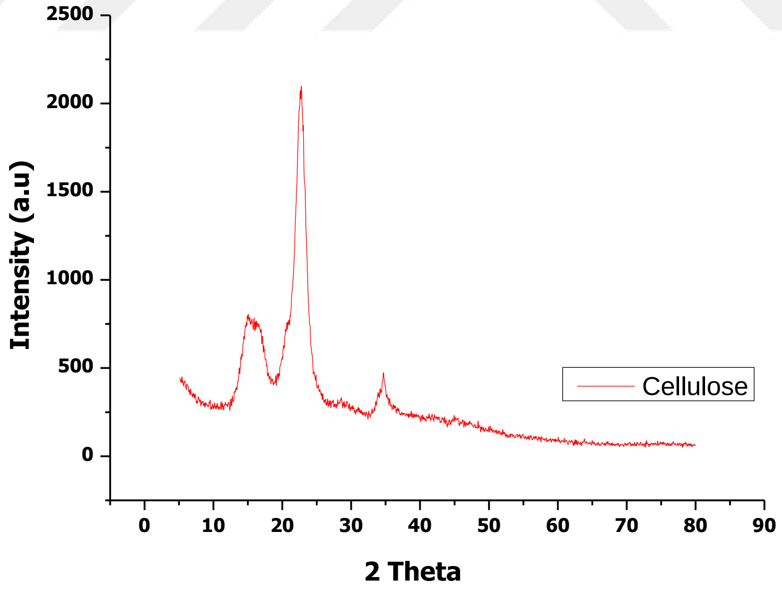

Figure 3.3 XRD pattern of cellulose.

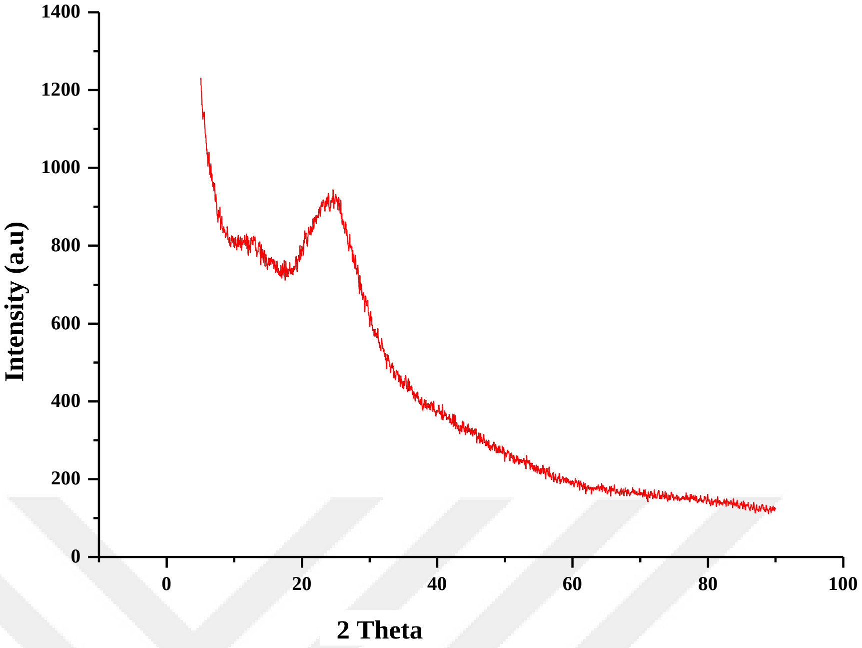

Figure 3.4 XRD pattern of Cel-PO$_4$.

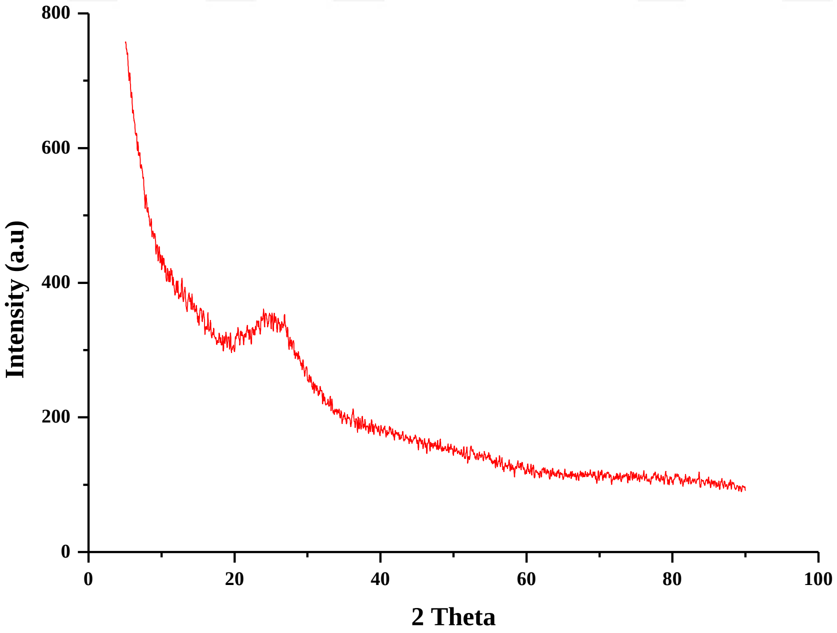

Figure 3.5 XRD pattern of Cel-PO$_4$-Gr0.2.

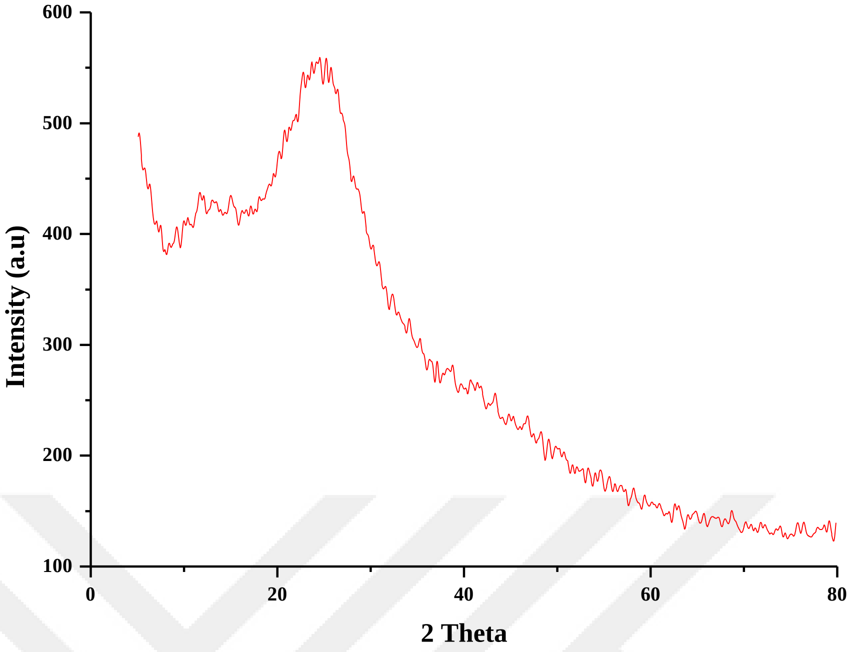

Figure 3.6 XRD pattern of Cel-PO_4-Gr0.4.

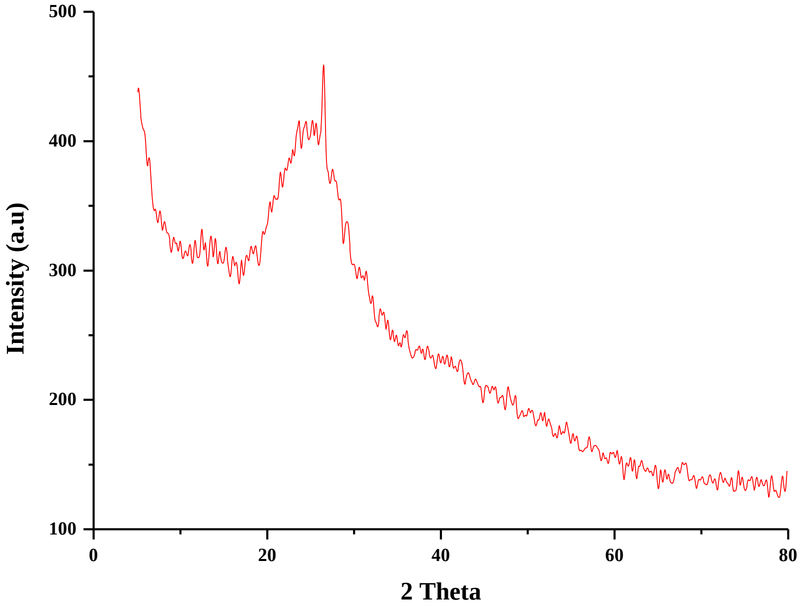

Figure 3.7 XRD pattern of Cel-PO_4-Gr0.6.

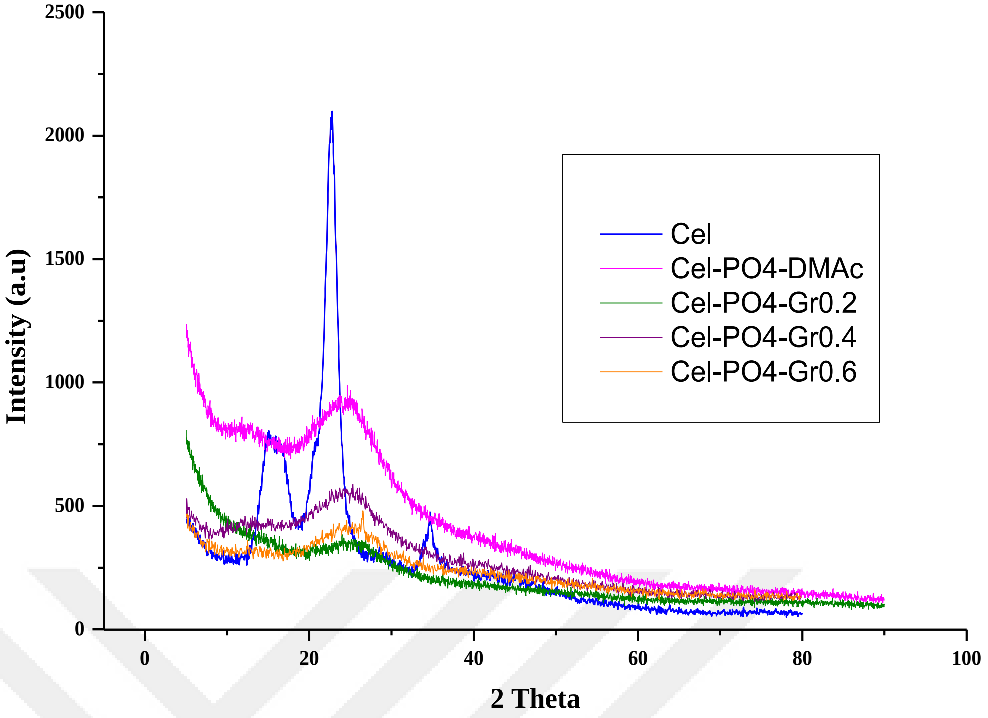

Figure 3.8 X-Ray patterns of Cellulose, Cel-PO_4, Cel-PO_4-Gr0.2, Cel-PO_4Gr0.4, and Cel-PO_4Gr 0.6 (Akar et al., 2015).

3.1.3 Thermogravimetric Analysis (TGA)

Figure 3.9 shows TGA curves of Cel, Cel-PO_4, Cel-PO_4-Gr0.2, Cel-PO_4Gr0.4, and Cel-PO_4Gr0.6 (Akar et al., 2015). The related TGA data of samples obtained from derivative thermogravimetric (DTG) curves, which were presented in Figures 3.9-3.14, were summarized in Table 3.1. The mass loss of the cellulose occurs in two stages (Akar et al., 2015). The first stage is resulted from evaporation of trapped moisture in cellulose (Sullivan and Ball, 2012). The second stage of the mass loss is due to the thermal decomposition of cellulose (Huang, 2012; Huang et al., 2012). The first mass losses of the samples are 1, 20, 21, 18, and 19 % for Cel, Cel-PO_4, Cel-PO_4-Gr0.2, Cel-PO_4-Gr0.4, and Cel-PO_4-Gr0.6, respectively. The increase in trapped moisture of the samples resulted from the hydrophilicity of the EMIMDEP ionic liquid (Nakashima et al., 2011).

Table 3.2. TGA data of the samples

Sample	**Mass Loss (25-110^{o}C)**	**Mass Loss (25-600^{o}C)**	**Mass Loss (up to T_{max})**	**$T_{initial}$**	**T_{max}**	**T_{final}**
Cel	1	88	38	312	340	364
Cel-PO_4	20	67	72	247	283	319
Cel-PO_4-Gr0.2	21	58	65	244	281	320
Cel-PO_4-Gr0.4	18	62	70	243	276	312
Cel-PO_4-G0.6	19	60	59	241	279	344

Cellulose began to decompose at 312 ^{o}C while the Cel-PO_4, Cel-PO_4-Gr0.2, Cel-PO_4Gr0.4, and Cel-PO_4Gr0.6 started to decompose at around 245 ^{o}C. As can be seen in Table 3.1, thermal stability of the Cel-PO_4 and graphene loaded Cel-PO_4 (279-283 ^{o}C) was lower than that of original cellulose (340 ^{o}C) on the basis of maximum decomposition temperatures (Akar et al., 2015). The decrease in the thermal stability was probably due to the partial destruction of crystalline part and hydrolysis of the cellulose (Zhao et al., 2012). However, graphene loading into Cel-PO_4 has not led to significant variation in maximum decomposition temperature. Besides, graphene loading of 0.6 wt.% decreased the initial decomposition temperature of Cel-PO_4 by 6°C. The decrease in thermal stability of graphene loaded samples can also be associated with the catalyzing effect of the graphene on thermal decomposition of Cel- PO_4 (Castelaín, Martínez, Ellis, & Salavagione, 2013; Akar et al., 2015; Altınkaya et al., 2016).

The mass losses in the temprature range 25-600°C for Cel, Cel-PO_4, Cel-PO_4-Gr0.2, Cel-PO_4-Gr0.4, and Cel-PO_4-Gr0.6 are 88.2, 67.3, 57.6, 62.3, and 59.6%, respectively. The total mass loss of cellulose is higher than those of Cel-PO_4 and graphene loaded Cel-PO_4 samples. The char residue of cellulose, Cel, Cel-PO_4, Cel-PO_4-Gr0.2, Cel-PO_4Gr0.4, and Cel-PO_4Gr0.6 were obtained to be 11.8, 32.7, 42.4, 37.7, and 40.4%, respectively. It is seen that graphene loading into Cel-PO_4 sligthly increased the pyrolysis residue. Since the formation of the char layer is important for thermal insulation and flame retardant properties of samples, it can be expected that graphene loading into Cel-PO_4 has led to better thermal insulation and flame retardant properties (Huang et al., 2012;Akar et al., 2015; Altınkaya et al., 2016).

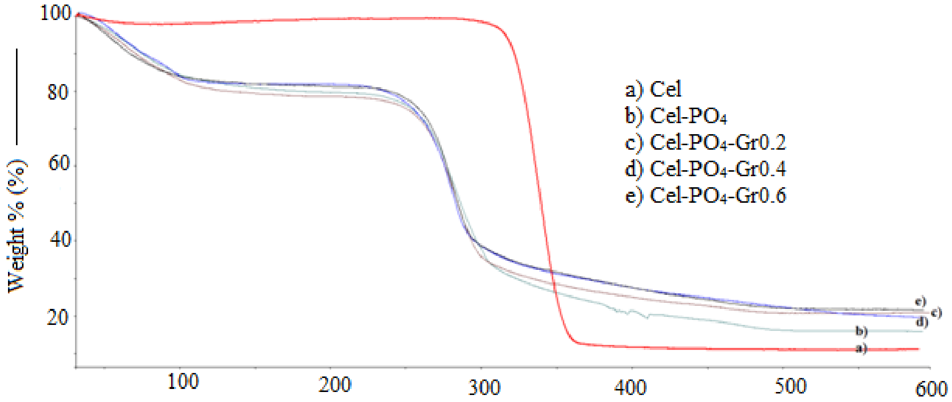

Figure 3.9 Thermograms of samples. a) Cel, b) Cel-PO_4, c) Cel-PO_4-Gr0.2, d) Cel-PO_4-Gr0.4, and e) Cel-PO_4-Gr0.6 (Akar et al., 2015).

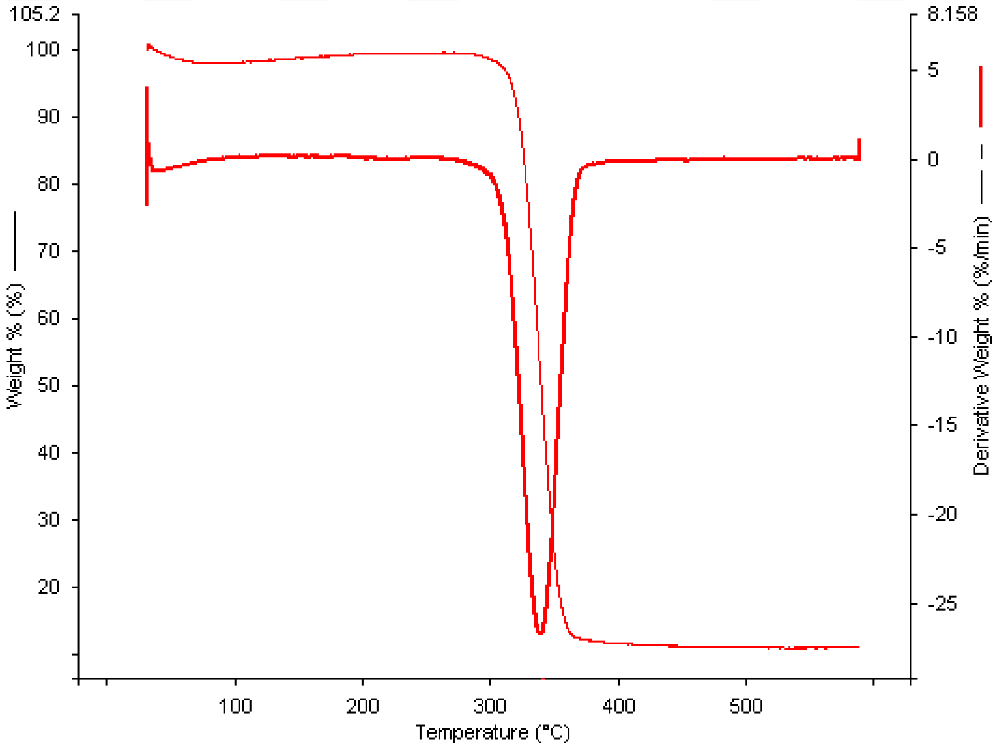

Figure 3.10 TG and DTG curves of cellulose.

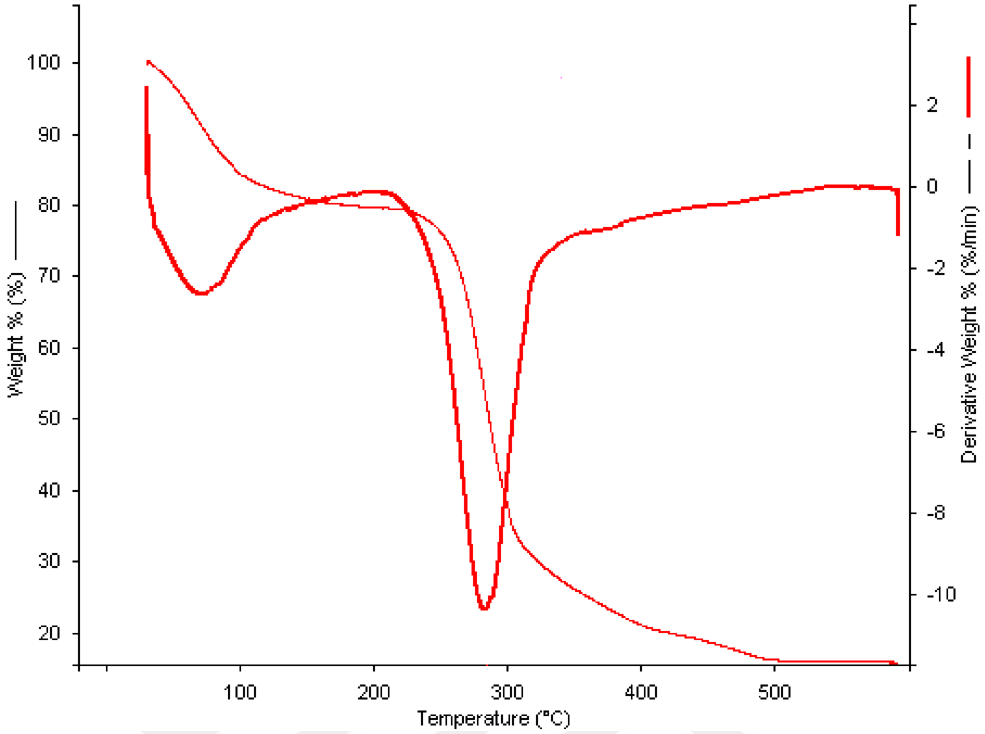

Figure 3.11 TG and DTG curves of Cel-PO$_4$.

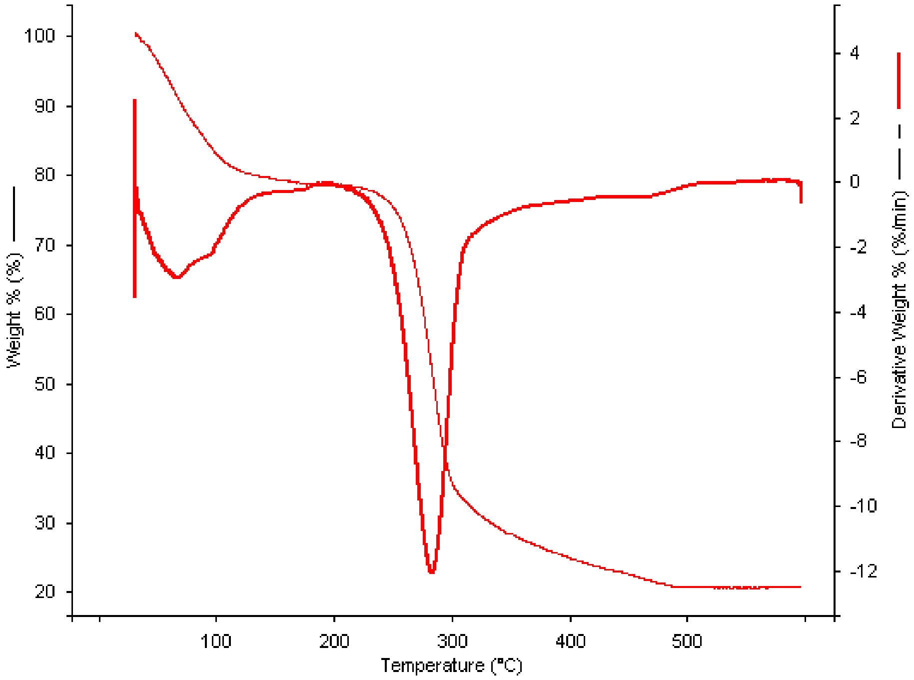

Figure 3.12 TG and DTG curves of Cel-PO$_4$-Gr0.2.

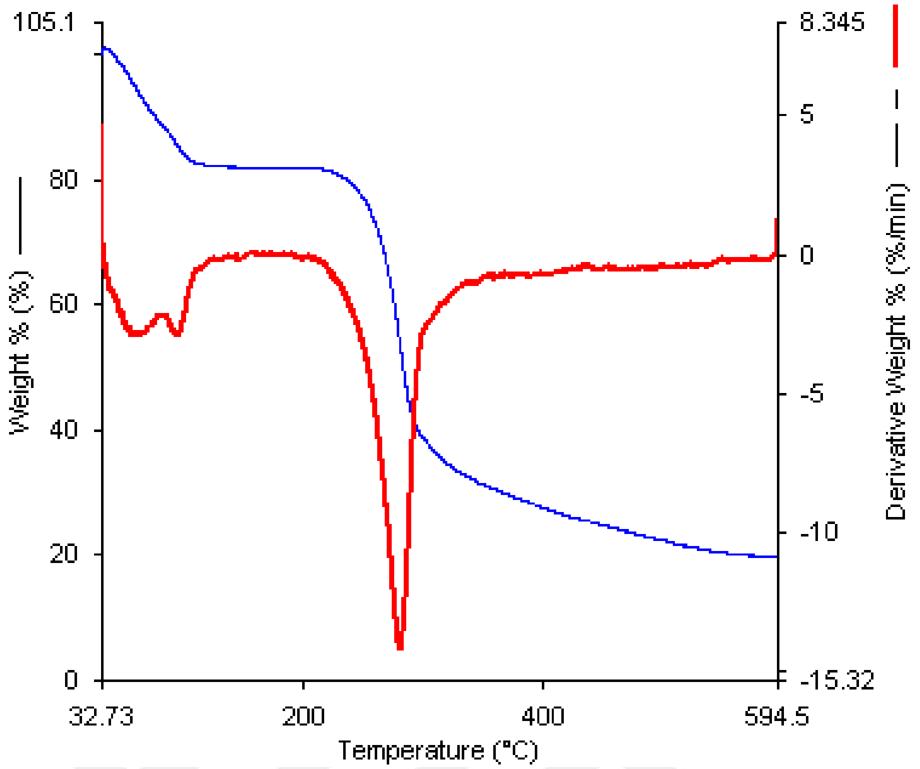

Figure 3.13 TG and DTG curves of Cel-PO$_4$-Gr0.4.

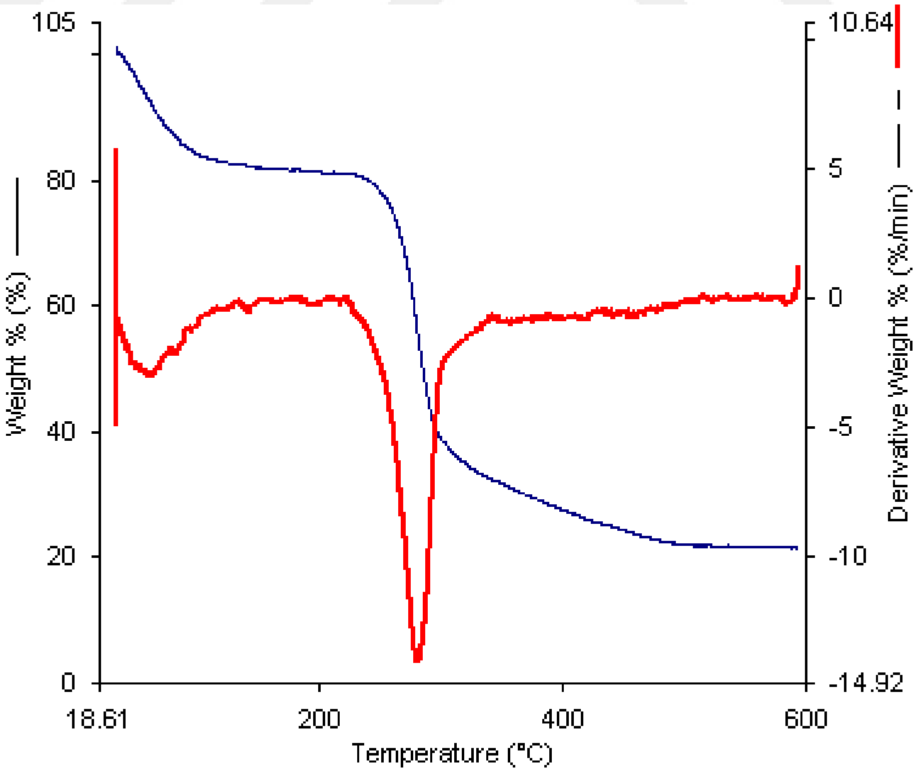

Figure 3.14 TG and DTG curves of Cel-PO$_4$-Gr0.6.

3.1.4 Scanning Electron Microscopy (SEM)

SEM micrographs of graphene, Cel-PO_4, and Gr loaded Cel-PO_4 films were shown in Figure 3.15, and 3.16. Graphene flakes can be clearly seen in Figure 3.15 a-d. As can be seen from Figure 3.16 (a, b, and e,) film surfaces seem to be smooth and fairly homogenous without any pores. In order to see the graphene particles, cross-section of films (Figure 3.16c, 3.16d, 3.16f, 3.16g, and 3.16h) were examined by SEM analysis. Closer examination on the cross-section of films is given in Figure 3.16d, 3.16f, and 3.16h for Cel-PO_4-Gr0.2, Cel-PO_4-Gr0.4, and Cel-PO_4-Gr0.6, respectively. Graphene particles cannot be seen on the surface of films and cross-section of films even at high magnifications. It may be due to the homogeneous distribution of graphene in the samples (Akar et al., 2015).

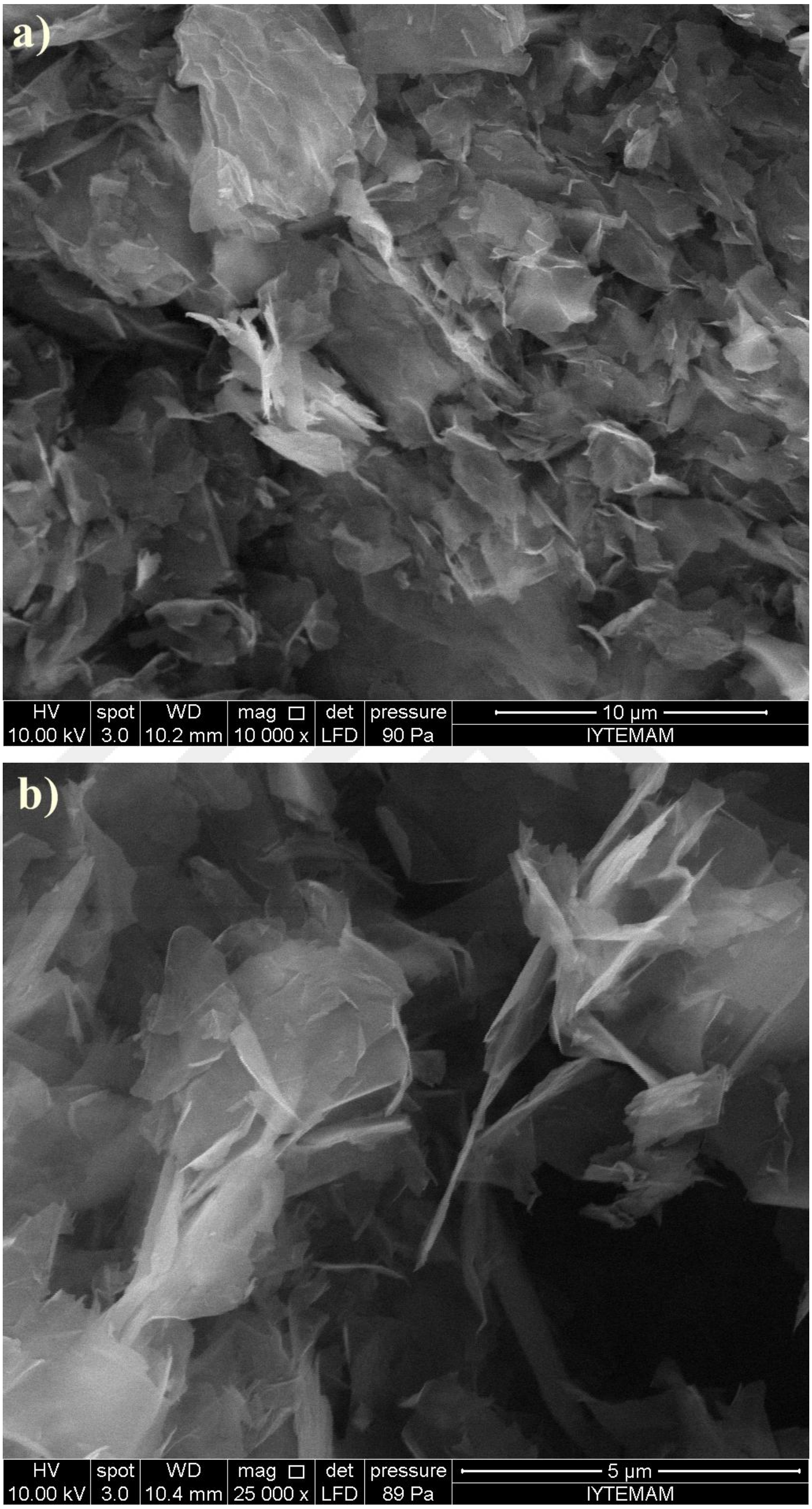

Figure 3.15 SEM micrographs of graphene a) x10000, b) x25000, c) x50000, d) x100000 times magnified.

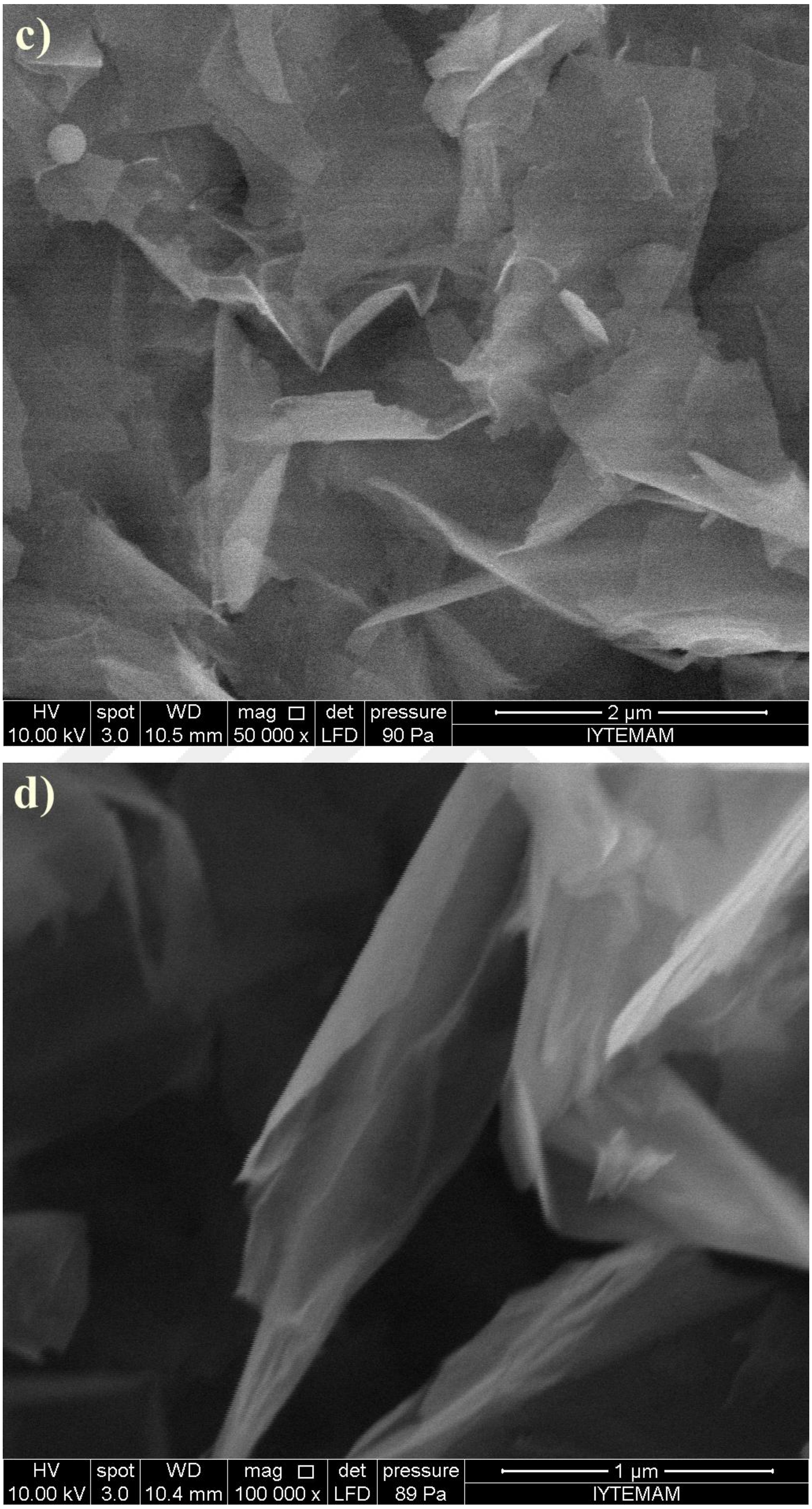

Figure 3.15 SEM micrographs of graphene a) x10000, b) x25000, c) x50000, d) x100000 times magnified (continue).

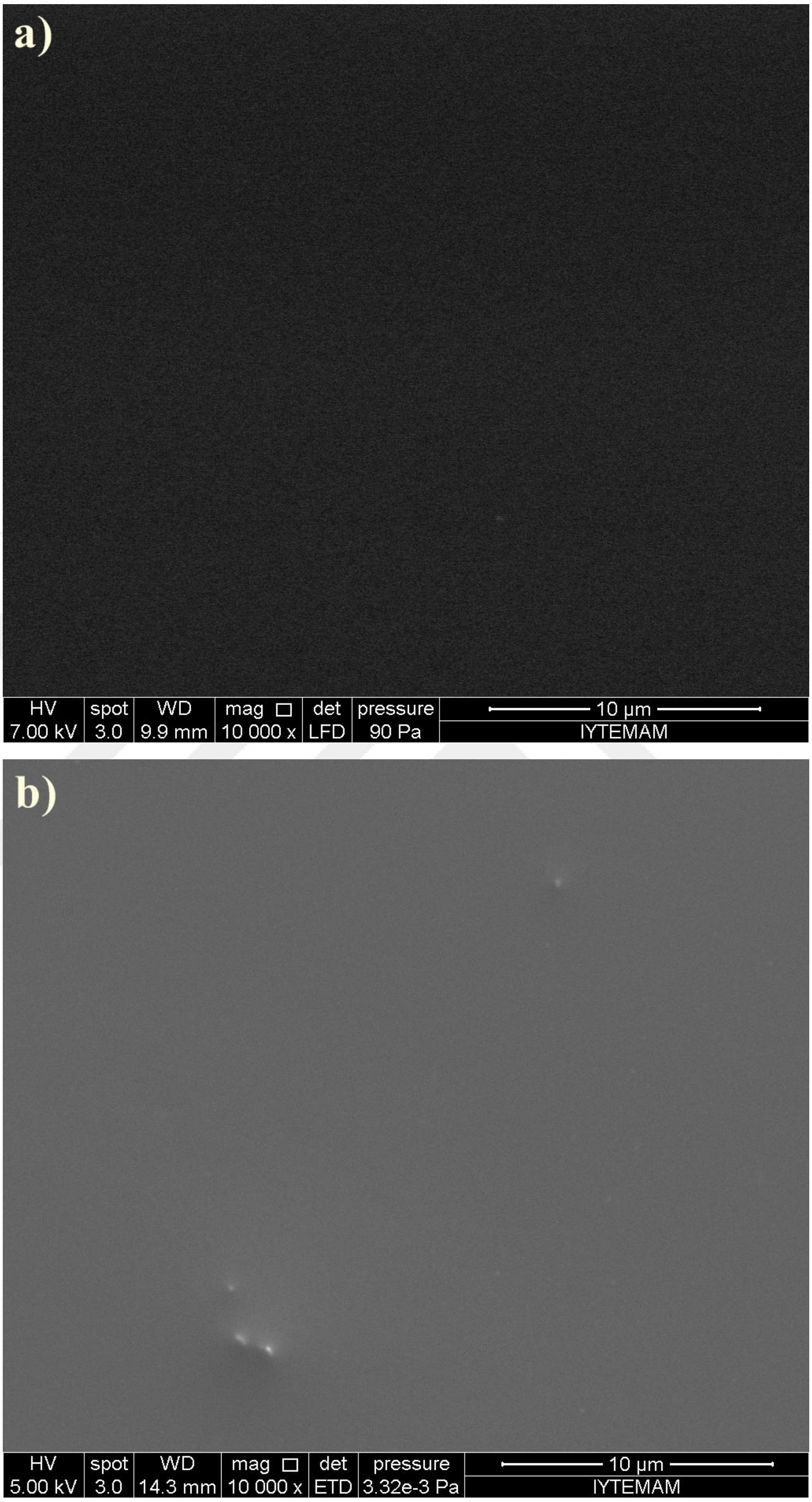

Figure 3.16 SEM micrographs of a) Cel-PO_4, b) Cel-PO_4-Gr0.2, c-d) Cel-PO_4-Gr0.2-cross section, e) Cel-PO_4-Gr0.4, f-g) Cel-PO_4-Gr0.4-cross section, h) Cel-PO_4-Gr0.6-cross section.

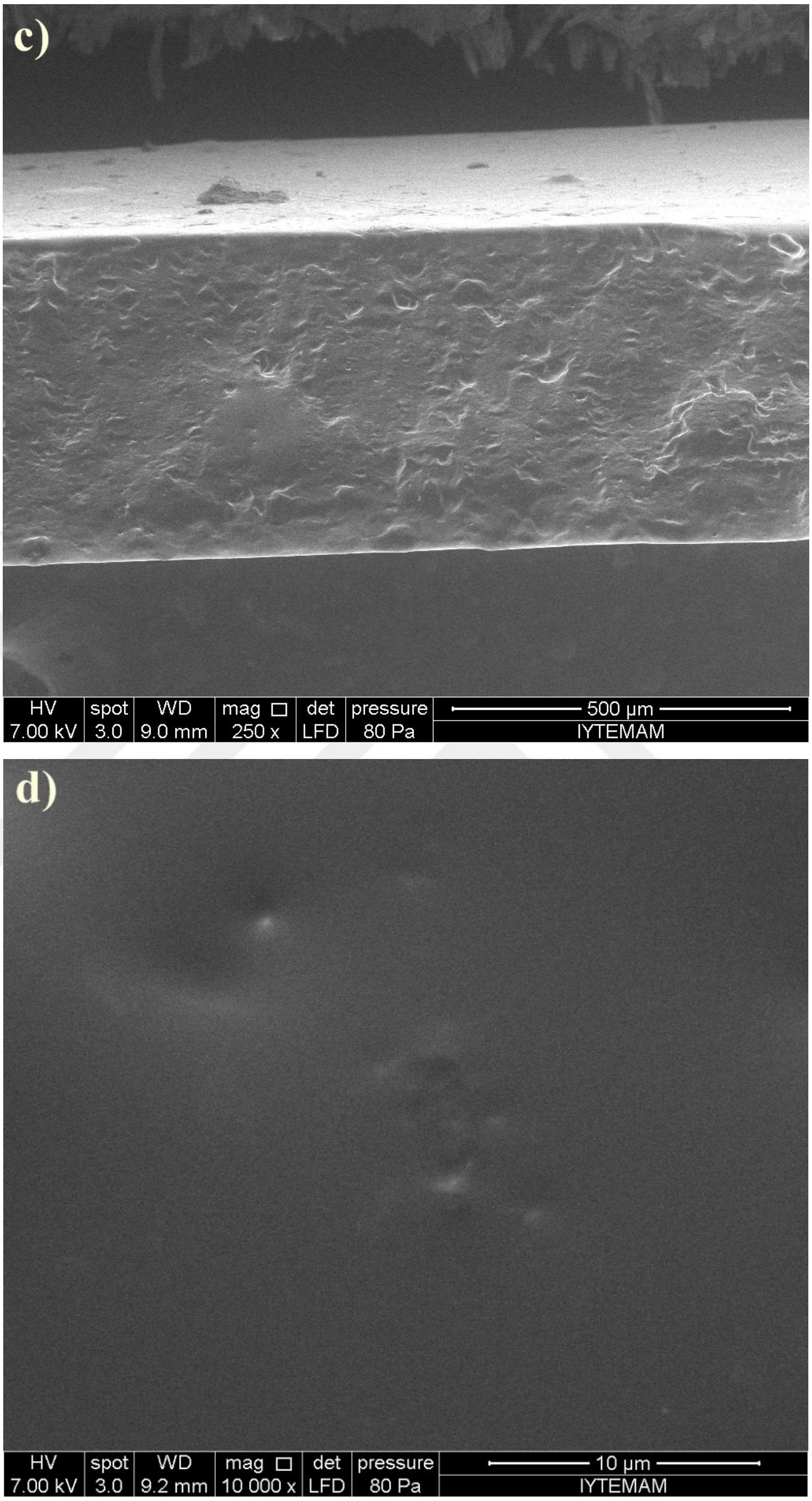

Figure 3.16 SEM micrographs of a) Cel-PO4, b) Cel-PO4-Gr0.2, c-d) Cel-PO4-Gr0.2-cross section, e) Cel-PO4-Gr0.4, f-g) Cel-PO4-Gr0.4-cross section, h) Cel-PO4-Gr0.6-cross section (continue).

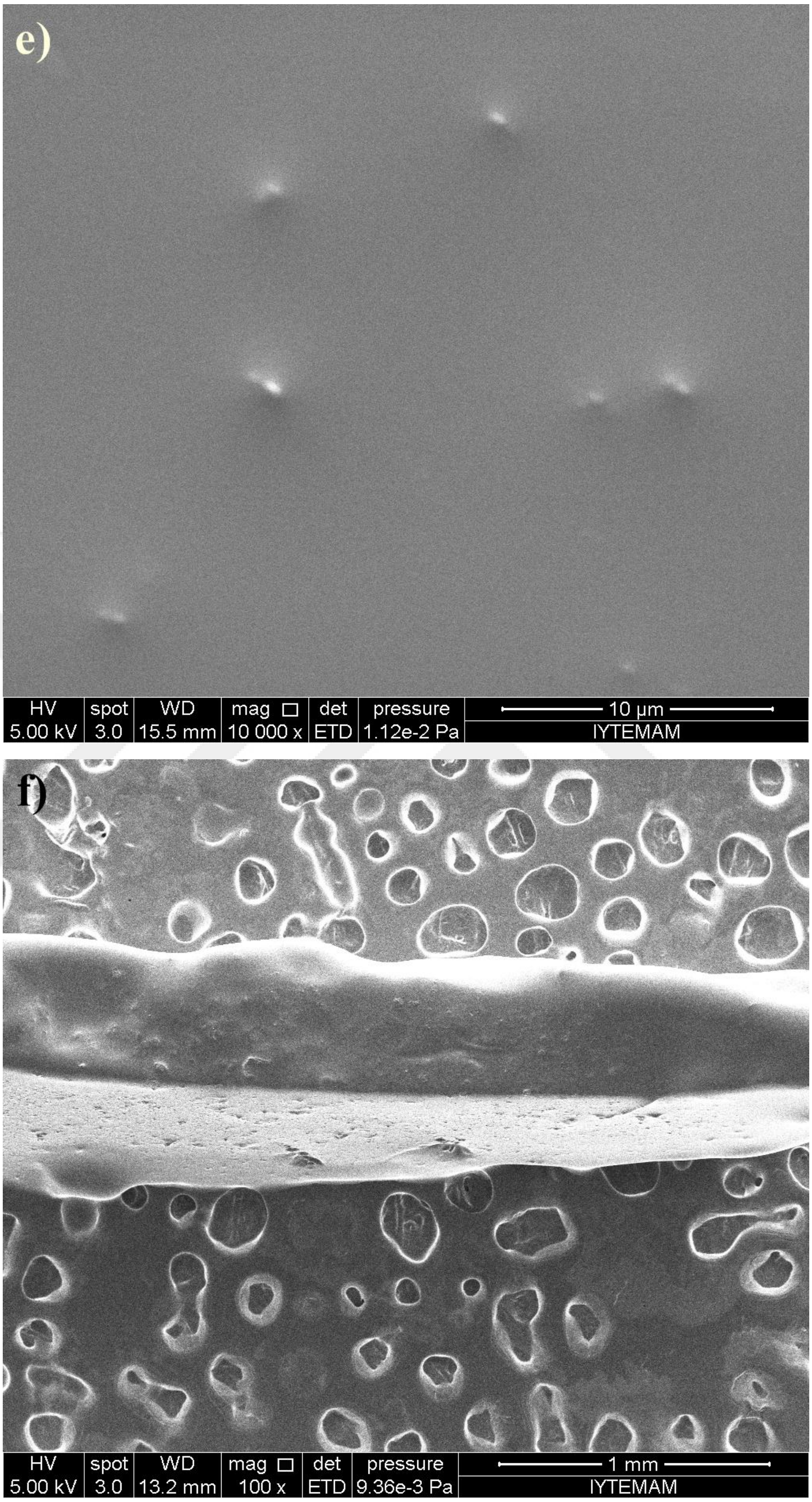

Figure 3.16 SEM micrographs of a) Cel-PO_4, b) Cel-PO_4-Gr0.2, c-d) Cel-PO_4-Gr0.2-cross section, e) Cel-PO_4-Gr0.4, f-g) Cel-PO_4-Gr0.4-cross section, h) Cel-PO_4-Gr0.6-cross section (continue).

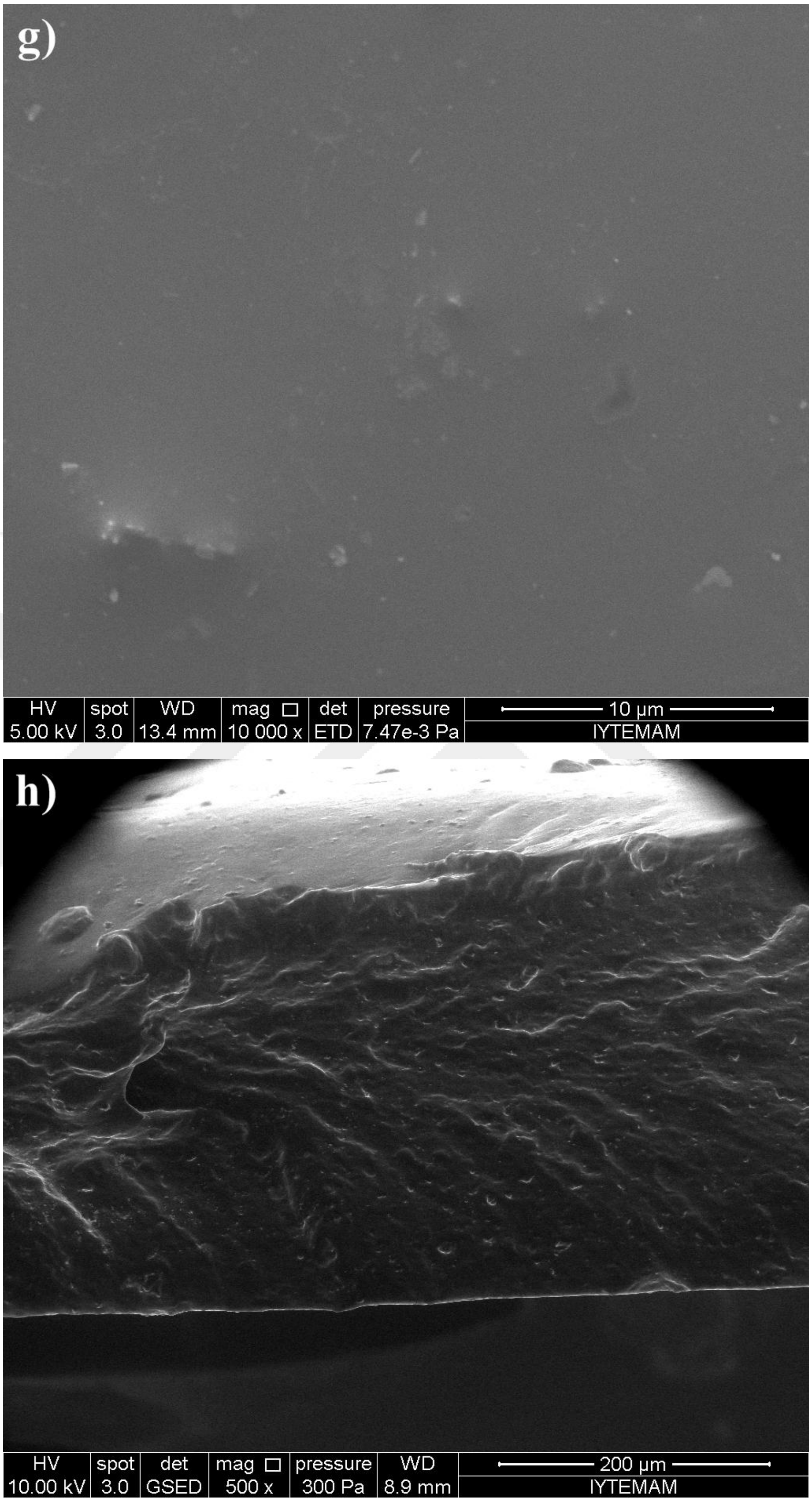

Figure 3.16 SEM micrographs of a) Cel-PO_4, b) Cel-PO_4-Gr0.2, c-d) Cel-PO_4-Gr0.2-cross section, e) Cel-PO_4-Gr0.4, f-g) Cel-PO_4-Gr0.4-cross section, h) Cel-PO_4-Gr0.6-cross section.

3.1.5 Mechanical Properties

Mechanical tests of the samples were carried out at room temperature for three times carried out.

Tensile strength and elastic modulus of the cellulose based samples are given in Figure 3.17 and 3.18. The effect of graphene concentration on mechanical properties was investigated. The increase in graphene concentration up to the 0.4 wt% Gr concentration enhanced the tensile strength of the samples. However, 0.6 wt% Gr loading decreased the tensile strength of sample probably due to poor dispersion of graphene. The decrease in tensile strength may be due to the non-homogenous structure created with aggregation of excess graphene content. The decrease in mechanical mechanical properties is associated with aggregation of filler at higher graphene content. Having high surface area creates a tendency to the aggregation of graphene particles (Dhakate, Mathur, Sharma, Borah, & Dhami, 2009; May, Khan, O'Neill, & Coleman, 2012). Poor dispersion may lead to agglomeration of the graphene, thus decreasing the tensile properties. It is probable that these agglomerates behave as a stress concentrator leading the composite to an early failure (Akar et al., 2015).

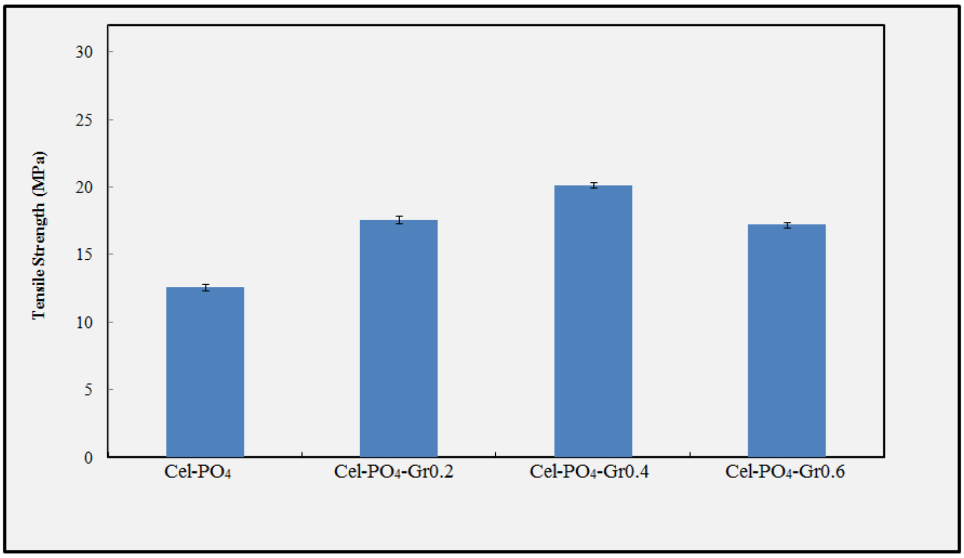

Figure 3.17 Tensile strength values of Cel-PO_4, Cel-PO_4-Gr0.2, Cel-PO_4-Gr0.4, and Cel-PO_4-Gr0.6 (Akar et al., 2015).

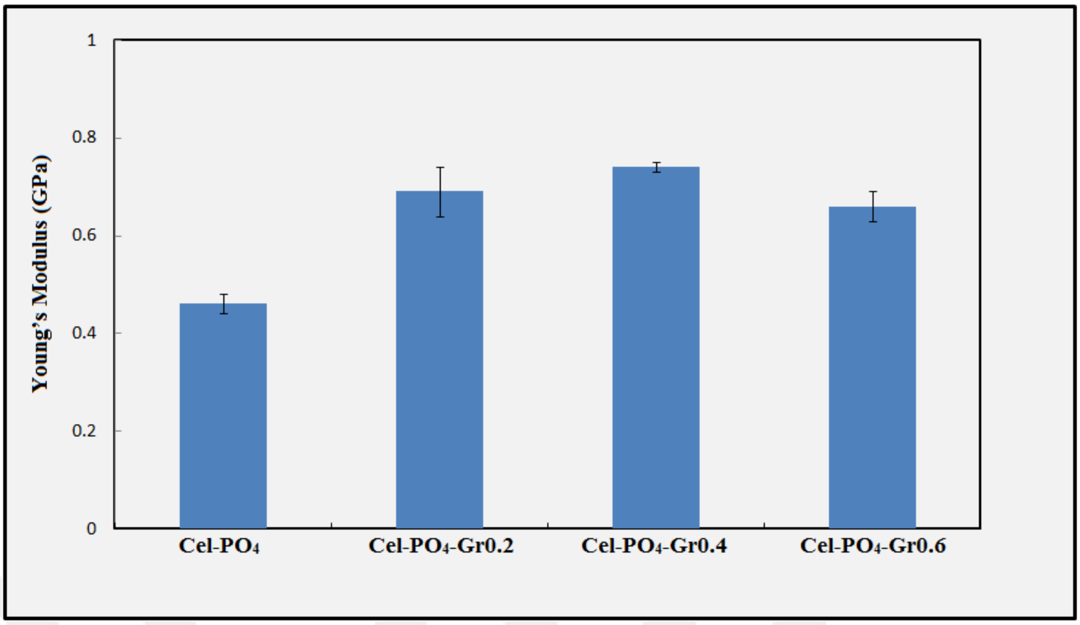

Figure 3.18 Young's Modulus values of Cel-PO_4, Cel-PO_4-Gr0.2, Cel-PO_4-Gr0.4, and Cel-PO_4-Gr0.6 (Akar et al., 2015).

3.1.6 Electroactive Properties

Tip displacement of the Cel-Po_4 and Cel-PO4-Gr samples under the DC voltages (1, 3, 5, and 7) are given in Figure 3.19-3.28 and Figure 3.29-3.61, respectively.

The Cel-PO_4 exhibited 0.05, 0.06, 0.04, and 0.25 mm tip displacements under the DC voltages 1, 3, 5 and 7V, respectively. Max tip displacement for positive voltages was exhibited under 7V. Tip displacements under 1, 3, and 5V have similar results but the result of 7V is approximately 5 fold of 3V result. The tip displacement of the Cel-PO_4 under the negative voltages -1, -3, -5 and -7V are 0.07, 0.42, 0.18 and, 0.05 mm, respectively. The greatest tip displacement was obtained under -3V. It can be said that optimum voltages for Cel-PO_4 samples were obtained to be 7V in positive and -3V in negative DC voltages. It can be seen clearly in Figure 3.27 and Figure 3.28 (Akar et al., 2015).

Tip displacements of graphene loaded samples (Cel-PO4-Gr0.2, Cel-PO4-Gr0.4, and Cel-PO4-Gr0.6) under the DC voltages (1, 3, 5, and 7V) were investigated. The max tip displacement values of Cel-PO4-Gr0.2 are 0.17, 0.25, 0.15, 0.12, 0.06, 0.53, 0.24 and 0.33 mm under the DC voltages 1, 3, 5, 7, -1, -3, -5 and, -7V, respectively. The greatest tip displacement values were obtained to be 0.25 mm under 3V and 0.53 mm under -3V (Akar et al., 2015).

The max tip displacement of Cel-PO_4-Gr0.4 under the DC voltages 1, 3, 5, 7, -1, -3, -5 and, -7V are 0.1, 0.17, 0.05, 0.06, 0.35, 0.14, 0.04, and 0.02 mm, respectively. The greatest tip displacement results were obtained as 0.17 and 0.35 mm under DC voltages 3V and -1V, respectively (Akar et al., 2015).

The max tip displacement values were investigated for Cel-PO_4-Gr0.6 under the DC voltages 1,3, 5, 7, -1, -3, -5 and, -7V are 0.04, 0.02, 0.03, 0.12, 0.04, 0.02, 0.02 and 0.07 mm, respectively. The greatest tip displacement results were obtained as 0.12 and 0.07 mm under 7V and -7V, respectively (Akar et al., 2015).

When the best results of the whole samples were considered, the maximum tip displacement for cellulose based actuators obtained as 0.53 mm for Cel-PO_4-Gr0.2 under -3V, 0.35mm for Cel-PO_4-Gr0.4 under -1V, and 0.12 mm for Cel-PO_4-Gr0.6 under 7V. The greatest tip displacement was exhibited by Cel-PO_4-Gr0.2 under -3V (Akar et al., 2015). The decrease in tip displacement of Cel-PO_4-Gr0.4 and Cel-PO_4-Gr0.6 can be explained with short circuit of the samples. The increase of Gr content give rise to increase in conductivity of samples and so short circuit occurred. Short circuit damaged the polymer.

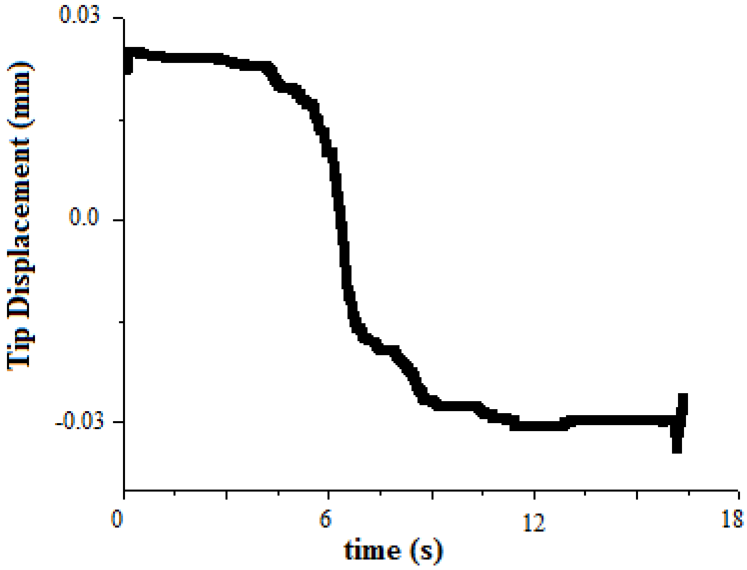

Figure 3.19 Tip displacement variations for Cel-PO_4 under 1V.

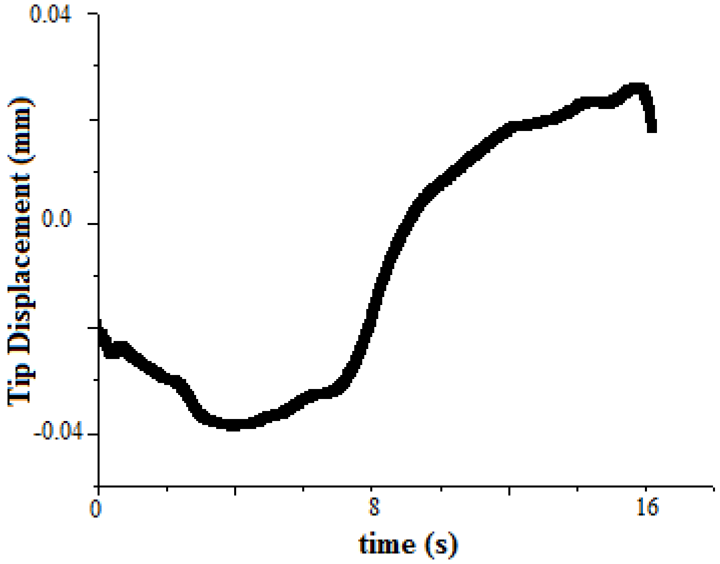

Figure 3.20 Tip displacement variations for Cel-PO_4 under 3V.

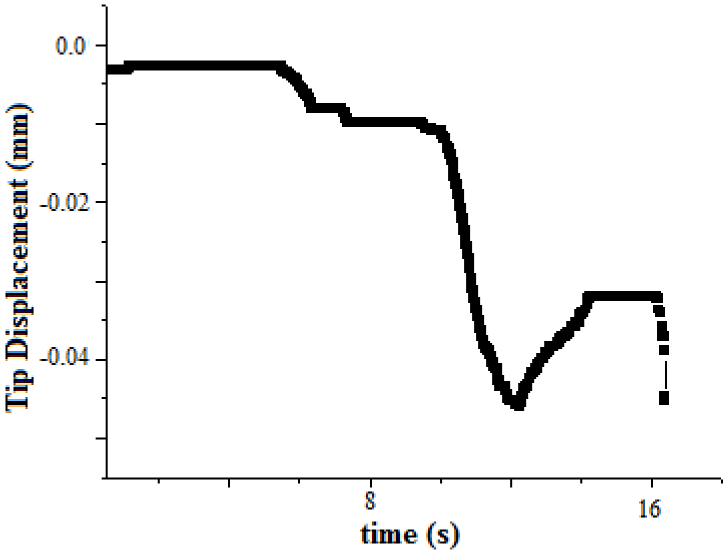

Figure 3.21 Tip displacement variations for Cel-PO_4 under 5V.

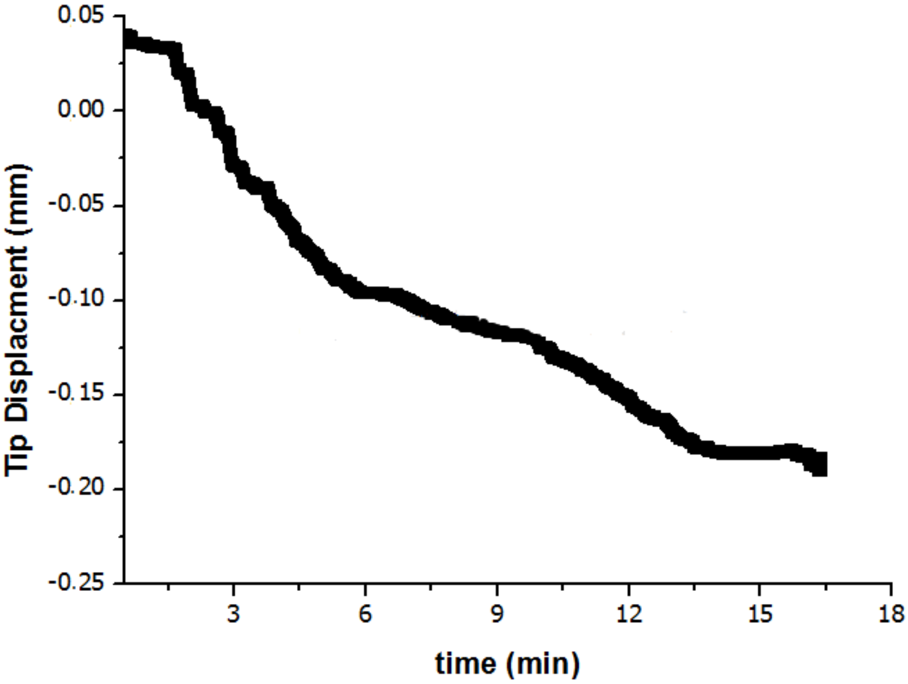

Figure 3.22 Tip displacement variations for Cel-PO_4 under 7V.

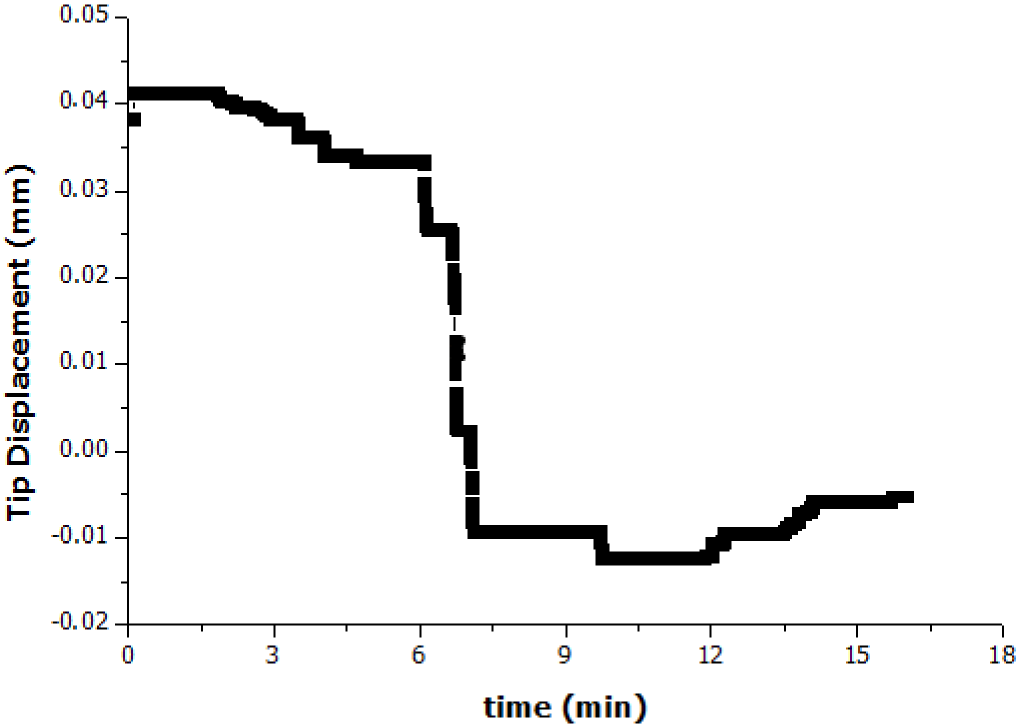

Figure 3.23 Tip displacement variations for Cel-PO$_4$ under -1V.

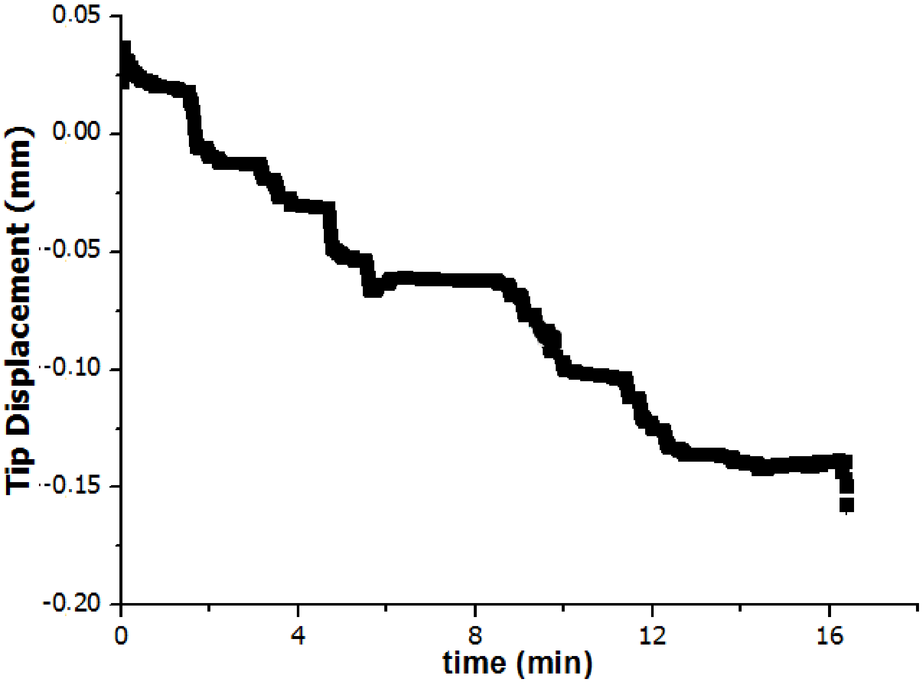

Figure 3.24 Tip displacement variations for Cel-PO$_4$ under -3V.

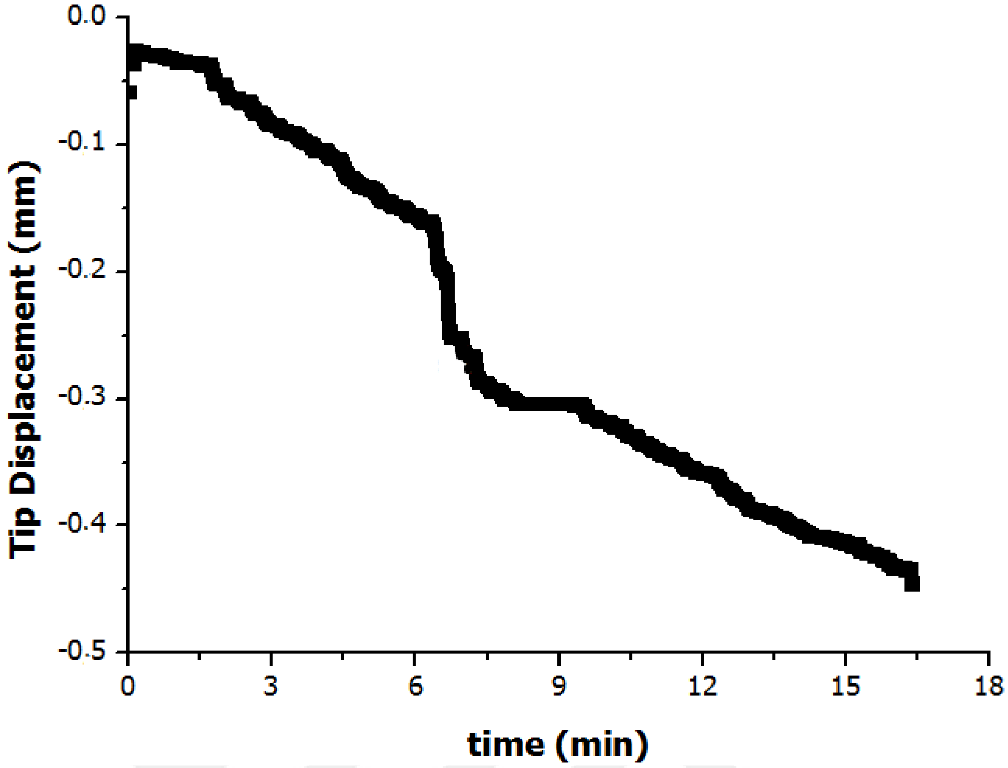

Figure 3.25 Tip displacement variations for Cel-PO$_4$ under -5V.

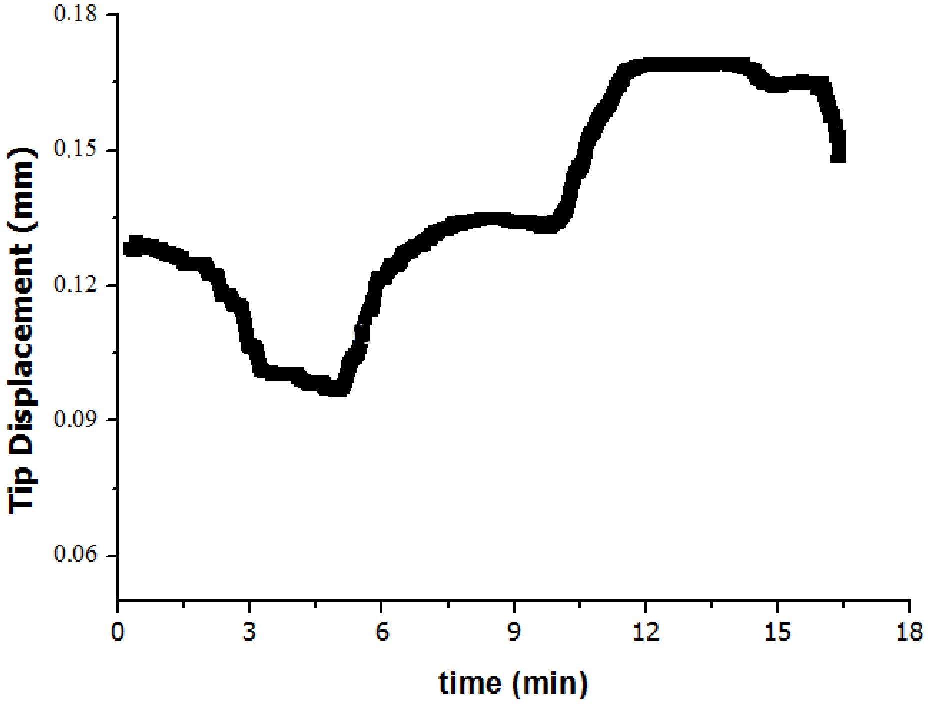

Figure 3.26 Tip displacement variations for Cel-PO$_4$ under -7V.

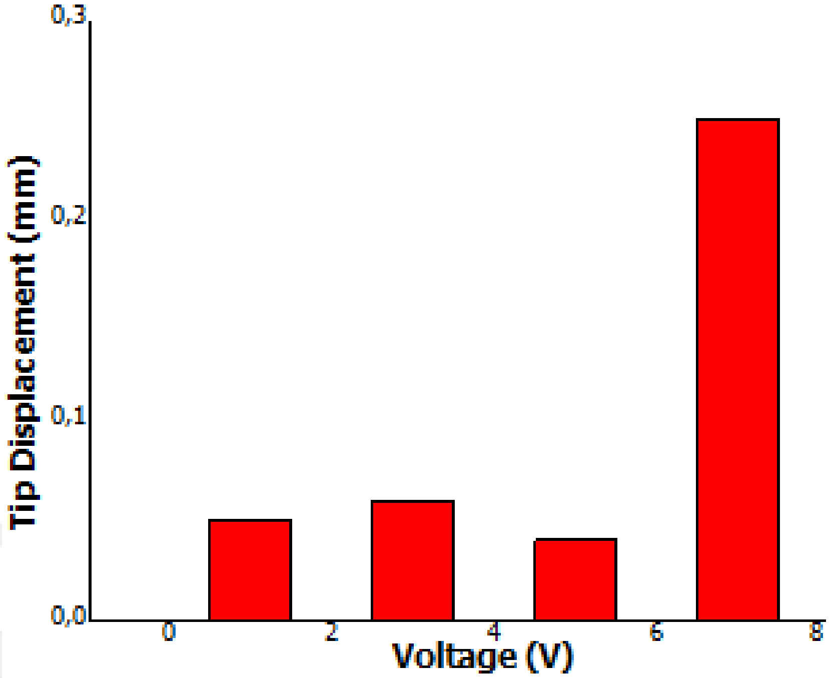

Figure 3.27 Tip displacements of Cel-PO$_4$ samples under positive voltage.

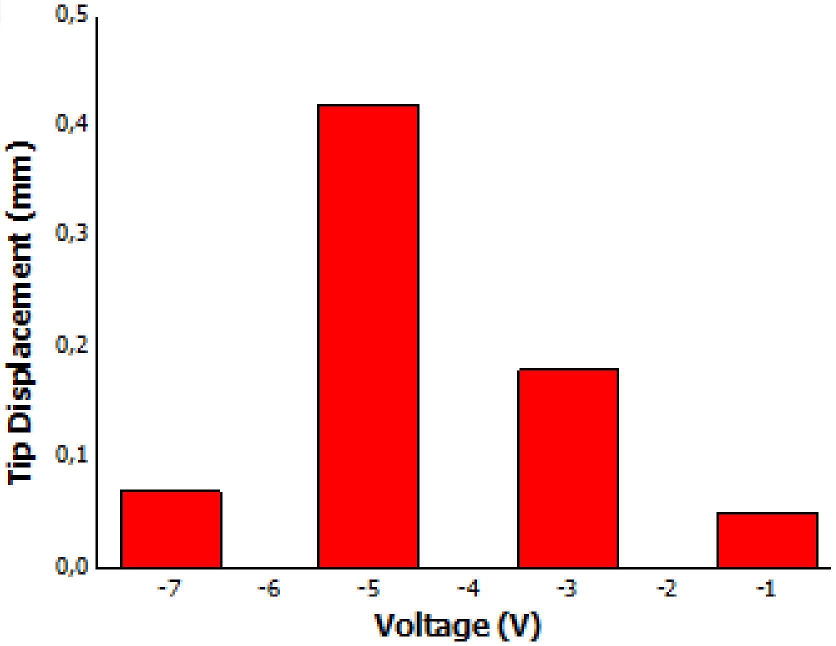

Figure 3.28 Tip displacements of Cel-PO$_4$ samples under negative voltage.

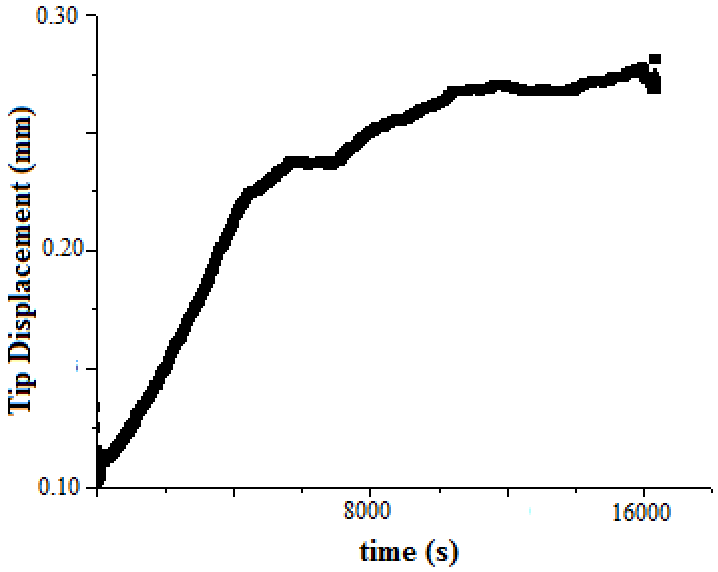

Figure 3.29 Tip displacement variations for Cel-PO_4-Gr0.2 under 1V.

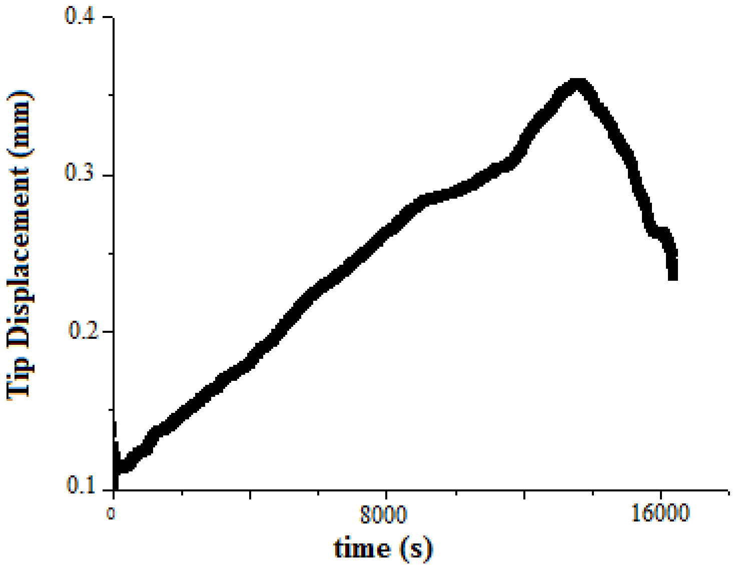

Figure 3.30 Tip displacement variations for Cel-PO_4-Gr0.2 under 3V.

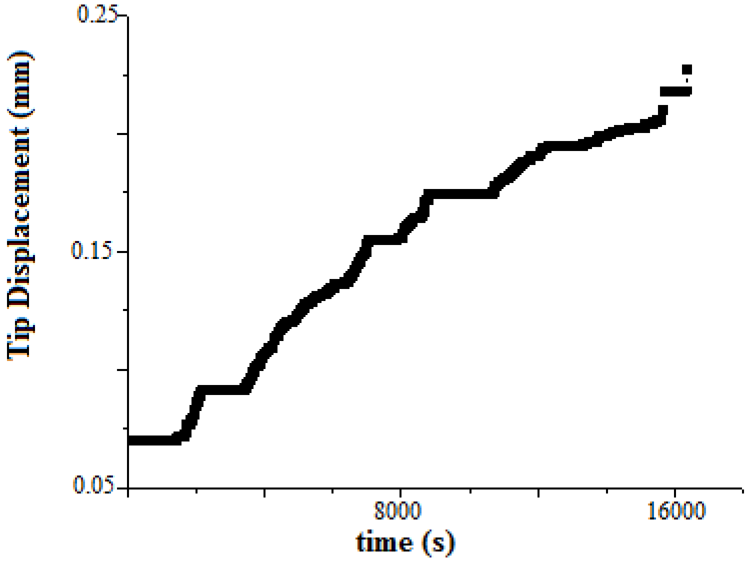

Figure 3.31 Tip displacement variations for Cel-PO_4-Gr0.2 under 5V.

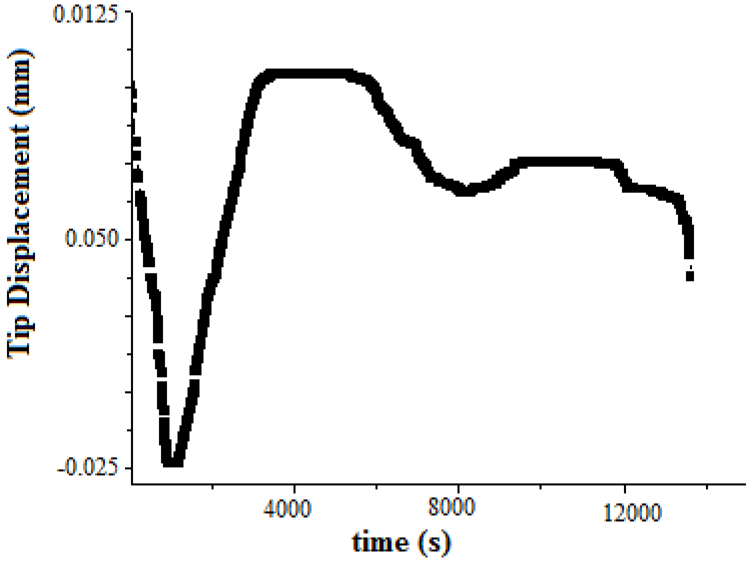

Figure 3.32 Tip displacement variations for Cel-PO_4-Gr0.2 under 7V.

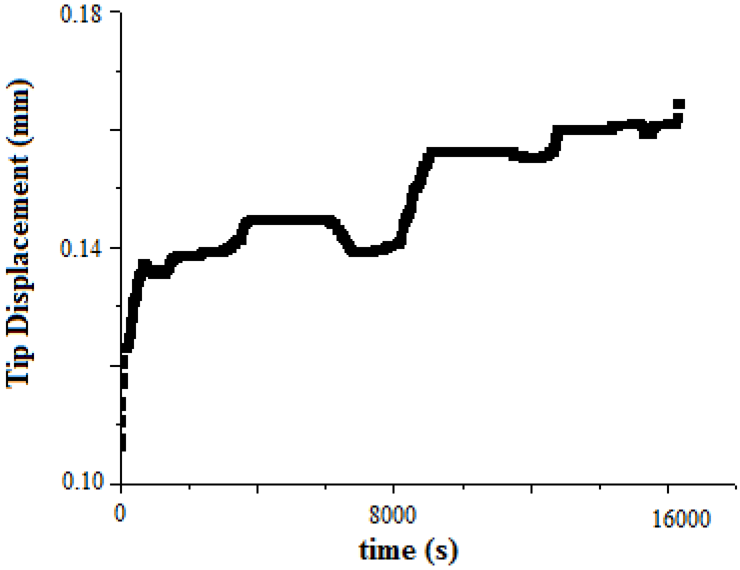

Figure 3.33 Tip displacement variations for Cel-PO_4-Gr0.2 under -1V.

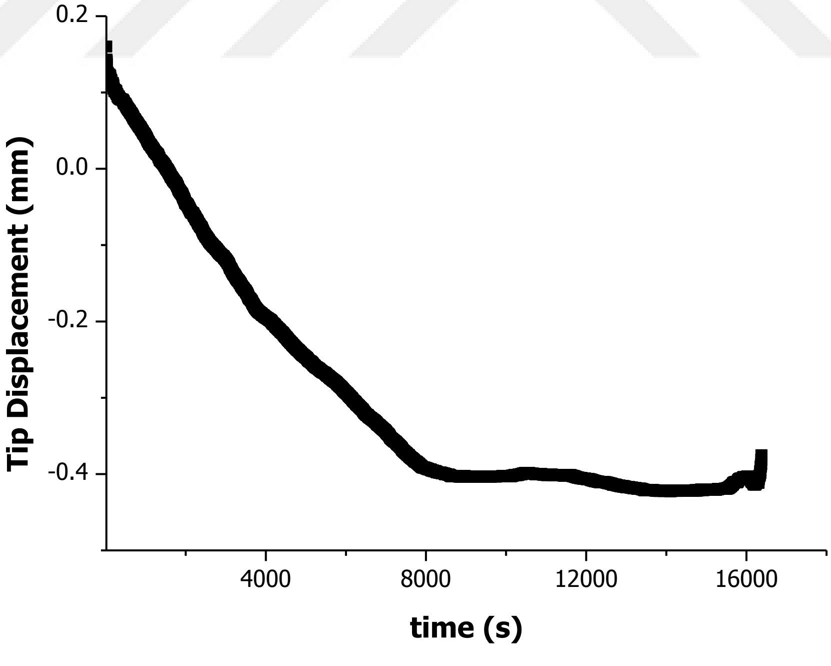

Figure 3.34 Tip displacement variations for Cel-PO_4-Gr0.2 under -3V.

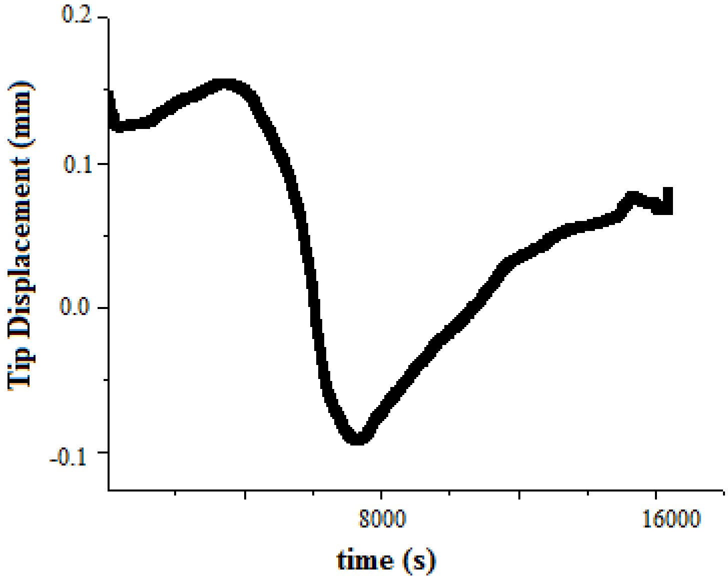

Figure 3.35 Tip displacement variations for Cel-PO_4-Gr0.2 under -5V.

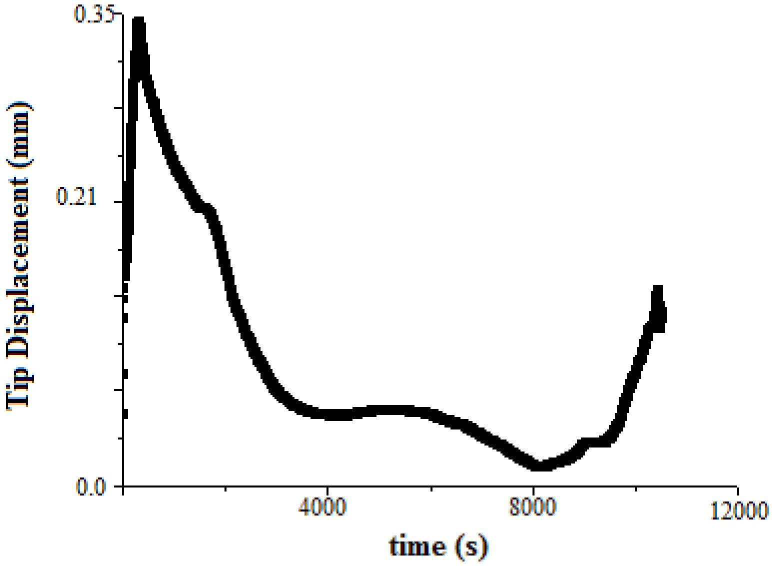

Figure 3.36 Tip displacement variations for Cel-PO_4-Gr0.2 under -7V.

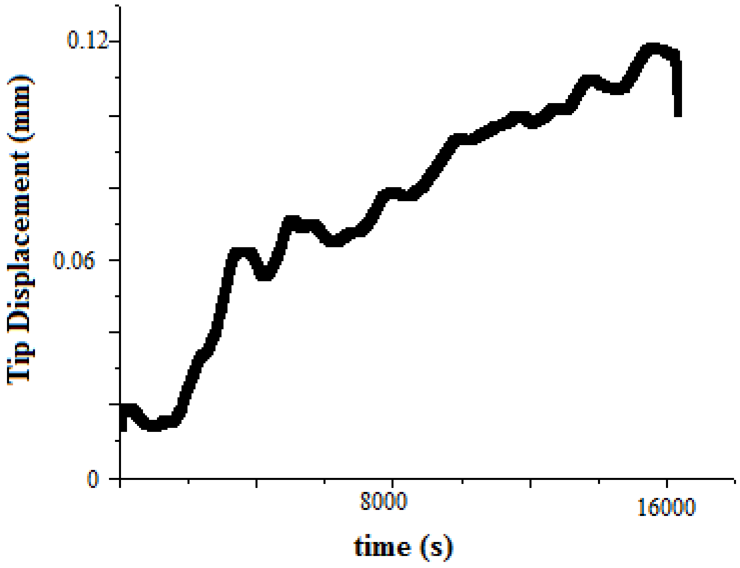

Figure 3.37 Tip displacement variations for Cel-PO_4-Gr0.4 under 1V.

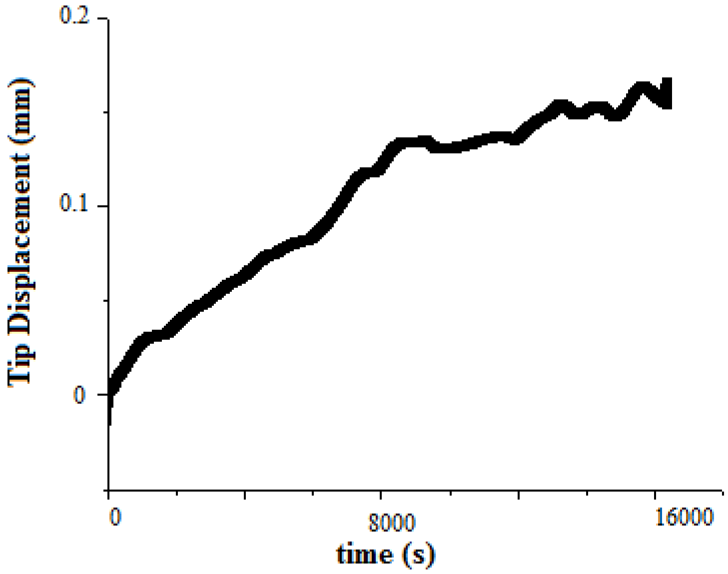

Figure 3.38 Tip displacement variations for Cel-PO_4-Gr0.4 under 3V.

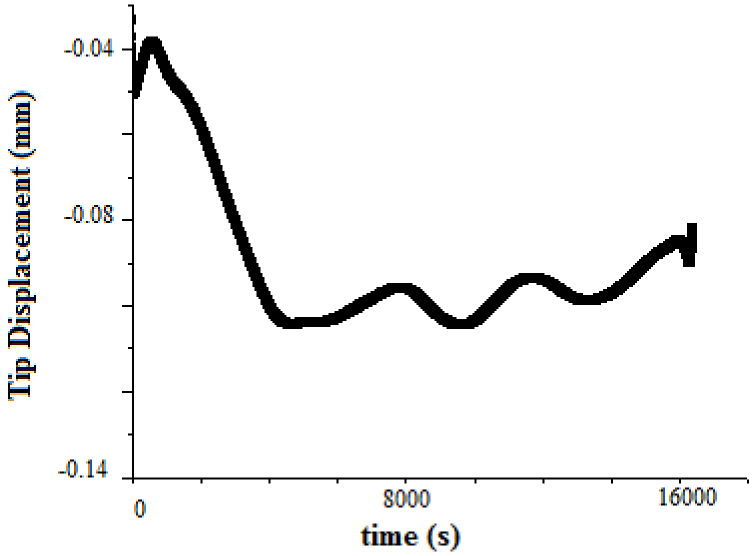

Figure 3.39 Tip displacement variations for Cel-PO_4-Gr0.4 under 5V.

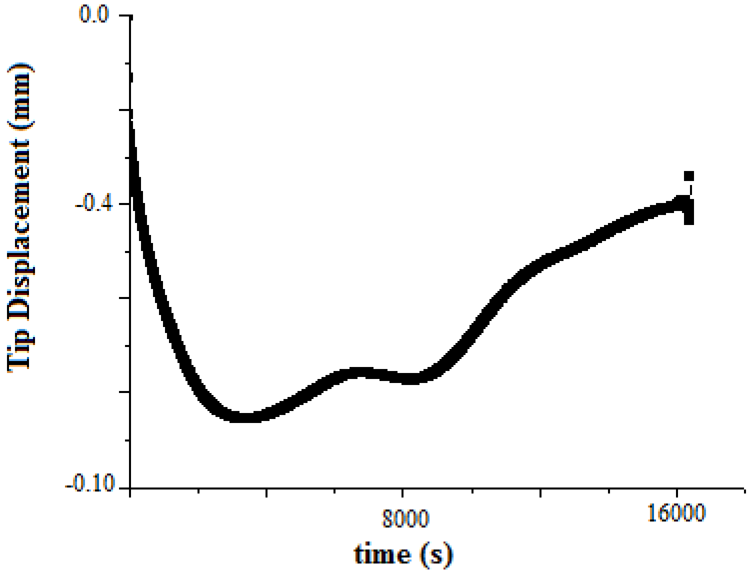

Figure 3.40 Tip displacement variations for Cel-PO_4-Gr0.4 under 7V.

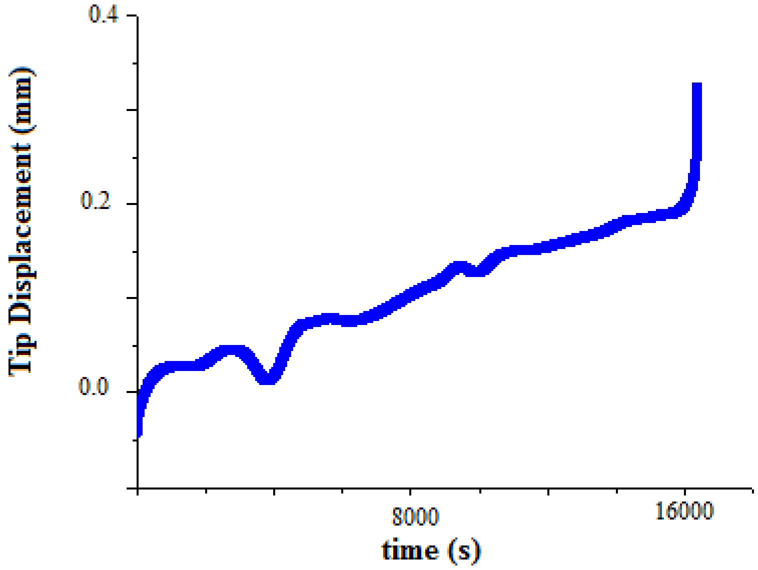

Figure 3.41 Tip displacement variations for Cel- Cel-PO_4-Gr0.4 under -1V.

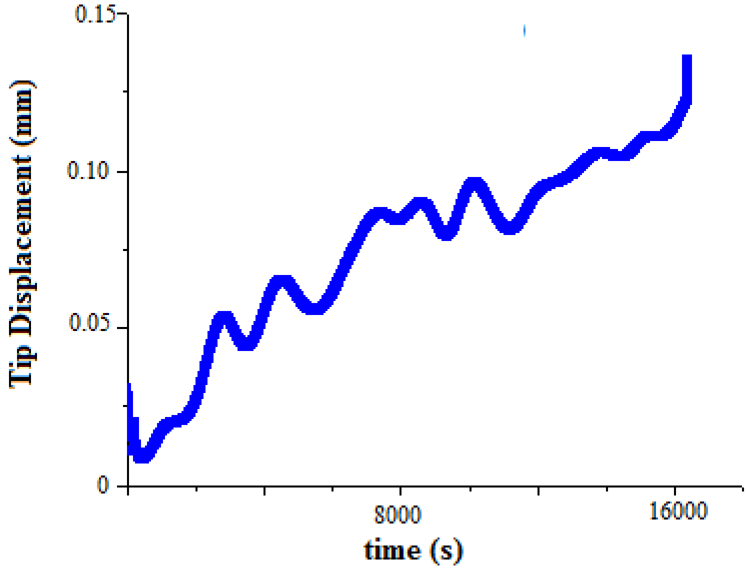

Figure3.42 Tip displacement variations for Cel-PO_4-Gr0.4 under -3V.

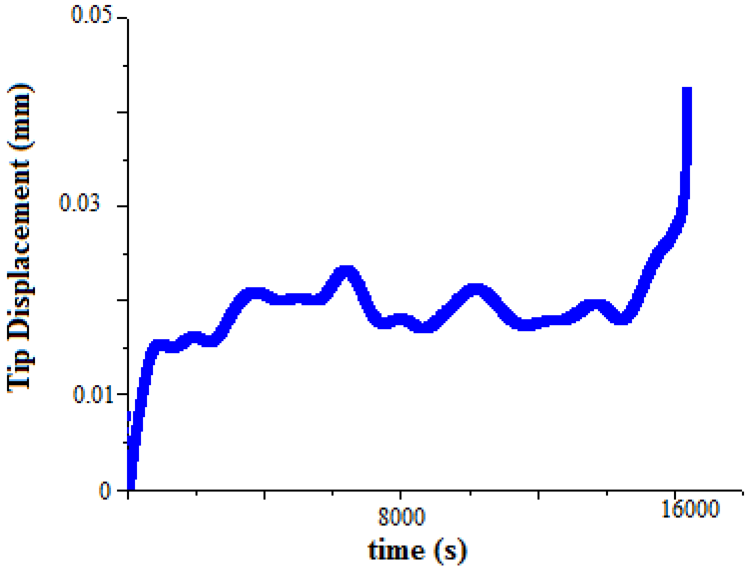

Figure 3.43 Tip displacement variations for Cel-PO_4-Gr0.4 under -5V.

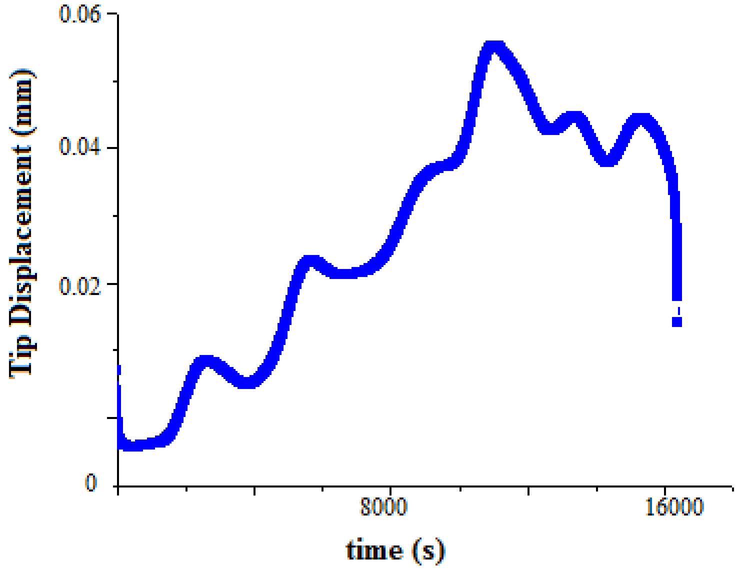

Figure 3.44 Tip displacement variations for Cel-PO_4-Gr0.4 under -7V.

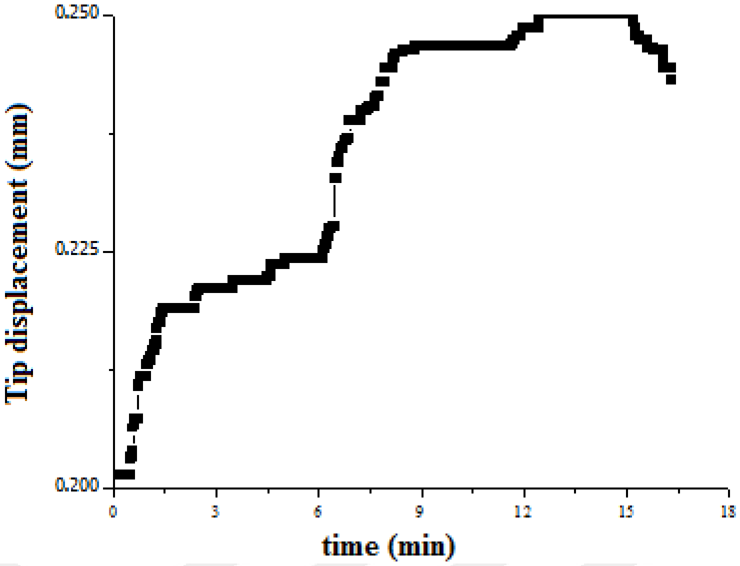

Figure 3.45 Tip displacement variations for Cel-PO_4-Gr0.6 under 1V.

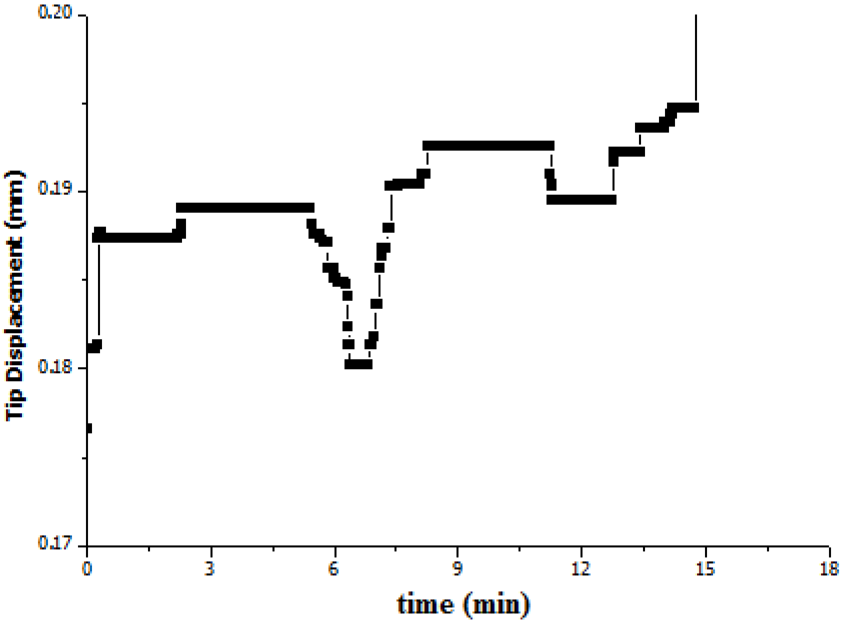

Figure 3.46 Tip displacement variations for Cel-PO_4-Gr0.6 under 3V.

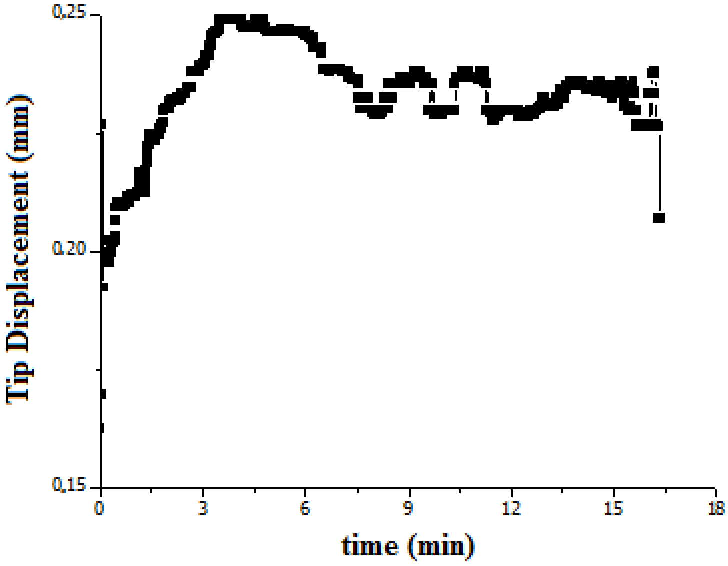

Figure 3.47 Tip displacement variations for Cel-PO_4-Gr0.6 under 5V.

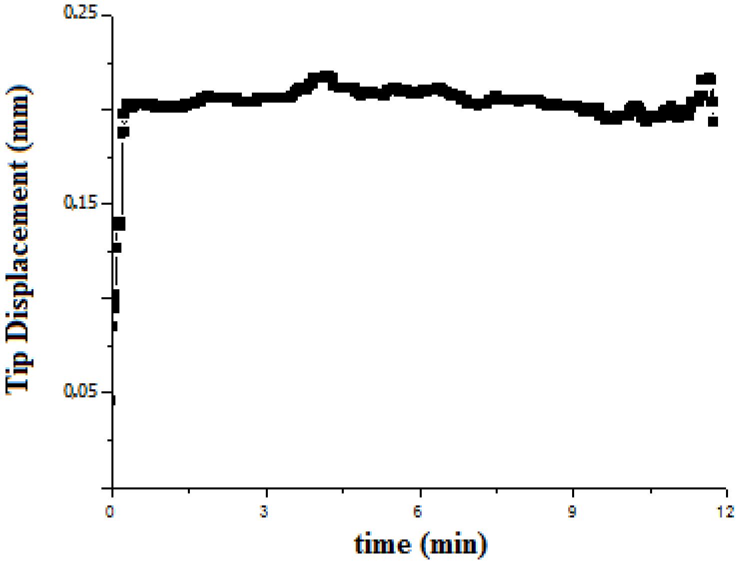

Figure 3.48 Tip displacement variations for Cel-PO_4-Gr0.6 under 7V.

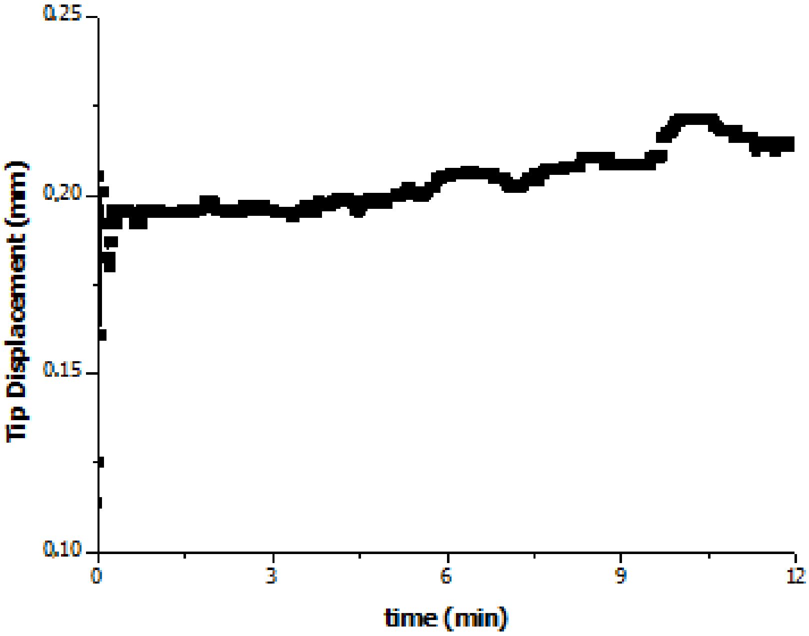

Figure 3.49 Tip displacement variations for Cel-PO$_4$-Gr0.6 under -1V.

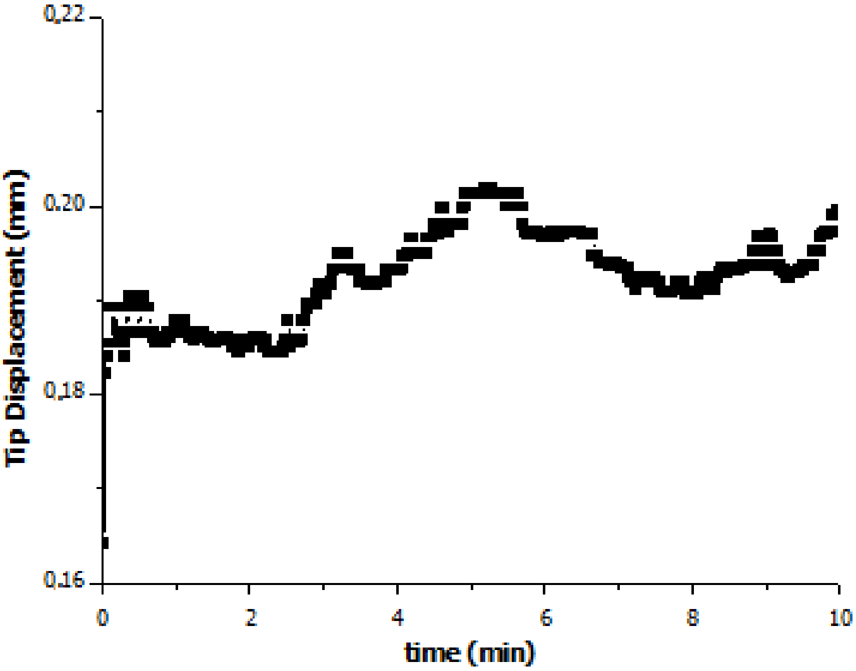

Figure 3.50 Tip displacement variations for Cel-PO$_4$-Gr0.6 under -3V.

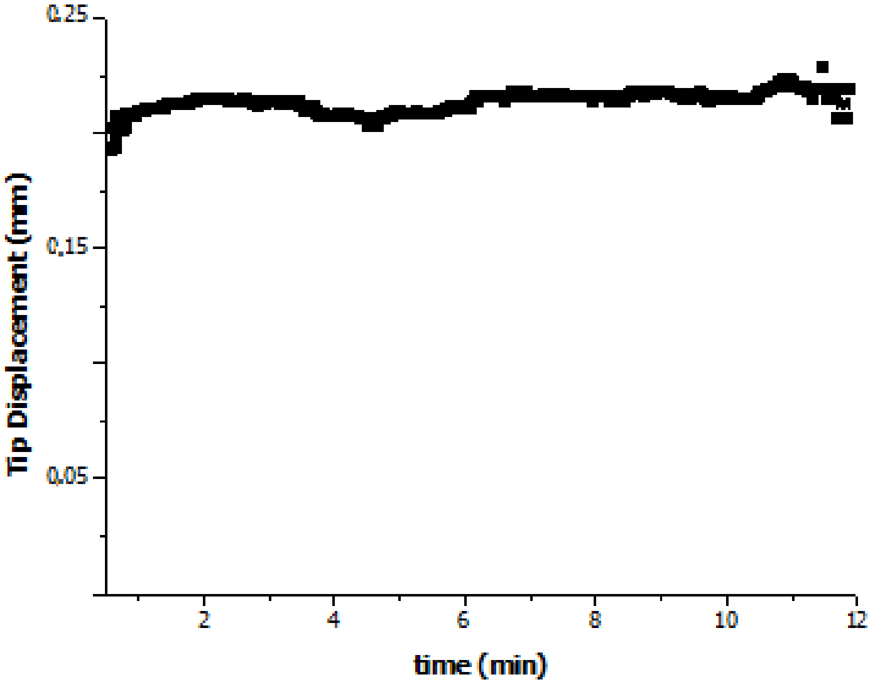

Figure 3.51 Tip displacement variations for Cel-PO_4-Gr0.6 under -5V.

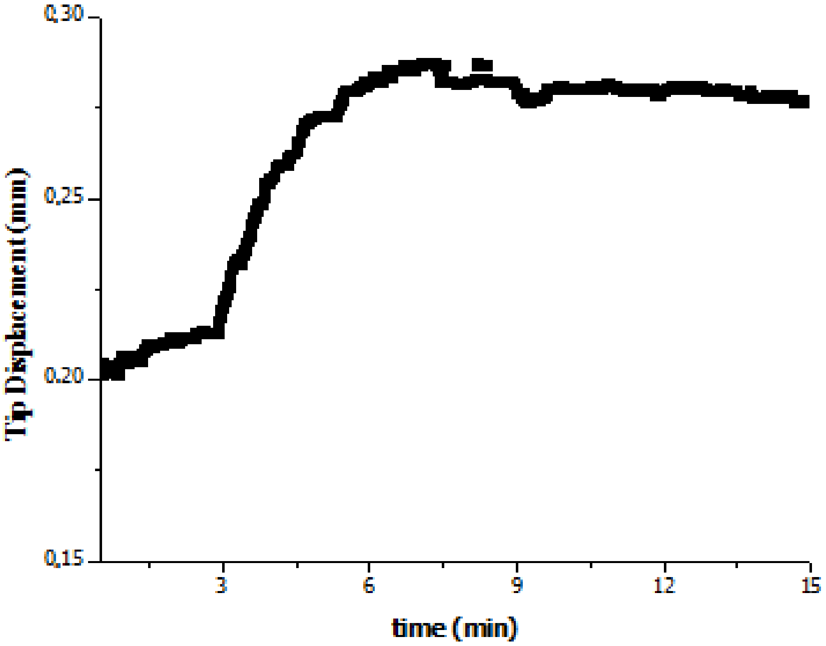

Figure 3.52 Tip displacement variations for Cel-PO_4-Gr0.6 under -7V.

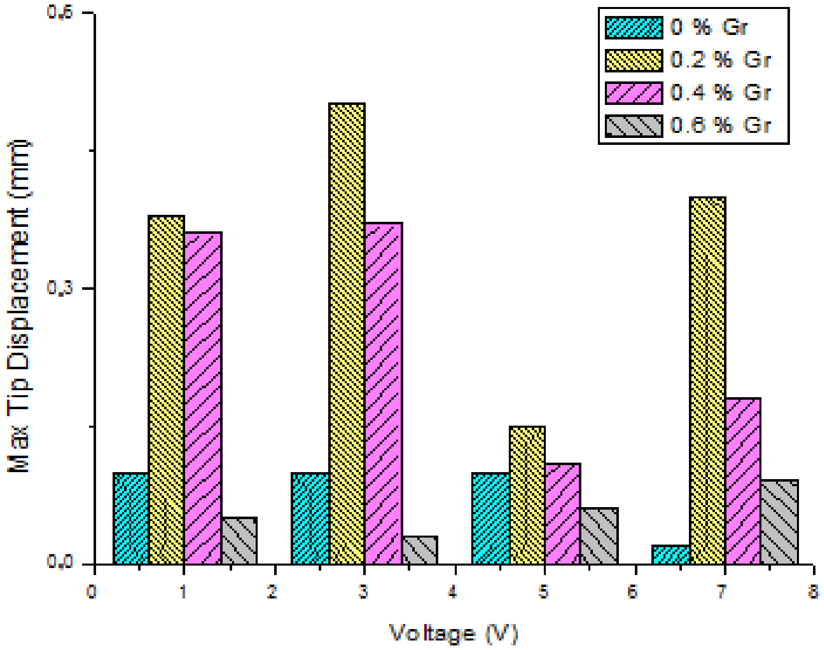

Figure 3.53 Max tip displacements of Cel-PO4, Cel-PO_4-Gr0.2, Cel-PO_4-Gr0.4, and Cel-PO_4-Gr0.6 samples.

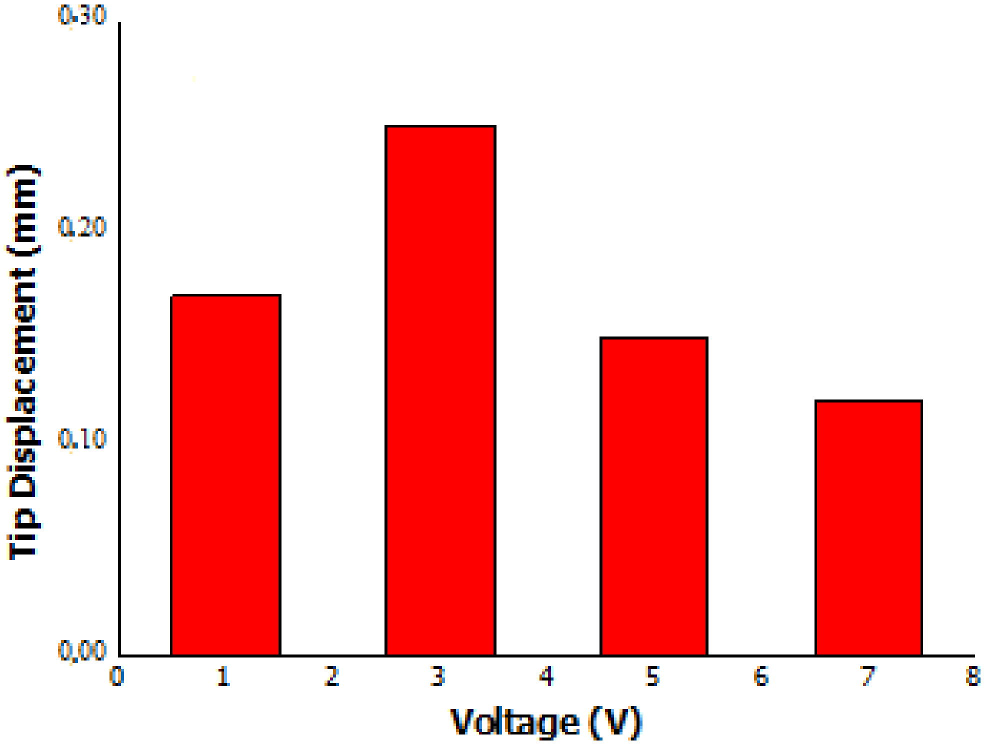

Figure 3.54 Tip displacements of Cel-PO_4-Gr0.2 samples under positive voltage.

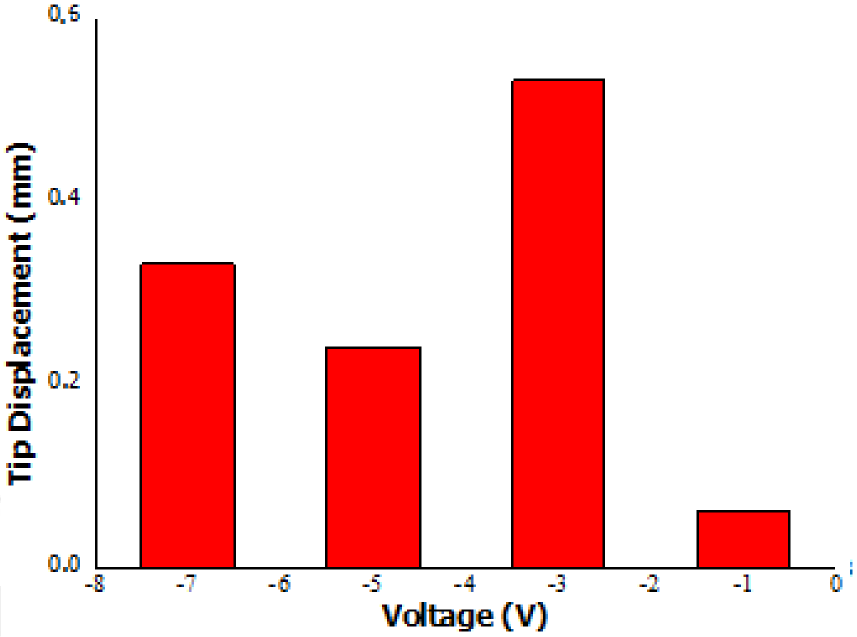

Figure 3.55 Tip displacements of Cel-PO_4-Gr0.2 samples under negative voltage.

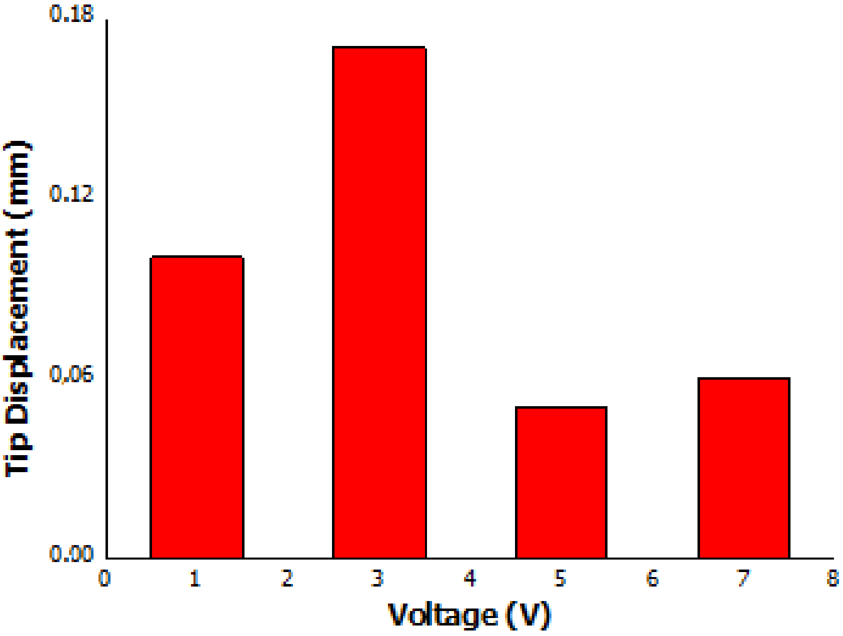

Figure 3.56 Tip displacements of Cel-PO_4-Gr0.4 samples under positive voltage.

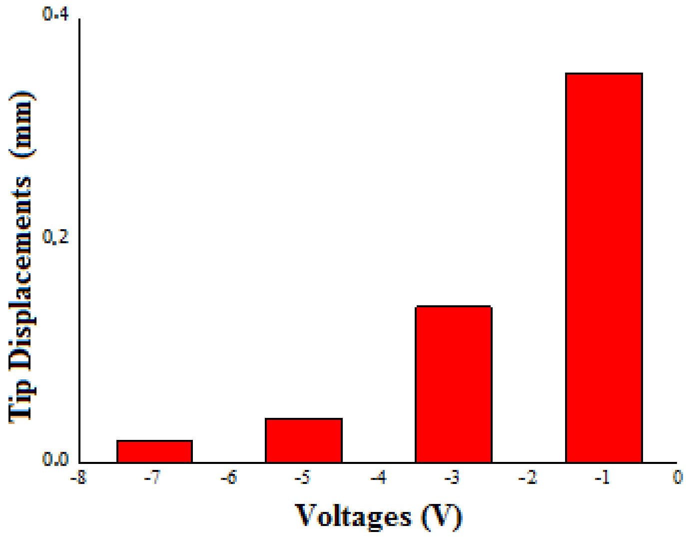

Figure 3.57 Tip displacements of Cel-PO_4-Gr0.4 samples under negative voltage.

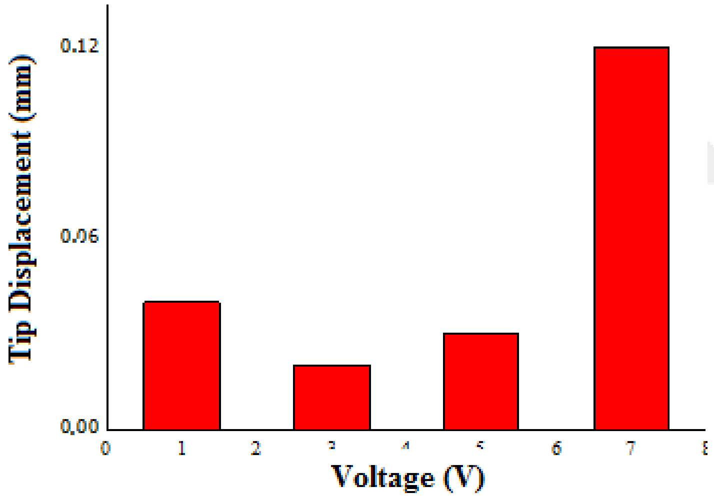

Figure 3.58 Tip displacements of Cel-PO_4-Gr0.6 samples under positive voltage.

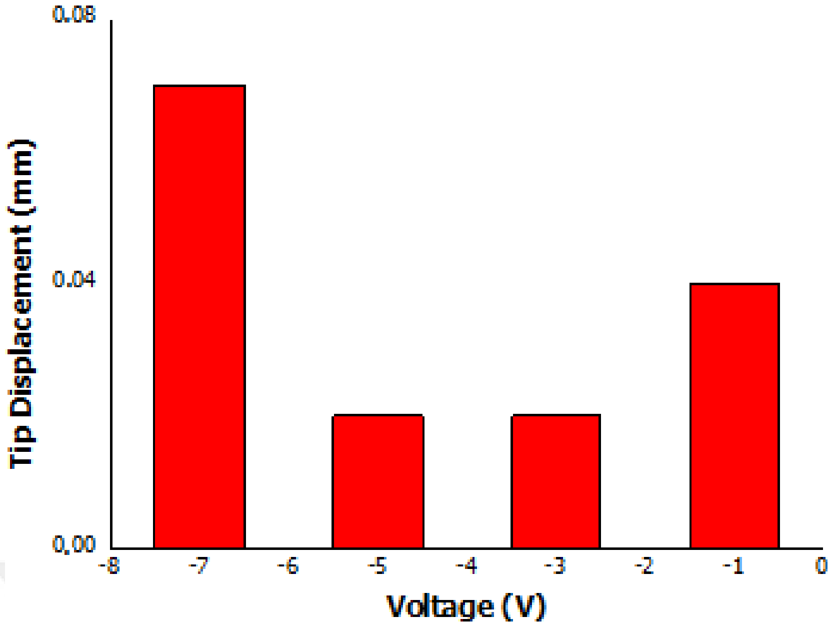

Figure 3.59 Tip displacements of Cel-PO_4-Gr0.6 samples under negative voltage.

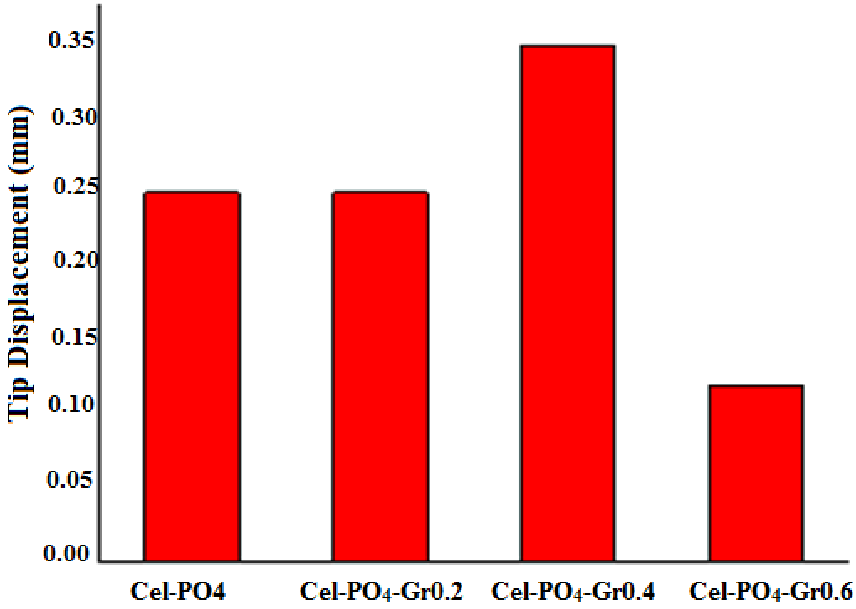

Figure 3.60 Comparison of the max tip displacements of Cel-PO4 (1, 3, and 5 V), Cel-PO_4-Gr0.2 (3V), Cel-PO_4-Gr0.4 (3V), and Cel-PO_4-Gr0.6 (7V) under positive voltage.

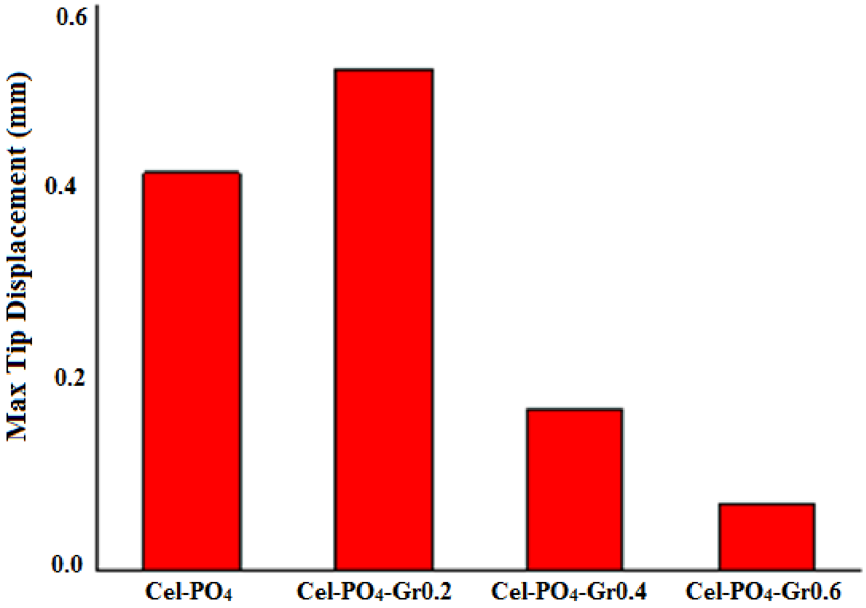

Figure 3.61 Comparison the max tip displacements of Cel-PO4 (-5V), Cel-PO_4-Gr0.2 (-3V), Cel-PO_4-Gr0.4 (-1V), and Cel-PO_4-Gr0.6 (-7V) under negative voltage.

3.2 Chi-Based IPMC Actuators

3.2.1 Fourier Transforms Infrared Spectroscopy (FTIR) Analysis

FTIR curves of the chitosan, ChiPM-1, ChiPM-2, ChiPM-3, and ChiM-2 (Altınkaya et al., 2016) are exhibited in Figure 3.62-3.67. The FTIR spectrum of chitosan exhibits a broad and strong band at about 3460 cm^{-1} associated with O–H and N–H stretching. An absorption band at around 2920 cm^{-1} corresponds to C-H stretching. Absorption bands at 1646 and 1562 cm^{-1} may be attributed to C=O stretching of amide I group (acetamido group) and N-H angular deformation of amide II, respectively. The stretching band observed in the range 1408-1450 cm^{-1} due to coupling of N-H angular deformation and C–N stretching. A band around 1370 cm^{-1} is ascribed to symmetrical deformation of the CH_3 group. The vibration bands between 1150 cm^{-1} and 900 cm^{-1} are assigned to the skeletal signals (C–O–C stretching, vibrations of glycosidic bonds and, C–O) (Altınkaya et al., 2016; Ravindra, Krovvidi, & Khan, 1998; Duarte, Ferreira, Marvao, & Rocha, 2001; Limam, Selmi, Sadok, & El Abed, 2013; Corazzari et al., 2015).

The vibration bands located at 3269 cm^{-1} for ChiPM-1, 3386 cm^{-1} for ChiPM-2, and 3467 cm^{-1} for ChiPM-3 are due to the -OH and N–H stretching vibrations (Altınkaya et al., 2016). The stretching band was observed at around 1400 cm^{-1}, which is attributed to the methyl and methylene groups of chitosan based samples. Vibration bands at around 1635 and 1550 cm^{-1} are assigned to the (C=O) and –NH– groups, respectively. The existence of vibrations of carbonyl bonds (C=O) of the amide group at 1635 cm^{-1} for ChiPM-1, at 1638 cm^{-1} for ChiPM-2, and 1647 cm^{-1} for ChiPM-1 show the availability of MBA in films (Altınkaya et al., 2016; Mano, Koniarova, & Reis, 2003; Xu, Kim, Hanna, & Nag, 2005).

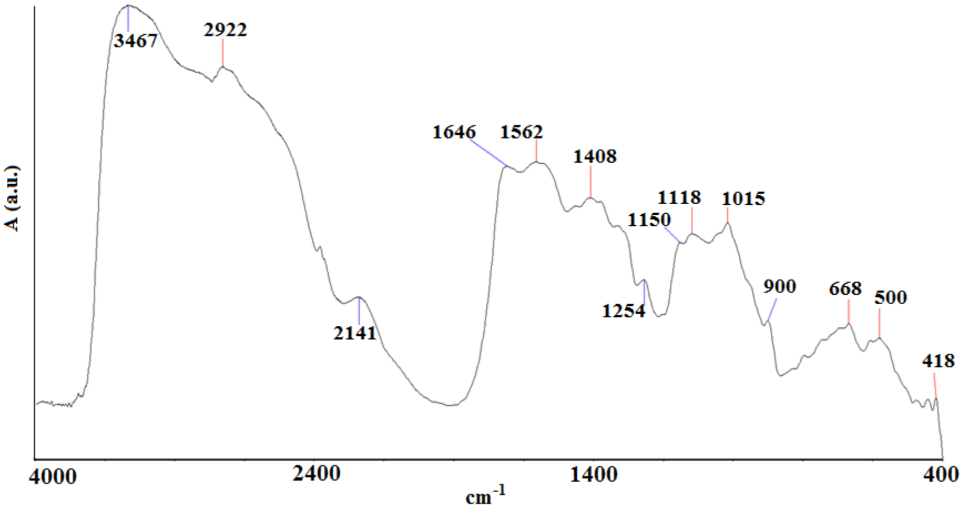

Figure 3.62 FTIR spectrum of chitosan.

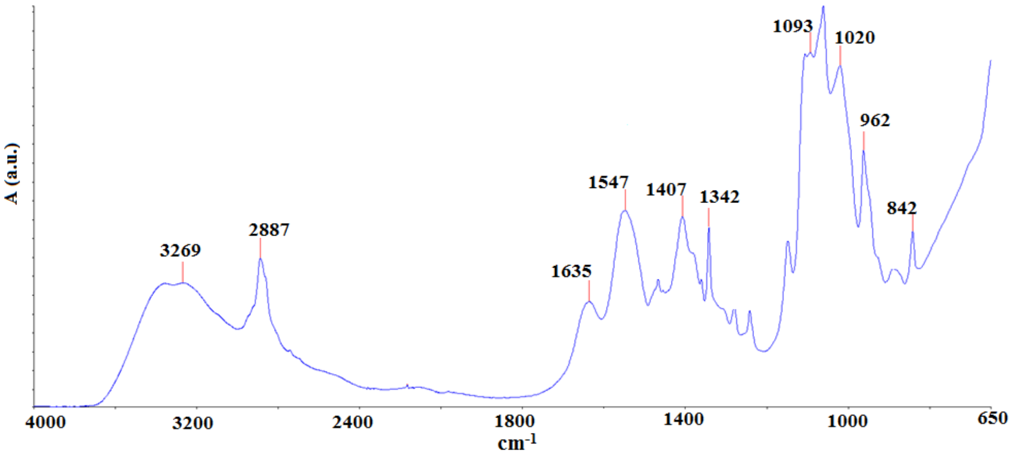

Figure 3.63 FTIR spectrum of ChiPM-1.

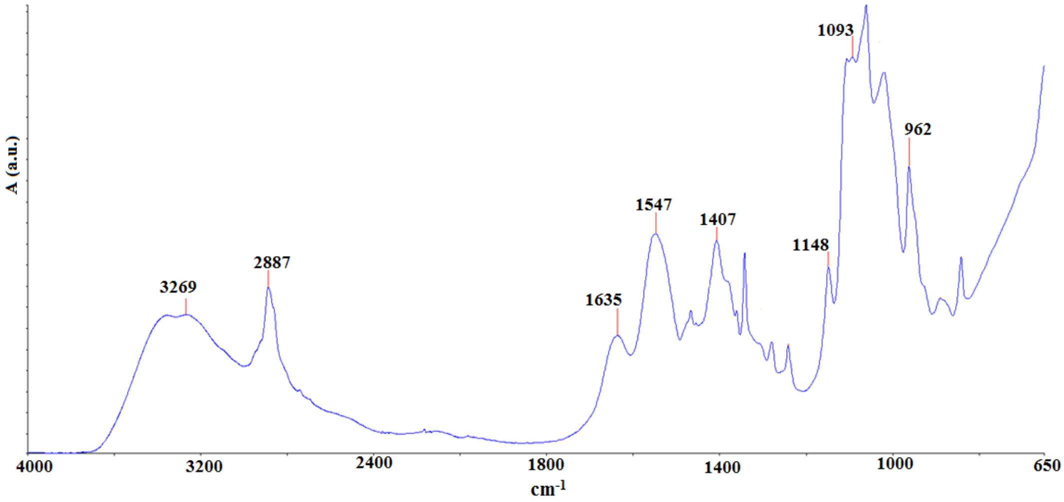

Figure 3.64 FTIR spectrum of ChiPM-2.

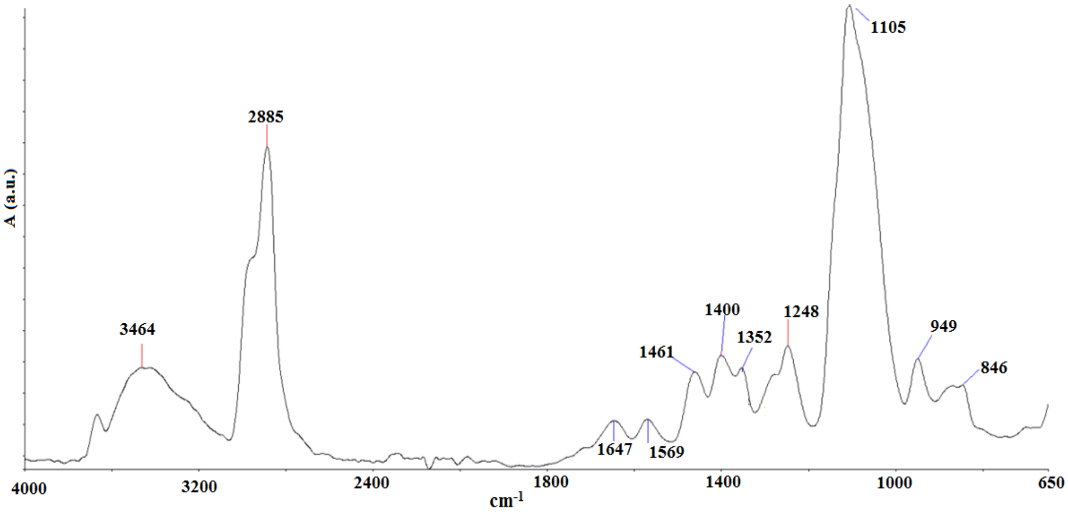

Figure 3.65 FTIR spectrum of ChiPM-3.

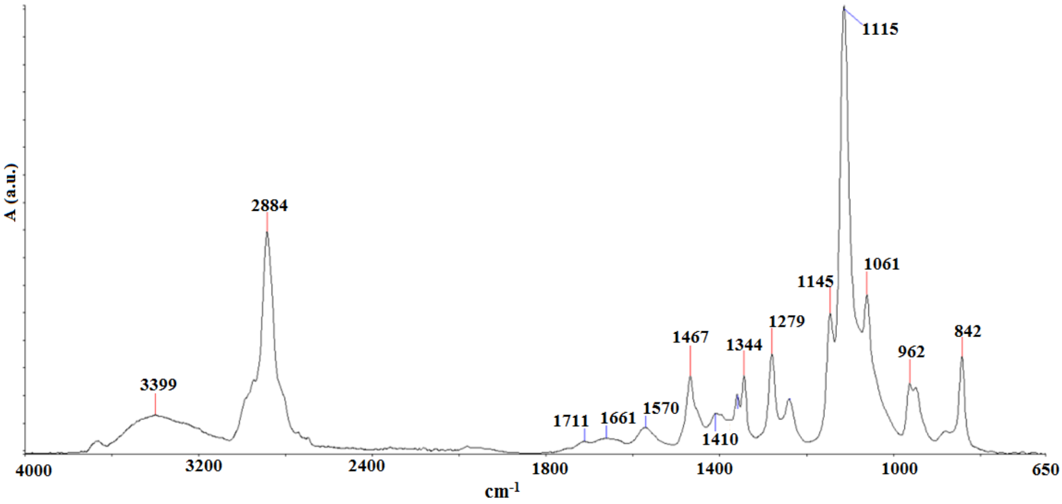

Figure 3.66 FTIR spectrum of ChiM-2.

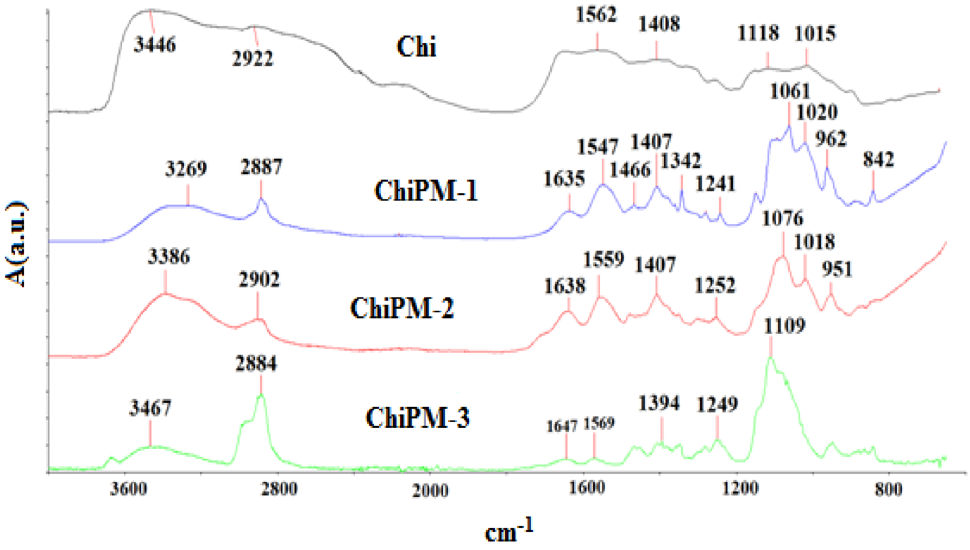

Figure 3.67 FTIR spectra of Chi, ChiM-1, ChiM-2 and, ChiM-3 (Altınkaya et al., 2016).

3.2.2 *X-Ray Diffraction Analysis (XRD)*

The XRD patterns of the samples are shown in Figure 3.68-3.71. Chitosan shows two distinct peaks (Sencadas et al., 2012) at around 11° and 20° whereas ChiMP samples have one peak at around 20-21°. It is known that the crystallinity of the chitosan can be reduced by various chemical treatments (Sencadas et al., 2012). Sreedhar et al. explained that the crosslinking decreased the crystallinity (Sreedhar, Sairam, Chattopadhyay, Rathnam, & Rao, 2005). The CI of the ChiM-1, ChiM-2 and, ChiM-3 are 18.7, 17.9, and 13.5 %. The CI results of the samples were confirmed by the results of Sencades et al. 2012. The amorpous regions for the samples increased as the crosslinker concentration was increased (Altınkaya et al., 2016).

The decrease in the crystallinity can be explained by the decrease in intermolecular and intramolecular hydrogen bonds which help the forming of crystalline structure.

The crosslinking inhibits the folding of macromolecular chains and so gives rise to decrease in the sizes of lamellae crystals. The crystal size is related with total crystallinity. The total crystallinity decreses with the increase in crosslink density due to formation of crosslink junctions at amorphous phase (melt state). The formation of crosslink junctions blocks the chain folding and reorganization during the crystallinization process and so gives rise to formation of smaller size crystallite (Altınkaya et al., 2016; Khonakdar, Morshedian, Wagenknecht, & Jafari, 2003).

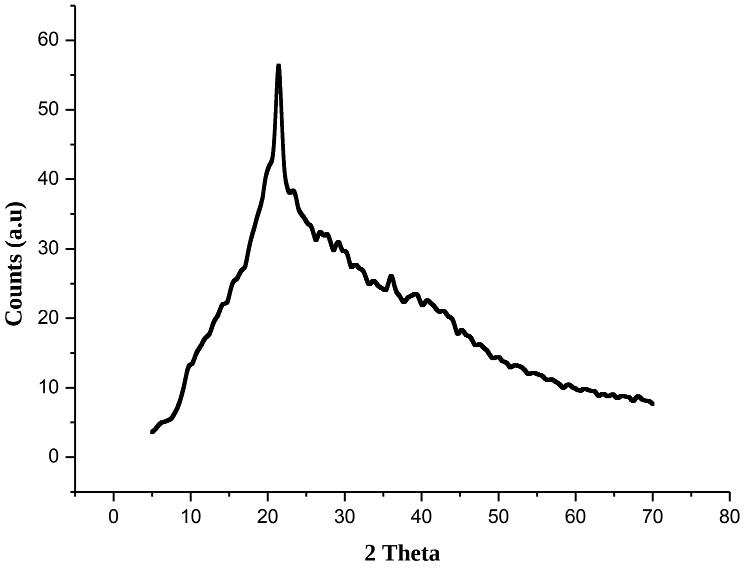

Figure 3.68 XRD pattern of ChiPM-1.

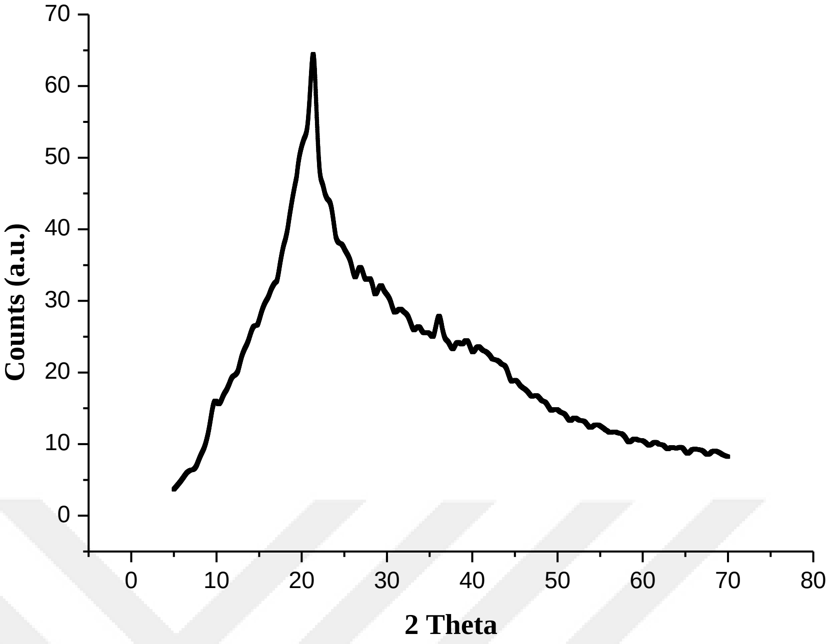

Figure 3.69 XRD pattern of ChiPM-2.

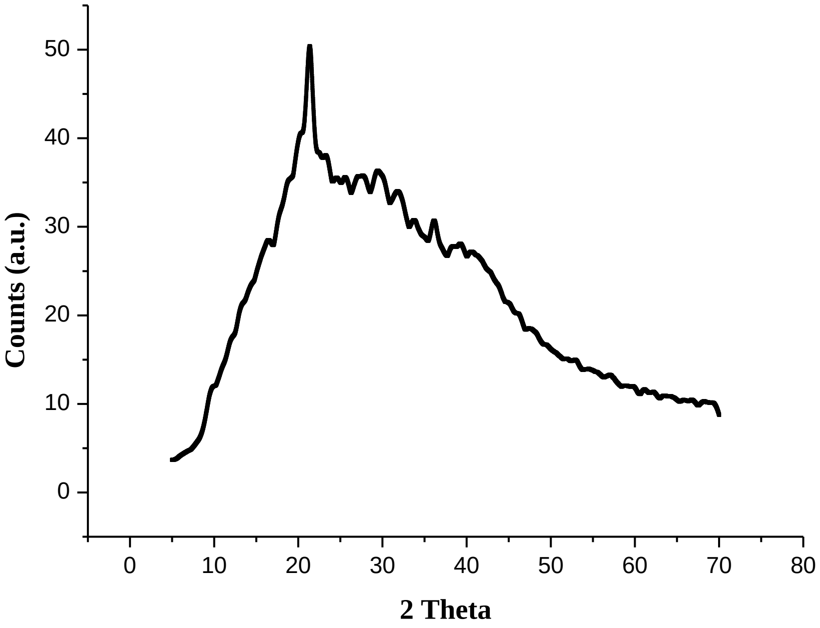

Figure 3.70 XRD pattern of ChiPM-3.

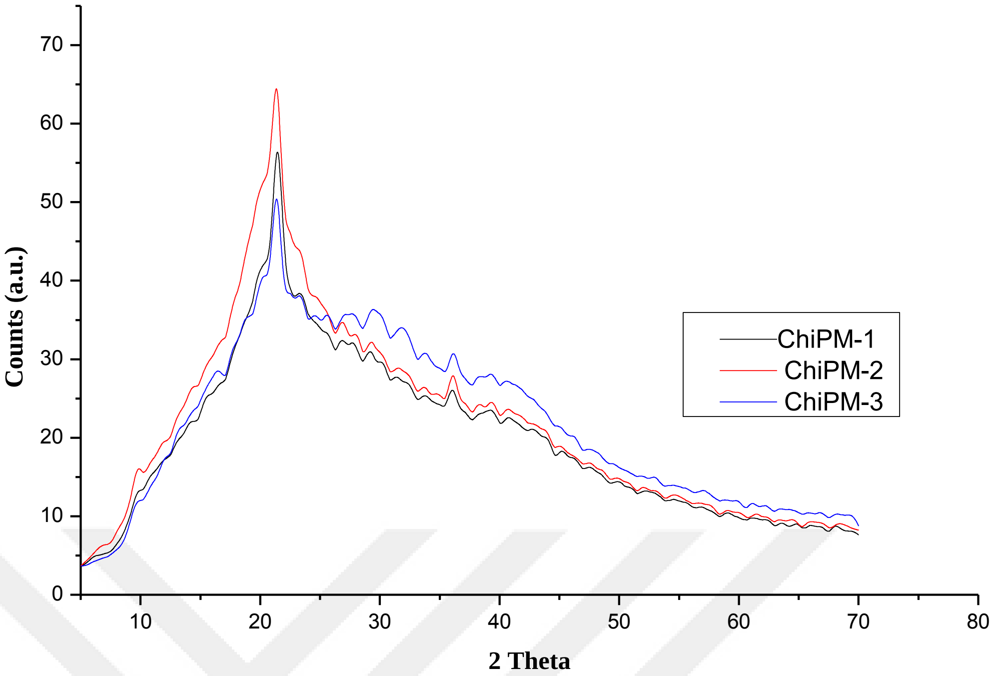

Figure 3.71 XRD patterns of ChiPM-1, ChiPM-2, and ChiPM-3 (Altınkaya et al., 2016).

3.2.3 Thermogravimetric Analysis (TGA)

TGA curves of Chi film, ChiPM-1, ChiPM-2, ChiPM-3 and, ChiM-2 (Altınkaya et al., 2016) were given in Table 3.2 and Figures 3.72-3.76, respectively. Chi film exhibited two mass loss stage (Chiono et al., 2008), as it can be seen in Figure 3.72. Mass loss in first stage is 13.2 % (in the temperature range 31-99 °C) and in second stage is 43.4 % (99-582 °C). The mass loss in first stage can be resulted from evaporation of water in samples (Chiono et al., 2008). The maximum temperature is 56.6 °C for the first stage. Mass loss in second stage may be due to the elimination and vaporization of volatile compounds resulted from further dehydration of water and degradation (thermal and oxidative) of chitosan such as deacetylation and depolymerization (Neto et al., 2005; de Britto and Campana-Filho, 2007; Tripathi, Mehrotra, & Dutta, 2009).

TGA data of the ChiPM-1, ChiPM-2, ChiPM-3, and ChiM-2 (Altınkaya et al., 2016) calculated from TG and DTG curves are summarized in Table 3.2. The samples have three major mass loss stages. The chitosan has two mass loss stages.

However, crosslinked ChiPM samples have three mass loss stages, it can be due to the decomposition of other components. First stage is related with the evaporation of water in samples. Mass loss in the first stage is between 12-28 %. Second and third stages can be attributed to the thermal degradation of samples. As can be seen from Table 3.2 the mass losses of the second stages of ChiPM samples are greater than the third stages. By taking second stage into consideration, the maximum decomposition temperature (T_{max}) of the chitosan film was obtained to be 250°C. For crosslinked samples ChiPM-1, ChiPM-2, ChiPM-3 and, ChiM-2 (Altınkaya et al., 2016) maximum decomposition temperatures were obtained to be 240, 239, 238, 243 °C, respectively. After crosslinking reaction, maximum decomposition temperatures decreased by about 7°C. Sreedhar et al explained that thermal decomposition of sample decreased due to the crosslinking (Sreedhar et al., 2005). The disappearance of H bonding cooperation along the backbone of chitosan due to the crosslinking effect gave rise to decrease in decomposition temperature (Poon, Wilson, & Headley, 2014). Besides, pDADMAC addition into mixture decreased the maximum decomposition temperature of crosslinked chitosan film as well. By taking the third stage into account, while chitosan film has no decomposition in third step, crosslinked chitosan films have decomposition in this stage. Maximum decomposition temperatures (Altınkaya et al., 2016) for ChiPM-1, ChiPM-2, ChiPM-3 and, ChiM-2 were determined to be 393, 387, 375, and 405 °C, respectively. ChiM-2 showed the highest decomposition temperature in the third stage. It is seen that pDADMAC addition gave rise to decrease in the maximum decomposition temperature (Altınkaya et al., 2016) in the third stage. The results show that addition of pDADMAC gave rise to decrease in the thermal stability of crosslinked chitosan. The decrease in decomposition temperatures resulted from chemical or physical interaction of components. For second stage, the crosslinking negatively affected the thermal stability but the difference in the concentration slightly affected the decomposition temperature. For third stage, the negative effect of crosslink concentration can be seen clearly from the results.

Table 3.3 TGA data of chitosan based samples (Altınkaya et al., 2016)

Sample	**First Mass loss (%)**	**Second Mass loss (%)**	**Third Mass loss (%)**	$T_{max}1$ (°C)	$T_{max}2$ (°C)	$T_{max}3$ (°C)
Chi film	13	43		57	250	-
ChiPM-1	19	32	18	68	240	393
ChiPM-2	28	31	15	64	239	387
ChiPM-3	12	27	22	68	238	375
ChiM-2	12	33	20	96	243	405

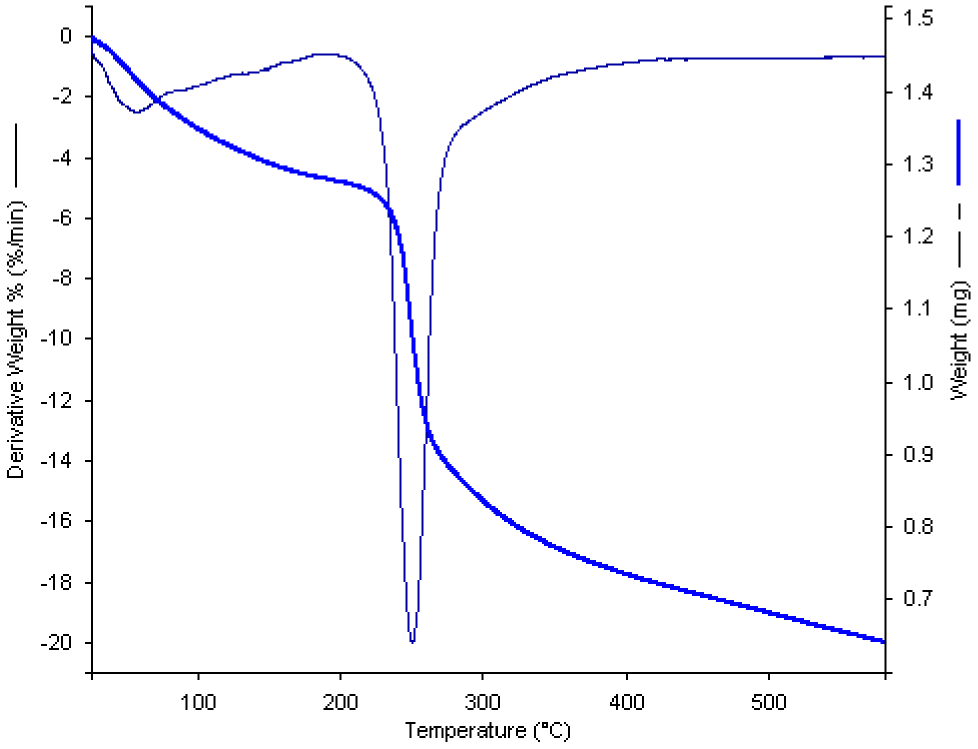

Figure 3.72 TG and DTG curves of chitosan film.

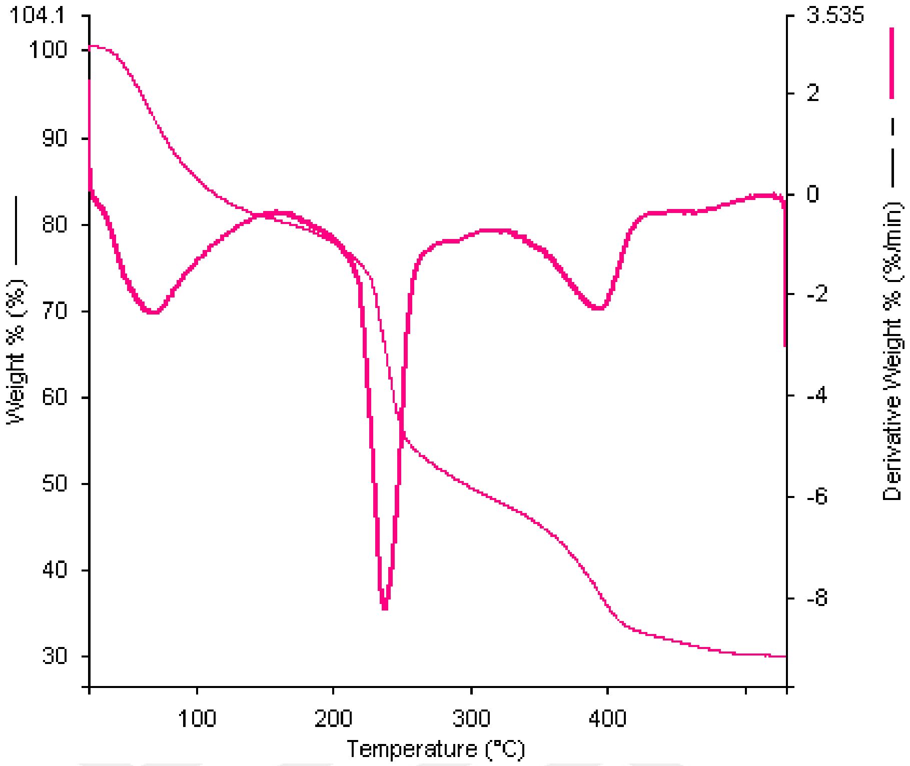

Figure 3.73 TG and DTG curves of ChiPM-1.

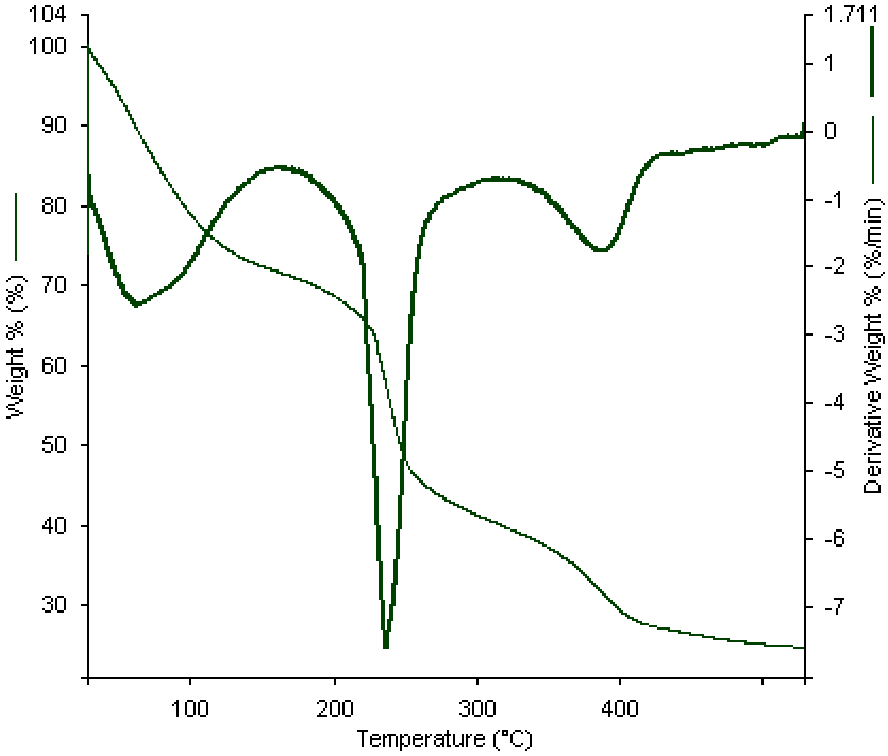

Figure 3.74 TG and DTG curves of ChiPM-2.

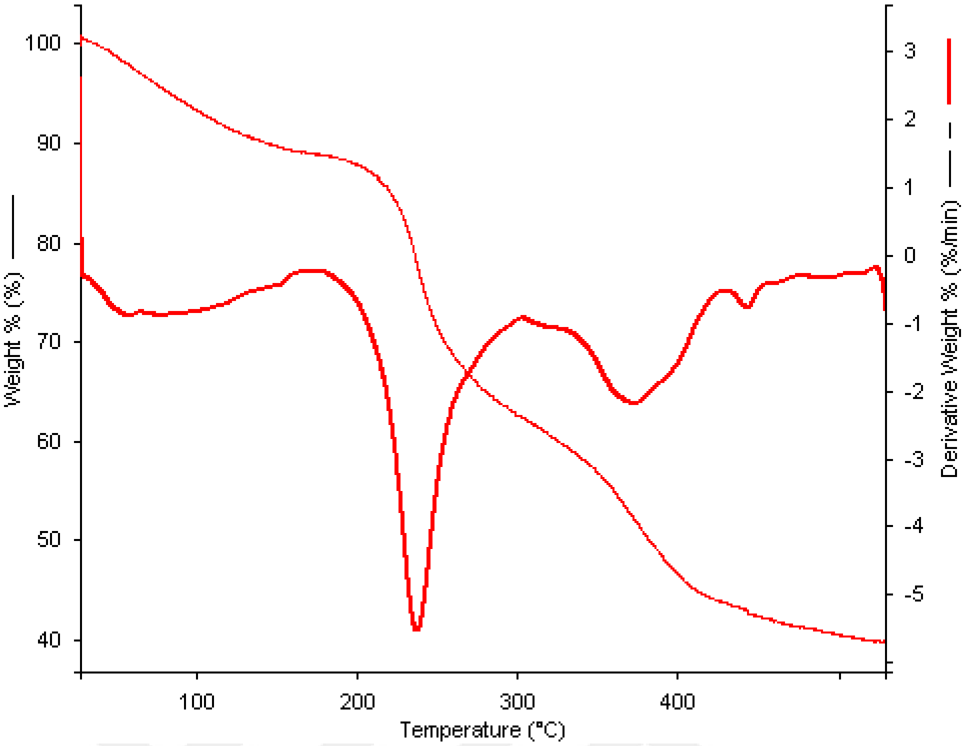

Figure 3.75 TG and DTG curves of ChiPM-3.

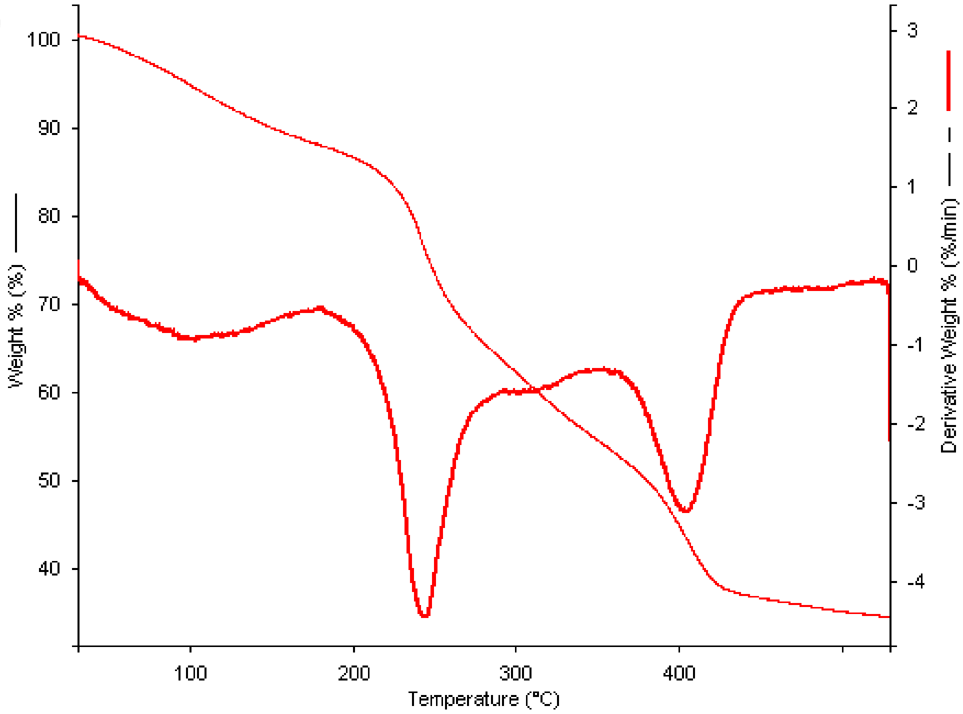

Figure 3.76 TG and DTG curves of ChiM-2.

3.2.4 Scanning Electron Microscopy (SEM)

SEM images of the samples are presented in Figure 3.77-3.100. The images were taken from the surface and cross section of the samples. Figures indicate that the ChiMP-1 has a porous structure. The pores can also be seen from the cross section of the samples (Altınkaya et al., 2016).

The SEM images of ChiMP-1 are shown in Figure 3.77 - Figure 3.82 with different magnification sizes. There are many pores on the sample surface,as can be seen in Figure 3.77. The size and shape of the pore on the surface can be seen clearly in Figure 3.78 magnified 25000 times. The cross-sections of the sample are exhibited in Figure 3.79-3.82. The pores at the cross-section can be seen clearly as the magnification size was increased. For ChiMP-1, the diameters of the pores are approximately in the range 4-13 µm (Altınkaya et al., 2016).

The SEM images of the ChiMP-2 are exhibited in Figure 3.83-88. Many pores on ChiMP-2 can be seen in Figure 3.83 at 500 magnification size. The pores can be seen clearer at the higher magnification sizes. Besides, the pores are clearer in the cross-section of images. The mean diameter of the pores is approximately ~ 13 µm for ChiMP-2. The pore size shows variations at different regions. There are spots on SEM images of ChiMP-3 at 500 magnification size in Figure 3.89. In figure 14 pores can be seen clearly. The pores were seen as spot in Figure 3.89 at smaller magnification size. It can be seen clearly that the pore sizes of ChiMP-3 are smaller than ChiMP-1 and ChiMP-2. For ChiMP-3, the pore sizes are in the range 1-6 µm. The pore sizes of ChiMP-1 and ChiMP-2 are similar whereas the pore sizes of ChiMP-3 are smaller. It is expected that the stiffness of the sample structure increased with the increase in crosslinking (Powell and Boyce, 2006), thus the size of the pores decreased. The supportive results were reported by Servant et al. The results explained that the pore size of the structure decreased as the crosslinker concentration was increased (Servant, Bussy, Al-Jamal, & Kostarelos, 2013). In addition, Rudra et al. 2015 obtained similar results They explained that the increase in crosslink density gave rise to decrease in pore size of structure (Rudra, Kumar, &

Kundu, 2015). There is no pDADMAc in ChiM-2 sample. The SEM images of ChiM-2 are indicated in Figure 3.96-100 (Altınkaya et al., 2016).

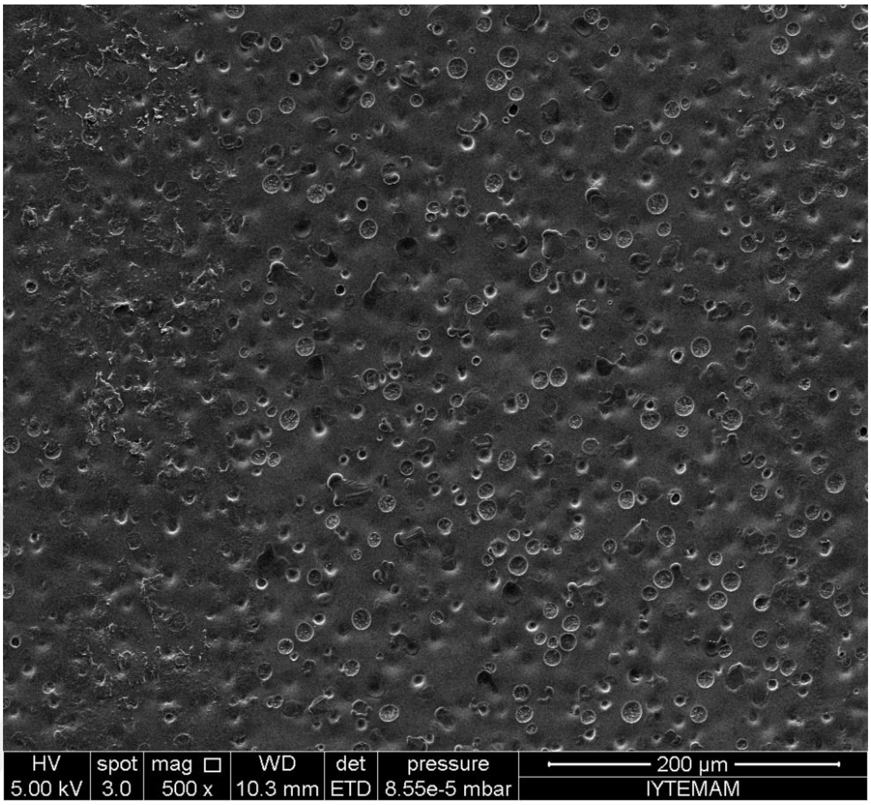

Figure 3.77 SEM image of ChiMP-1 at 500x.

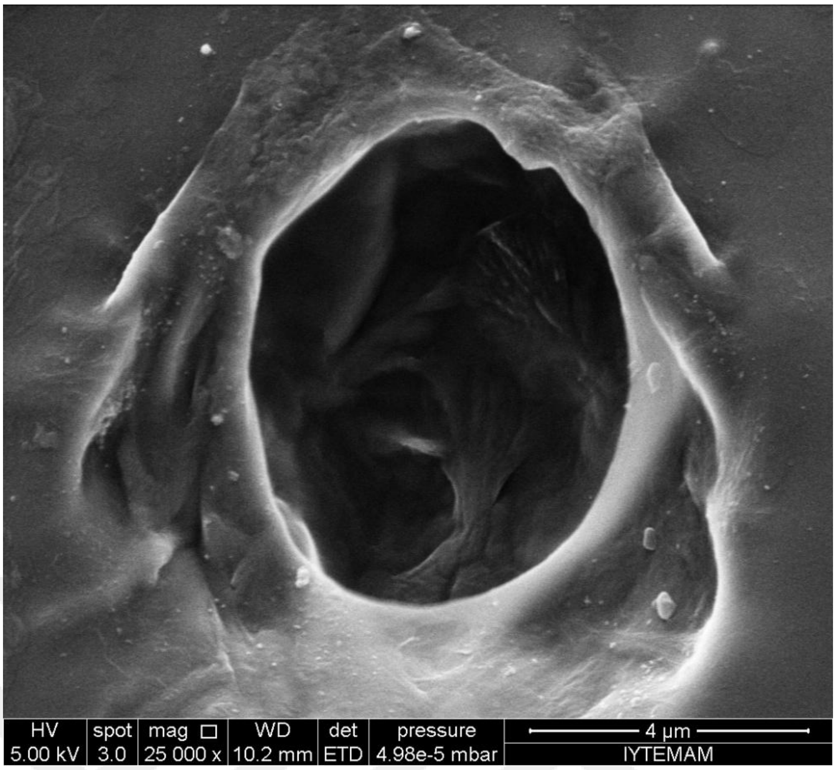

Figure 3.78 SEM image of ChiMP-1 at 25000x.

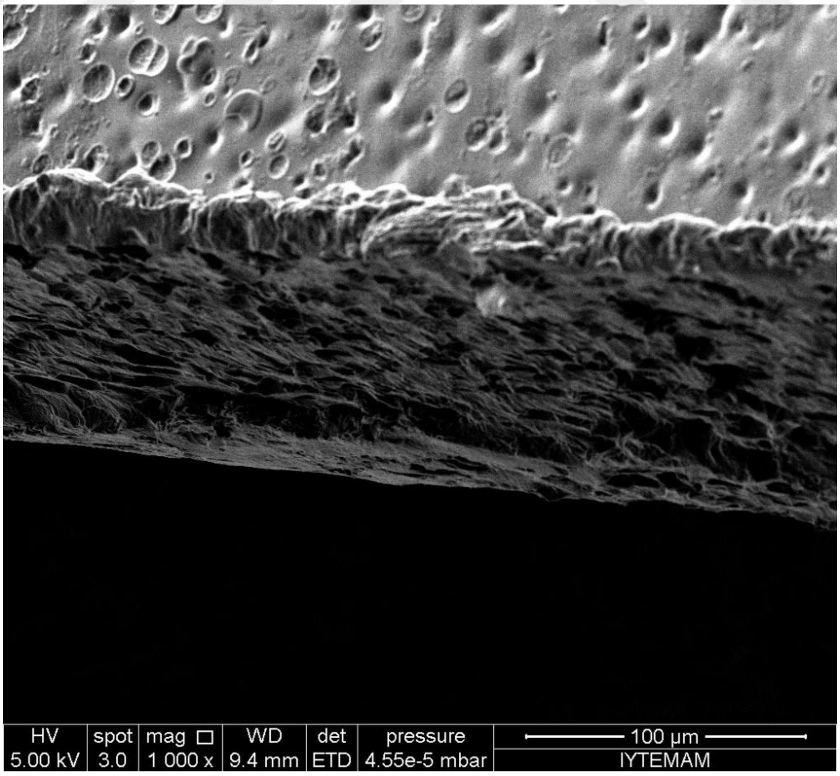

Figure 3.79 SEM image of cross-section of ChiMP-1 at 1000x.

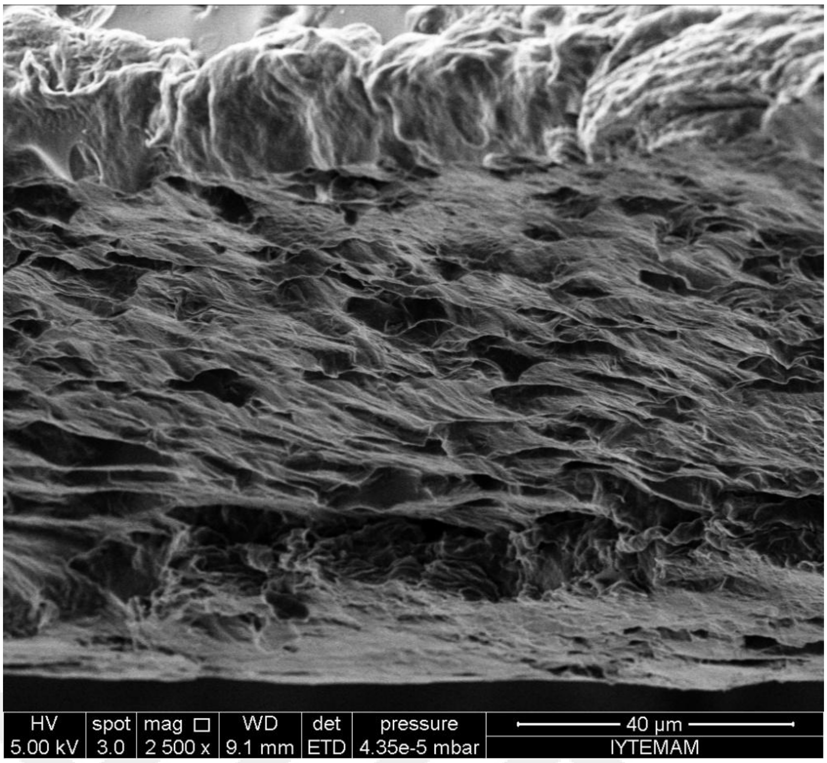

Figure 3.80 SEM image of cross-section of ChiMP-1at 2500x.

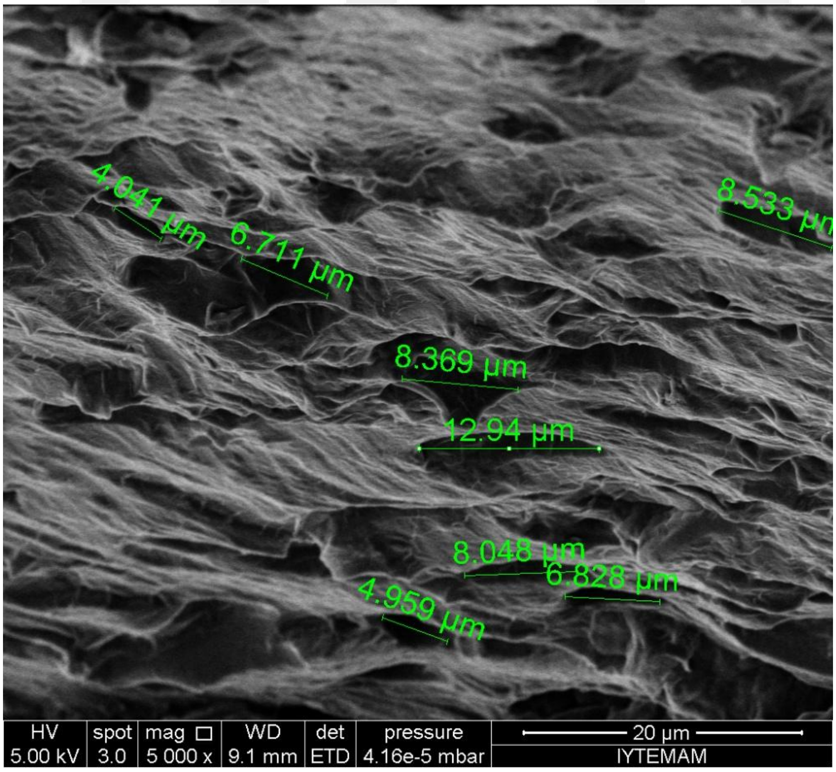

Figure 3.81 SEM image of cross-section of ChiMP-1 at 5000x.

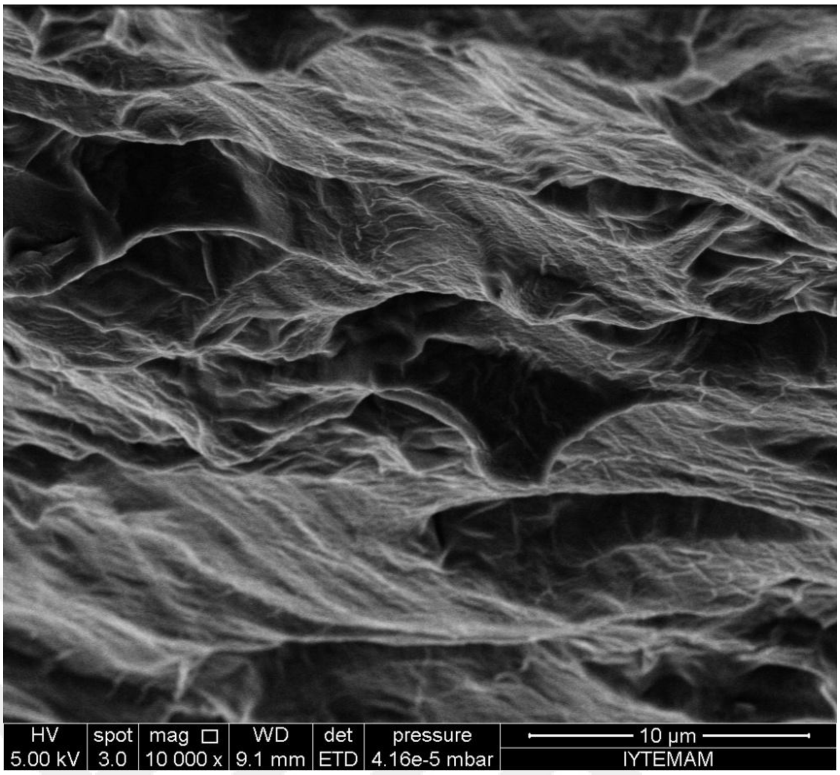

Figure 3.82 SEM image of cross-section of ChiMP-1at 10000x.

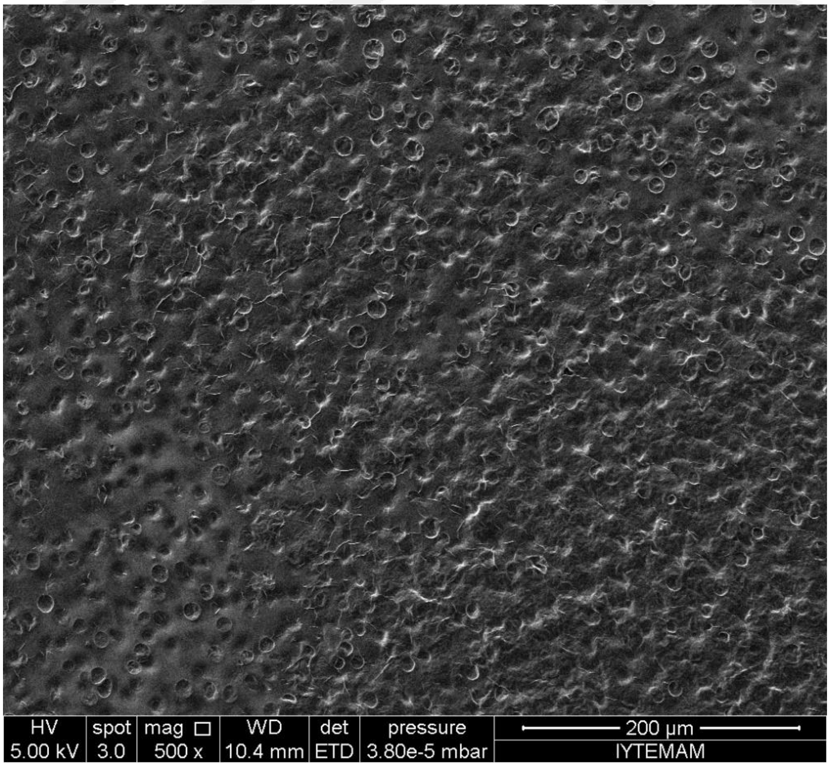

Figure 3.83 SEM image of ChiMP-2 at 500x.

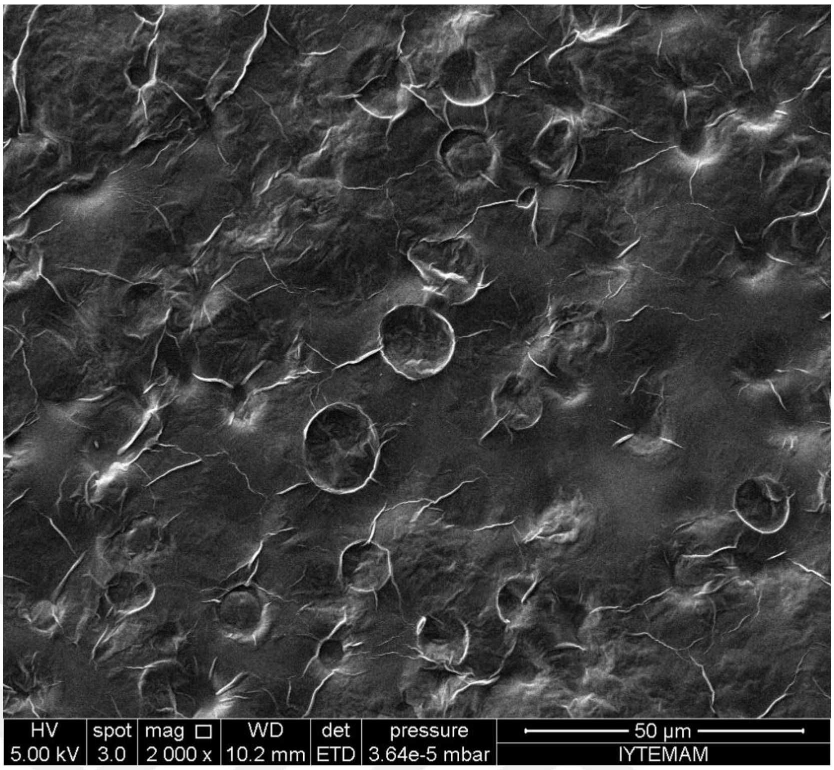

Figure3.84 SEM image of ChiMP-2 at 2000x.

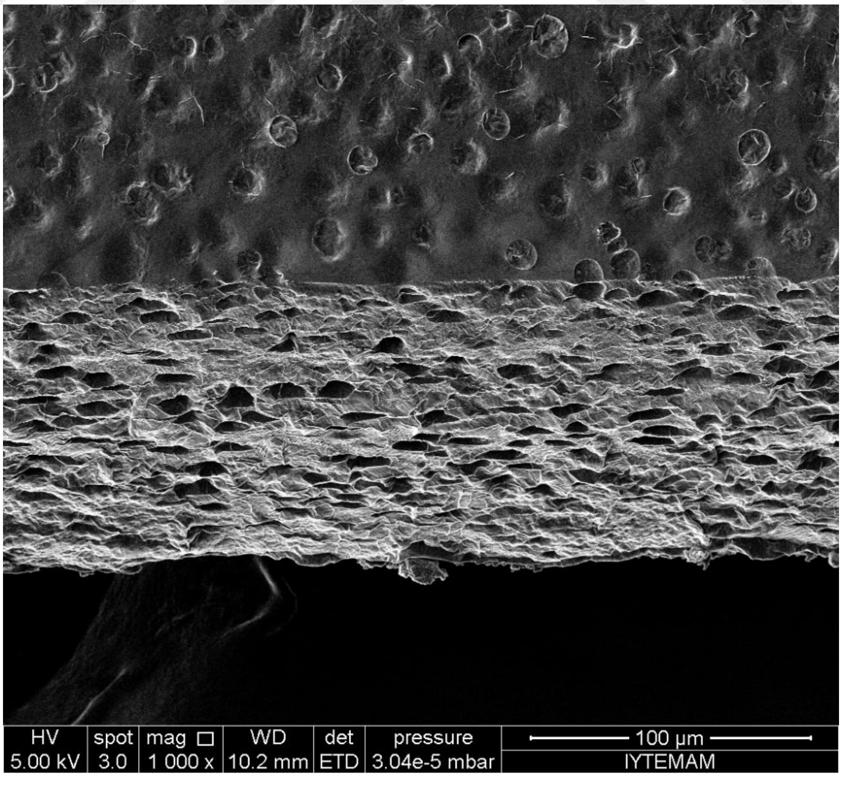

Figure 3.85 SEM image of cross-section of ChiMP-2 at 1000x.

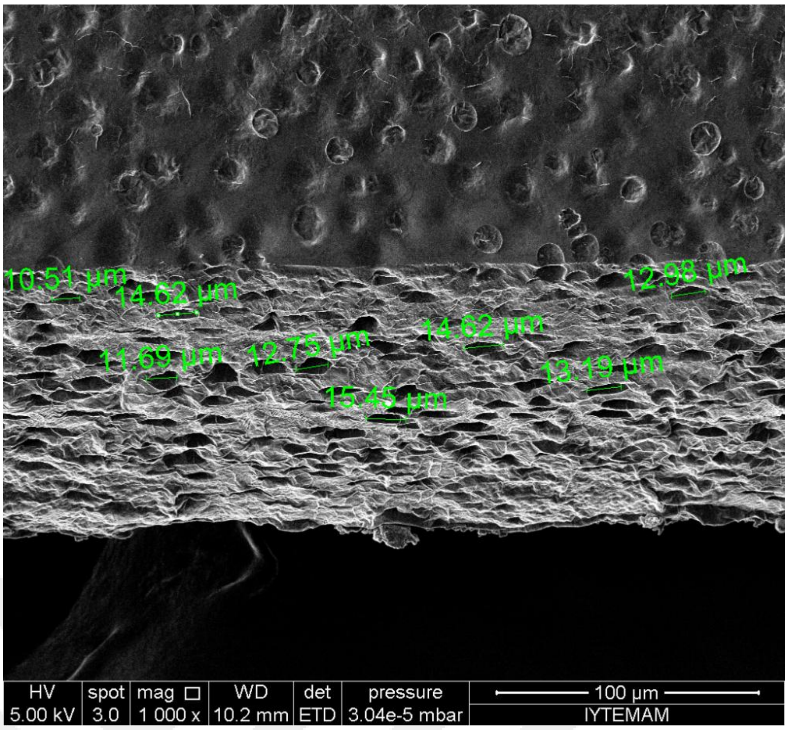

Figure 3.86 SEM image of cross-section of ChiMP-2.

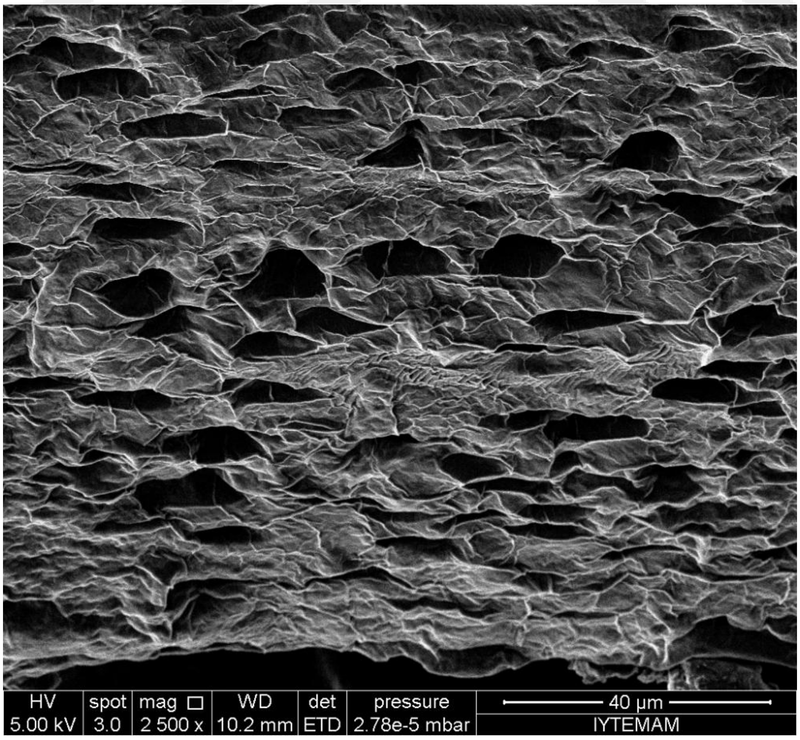

Figure 3.87 SEM image of cross-section of ChiMP-2 at 2500x.

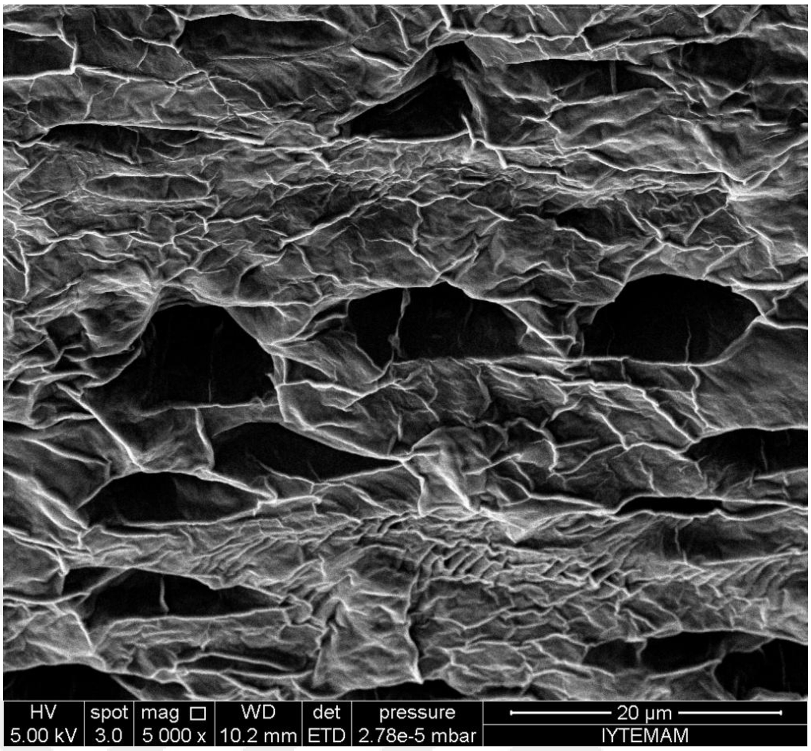

Figure 3.88 SEM image of cross-section of ChiMP-2 at 5000x.

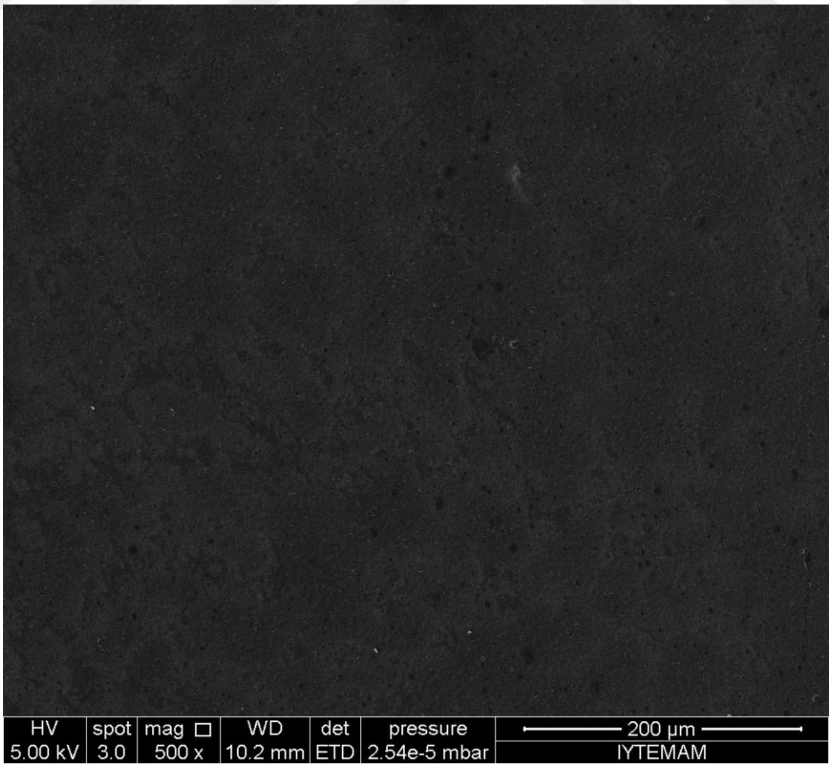

Figure 3.89 SEM image of ChiMP-3 at 500x.

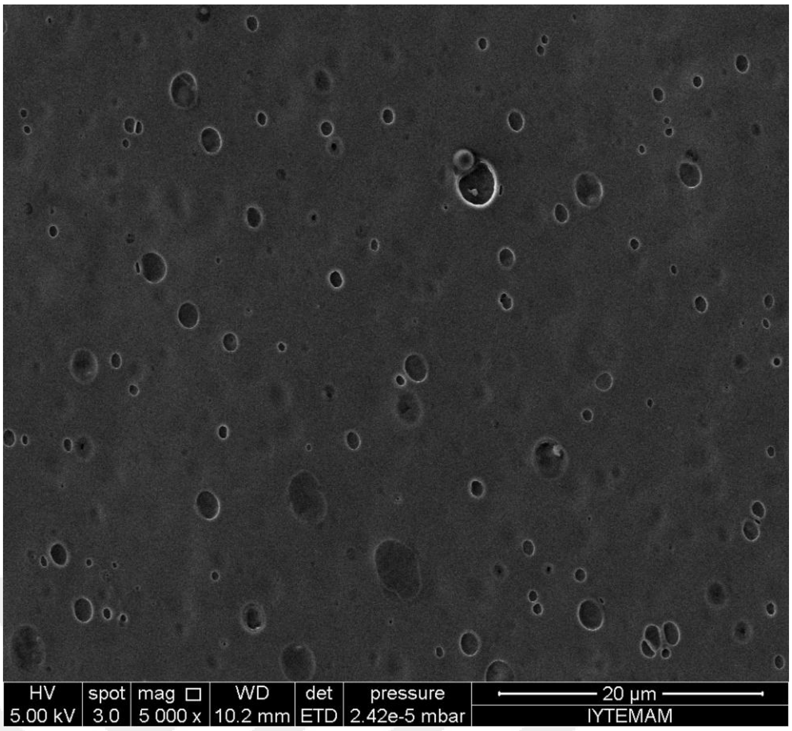

Figure 3.90 SEM image of ChiMP-3 at 5000x.

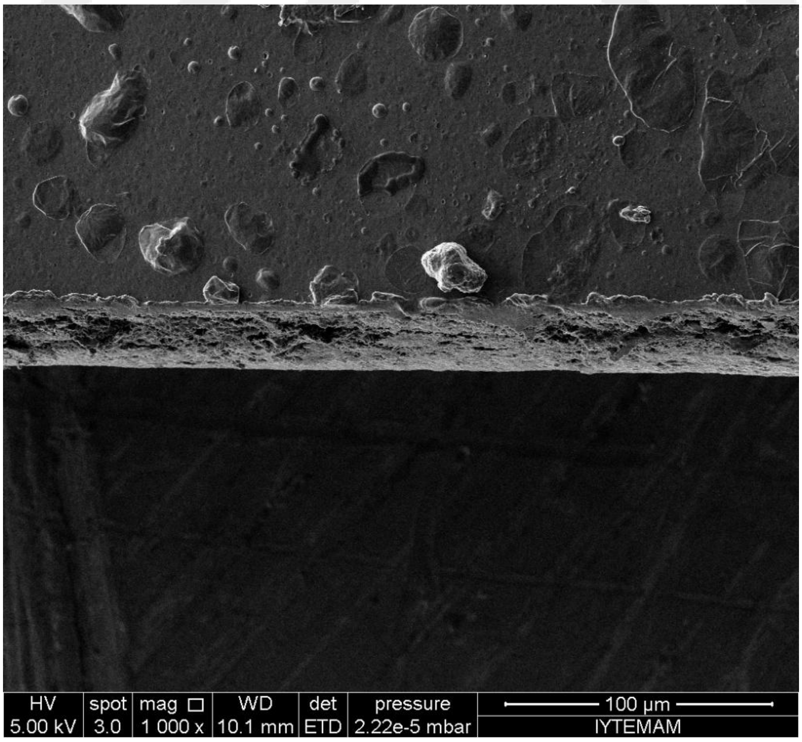

Figure 3.91 SEM image of ChiMP-3 at 1000x.

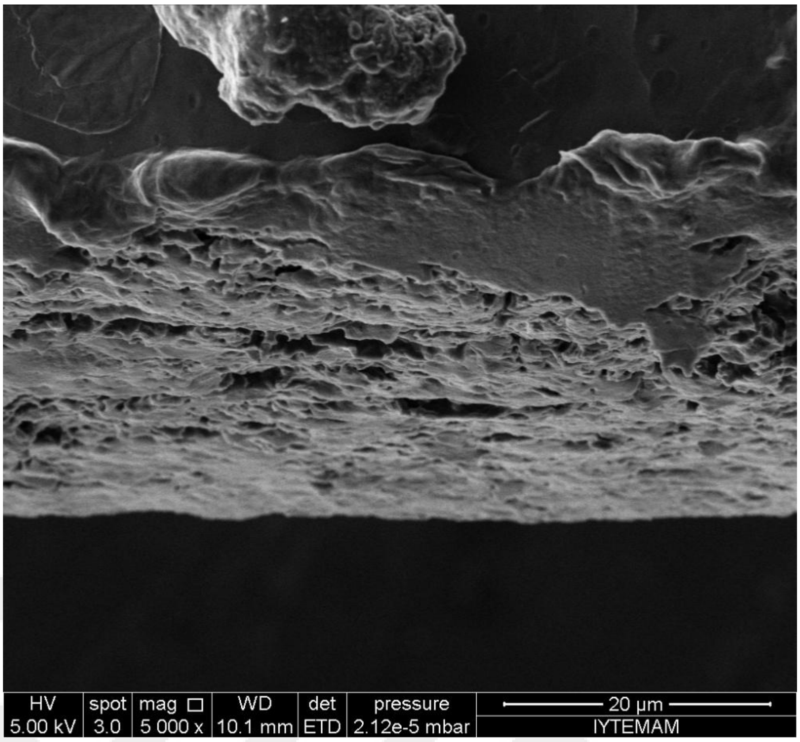

Figure 3.92 SEM image of cross-section of ChiMP-3.

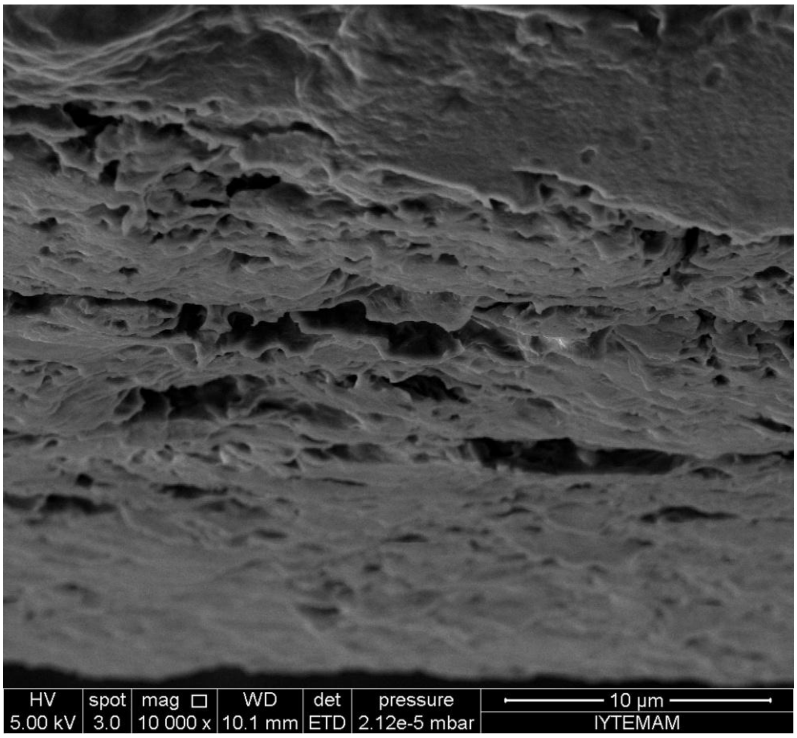

Figure 3.93 SEM image of cross-section of ChiMP-3 at 10000x.

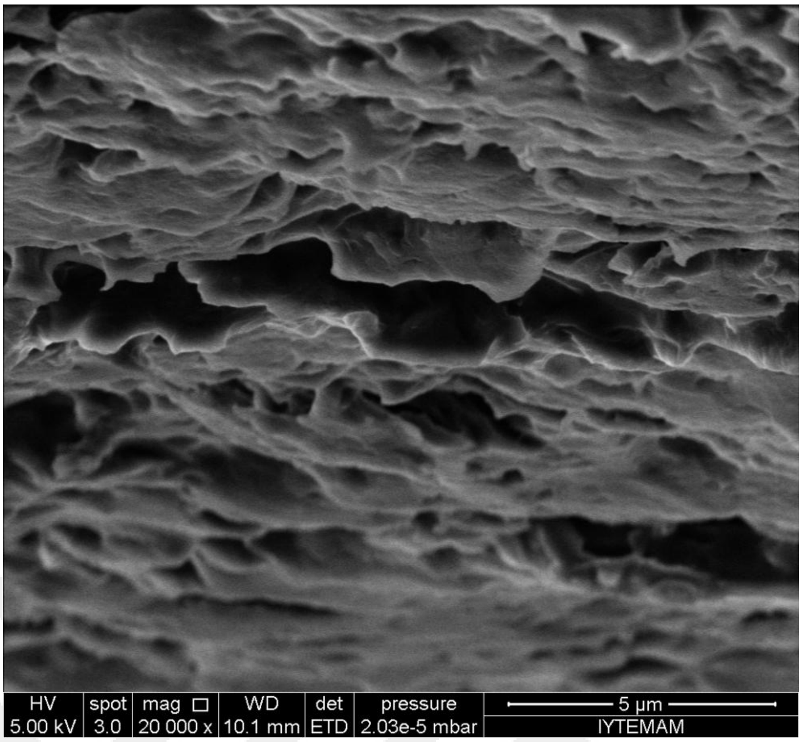

Figure 3.94 SEM image of cross-section of ChiMP-3 at 20000x.

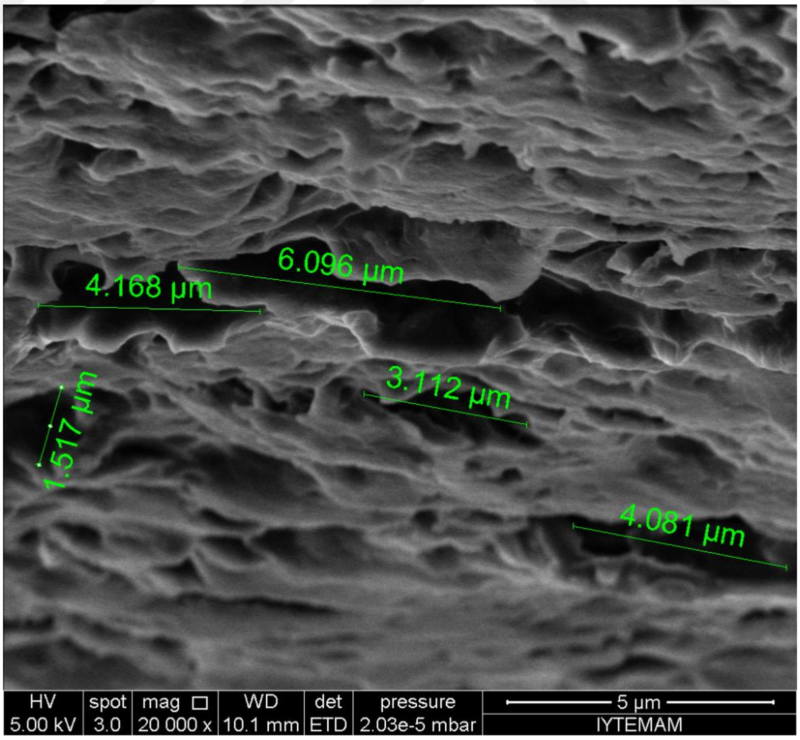

Figure 3.95 SEM image of cross-section of ChiMP-3 at 20000x.

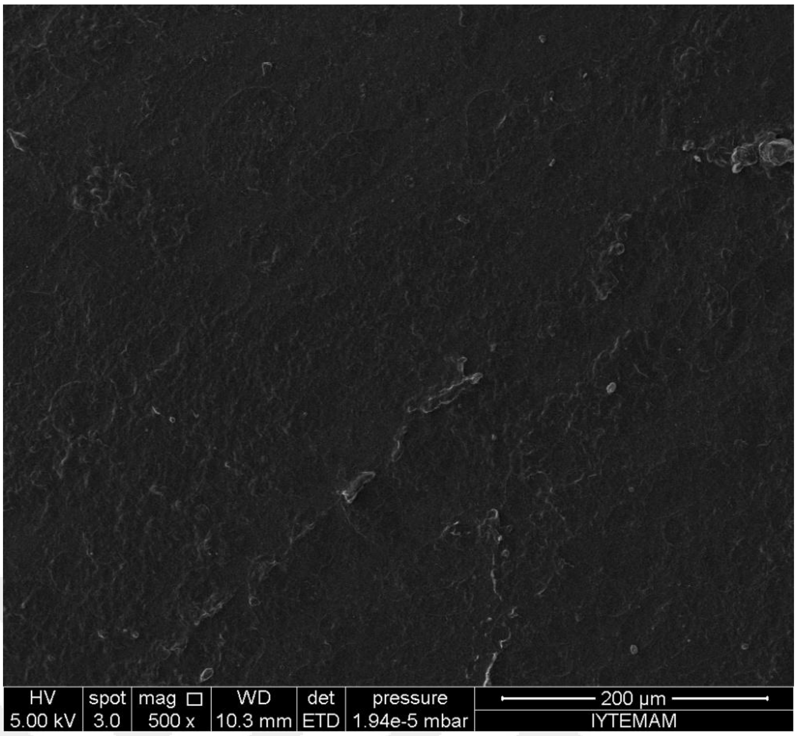

Figure 3.96 SEM image of ChiM-2 at 500x.

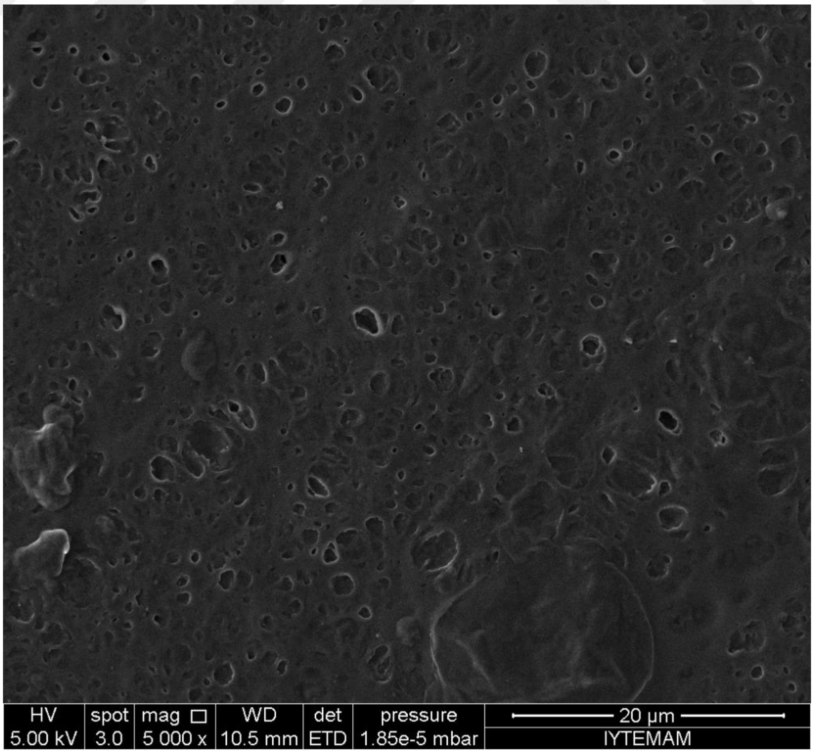

Figure 3.97 SEM image of ChiM-2 at 5000x.

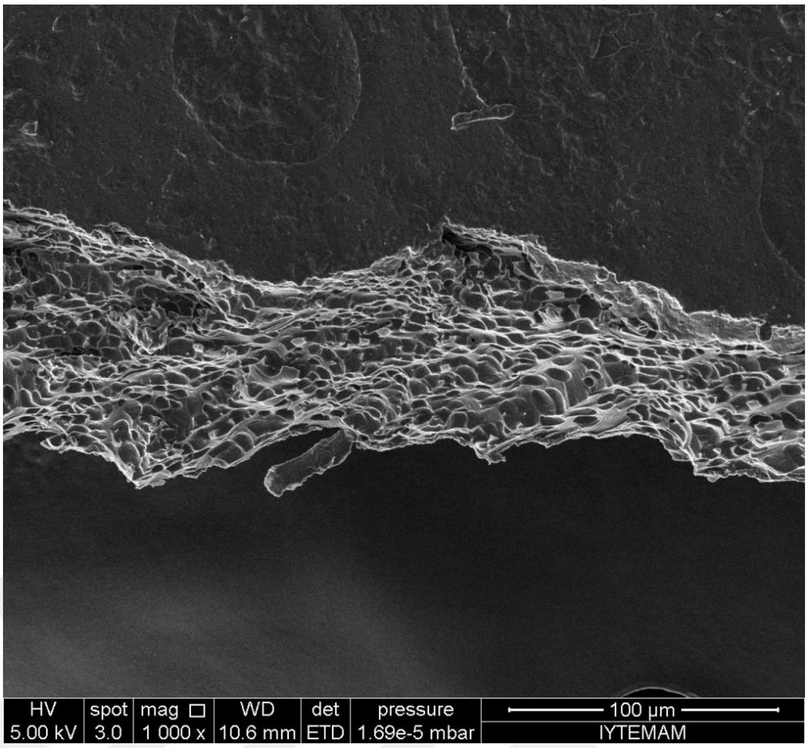

Figure 3.98 SEM image of ChiM-2 at 1000x.

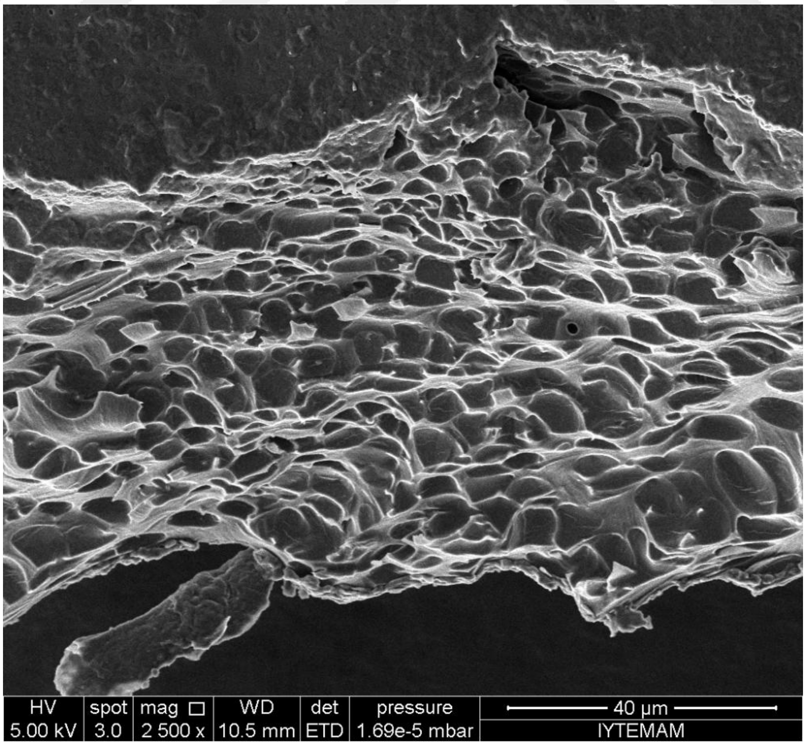

Figure 3.99 SEM image of ChiM-2 at 2500x.

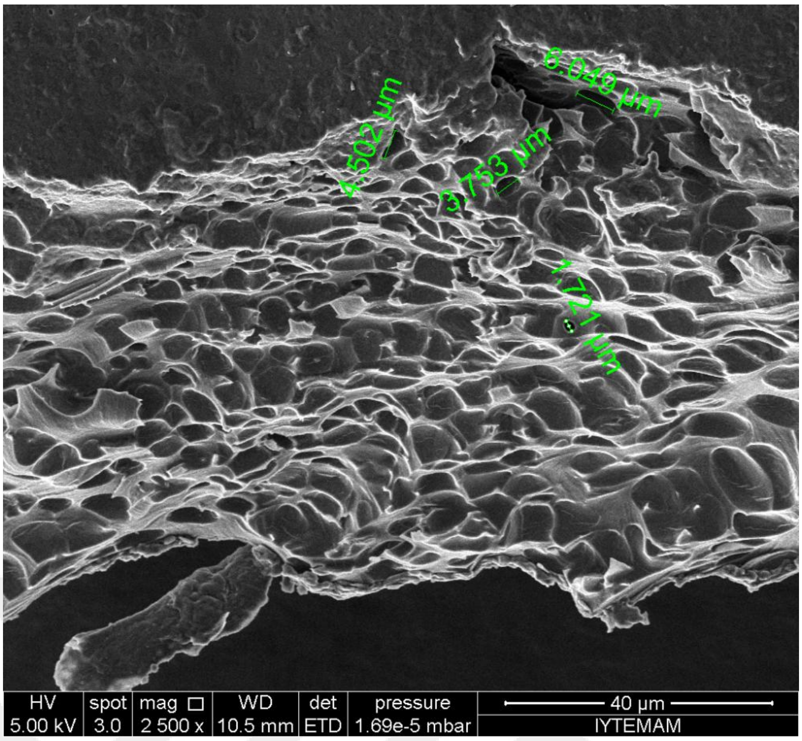

Figure 3.100 SEM image of ChiM-2 at 2500x.

3.2.5 Mechanical Properties

The mechanical properties of ChiPM-1, ChiPM-2, and ChiPM-3 (Altınkaya et al., 2016) are given in Figures 3.101, 3.102, and Table 3.3. The mechanical properties were evaluated according to the crosslinker concentration in Table 3.3. Tensile strengths of the chitosan based samples decreased as the crosslinker concentration was increased (Alimohammadi, Gashti, & Shamei, 2012). The crosslinker concentration gives rise to decrease in ductility of samples (Yeng, Husseinsyah, & Ting, 2015).

Young's modulus, is a measure of a material's tensile stiffness, of the samples was increased with increasing the crosslinker concentration (Frohbergh et al., 2012; Yeng et al., 2015).

Tensile strength values of ChiPM-1, ChiPM-2, and ChiPM-3 (Altınkaya et al., 2016) were obtained to be 21.21 MPa, 18.69 MPa, and 14.65 MPa, respectively. In the presence of pDADMAC, increasing the crosslinker concentration decreased the tensile strentgh. Young’s moduli of ChiPM-1, ChiPM-2, and ChiPM-3 (Altınkaya et al., 2016) were obtained to be 417.65, 571. 37, and 666.67 MPa, respectively. It can be inferred that increase in crosslinker concentration led to increase in Young’s modulus. ChiPM films became more brittle with the increase in crosslink density. The increase in crosslink density makes the films more brittle at small elongation. The decrease in tensile strength with the increasing crosslinking concentration was unusual (Liu, Su,& Lai, 2004). The similar results were obtained by Liu et al. (Liu et al., 2004) and Hsiue et al. (Hsiue, Chen, & Liu, 2000; Altınkaya et al., 2016).

Table 3.4 Mechanical properties of ChiPM-1, ChiPM-2, and ChiPM-3 (Altınkaya et al., 2016)

Sample	Tensile Strength MPa	Young’s modulus (MPa)
ChiPM-1	21.2±0.3	417.7±4.6
ChiPM-2	18.7±0.2	571.4±2.8
ChiPM-3	14.7±0.2	666.7±5.4

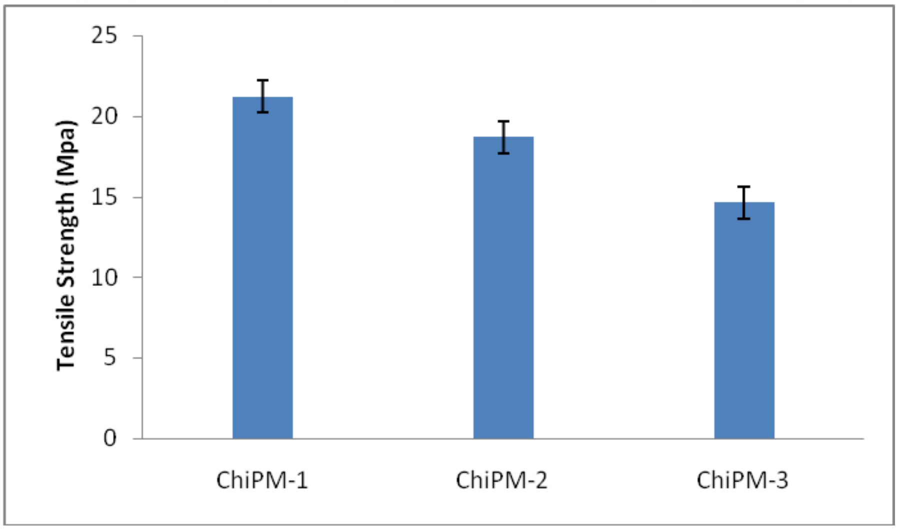

Figure 3.101 Tensile strength of ChiPM-1, ChiPM-2 and, ChiPM-3 (Altınkaya et al., 2016).

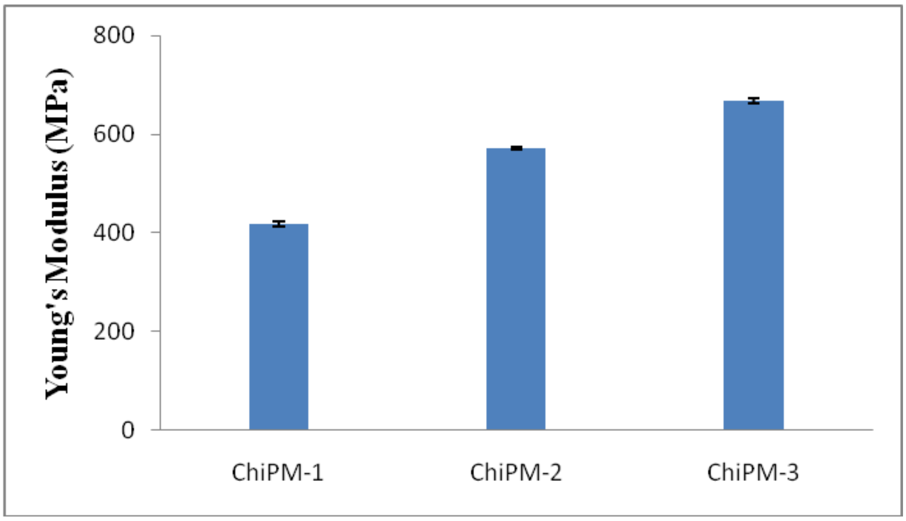

Figure 3.102 Young's Modulus values of the ChiPM-1, ChiPM-2 and, ChiPM-3 (Altınkaya et al., 2016).

3.2.6 Electroactive Properties

3.2.6.1 Motion Test

Two sets of experiment were carried out to represent the capability of actuator samples to move and generate force under DC voltages with two different polarities. The electroactive properties based motion capability of chitosan based films was investigated under the DC voltages (3, 5, 7, 9, 11, 13, 15, 17, and 21 V) with 500 s (0.002 Hz). The studies were carried out under the room temperature. Tip displacements of the chitosan based samples were investigated with CCD camera and recorded. The recorded data were processed and tip displacements were evaluated. Time versus tip displacement curves were obtained for each actuator. The curves of the samples are shown in Figures 3.103-3.108 (Altınkaya et al., 2016).

The max tip displacement of ChiPM-1 was determined to be 26.6 mm under the 15 V. The minimum tip displacements were observed as 3.11 mm under 5V and 21 V. Comparison of the max tip displacement of ChiMP-1 was exhibited in Figure 3.104.

The max tip displacement for ChiPM-2 was obtained as 19.6 mm under the 7V. Any displacement was not observed above 17 and 21 V. It is probable that these high voltages may degrade the actuator and thus any tip displacement was not seen. The max tip displacements of the ChiPM-2 for different voltages can be seen in Figure 3.106. Besides, ChiM-2 sample was studied under 3, 5, 7, 9, 13, 17, and 21 V but any displacement was not observed in this sample (Tip displacement graph of ChiM-2 was not given) (Altınkaya et al., 2016).

The max tip displacement of ChiPM-3 under DC voltages was shown in Figure 3.107. The max and min tip displacements for ChiPM-3 are 1.2 and 0.6 mm, respectively. Tip displacement of ChiPM-3 is less than those of ChiPM-1 and ChiPM-2. Motion was observed under 3, 5, 7, and 9 V. Under 11, 13, 15, 17, and, 21 V any motion was not observed. It is probable that the stiffness of the ChiMP-3 affects the mobility of film (Altınkaya et al., 2016).

The ion mobility is an important parameter for actuation of ionic actuator. Typical ionic actuators consist of mobile ions which help the motion of polymer due to ion diffusion. The diffusion occurs under the electrical potentials. The diffusion of hydrated cations diffused toward to the negatively charged electrode and so the motion occurs (Shahinpoor et al., 1998; Shahinpoor and Kim, 2001; Shahinpoor, Kim, & Leo, 2003; Akle, Leo, Hickner, & McGrath, 2005; Phillips and Moore, 2005; Wang, Oh, Lu, Ju, & Lee, 2007; Duncan, Akle, Long, & Leo, 2009; Lee, Kim, Goo, Lee, & Yoo, 2010; Lee, Wang, Yoon, Han, & Jho, 2010; Luqman, Lee, Moon, & Yoo, 2011; Kwon et al., 2015).

The mobility of the actuators decreased with the increasing crosslink density. Presumably there is a relation between crosslinking and stiffness. The stiffness adversely affects the mobility. Rudra et al. explained that the increase in crosslink density increased the stiffness and reduced the ion mobility (Rudra, Kumar, & Kundu, 2015). Redecuce in mobility negatively affected the motion of actuator (Altınkaya et al., 2016).

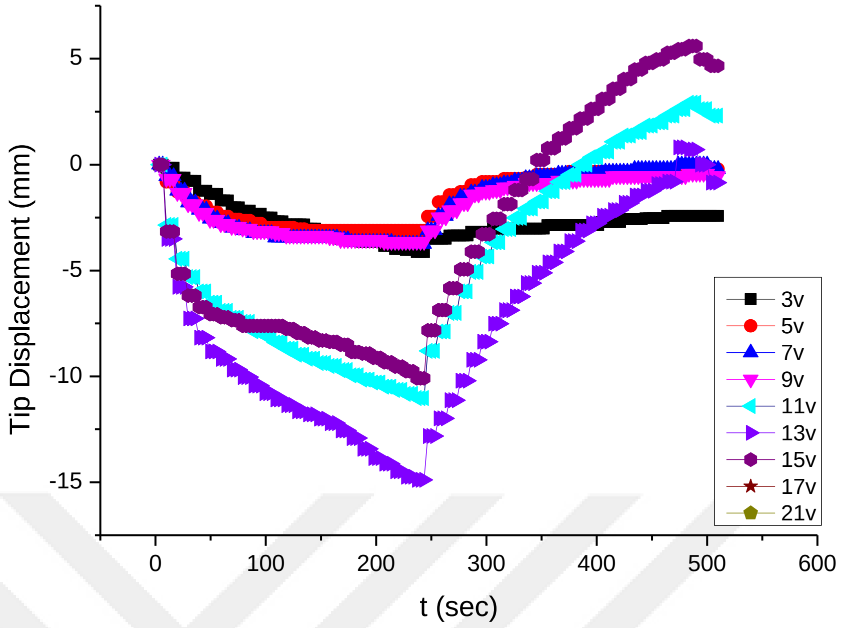

Figure 3.103 Tip displacements of ChiPM-1 under various DC voltages.

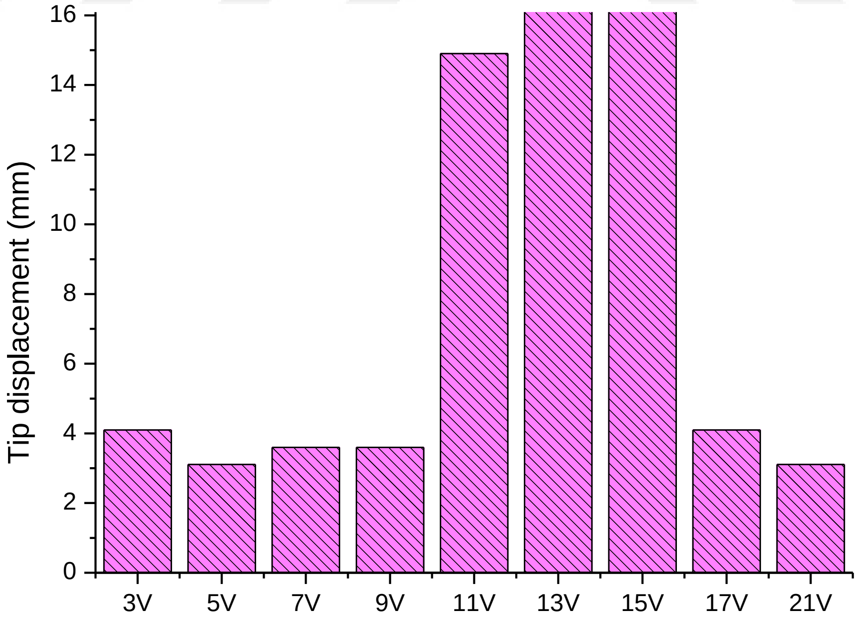

Figure 3.104 Comparison of the max tip displacement of ChiPM-1 under various DC voltages.

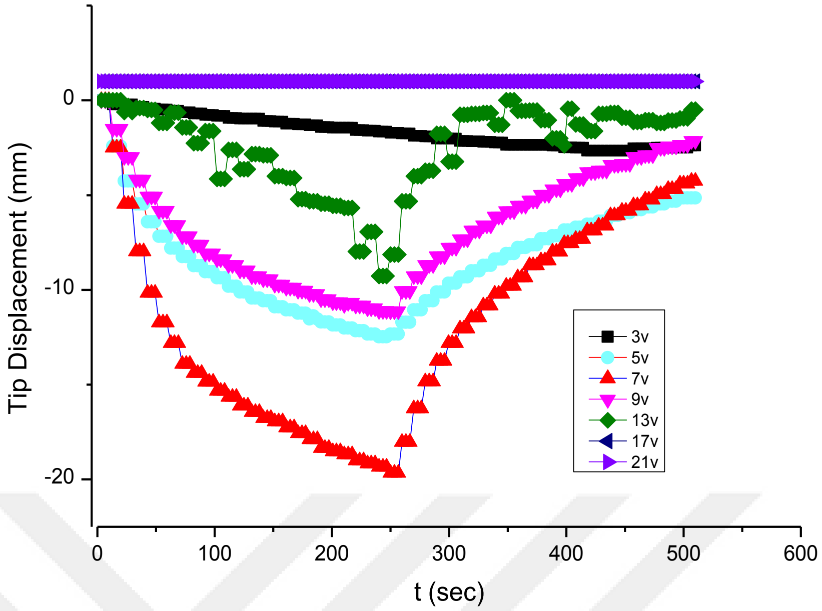

Figure 3.105 Tip displacements of ChiPM-2 under various DC voltages.

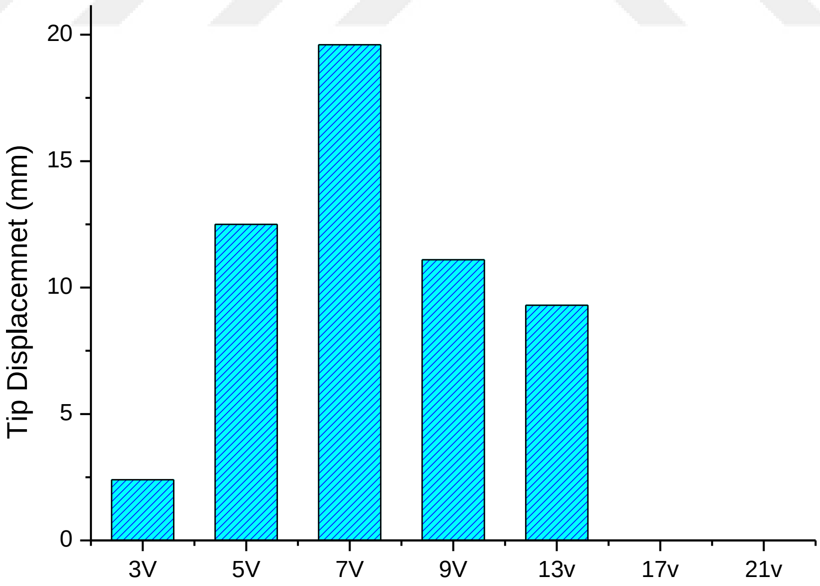

Figure 3.106 Comparison of the max tip displacements of ChiPM-2 under various DC voltages.

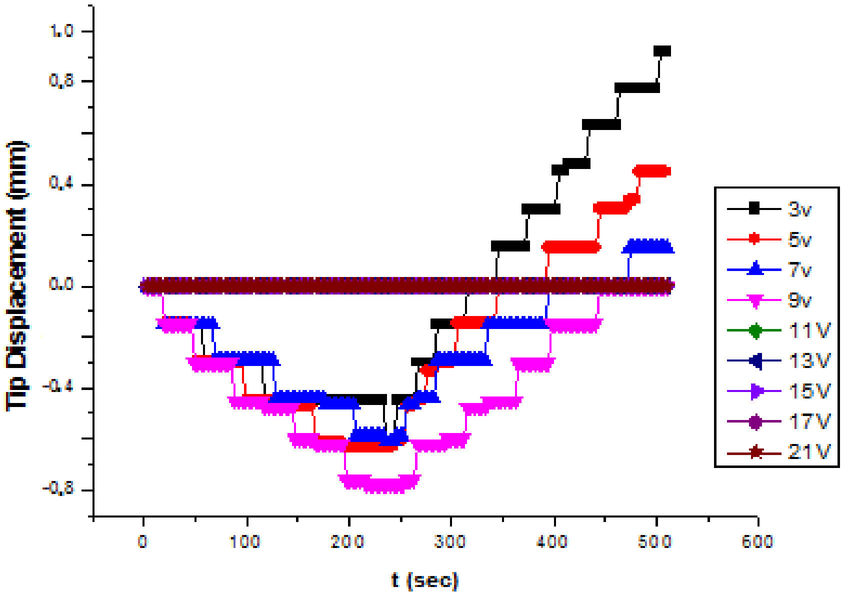

Figure 3.107 Tip displacements of ChiPM-3 under various DC voltages.

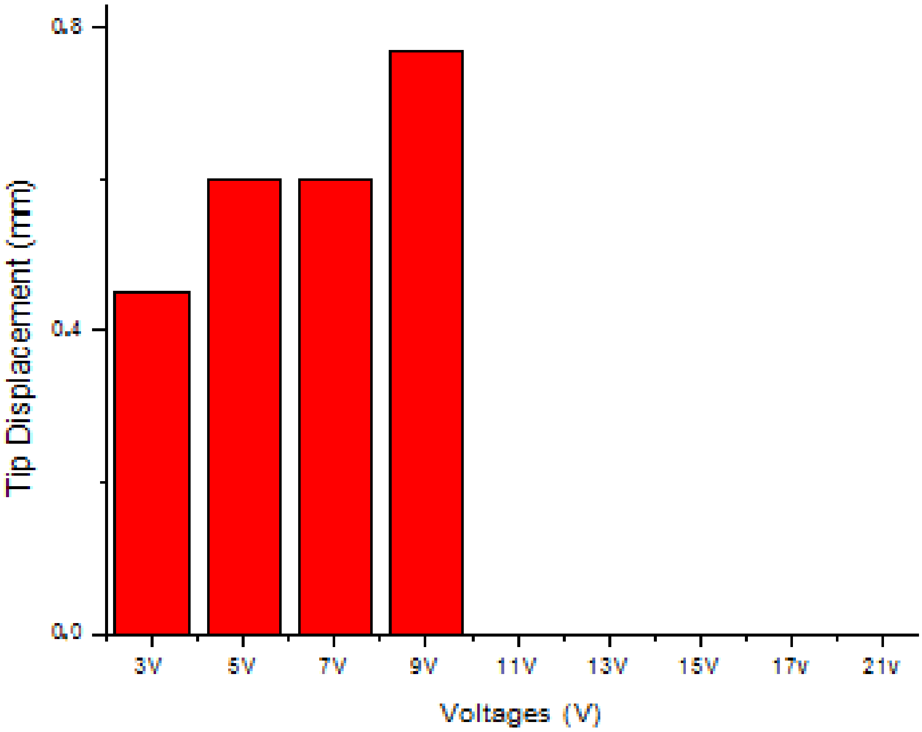

Figure 3.108 Comparison of the max tip displacements of ChiPM-3 under various DC voltages.

3.2.6.2 Blocking Force

The force generation capabililty of chitosan based actuators were analyzed by measuring the blocking force. The actuator samples were put on the precision balance and DC excitations were applied and so the force generation capability was evaluated (Altınkaya et al., 2016). The results are indicated in Table3.4.

Table 3.5 The blocking force results

Applied Voltage	**ChiMP-1 (g)**		**ChiMP-2 (g)**		**ChiMP-3 (g)**	
	max	**min**	**max**	**min**	**max**	**min**
3V	0.026	-0.032	0.066	0	0	-0.073
5V	0.064	0	0.097	0.064	0.041	-0.058
7V	0.044	-0.01	0.01	-0.16	0.04	-0.035
9V	0.057	-0.01	0.028	0.055	0.012	-0.096
13V	0.04	-0.034	0.015	-0.04	0.049	-0.095
17V	0.069	-0.01	0.014	-0.04	0.048	-0.11
21V	0.072	-0.01	0.017	0.036	0.024	-0.054

3.2.7 Dynamic Mechanical Analysis

The dynamic mechanical analysis curves were exhibited in Figures 3.109, 3.110, and 3.111 for Dynamic Storage Modulus E’, Dynamic Loss factor $\tan\delta$, and Dynamic Loss Modulus E’’, respectively. The storage modulus generally is used to measure of stiff or flimsy of the sample. The variation of dynamic storage modulus E' with temperature are shown in Figure 3.109. The storage modulus of ChiPM-3 has the lowest value as shown in Figure 3.109. The difference between the storage modulus values can be seen clearly at lower temperatures. The storage modulus values of samples show closer results at high temperatures. The storage modulus E’ decreased as the temperature was increased. Many studies confirmed this result (Idicula, Malhotra, Joseph, & Thomas, 2005; Su et al., 2012; Jawaid, Khalil, Hassan, Dungani, & Hadiyane, 2013). The storage modulus is generally associated with stiffness of the sample and the Young’s modulus. The Young’s modulus of the samples increased as the crosslink concentration was increased (Frohbergh et al., 2012; Yeng et al.,2015). The viscoelastic properties of the samples change depending on the type of crosslinker concentration (Hagen, Salmén, & Stenberg, 1996). The crosslinker which was used in the film samples gave rise to decrease in storage modulus as the concentration was increased (Altınkaya et al., 2016).

The variances in the storage modulus based on temperature increase can be evaluated with retention ratio (Yang, Wang, Fan, & Gu, 2013). The retention ratio gives the information about the mechanical properties of the samples with the temperature (Yadav, Rhee, Jung, & Park, 2013). It can be identified as the ratio of storage modulus at given temperature to storage modulus at initial temperature. The retention ratios of the ChiPM-1, ChiPM-2, and ChiPM-3 were calculated using the given equation (Han, Yan, Chen, & Li, 2011; Yadav et al., 2013; Yang et al., 2013).

$$\text{Retention Ratio: Storage modulus at 153 °C/ Storage modulus at 31 °C} \qquad (3.2)$$

The results were obtained as 0.405, 0.467 and 0.490 for ChiPM-1, ChiPM-2 and ChiPM-3(Altınkaya et al., 2016), respectively. The effect of the crosslinker concentration on retention ratio can be seen from the results. The retention ratio decreased as the crosslinker density was decreased (Altınkaya et al., 2016).

The Tan delta values increased as the temperature was increased. Nge et al. reported that there are distinct peaks for chitosan based samples at 124, 117, and 115 ºC (Nge, Yamaguchi, Hori, Takemura, & Ono, 2002). In this study, in loss modulus graph, distinct peaks were not obtained. There are slightly bands at around 110 ºC in Loss modulus graph (Altınkaya et al., 2016).

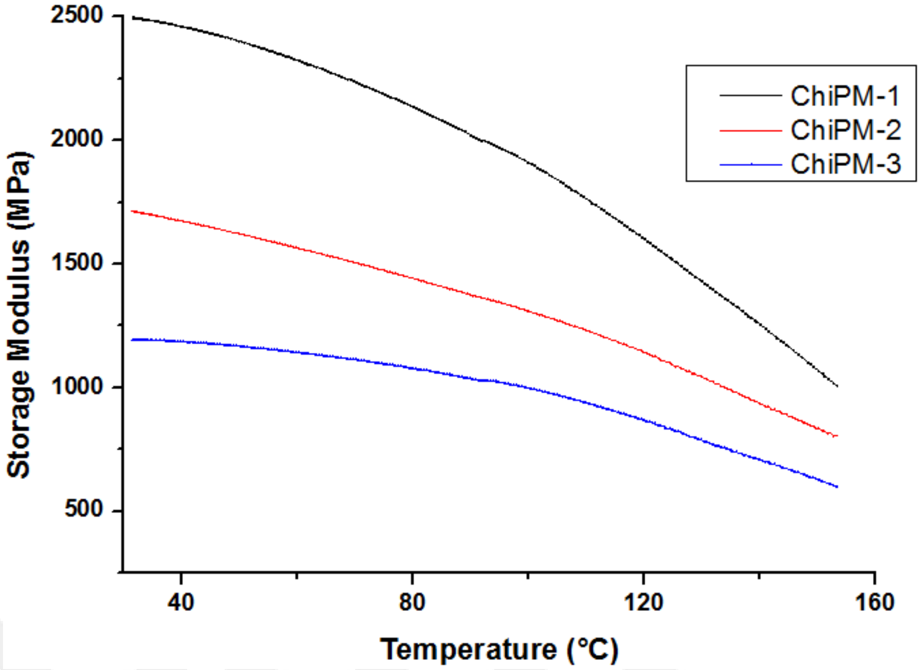

Figure 3.109 The variation of storage moduli of ChiPM-1, ChiPM-2, and ChiPM-3 with temperature.

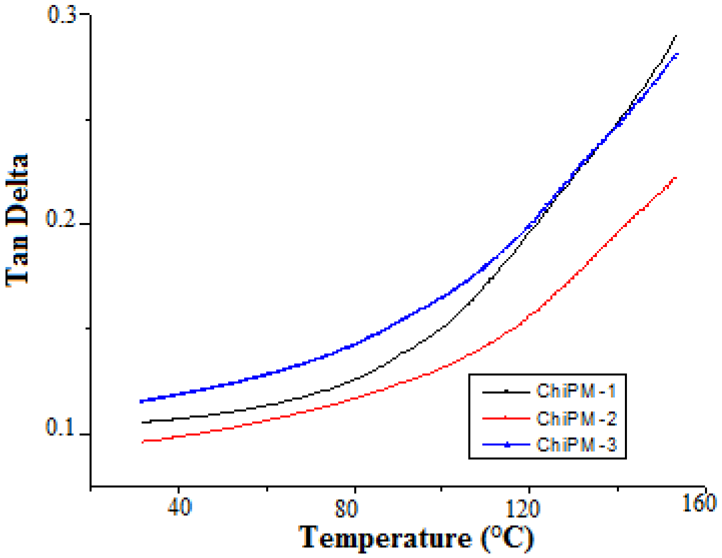

Figure 3.110 The variation of Tan Delta curves of ChiPM-1, ChiPM-2 and ChiPM-3 with temperature.

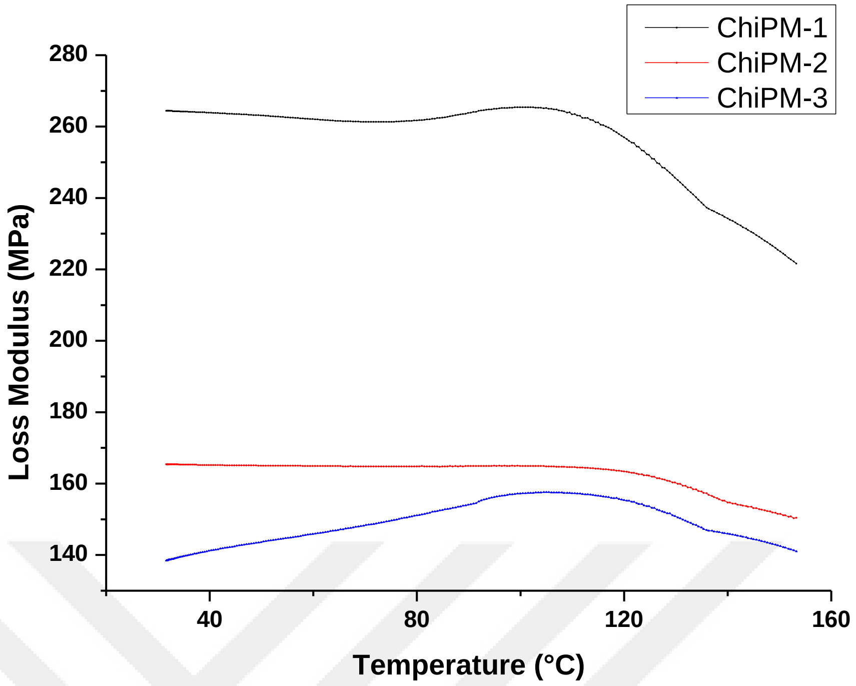

Figure 3.111 The variation of Loss moduli of ChiPM-1, ChiPM-2 and ChiPM-3 with temperature.

3.2.8 Electrical Performance of Chitosan Based Samples

The electrical capacitances and resistance were measured with with Tek AFG3051C Signal Generator and Tek TPS2014 Oscilloscope to investigate the actuation mechanism of actuators ChiPM-1, ChiPM-2, and ChiM-3 (Altınkaya et al., 2016). A series RC circuit is formed with actuator and a series connected to 10 kOhm resistor and a pulse signal is applied on the test circuit at various frequencies and amplitudes. The voltages between the sample electrodes were measured with oscilloscope. The capacitance and resistance of samples were estimated via measeured voltage responses. The dimension of samples is 10mm x 10 mm, thickness is 250 µm (Altınkaya et al., 2016).

The resistance of samples is directly proportion to amount of MBA. And also the capacitance of samples is inversely proportional to the amount of MBA (Altınkaya et al., 2016). As the amount of MBA increased the resistance values increased but the capacitance values decreased (Altınkaya et al., 2016).

Table 3.6 Electrical properties of actuators (Altınkaya et al., 2016)

Electrical Properties of Actuators		
Samples	**Resistance (kOhm)**	**Capacitance (pF)**
ChiPM-1	102	409.6 pF±37.88
ChiPM-2	218	103.2 pF±16.22
ChiPM-3	7820	-

3.3 Chi-Based IPMC Actuators Including Different Amount of pDADMAc

3.3.1 FTIR

FTIR spectra of the chitosan, ChiM, ChiPM-25, ChiPM-50, and ChiM-75 are exhibited in Figures 3.112-3.117.

The FTIR spectrum of chitosan exhibits a characteristic broad and strong band at about 3460 cm^{-1} associated with O–H and NH_2 stretching. An absorption band at around 2920 cm^{-1} corresponds to C-H stretching. Absorption bands at 1646 and 1562 cm^{-1} may be attributed to C=O stretching of amide I group (acetamido group) and N-H angular deformation of amide II, respectively. The stretching band was observed in the range 1408-1450 cm^{-1} due to coupling of N-H angular deformation and C–N stretching. A band around 1370 cm^{-1} is ascribed to symmetrical deformation of the CH_3 group. The vibration bands between 1150 cm^{-1} and 900 cm^{-1} are assigned to the skeletal signals (C–O–C stretching, vibrations of glycosidic bonds and, C–O) (Ravindra et al., 1998; Duarte et al., 2001; Kim, Yoon, Kim, & Kim, 2004; Limam et al., 2013; Corazzari et al., 2015).

Kim et al. reported that pDADMAc has stretching bands at 1465 cm^{-1}, 2900 cm^{-1}, and 2100 cm^{-1} for –CH_3, CH_2, and –CN, respectively (Kim et al., 2004). For the ChiPM-25, ChiPM-50, and ChiPM-75, the absorption peaks at 1648 cm^{-1} and1344 cm^{-1} were due to amide I and amide III of chitosan, and also the bands at 1466 cm^{-1}, 2884 cm^{-1}, and 2167 cm^{-1} were due to the –CH$_3$, -CH$_2$, and –CN groups of pDADMAc, respectively (Kim et al., 2004). The vibration bands located at 3399 cm^{-1} for ChiM, 3390 cm^{-1} for ChiPM-25, 3395 cm^{-1} for ChiPM-50, and 3360 cm^{-1} for ChiPM-75 are due to the -OH and N–H stretching vibration. The intensity of the –OH vibration band of chitosan decreased with crosslinker concentration and addition of other components. The stretching band was observed at around 1400 cm^{-1}, which is attributed to the methyl and methylene groups of ChiM and ChiPM samples. Vibration bands at around 1635 and 1550 cm^{-1} are assigned to the (C=O) and –NH– groups, respectively. The existence of vibrations of carbonyl bonds (C=O) of the amide group at 1661 cm^{-1} for ChiM, at 1648 cm^{-1} for ChiPM-25, at 1644 cm^{-1} for ChiPM-50 and ChiPM-75 show the availability of MBA in films (Altınkaya et al., 2016; Mano et al., 2003; Xu et al., 2005). The band at around 1661 cm^{-1} was shifted to 1644-1648 cm^{-1} for ChiPM samples and also the band intensity increased.

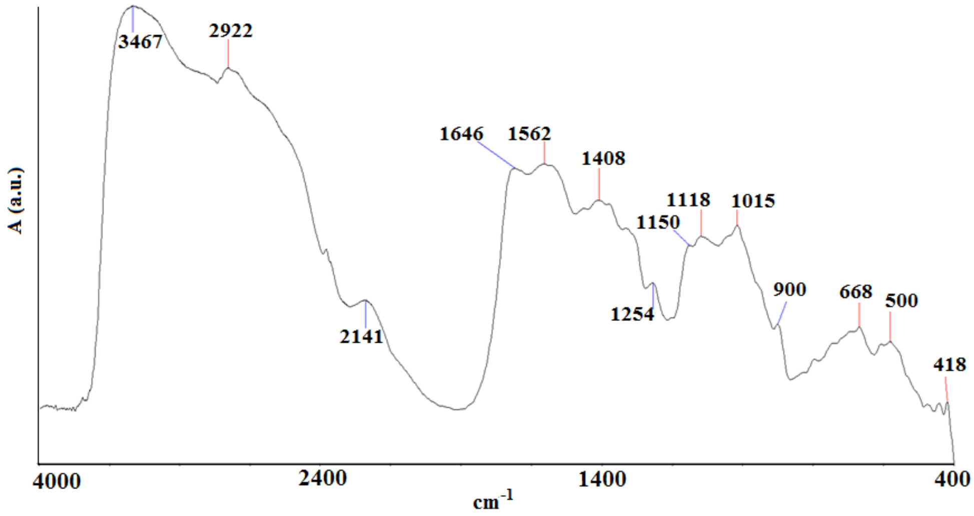

Figure 3.112 FTIR spectrum of chitosan.

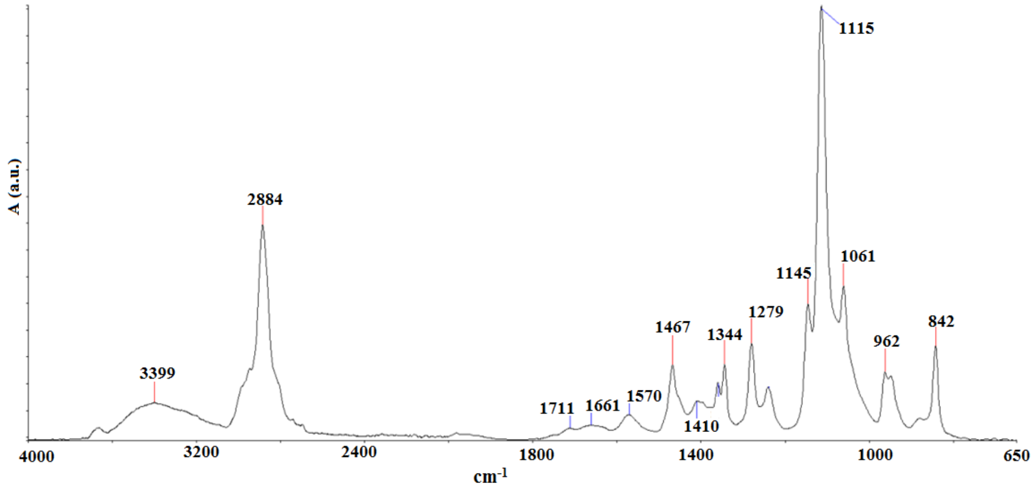

Figure 3.113 FTIR spectrum of ChiM.

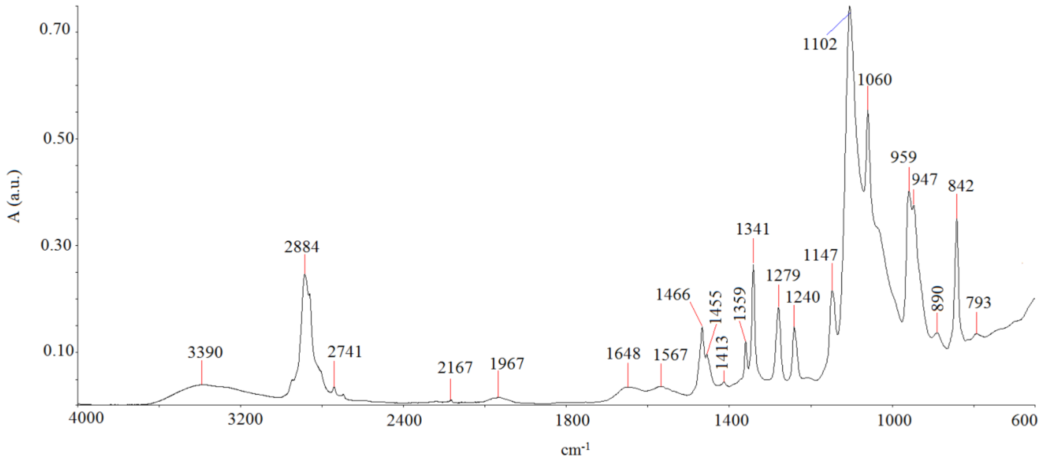

Figure 3.114 FTIR spectrum of ChiPM-25.

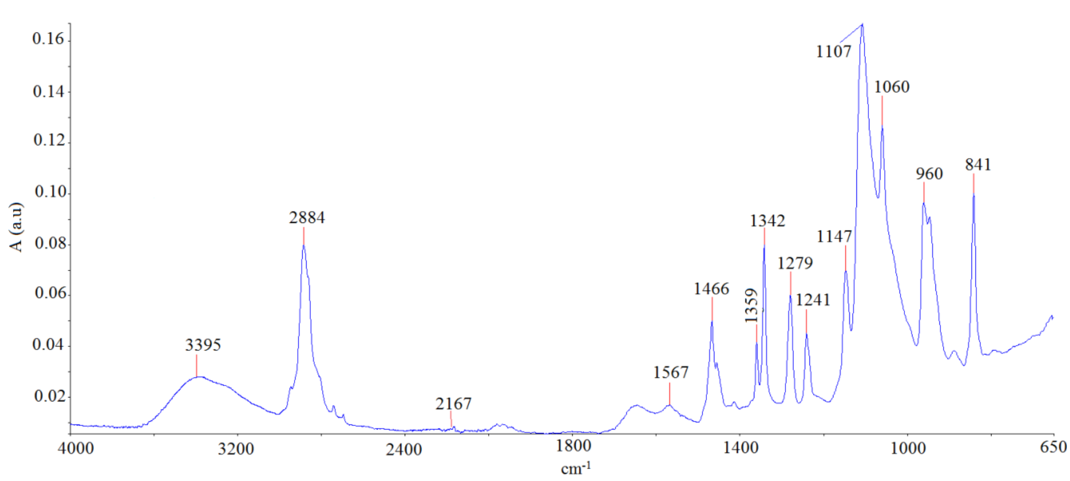

Figure 3.115 FTIR spectrum of ChiPM-50.

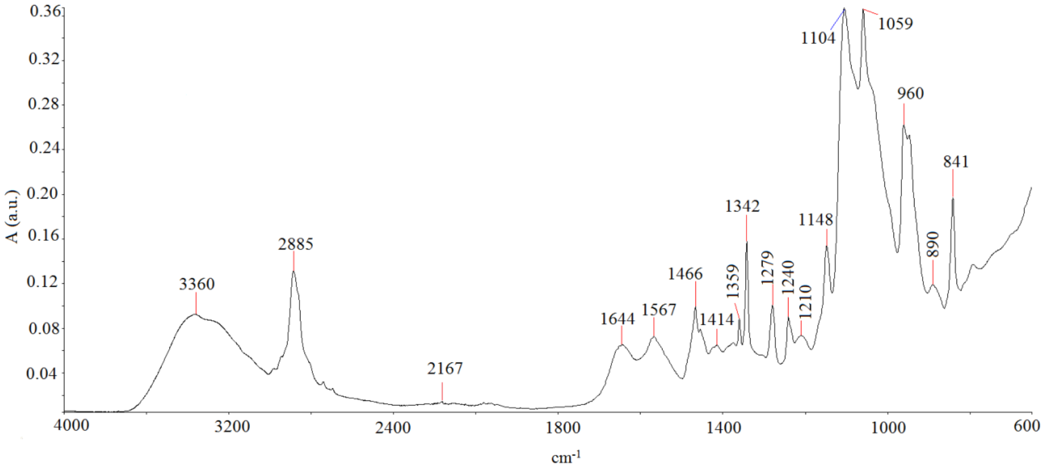

Figure 3.116 FTIR spectrum of ChiPM-75.

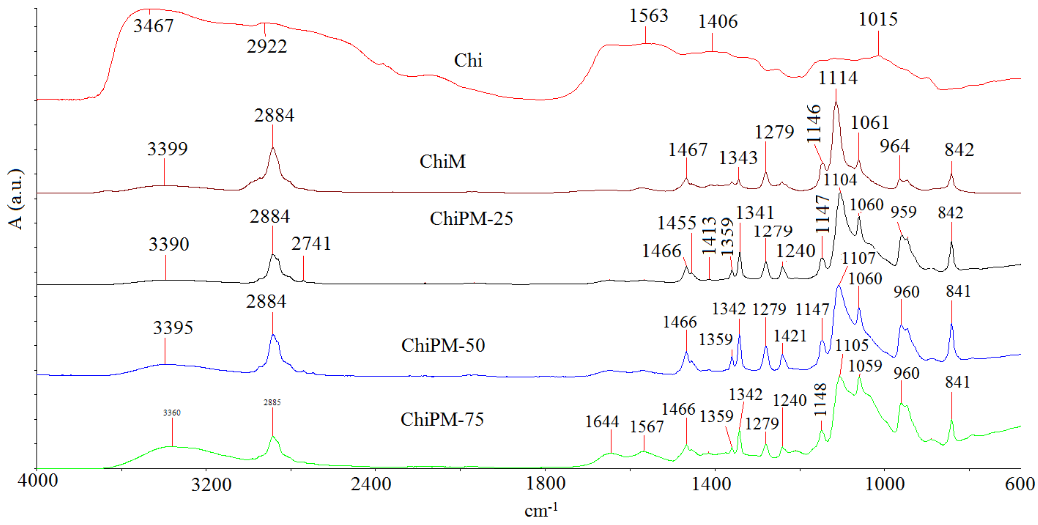

Figure 3.117 FTIR spectra of Chi, ChiPM, ChiPM-25, ChiPM-50, and ChiPM-75.

3.3.2 XRD

Chitosan has an amorphous band at around 2θ at = 10° and has a main peak at around 2θ = 20° since chitosan is an amorphous polymer (Yamaguchi et al., 2001; Qi, Xu, Jiang, Hu, & Zou, 2004; Yang et al., 2012). The XRD patterns of the samples ware exhibited in Figures 3.118-3.121.

The distict two peaks of chitosan were changed into the broad bands for ChiM and ChiPM samples. There are two bands in the diffractogram of ChiM at around 2θ at 22° and 32.4°. Besides, the crytallinity index (CI) was obtained to be 10 %. The new peaks appeared in the diffractograms of ChiPM-25, ChiPM-50, and ChiPM-75. ChiPM samples have three peaks in the diffractograms. The peak values of ChiPM-25, ChiPM-50, and ChiPM-75 were seen at 2θ =18.7°, 18.4°, and 17.9° for first peak; at 2θ = 22.1°, 22.2°, and 22.1° for second peak, at 2θ =33.4°, 35.7°, and 33.7° for third peak, respectively. The CI values of ChiPM-25, ChiPM-50, and ChiPM-75 are 18, 10, and 9 %, respectively. The CI value of the ChiPM-25 is higher than ChiM but the CI values decreased as the pDADMAc concentration was increased. The presence of the pDADMAc increased the viscosity of the solution then can inhibit the nucleation and the solution activity. And also the pDADMAc can adsorp on the crystal surfaces and therefore lead to decrease in crystallinity. The results ere also confirmed by Pookrod at all. 2012 (Pookrod, Dungkaew, Un-Arn, & Haller, 2012).

Table 3.7 The XRD values of ChiM, ChiPM-25, ChiPM-50, and ChiPM-75

Samples	**2*θ***		**CI %**
ChiM	22	32.4	10
ChiPM-25	22.1	33.4	18
ChiPM-50	22.2	35.7	10
ChiPM-75	22.1	33.7	9

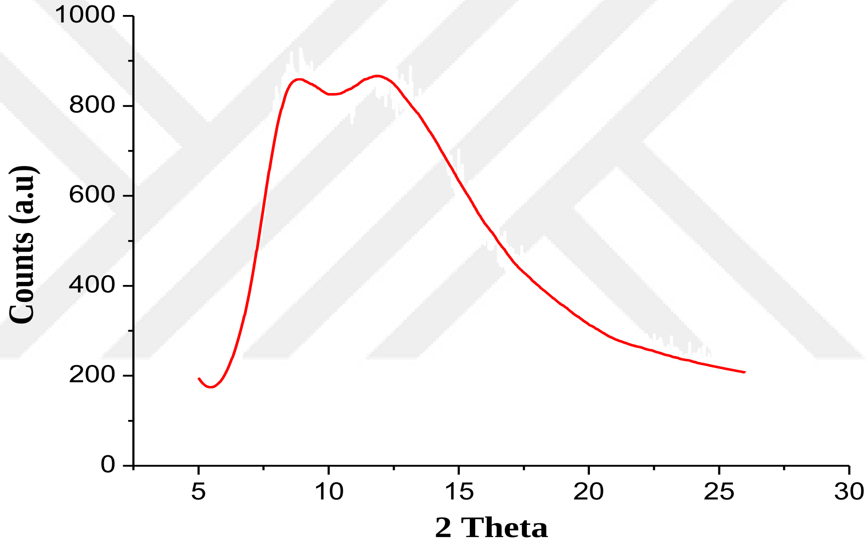

Figure 3.118 XRD pattern of ChiM.

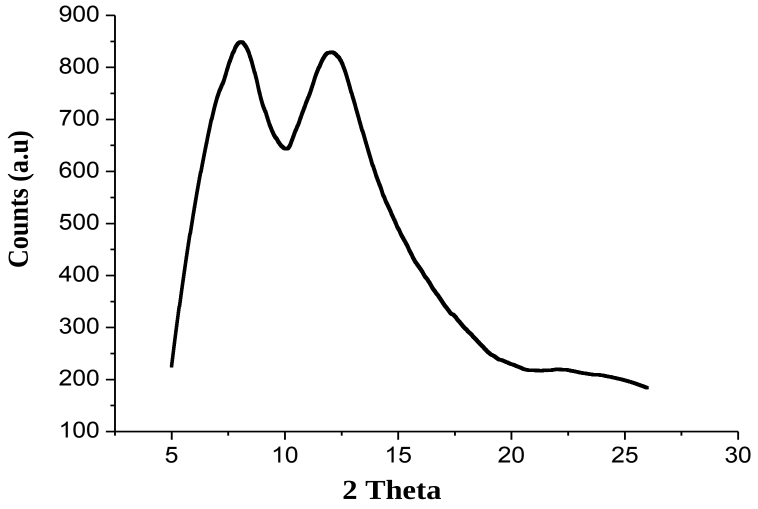

Figure 3.119 XRD pattern of ChiPM-25.

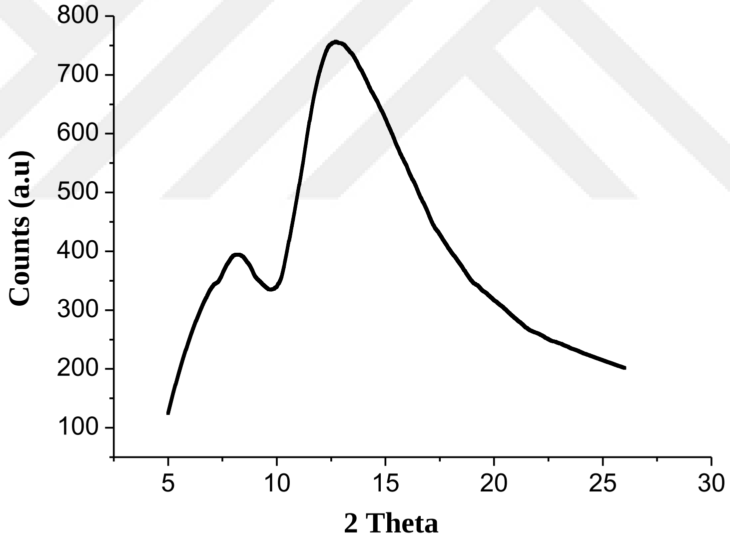

Figure 3.120 XRD pattern of ChiPM-50.

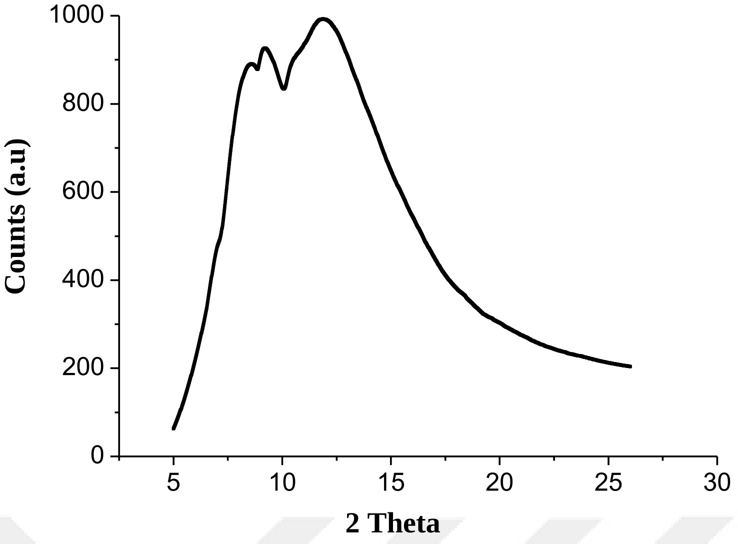

Figure 3.121 XRD pattern of ChiPM-75.

3.3.3 Thermogravimetric Analysis (TGA)

Thermal behavior of samples was determined by using TGA (Shimadzu, TGA 50) (Altınkaya et al., 2016). Thermogravimetric analysis (TGA) was performed at a heating rate of 10°C/min in the range from 30 to 600°C under nitrogen atmosphere with a flow rate of 1.0 mL/min (Altınkaya et al., 2016). TG/DTG curves of Chi film, ChiM, ChiPM-25, ChiPM-50 and, ChiPM-75 are given in Table 3.6 and Figures 3.122-3.126, respectively.

Chi film has two mass loss stages as shown in Figure 3.122 (Chiono, Pulieri et al., 2008). Mass loss is 13.2 % (in the temperature range 31-99 °C) in first stage and is 43.4 % (99-582 °C) in second stage. The mass loss in first stage can be resulted from evaporation of water in samples (Chiono et al., 2008). The maximum temperature is 57 °C for the first stage. Mass loss in second stage may be resulted from the elimination and vaporization of volatile compounds due to the further dehydration of water and degradation (thermal and oxidative) of chitosan such as deacetylation and depolymerization (Neto et al., 2005; de Brito and Campana-Filho, 2007; Tripathi, Mehrotra, & Dutta, 2009).

The TGA values of samples obtained from TG/DTG curves are summarized in Table 3.6. As can be seen from Table 3.6 the samples have three mass loss steps. It is probable that the interactions of the components gave rise to changes in number of mass loss steps, degradation temperature, etc. First stage is related with the evaporation of water in samples. Mass loss in the first stage is between 8.5-14.8 %. Max mass losses were investigated in the second stage at around 239-258 °C. The second stage, mass losses are 32.9, 31, 34, and 31.3 % for ChiM, ChiPM-25, ChiPM-50 and, ChiPM-75, respectively. The maximum mass loss temperatures for ChiM, ChiPM-25, ChiPM-50, and ChiPM-75 are 243, 258.2, 246.5, and 239.3°C, respectively.

The degradation temperature firstly increased with the addition of pDADMAc. It can be resulted from the higher thermal decomposition temperature of pDADMAc. pDADMAc has three mass loss stages, second mass loss was obtained to be 320°C (Francis, Varshney, & Sabharwal, 2007). Addition of pDADMAc increased the thermal decomposition temperature of chitosan. However the degradation temperature of samples decreased as the pDADMAc concentration was increased. It can be related with the decomposition of pDADMAc. The thermal degradation of pDADMAc results in the formation of alkyl halide (Francis, Varshney, & Sabharwal, 2007). As the pDADMAc is increased in sample, formation of alkyl halide will increase.

Crosslinking of the sample affected the degradation temperature. Sreedhar et al explained that thermal decomposition of sample decreased due to the crosslinking (Sreedhar et al., 2005). The disappearance of H bonding cooperation along the backbone of chitosan due to the crosslinking effect gave rise to decrease in decomposition temperature (Poon et al., 2014).

Table 3.8 TGA data of chitosan based samples

Sample	First Mass loss (%)	Second Mass loss (%)	Third Mass loss (%)	First Stage T_{max} (°C) (39-109 °C)	Second Stage T_{max} (°C) (226-282°C)	Third Stage T_{max} (°C) (342-420°C)
Chi film	13.2	43.4	-	57	250	-
ChiM	12.2	32.9	20.4	96	243	405
ChiPM-25	10	31	19.8	57	258.2	365.4
ChiPM-50	8.5	34	19.4	37.2	246.5	352.7
ChiPM-75	14.8	31.3	21.7	75.8	239.3	354.4

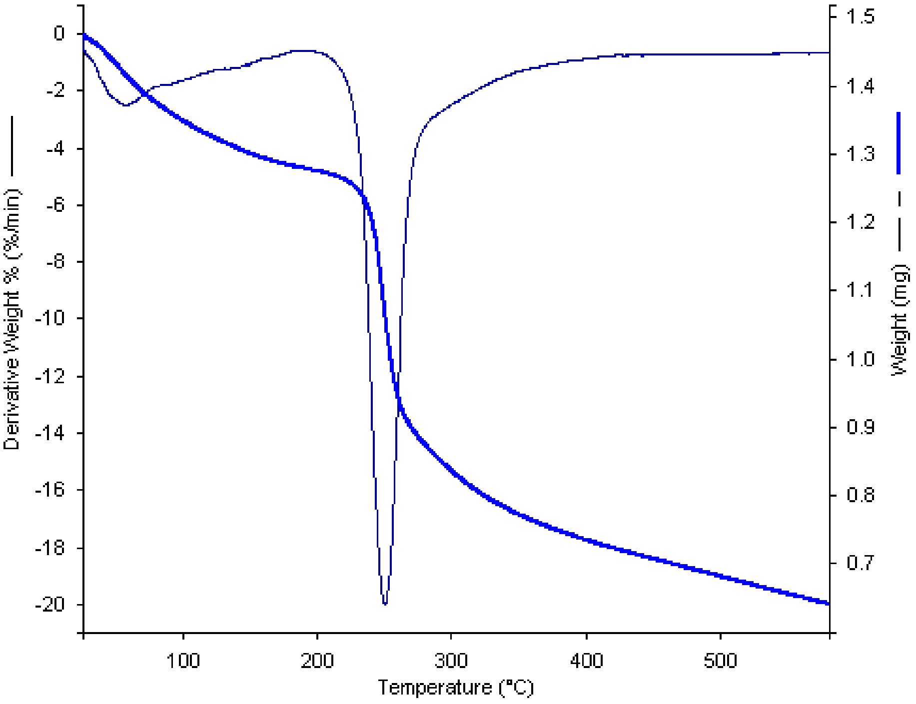

Figure 3.122 TG and DTG curves of chitosan film.

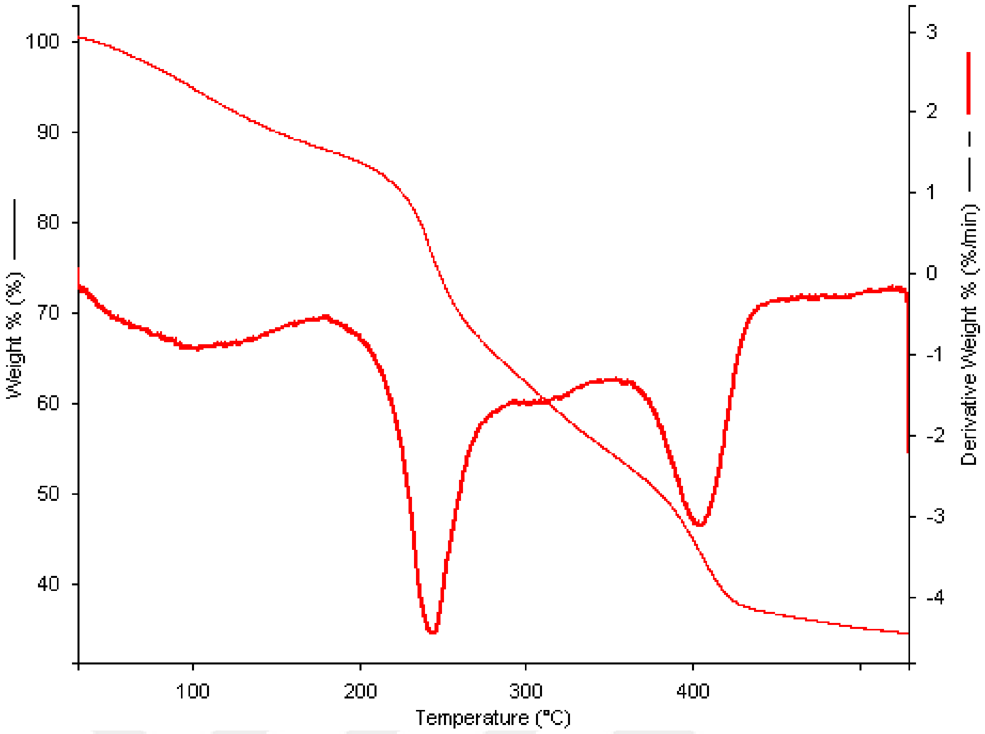

Figure 3.123 TG and DTG curves of ChiM.

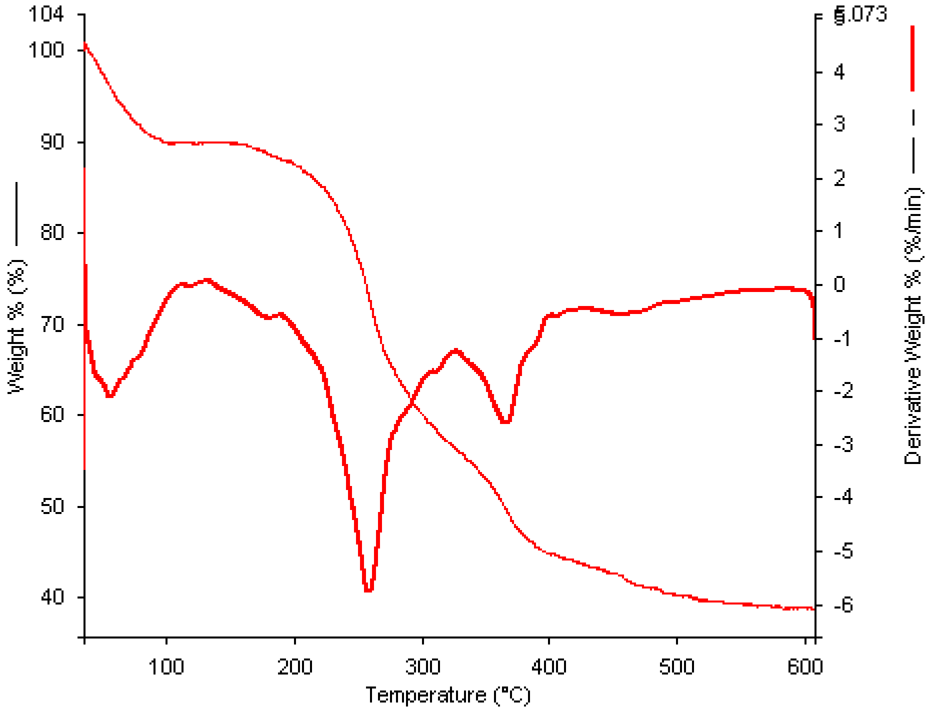

Figure 3.124 TG and DTG curves of ChiPM-25.

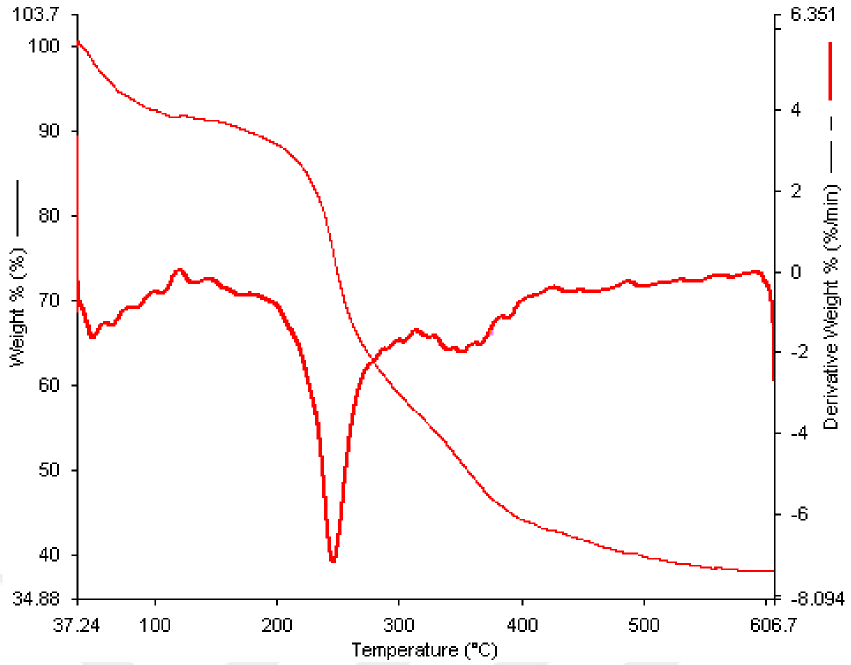

Figure 3.125 TG and DTG curves of ChiPM-50.

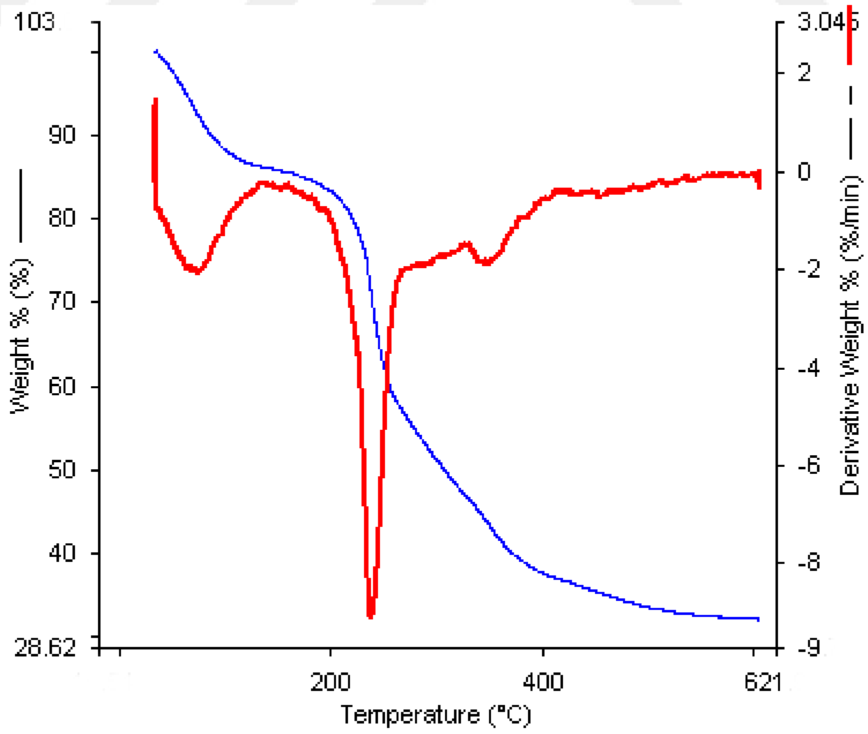

Figure 3.126 TG and DTG curves of ChiPM-75.

3.3.4 Scanning Electron Microscopy (SEM)

The effect of pDADMAc concentration on morphological properties of samples was investigated by taking SEM images of samples. The SEM micrographs of ChiPM-25, ChiPM-50, and ChiPM-75 are presented in Figures 3.127-3.129. The SEM images were taken at various magnification levels.

The SEM images exhibited that there are many pores on the surface of samples. The pores can be clearly seen in higher magnification levels. The sizes of pores exhibited variations according to the sample.

Figure 3.127 exhibits the SEM images of ChiPM-25 at various magnification levels from 10^3 to 10^4. The pores of the sample can be seen in Figure 3.127 a, b, c, d, and e. The pore sizes of ChiPM-25 were determined at different sizes from 9.3 to 13.1 μm. The mean pore size of ChiPM-25 was calculated as 11.7±1.5 μm. Figure 3.128 exhibits the SEM micrographs of ChiPM-50 at various magnification levels from 10^3 to 10^4. The pore sizes of ChiPM-50 were determined at different sizes from 8.7 to 12.5 μm. The average pore size of ChiPM-50 was calculated as 10.5±1.9 μm. The pore sizes of ChiPM-50 are smaller than ChiPM-25. Figure 3.129 exhibits the SEM micrographs of ChiPM-75 at various magnification levels from 10^3 to 10^4. The pore sizes of ChiPM-75 were determined at different sizes from 7.1 to 9.7 μm. The average pore size of ChiPM-75 was calculated as 8.6±1.1 μm.

The average sizes of the ChiPM-25, ChiPM-50, and ChiPM-75 are 11.7±1.5, 10.5±1.9, and 8.6±1.1, respectively. The pore sizes decreased as the pDADMAc concentration was increased in the structure of the samples. It can be explained that the added pDADMAC filled the pores of the membrane and thus smaller pores on the surface of the samples was seen (Altınkaya et al., 2016).

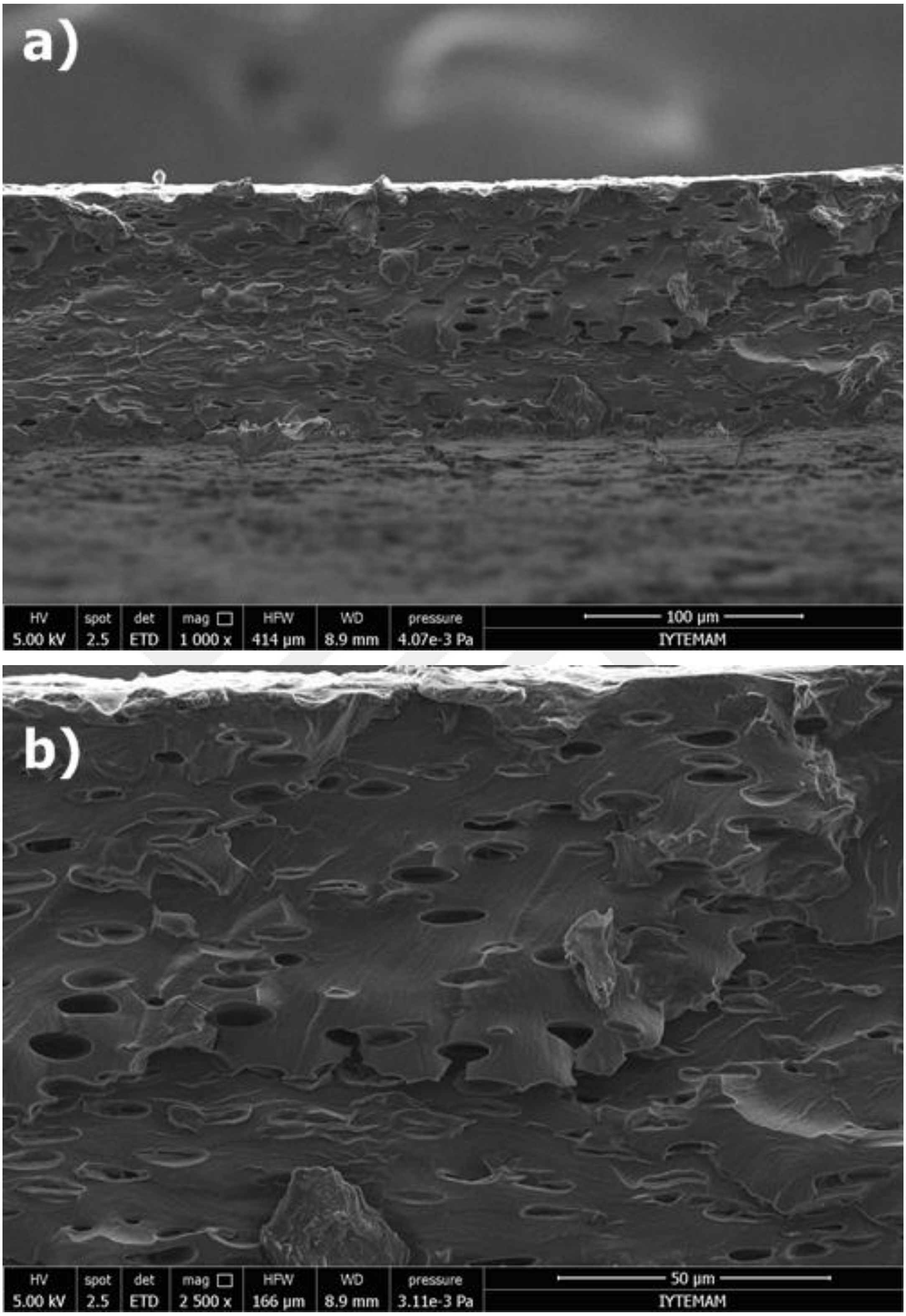

Figure 3.127 SEM micrographs of ChiPM-25 a) 1000, b) $2.5x10^3$,c) $3.313x10^3$, d) $5x10^3$, e) $10x10^3$.

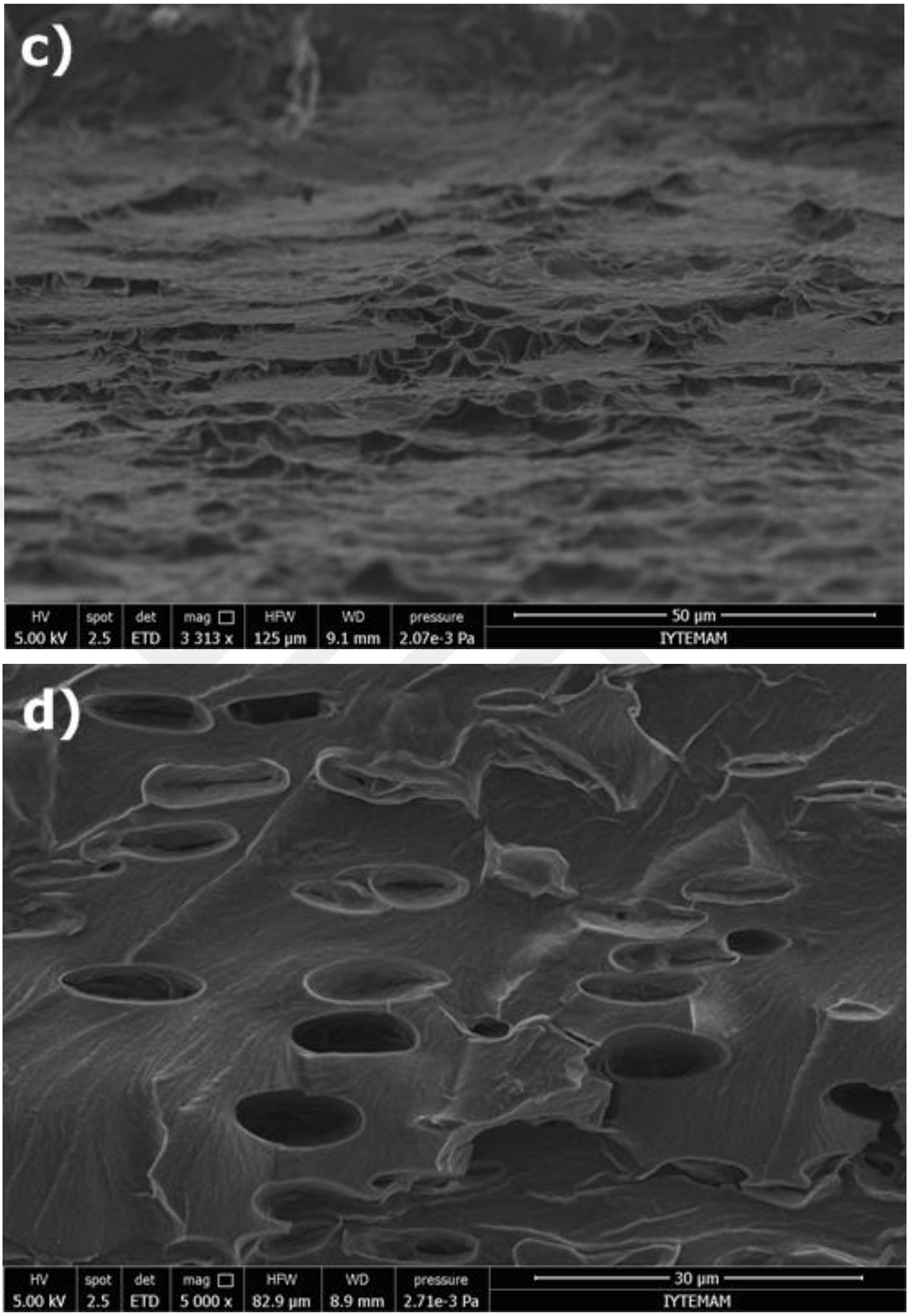

Figure 3.127 SEM micrographs of ChiPM-25 a) 1000, b) 2.5x10^3,c) 3.313x10^3, d) 5x10^3, e) 10x10^3 (continue).

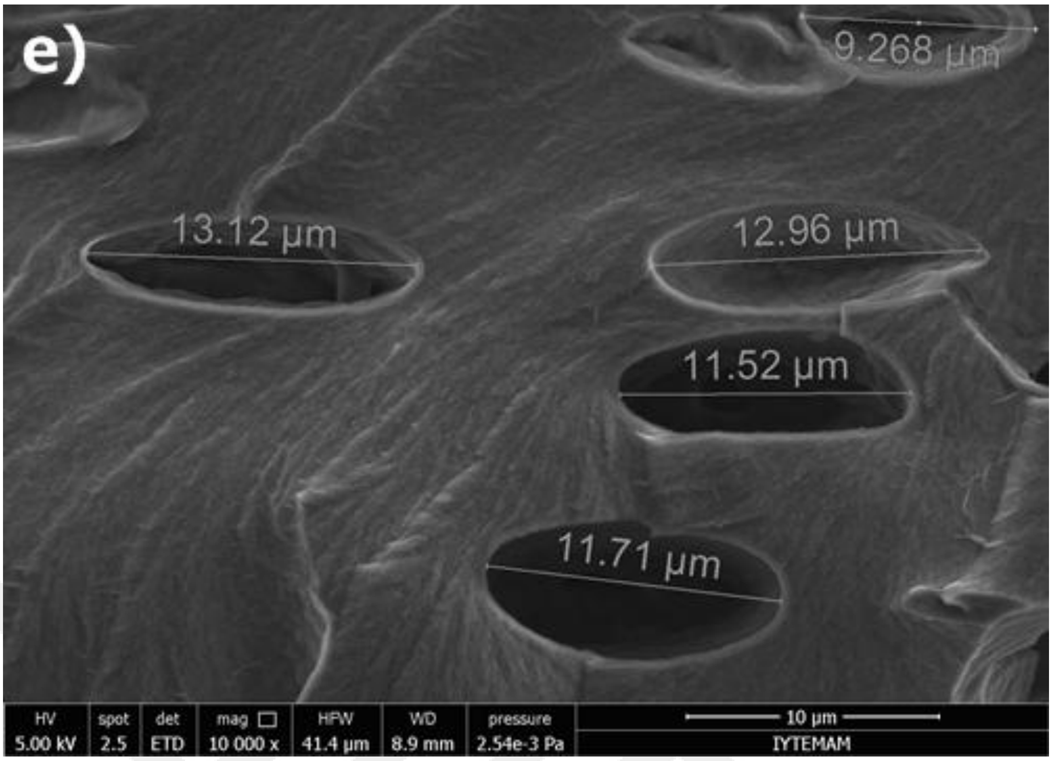

Figure 3.127 SEM micrographs of ChiPM-25 a) 1000, b) $2.5x10^3$,c) $3.313x10^3$, d) $5x10^3$, e) $10x10^3$ (continue).

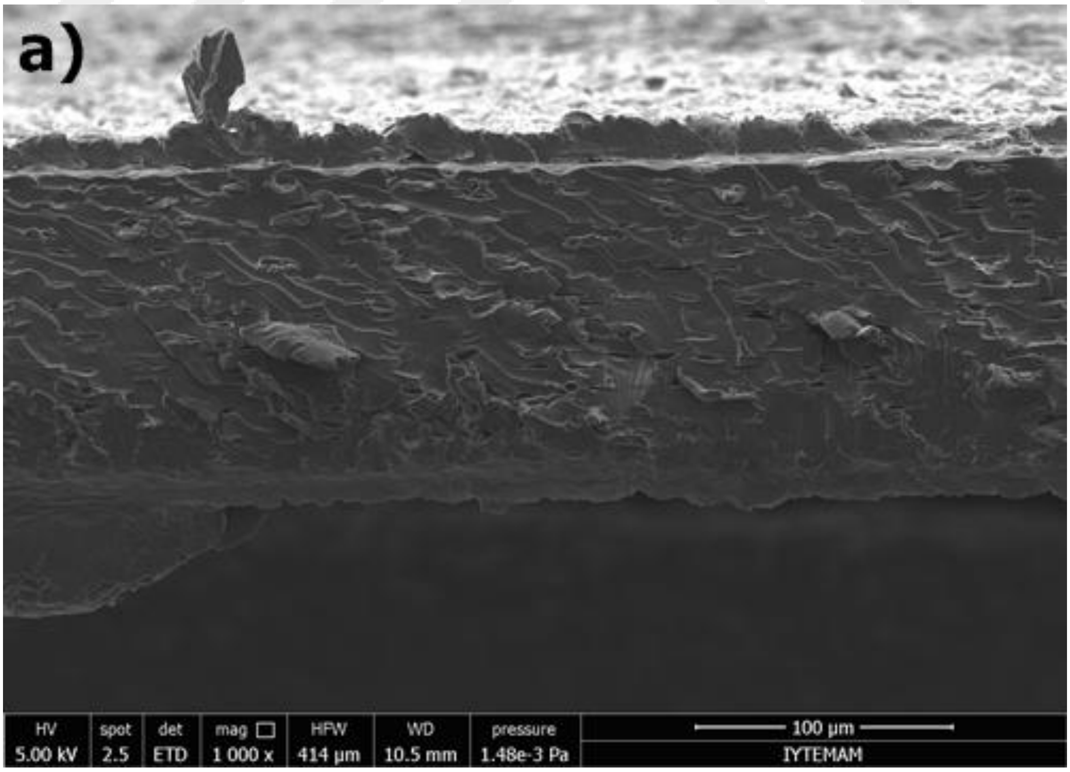

Figure 3.128 SEM micrographs of ChiPM-50 a) x1000, b) x2500,c) x5000, and d) x10000.

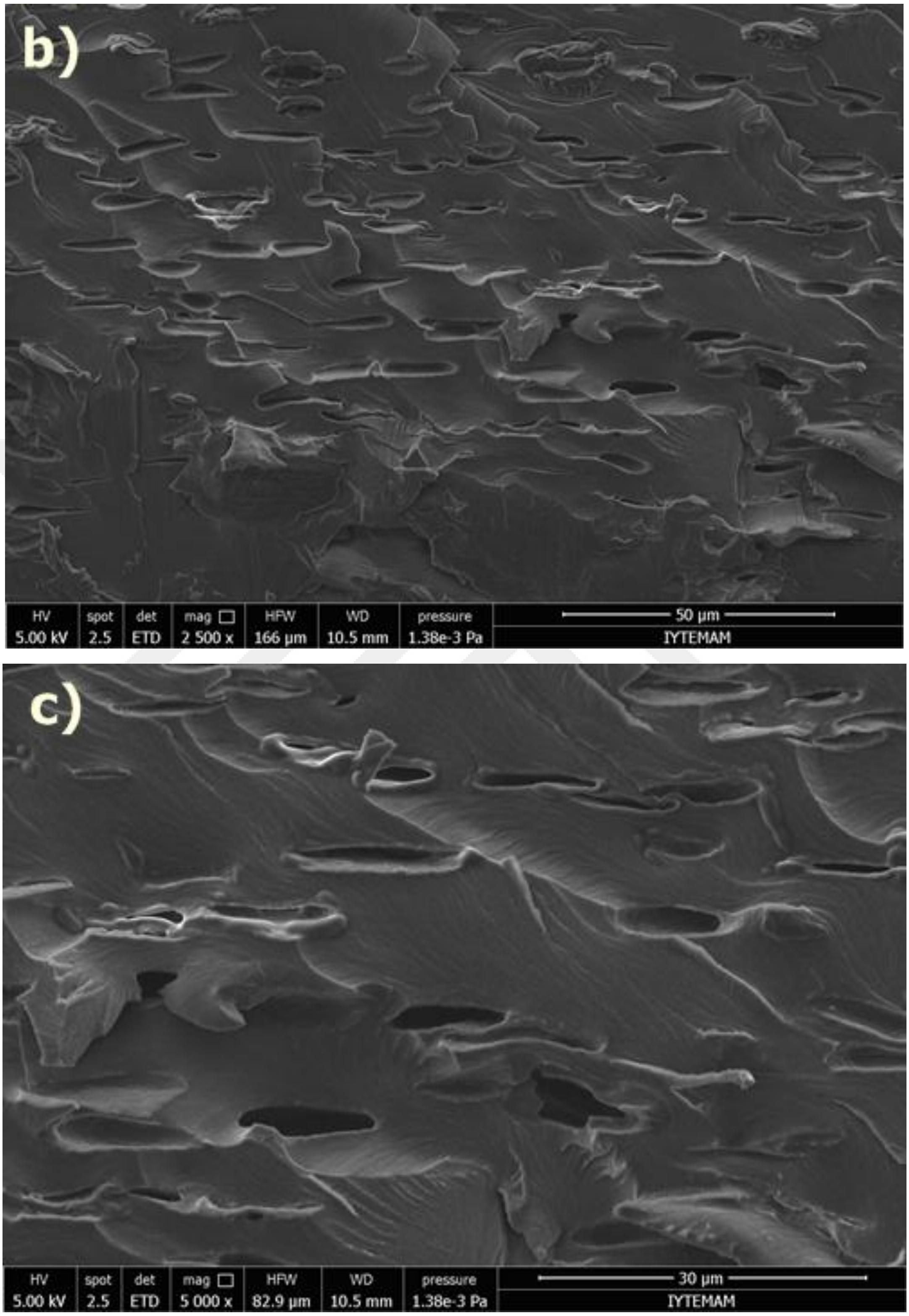

Figure 3.128 SEM micrographs of ChiPM-50 a) x1000, b) x2500,c) x5000, and d) x10000 (continue).

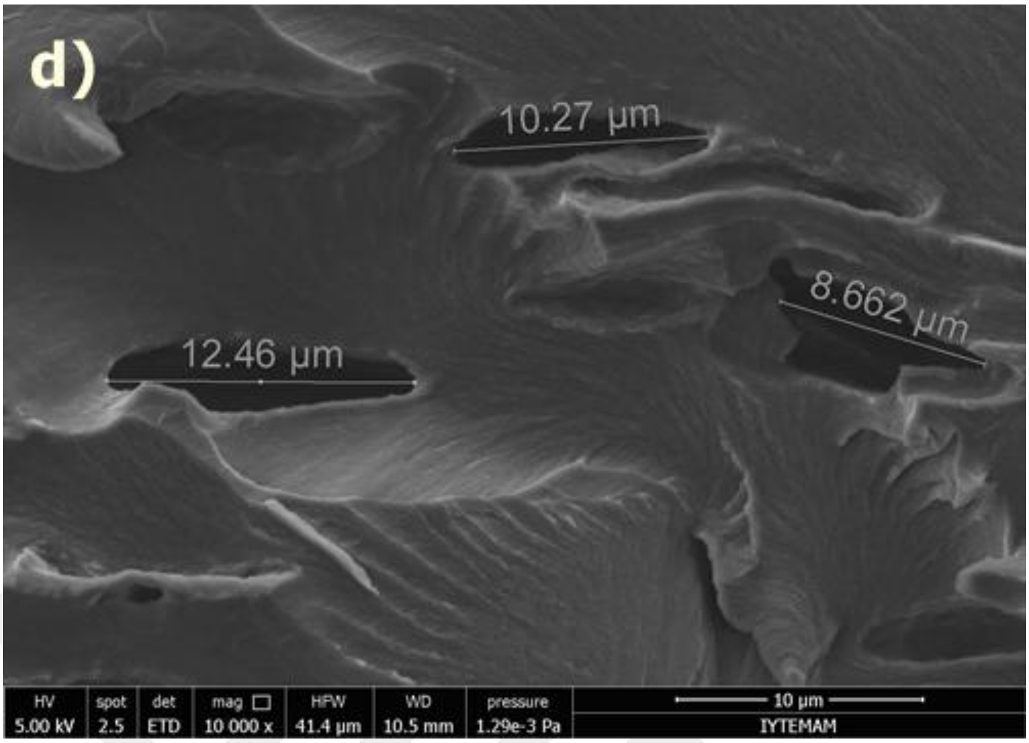

Figure 3.128 SEM micrographs of ChiPM-50 a) x1000, b) x2500,c) x5000, and d) x10000 (continue).

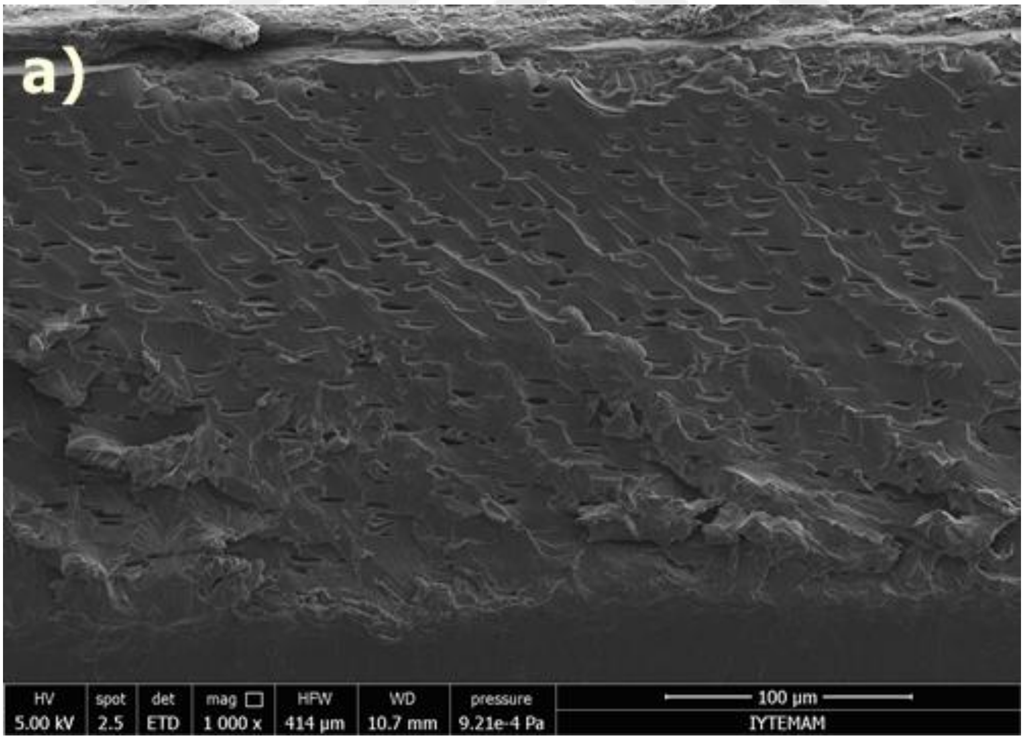

Figure 3.129 SEM micrographs of ChiPM-75 a) 1000, b) 2.5x10^3,c) 5x10^3, d) 10x10^3.

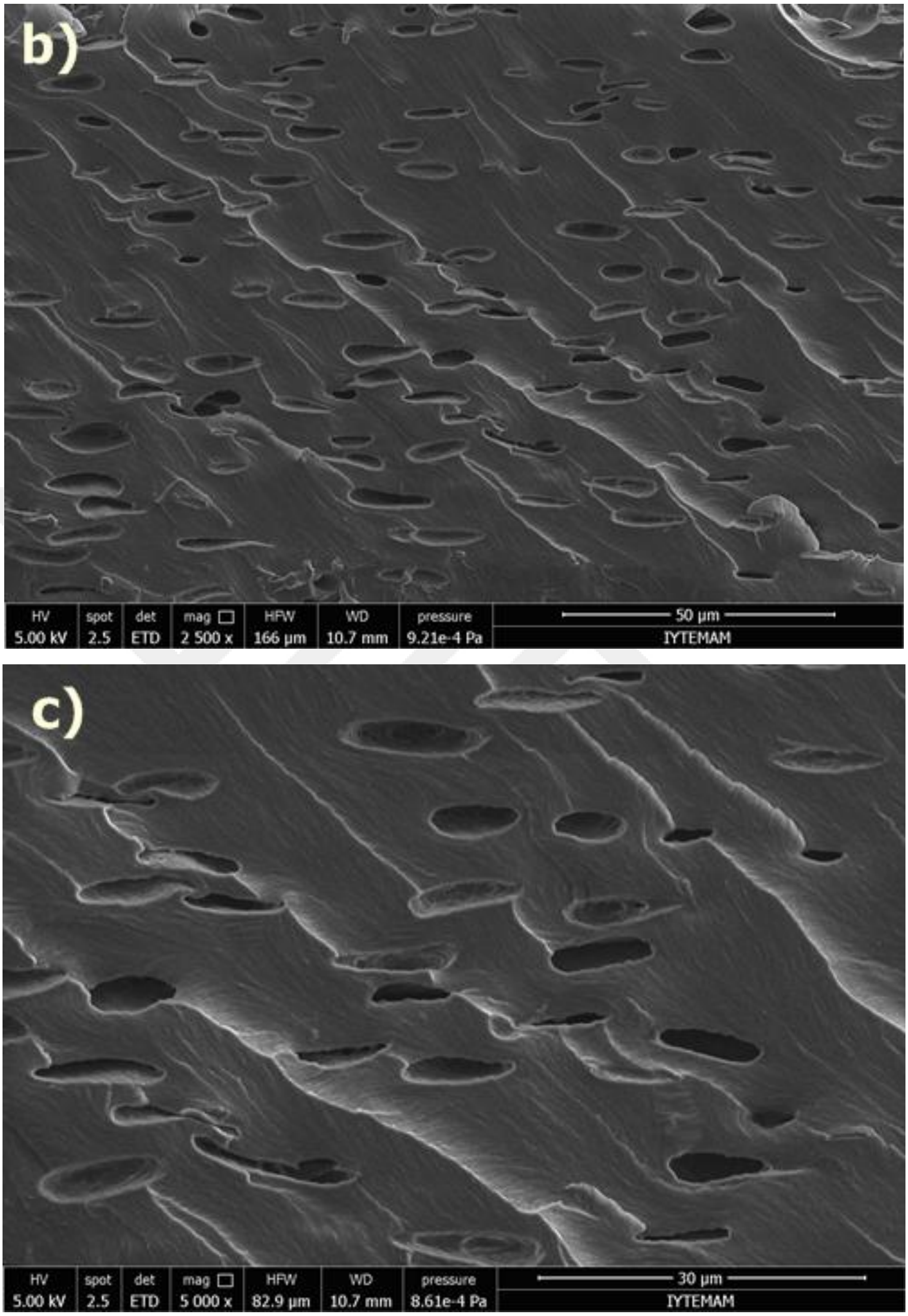

Figure 3.129 SEM micrographs of ChiPM-75 a) 1000, b) 2.5x10^3,c) 5x10^3, d) 10x10^3 (continue).

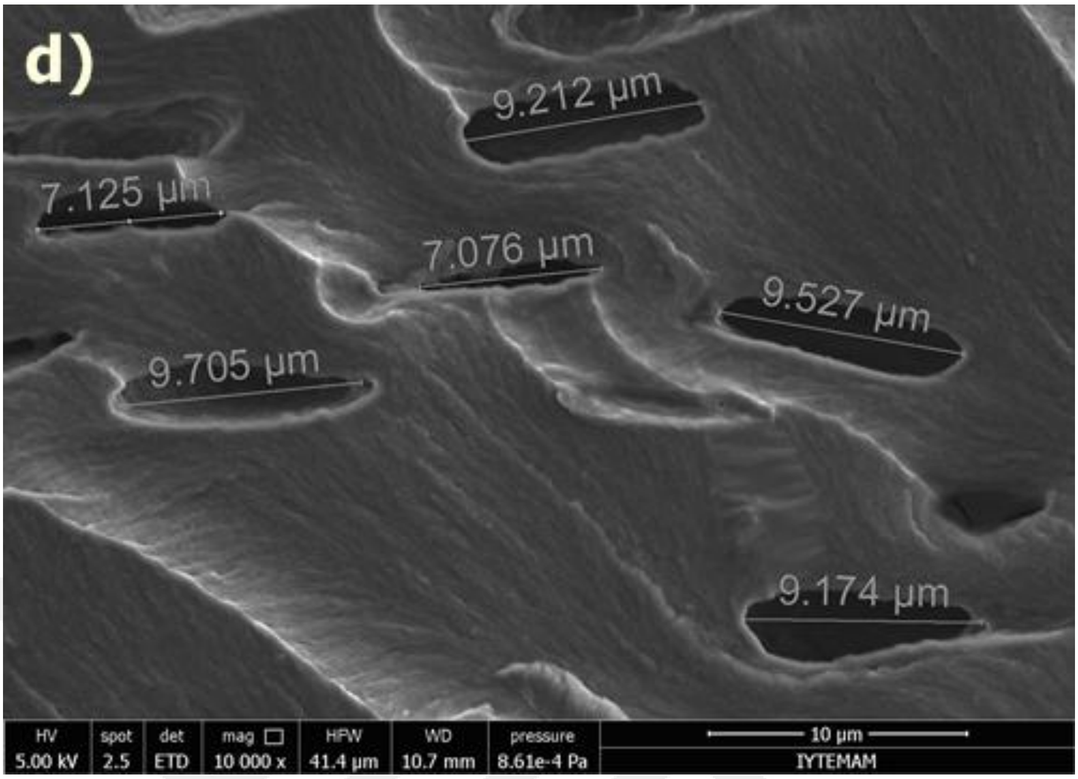

Figure 3.129 SEM micrographs of ChiPM-75 a) 1000, b) 2.5x10^3,c) 5x10^3, d) 10x10^3 (continue).

3.3.5 Dynamic Mechanical Analysis (DMA)

The loss modulus ε’’ (viscous response) and storage modulus ε’ (elastic response) of polymers were measured as a function of time or temperature as the polymer is deformed under an oscillatory load (stress) at a controlled temperature in a specified atmosphere. The loss modulus is related to damping and energy dissipation, the storage modulus to stiffness (Liu et al., 2012).

The dynamic mechanical properties of the samples (ChiM, ChiPM-25, ChiPM-50, and ChiPM-75) including different amounts of pDADMAc, were investigated via dynamic mechanical analysis. The DMA curves of the samples were exhibited in Figures 3.130-3.144.

The storage modulus versus temperature curves of ChiM, ChiPM-25, ChiPM-50, and ChiPM-75 are shown in Figure 3.130. The storage modulus (E’) is related to stiffness. The E’ value is higher at glassy state; it decreases to the glass transition temperature (Tg). Due to the loss of moisture, plasticizers, pDADMAc, and other components at high temperatures the loss and storage modulus values decreased (Altınkaya et al., 2016) as the temperature was increased (Meng, Heuzey, & Carreau, 2014). The loss and storage modulus values of ChiPM-25, ChiPM-50, and ChiPM-75 approached to zero at about 200 °C. The E' values at 30°C is called as initial storage modulus which , considerably decreased (Meng, Heuzey, & Carreau, 2014) from 4144 MPa for ChiM to 304.3 MPa for ChiPM-75 as a result of increasing pDADMAc content. The E' value of ChiM, ChiPM-25, ChiPM-50, and ChiPM-75 decreased from 4144, 1246, 375, and 304.3 MPa to 1932, 63.8, 11.68, and 11.67 MPa, respectively.

The pDADMAc absorbs the moisture (Kim et al., 2004) and creates a plasticizer effect. Different pDADMAc content and so different plasticizer content give rise to different crystallinity and microstructures, and also according to the results it can be said for this study that the decrease in initial E' depends only the pDADMAc level. The samples including different amounts of pDADMAc show different E'mainly due to different microstructures. ChiM exhibited the most considerable decrease among the samples. The decrease in E' is attributed to the relaxation, which is the sub-Tg transition, of the lateral group in chitosan ($-NH_2$, $-CH_2OH$, and $-NH-OC-CH_3$) and molecular sections of chitosan molecules in the amorphous phase (Meng, Heuzey, & Carreau, 2014).

The Loss modulus is attributed to the relaxation processes α and β. The β relaxation process has been assigned to the local mode of relaxation in the amorphous phase. The α relaxation related to the glass transition of the amorphous phase (Much and Pawlak, 2005). The Figure 3.132 shows the variation of Loss Modulus (E'') as a function of temperature for samples. For ChiM E'' value initially decreased to the 80°C, then started to increase to the Tg temperature. After the Tg temperature, it decreased again. The Tg value of ChiM can be obtained as 130 °C. It was closer to chitosan Tg value. In Dong et al. study, Tg value of chitosan was reported at around 140 °C (Dong, Ruan, Wang, Zhao, & Bi, 2004). The other samples exhibited two relaxation bands. First bands which are related with α

relaxation were seen at around 65, 66, and 73 °C for ChiPM-25, ChiPM-50, and ChiPM-75, respectively. Second bands were not seen clearly for ChiPM-50, and ChiPM-75 but seen at around 120°C.

The Figure 3.131 exhibits the variation of tan delta (δ) as a function of temperature for samples. ChiPM-25, ChiPM-50, and ChiPM-75 samples demonstrated two peaks. Two peaks for ChiPM-25, ChiPM-50, and ChiPM-75 are obtained at 65.3, 66.3, and 77°C for the first peaks, and at 166.7, 150, and 130.3°C for the second peaks. The amorphous phase comprised of amorphous chitosan molecule, and other components in the sample. The *β*-relaxation, which originates from the motion of rigid segments in the chitosan molecules and reordering of hydrogen bonds, is seen at about 65 °C (Much and Pawlak, 2005). The melting broad bands were observed at 166.7, 150, and 130.3°C for ChiPM-25, ChiPM-50, and ChiPM-75, respectively. The values were decreased as the pDADMAC concentration was increased.

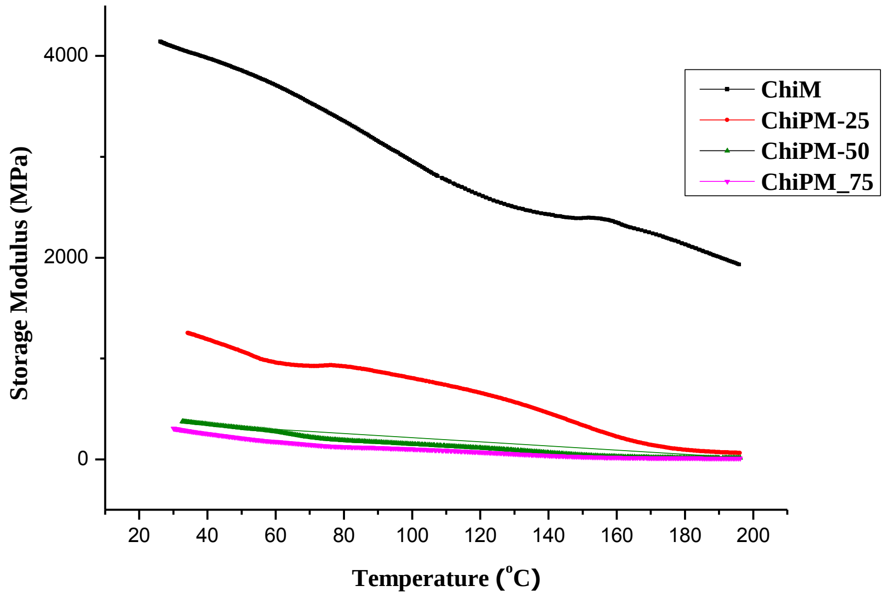

Figure 3.130 The variation of storage moduli of ChiM, ChiPM-25, ChiPM-50, and ChiPM-75 with temperatures.

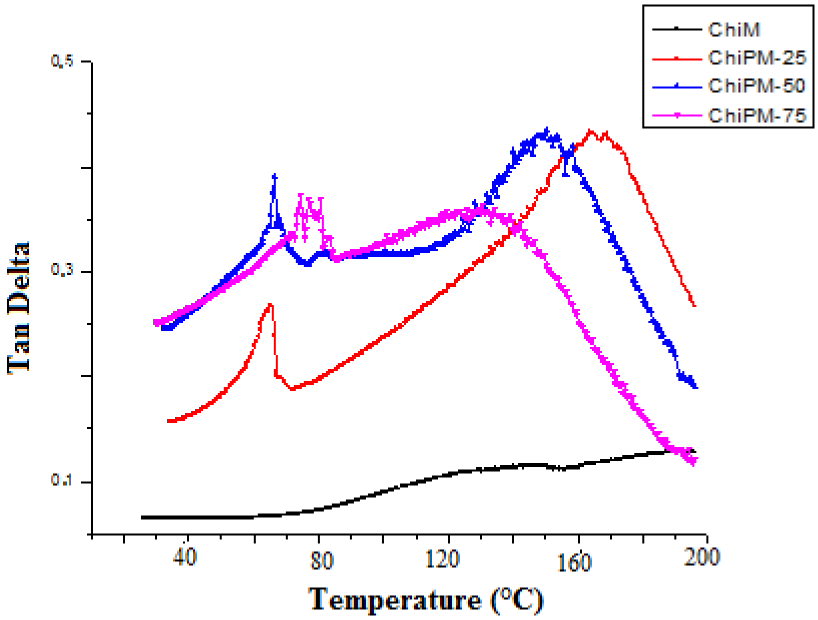

Figure 3.131 The variation of Tan delta values of ChiM, ChiPM-25, ChiPM-50, and ChiPM-75 with temperatures.

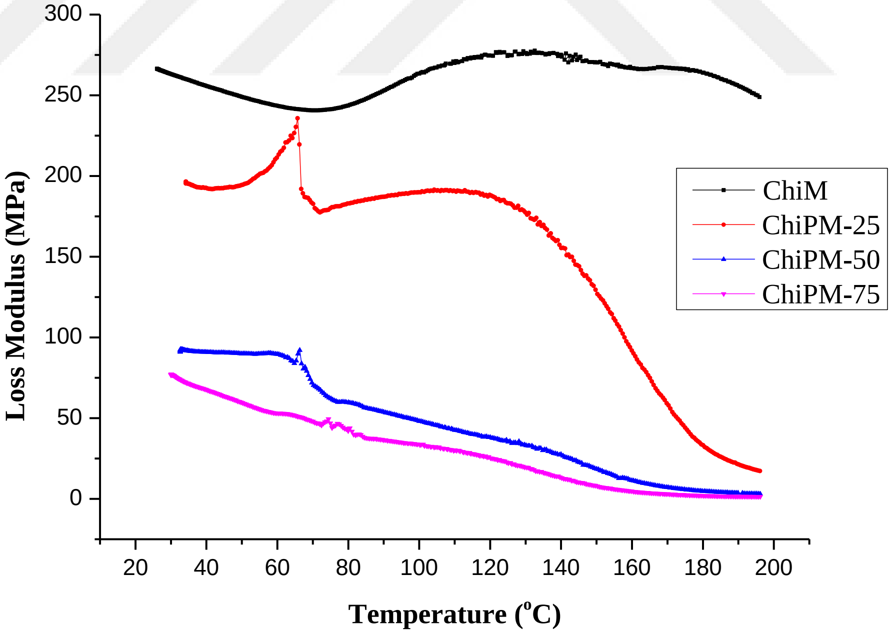

Figure 3.132 The variation of Loss moduliof ChiM, ChiPM-25, ChiPM-50, and ChiPM-75 with temperature.

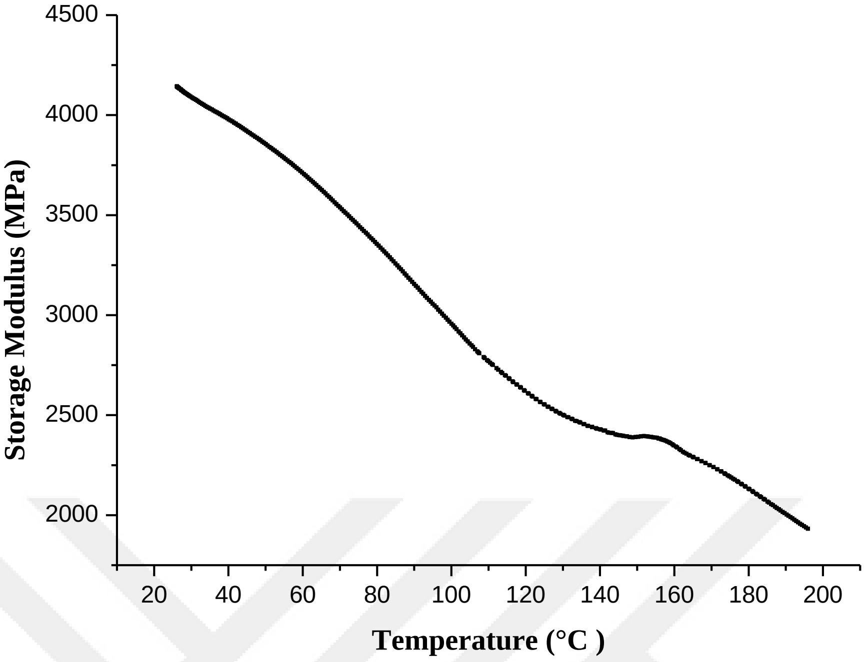

Figure 3.133 The variation of storage modulus of ChiM with temperature.

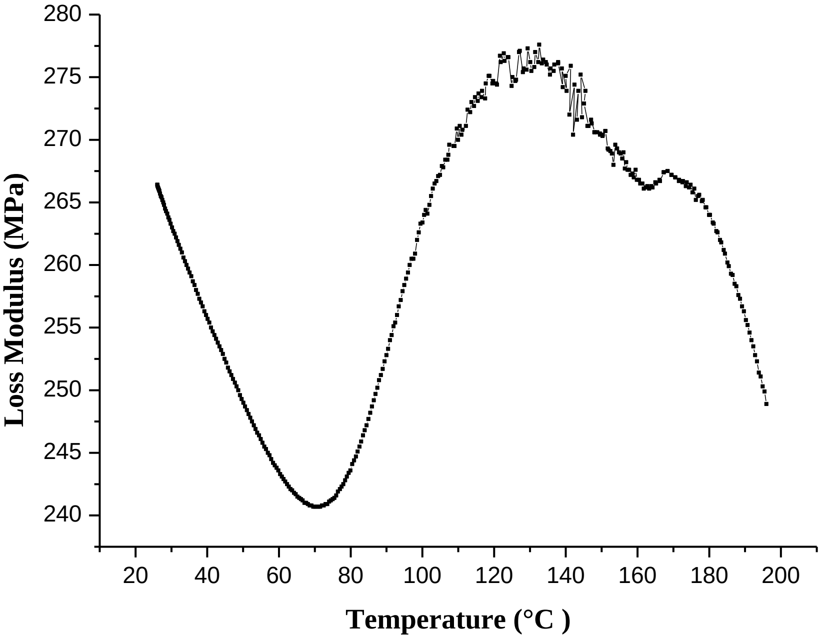

Figure 3.134 The variation of loss modulus of ChiM with temperature.

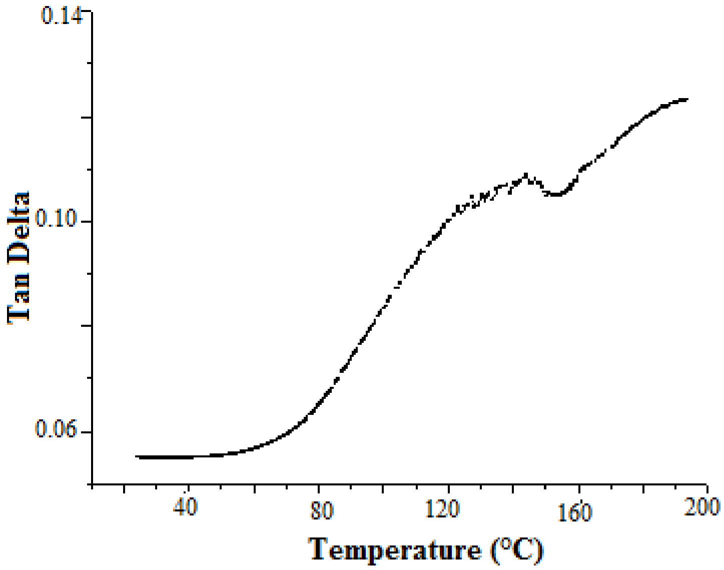

Figure 3.135 The variation of tan delta of ChiM with temperature.

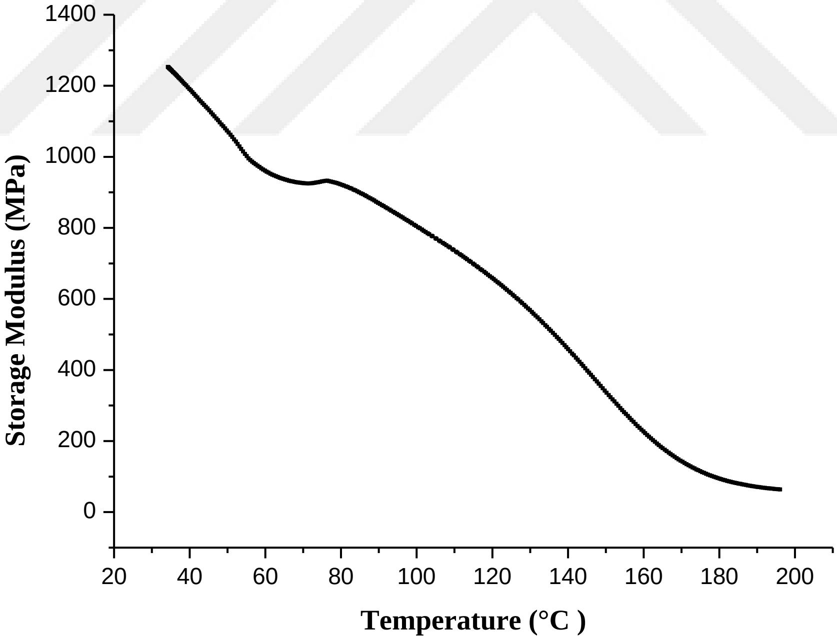

Figure 3.136 The variation of storage modulus of ChiPM-25 with temperature.

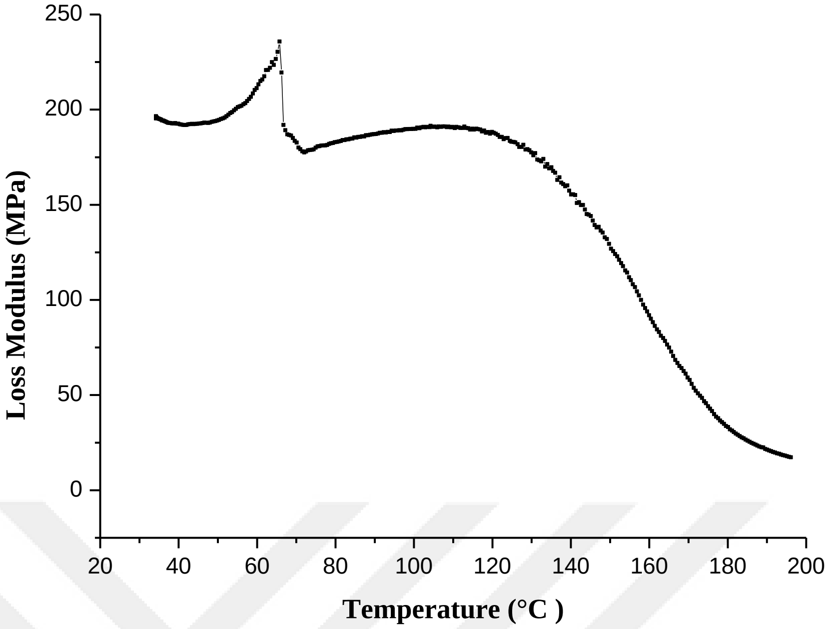

Figure 3.137 The variation of loss modulus of ChiPM-25 with temperature.

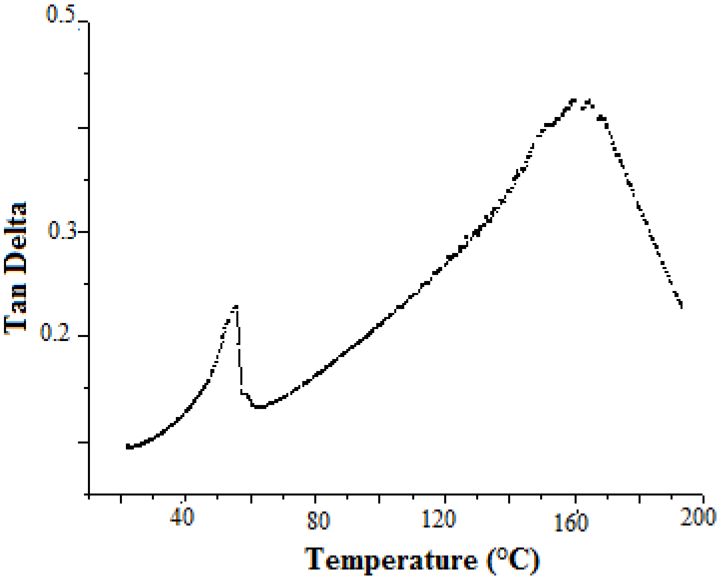

Figure 3.138 The variation of tan delta of ChiPM-25 with temperature.

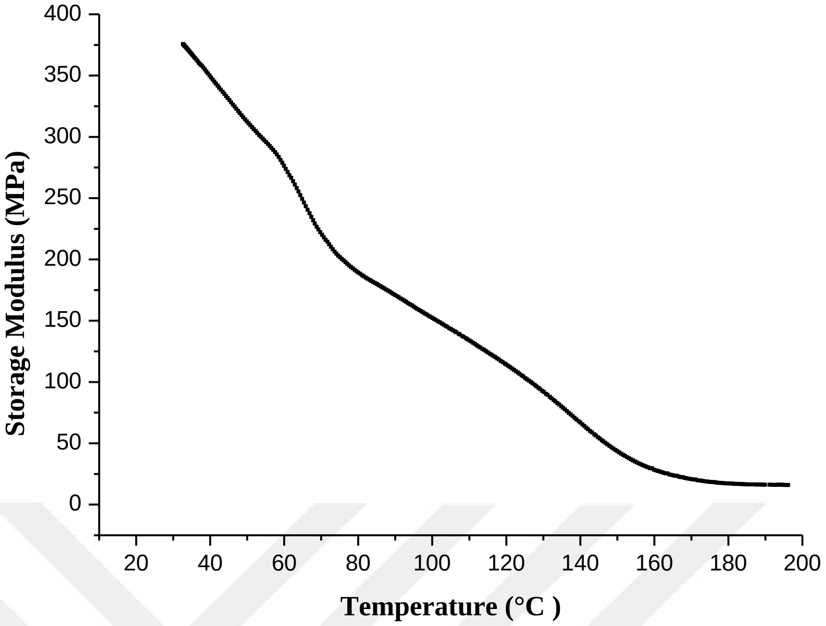

Figure 3.139 The variation of storage modulus of ChiPM-50 with temperature.

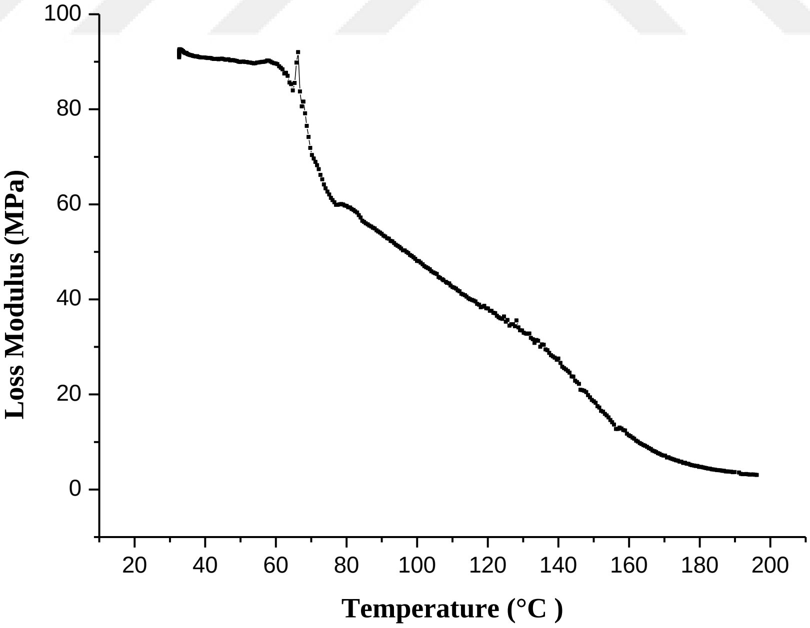

Figure 3.140 The variation of loss modulus of ChiPM-50 with temperature.

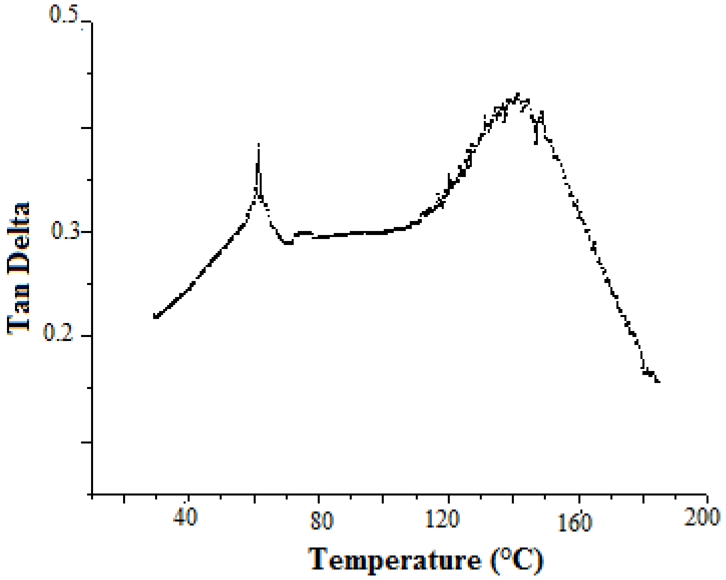

Figure 3.141 The variation of tan delta of ChiPM-50 with temperature.

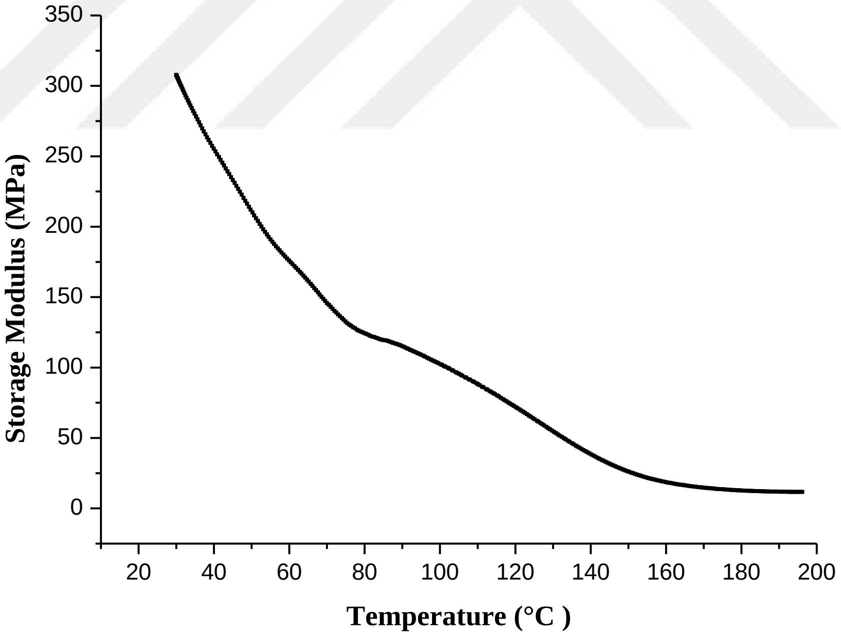

Figure 3.142 The variation of storage modulus of ChiPM-75 with temperature.

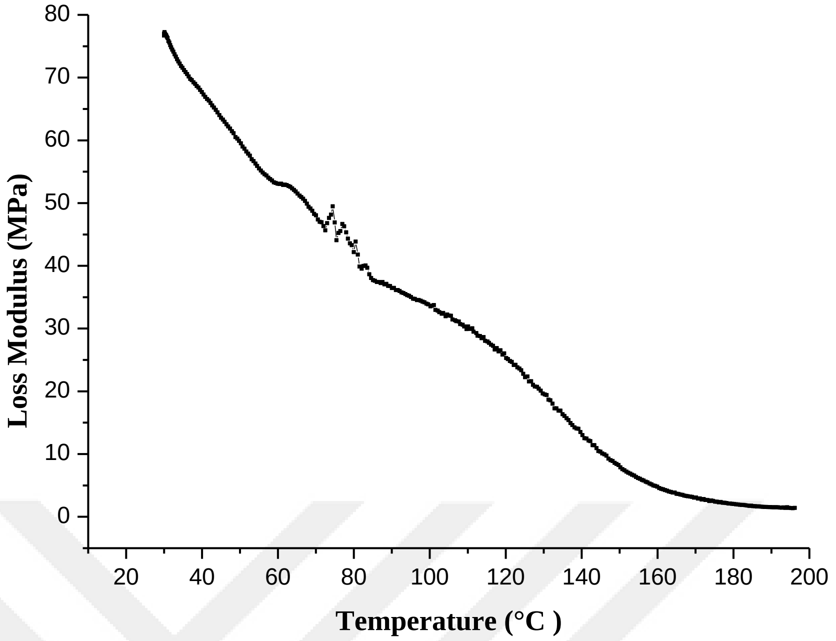

Figure 3.143 The variation of loss modulus of ChiPM-75 with temperature.

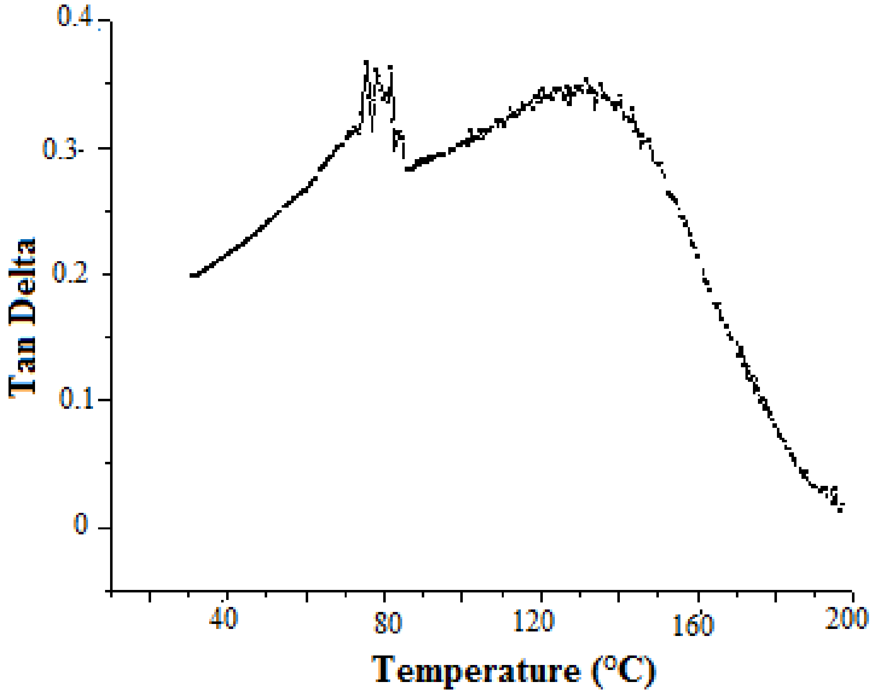

Figure 3.144 The variation of tan delta of ChiPM-75 with temperature.

3.3.6 Electroactive Properties

3.3.6.1 Motion Test

The electroactive properties based motion capability of samples were investigated under the DC voltages (3, 5, 7, 9, 11, 13, 17 V [first positive voltages then negative voltages were applied to the samples]) with 500 s (0,002 Hz). The studies were carried out under the room temperature. Tip displacements of the chitosan based samples were investigated with CCD camera. The recorded data were processed and tip displacements were evaluated. Time versus tip displacement curves were obtained for each actuator. The experimental setups are exhibited in Figure 3.145. The curves of the samples are shown in Figure 3.146-166. The max tip displacements of the actuators are exhibited in Table 3.7.

The tip displacement of ChiPM-25 is 4.5, 9.5, 12.8, 8.4, 6.3, and 6mm under the 5, 7, 9, 11, 13, and 17 V, respectively. Tip displacement of ChiPM-50 is 12.8, 9.4, 7.5, 5.8, 4.4, and 3.9 mm under the 5, 7, 9, 11, 13, and 17 V, respectively. The tip displacement of ChiPM-75 is 3.2, 1.1, 0, 0.2, 0.2, and 0.2 mm under the 5, 7, 9, 11, 13, and 17 V, respectively. For ChiPM-25, the maximum tip displacement was obtained to be 12.8 mm under 9 V. The tip displacement values of ChiPM-25 were initially increased to 9V then the values decreased. ChiPM-50 has the maximum motion value under 5V. The maximum tip displacement of ChiPM-50 is 12.8 mm. The motion values of ChiPM-50 decreased as the voltage values were increased. ChiPM-75 has a maximum motion value (3.2 mm) under 5V. ChiM has no motion under various DC voltages and so motion graph of ChiM was not given.

The ion mobility is important parameter for actuation of ionic actuator. Typical ionic actuators consist of mobile ions which help the motion of polymer due to ion diffusion. The diffusion occurs under the electrical potentials. The diffusion of hydrated cations diffused toward to the negatively charged electrode and so the motion occurs (Shahinpoor et al., 1998; Shahinpoor and Kim, 2001; Shahinpoor et al., 2003; Akle et al., 2005; Phillips and Moore, 2005; Wang et al., 2007; Duncan et al., 2009; Lee et al., 2010; Lee et al., 2010; Luqman et al., 2011; Kwon et al., 2015). Besides, moisture and ions in polymer matrix affect the electroactivity. The content of moisture affects the mobility of ions and the conductivity. There is a critical limit for the concentration of ion species and exceeding this limit does not contribute to the conductivity. And also above this limit ions are excluded from the matrix (Finkenstadt, 2005).

We used pDADMAc, which is a water soluable quaternary ammonium compound, to enhance the electroactive properties of actuators. pDADMAc is a polyelectrolyte gel which can absorb water and moisture and so help the increase of ion mobility in polymer matrix (Jing and Hongfei,2001; Jing, Yanqun, Jiuqiang, & Hongfei, 2001; Kim et al., 2003). The increase in ion mobility enhances the bending of actuators up to critical limit. Above the critical limit the actuator performance of samples decreased. The results can be seen in Figures 3.146-3.166 and Table 3.7. The max tip displacements of samples are 12.8 mm for ChiPM-25 under 9V, 12.8 mm for ChiPM-50 under 5V, and 3.2 mm for ChiPM-75 under 5V. ChiM, which does not include pDADMAc, did not exhibit any tip displacement under the electric field.

In a summary Table 3.7 can be evaluated as follows:

- The main observation of the motion experiments is that the loading of PDADMAC into Chitosan makes it an efficient actuator. In other words, standart chitosan gained electroactive properties with loading of PDADMAC.
- 0.50 and 0.75 mL loadings of PDADMAC results in similar motion ranges from 3.9 to 12.8 mm and from 4.5 to 12.8mm, repectively.
- Another critical issue observed in experiments is that the increase of pDADMAC loading results in observation of maximum of maximum tip displacement in lower electrical excitation values.

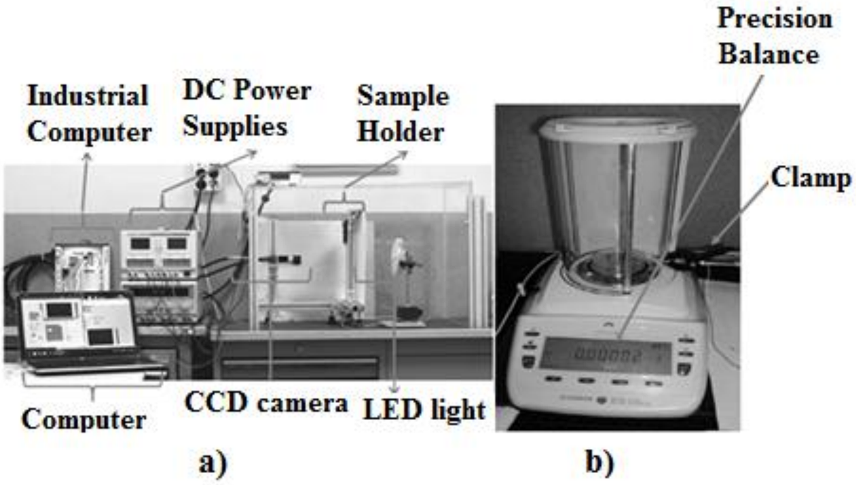

Figure 3.145 Experimental set-up: a) Tip displacement, b) Blocking force (Sen et al., 2015).

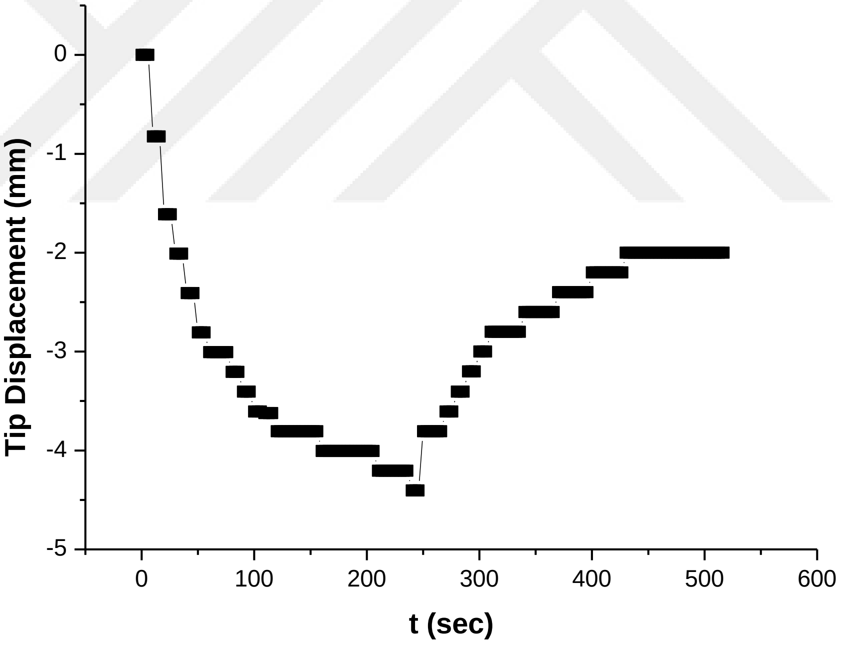

Figure 3.146 Tip displacements of ChiPM-25 under 5V.

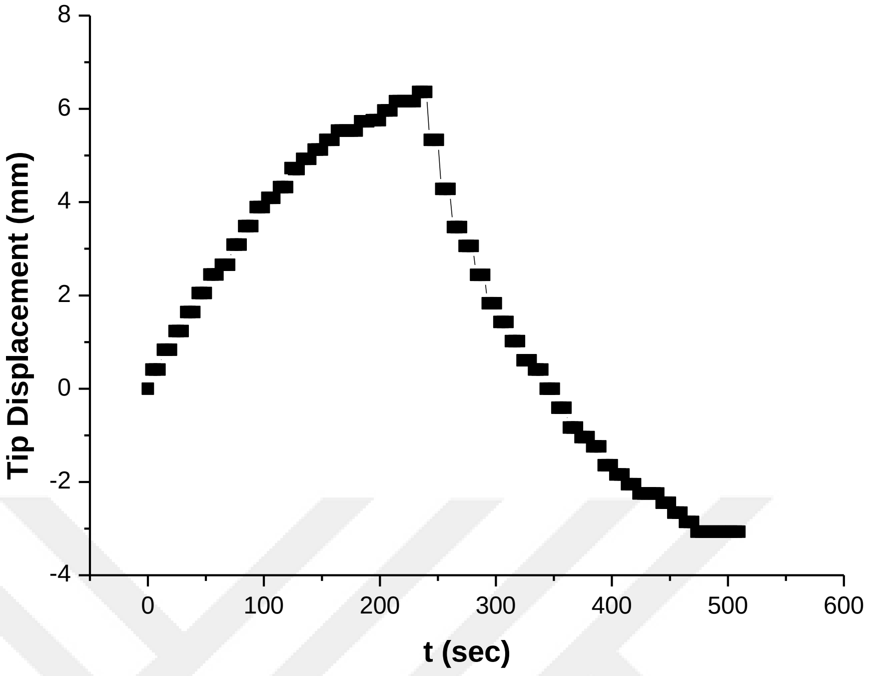

Figure 3.147 Tip displacements of ChiPM-25 under 7V.

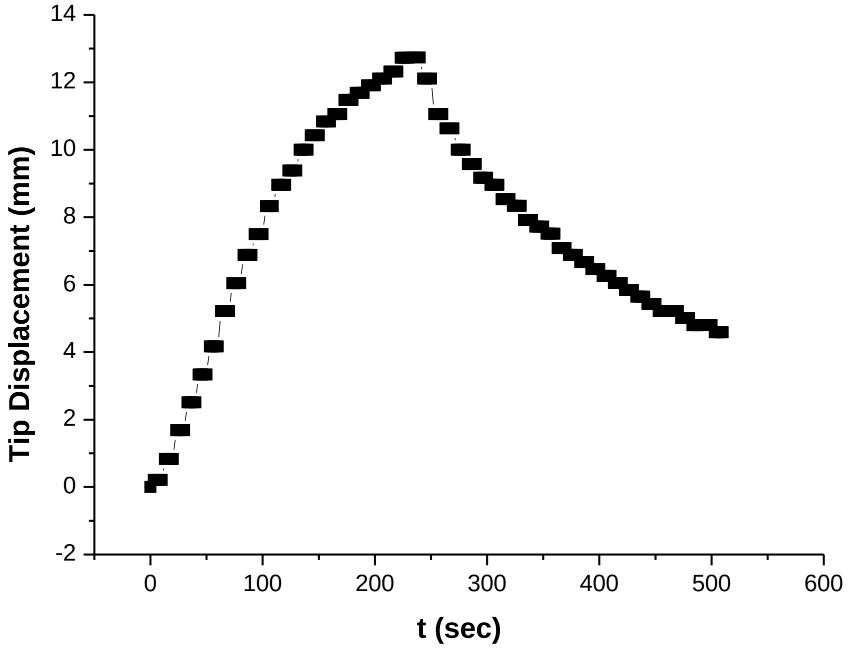

Figure 3.148 Tip displacements of ChiPM-25 under 9V.

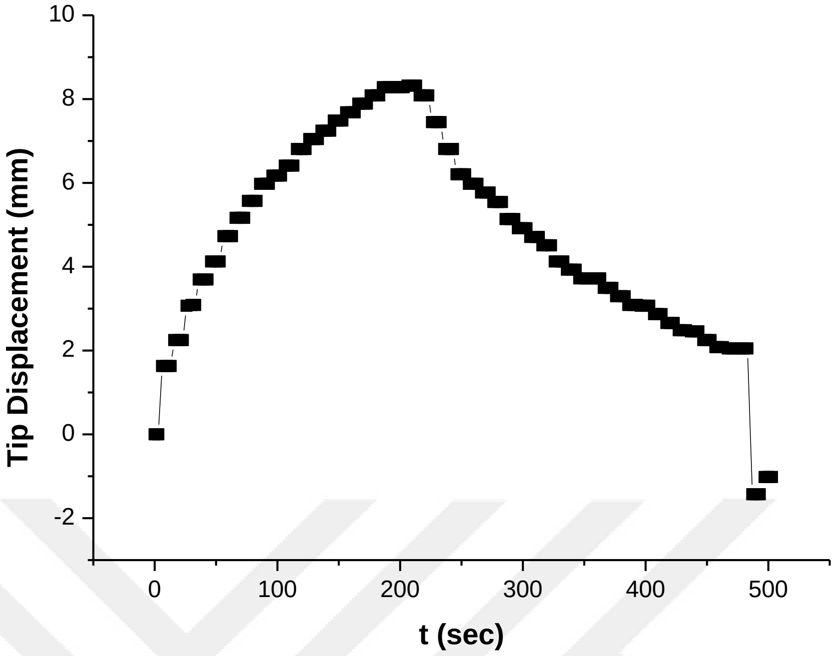

Figure 3.149 Tip displacements of ChiPM-25 under 11V.

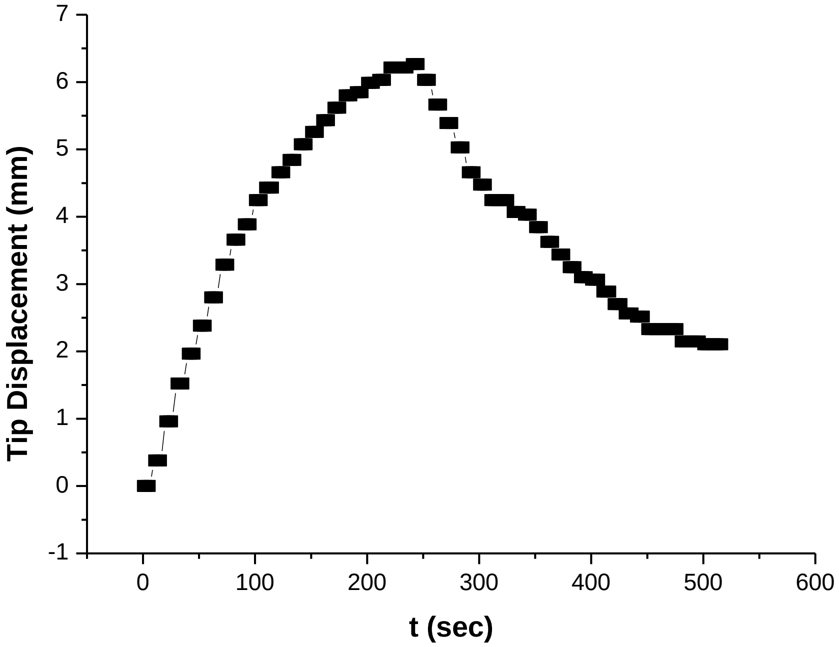

Figure 3.150 Tip displacements of ChiPM-25 under 13V.

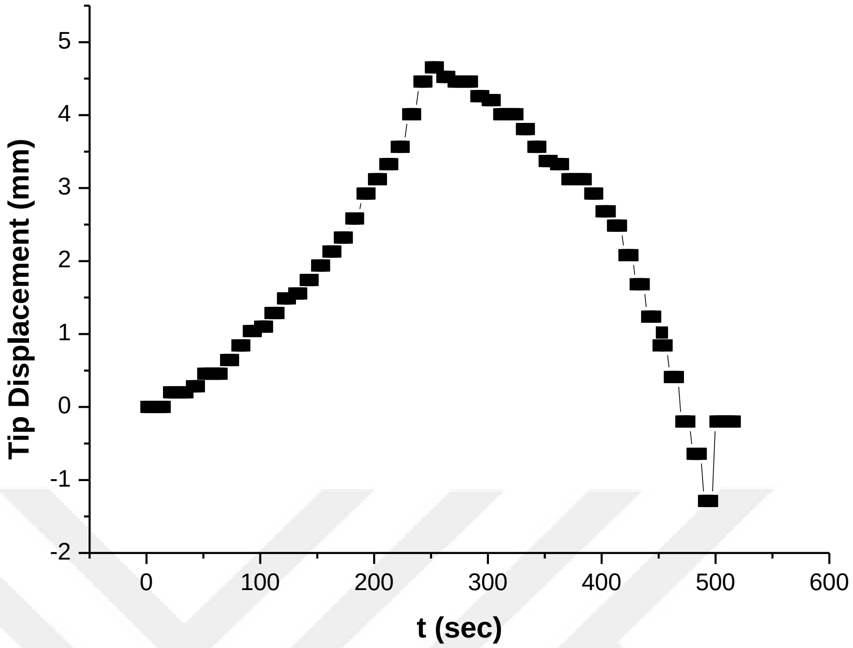

Figure 3.151 Tip displacements of ChiPM-25 under 17V.

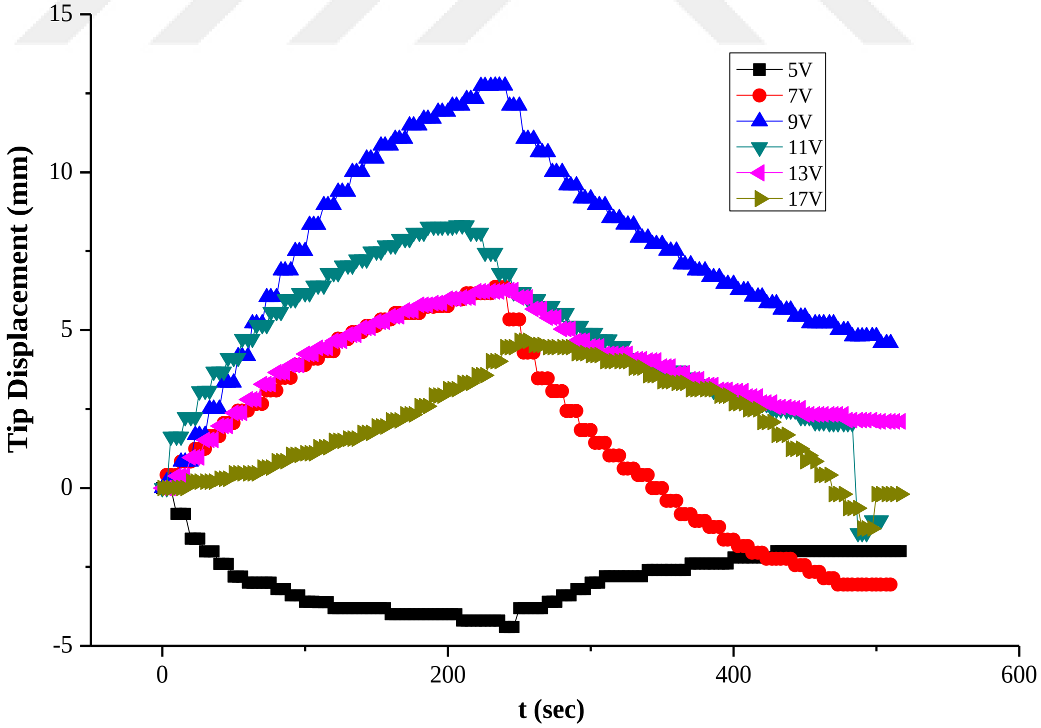

Figure 3.152 Tip displacements of ChiPM-25.

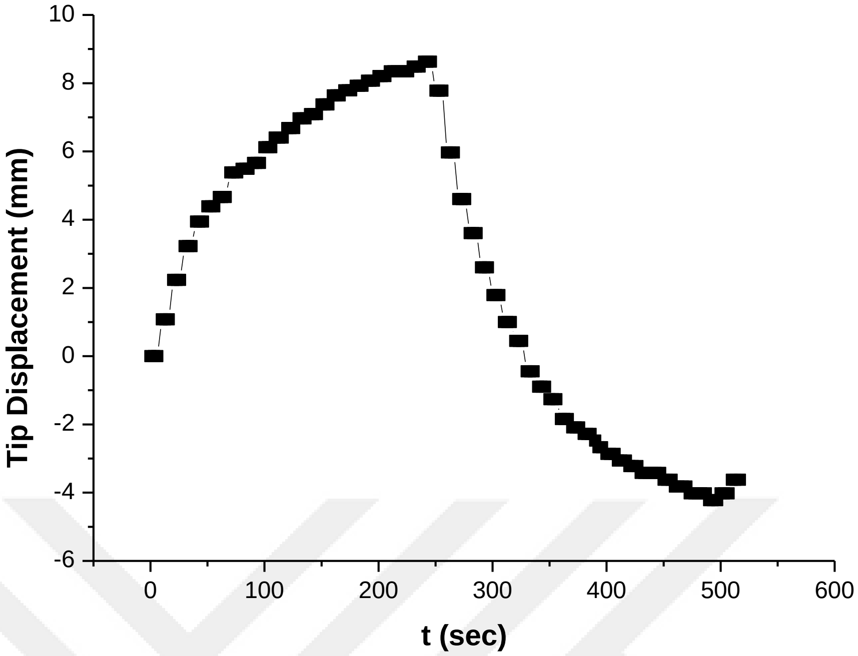

Figure 3.153 Tip displacements of ChiPM-50 under 5V.

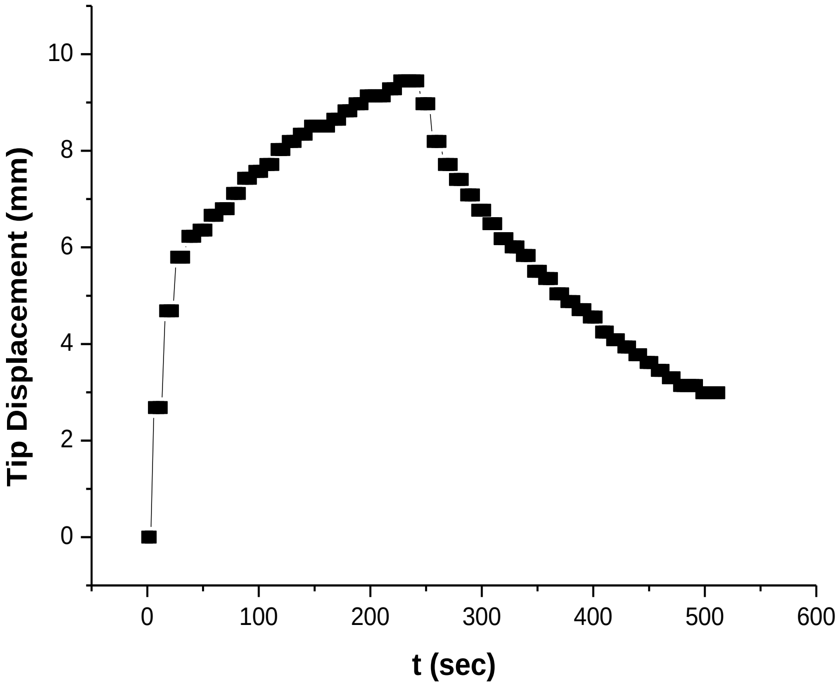

Figure 3.154 Tip displacements of ChiPM-50 under 7V.

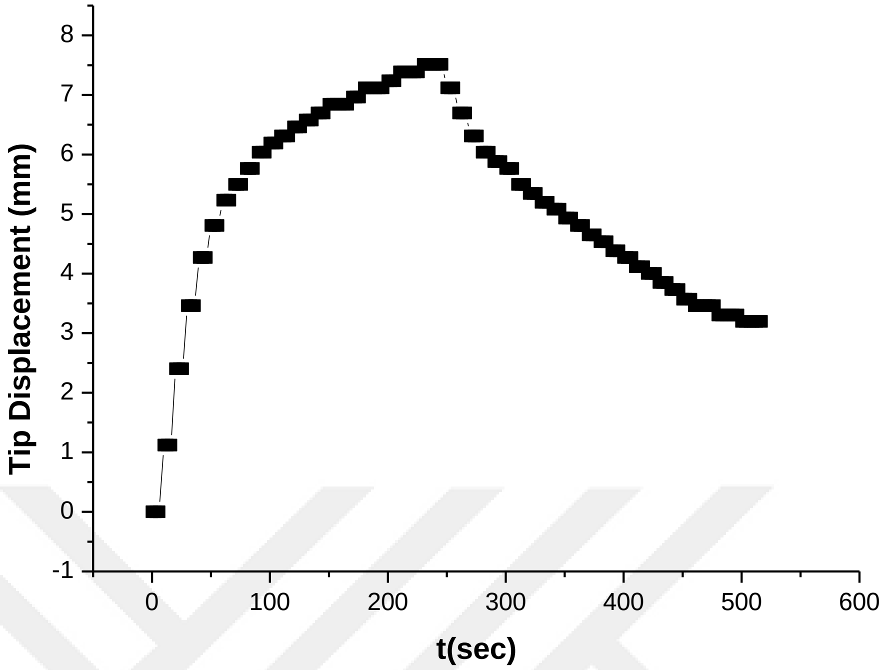

Figure 3.155 Tip displacements of ChiPM-50 under 9V.

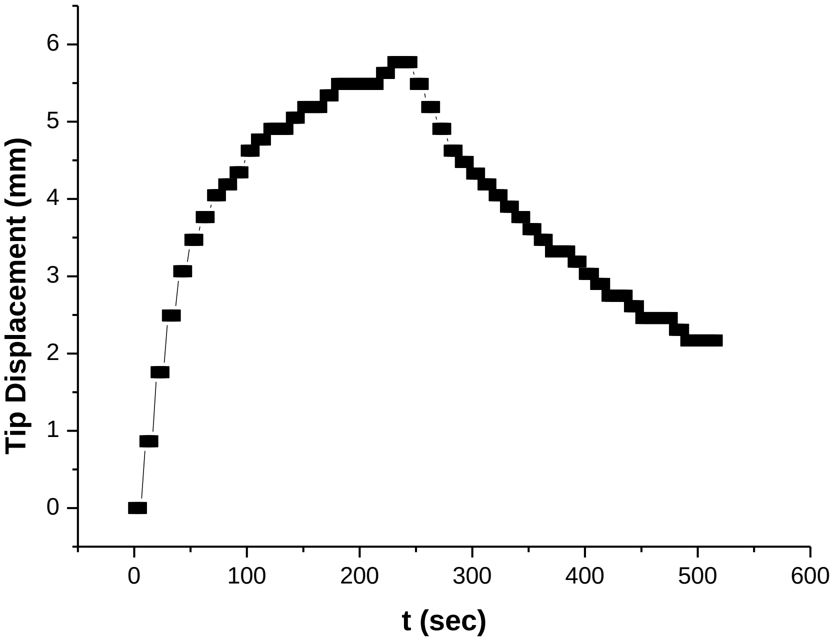

Figure 3.156 Tip displacements of ChiPM-50 under 11V.

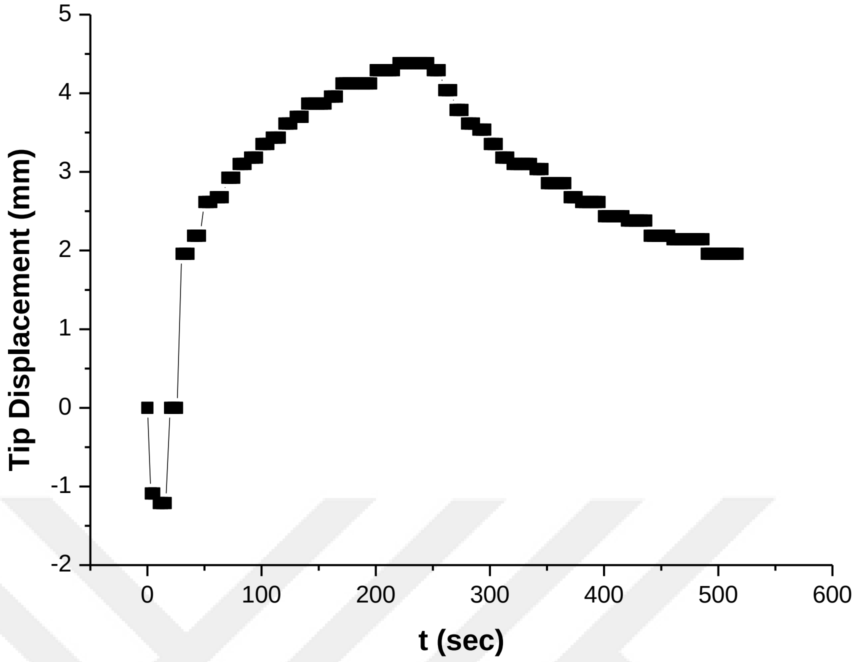

Figure 3.157 Tip displacements of ChiPM-50 under 13V.

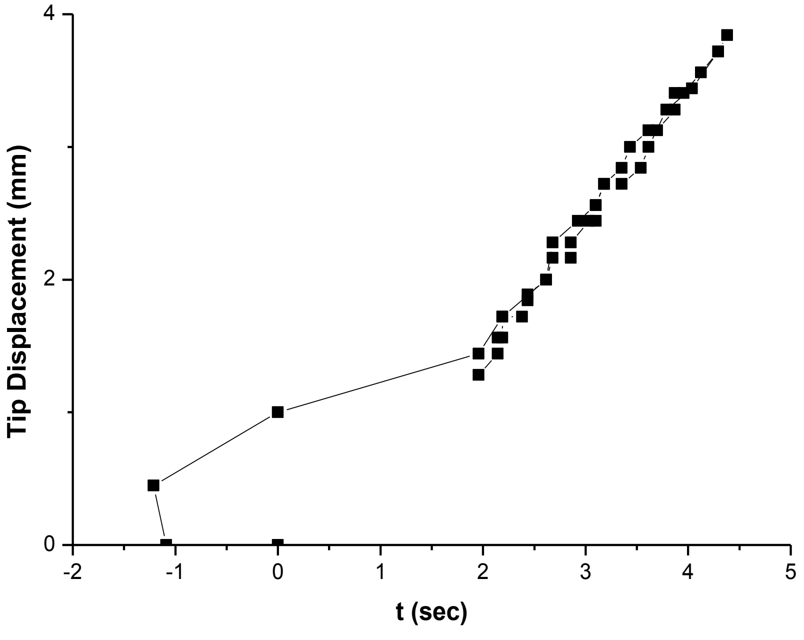

Figure 3.158 Tip displacements of ChiPM-50 under 17V.

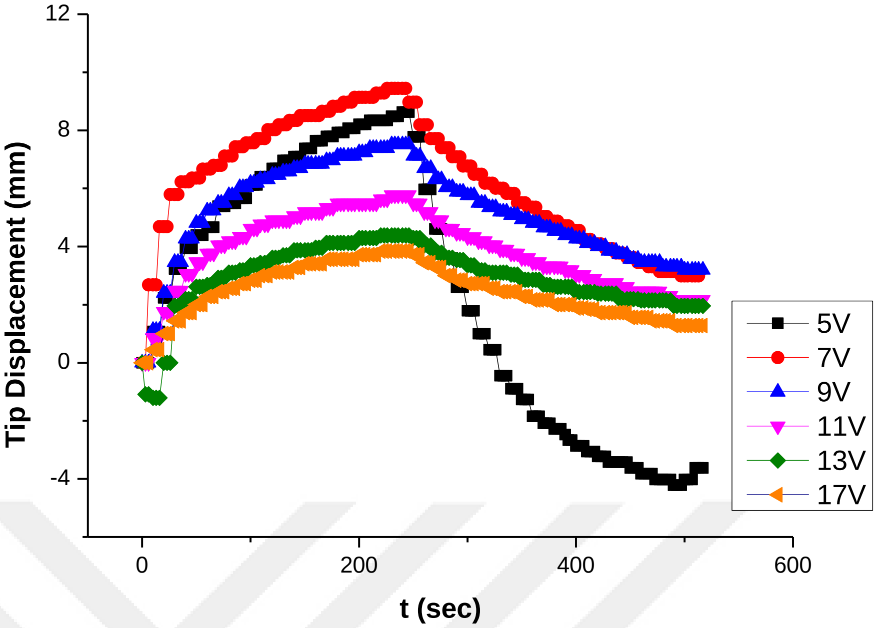

Figure 3.159 Tip displacements of ChiPM-50 under various DC voltages.

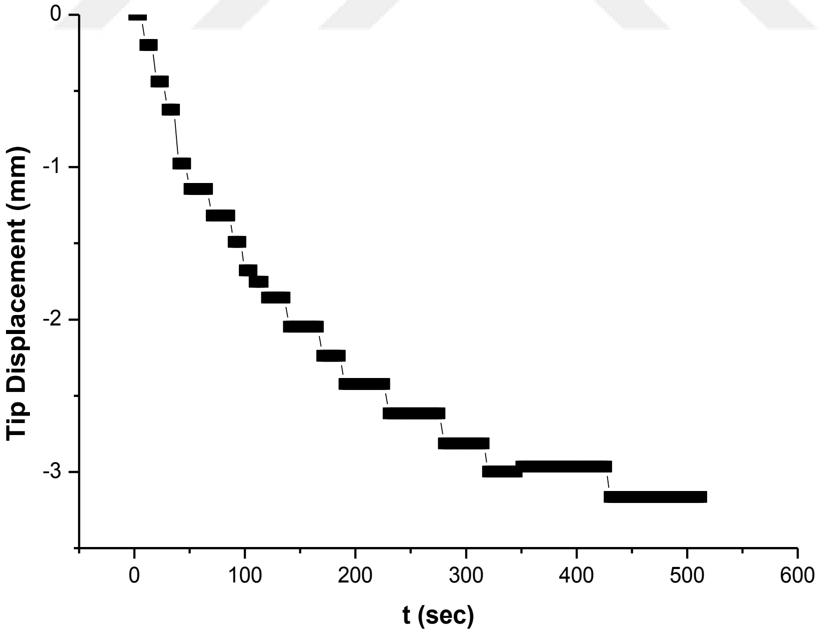

Figure 3.160 Tip displacements of ChiPM-75 under 5V.

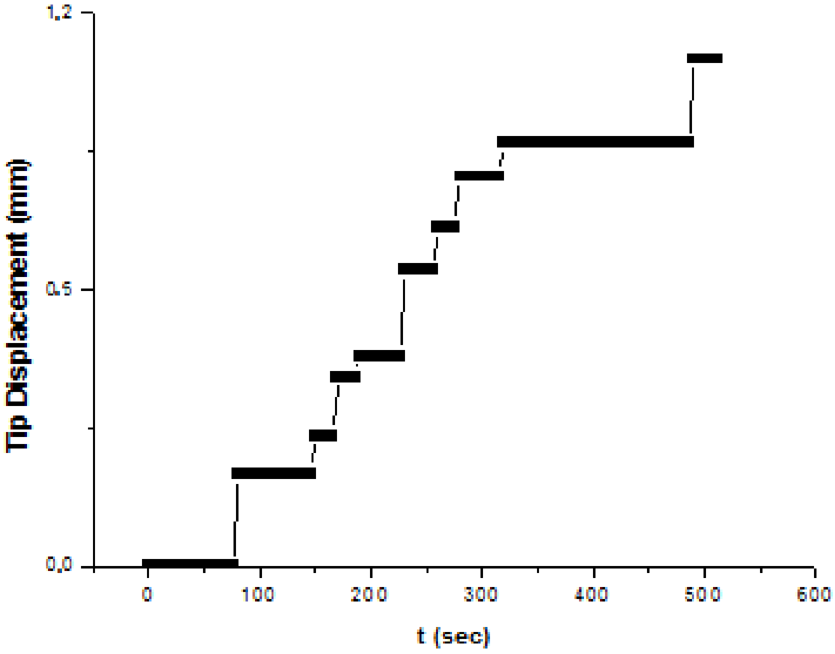

Figure 3.161 Tip displacements of ChiPM-75 under 7V.

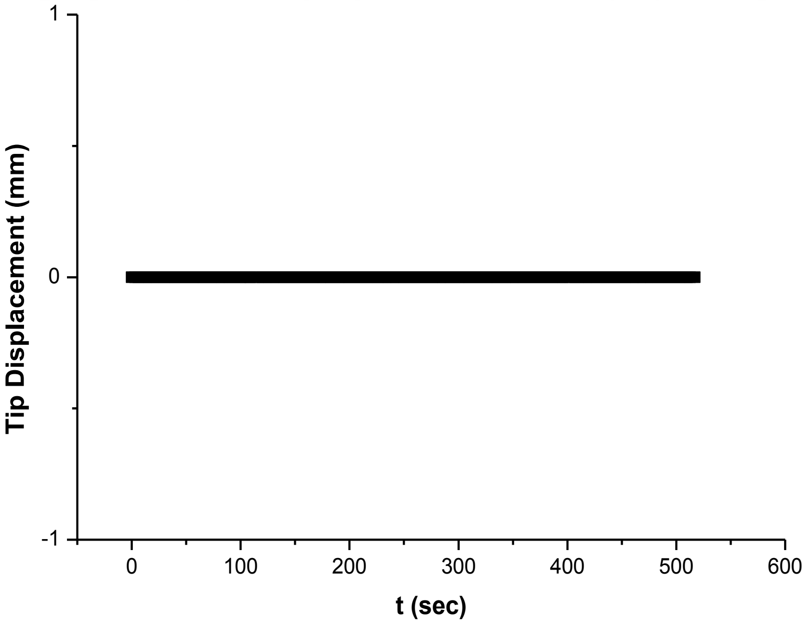

Figure 3.162 Tip displacements of ChiPM-75 under 9V.

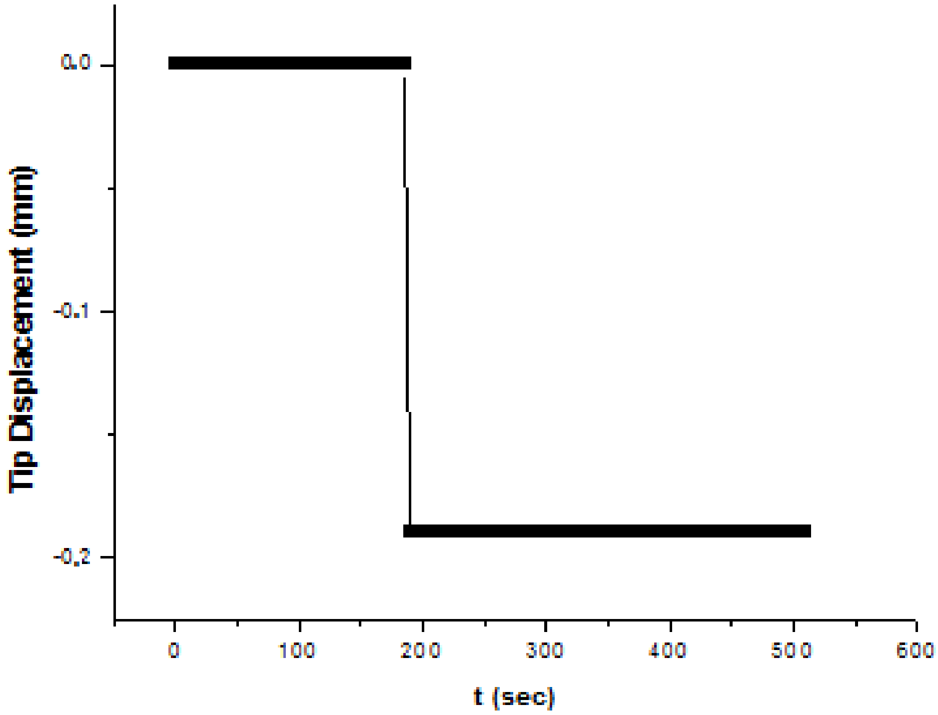

Figure 3.163 Tip displacements of ChiPM-75 under 11V.

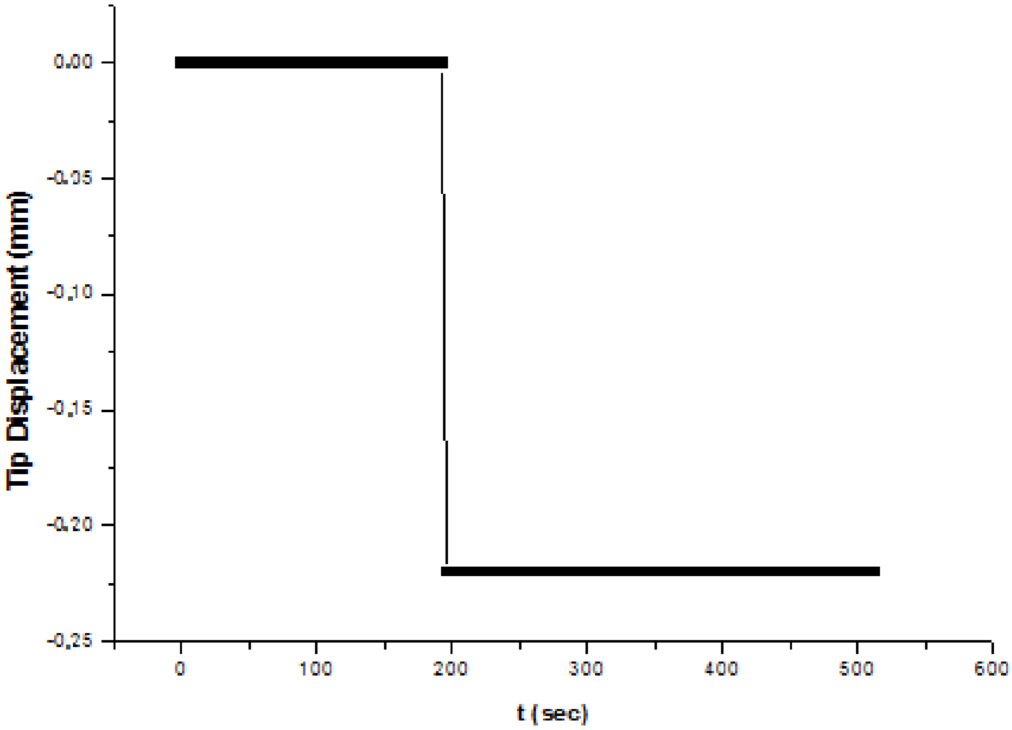

Figure 3.164 Tip displacements of ChiPM-75 under 13V.

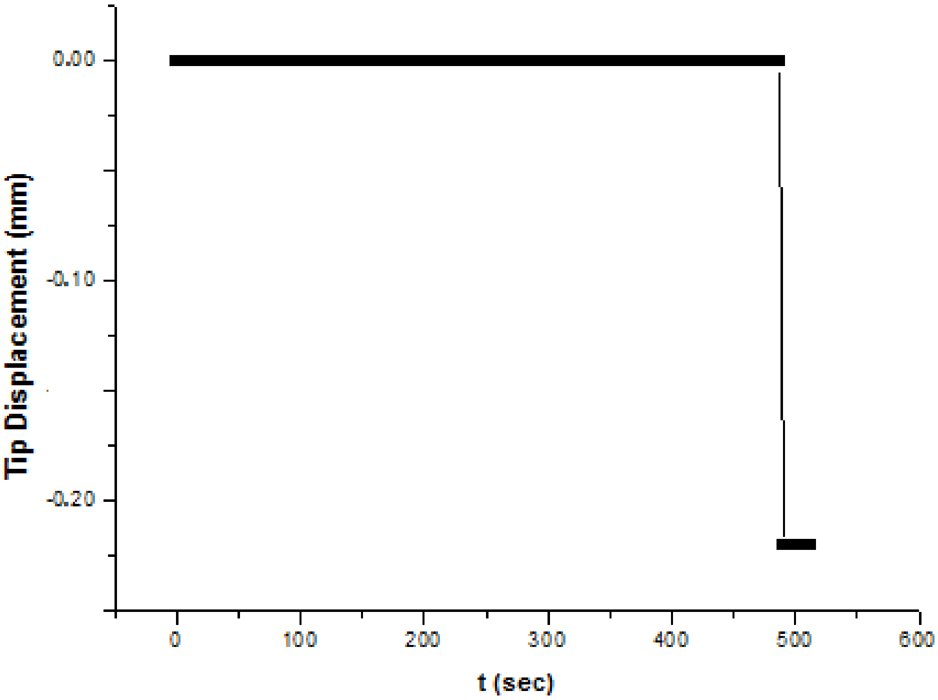

Figure 3.165 Tip displacements of ChiPM-75 under 17V.

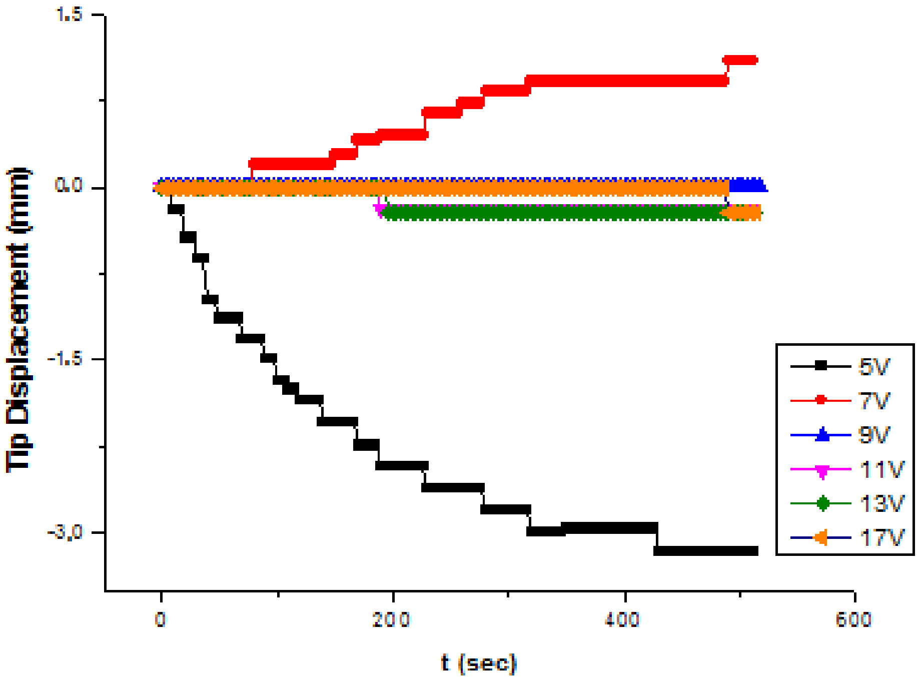

Figure 3.166 Tip displacements of ChiPM-75 under various DC voltages.

Table 3.9 Max tip displacements of ChiPM-25, ChiPM-50, ChiPM-75, and ChiM under various voltages

Applied Voltage	**ChiPM-25 Tip Displacement (mm)**	**ChiPM-50 Tip Displacement (mm)**	**ChiPM-75 Tip Displacement (mm)**	**ChiM Tip Displacement (mm)**
5	4.5	12.8	3.2	-
7	9.5	9.4	1.1	-
9	12.8	7.5	0	-
11	8.4	5.8	0.2	-
13	6.3	4.4	0.2	-
17	6	3.9	0.2	-

3.3.6.2 Transient analysis of motion

The actuator samples response to constant input voltages are alike to the time response of the first order system model which can be generalized as equation 3.2.

$$x(t) = K(1 - e^{\frac{-t}{T}}) \tag{3.2}$$

Given above matematical relationship, the time response data are used for regression. The regression results are used to determine the time (t) response T^+ and T^- which are time constants of the motion curves under the same voltage magnitude with different polarity. The observed results are as follows:

- The main observation of the motion experiments is that the more loading of PDADMAC into samples makes the actuator slower.
- When samples are compared concerning the polarity of input voltage, the motion of the actuators to the one side is faster then the otherside. The numerical values of bilateral motion of the actuators are given in Table 3.8 as T^{+} and T^-.

The faster response of the actuators is obtained in cases where the tip displacement values are larger.

Table 3.10 Bilateral motion of samples

Applied Voltage	ChiPM-25 T^+/T^- (s)	ChiPM-50 T^+/T^- (s)	ChiPM-75 T^+/T^- (s)	ChiM Tip T^+/T^- (s)
5	90/140	60/100	90/140	-/-
7	90/140	60/100	90/140	-/-
9	60/105	70/105	-/-	-/-
11	55/90	70/105	-/-	-/-
13	80/130	70/1054.4	-/-	-/-
17	80/130	70/105	-/-	-/-

3.3.6.3 Blocking Force

The force generation capabililty of chitosan based actuators were analyzed by measuring the blocking force. The actuator samples were put on the precision balance and DC excitations were applied and so the force generation capability was evaluated (Altınkaya et al., 2016). The results are indicated in Table 3.9. The significant observation on force experiments is that the ChiPM-50 and ChiPM-25 actuators have similar maximum tip displacement values where as their force generatting capabilitties are significantly different. It can be deduced that maximum force generation capability of the actuators are more likely dependent on the excitation voltage value.

Table 3.11 Blocking force results of samples

Applied Voltage	**ChiPM-25 (g)**		**ChiPM-50 (g)**		**ChiPM-75 (g)**	
	max	**min**	**max**	**min**	**max**	**min**
5V	0.02	-0.01	0.03	-0.06	0	-0.08
7V	0.02	-0.01	0.05	0	0	0
9V	0.02	-0.03	0.1	-0.03	0	0
11V	0.06	-0.06	0.1	0	0.01	-0.05
13V	0.06	-0.06	0.1	0	0.03	-0.04
17V	0.06	-0.06	0.1	0	0.03	-0.02

3.3.7 Mechanical Properties

The tensile strength and Young’s modulus of the Chitosan based films at different pDADMAc ratios are given in Table 3.9. As was seen from Table 3.9 that pDADMAc ratio affects the both tensile strength and Young modulus of the chitosan based films. The maximum tensile strength and Young’s modulus values were obtained at ChiPM-25. With increasing the pDADMAc ratio, both the tensile strength and Young’s modulus of the chitosan based films decreased. On the other hand, there is no significant difference in terms of the tensile strength and Young’s Modulus of ChiPM-50 and ChiPM-75 films. Besides, these films become more ductile with increasing the pDADMAc ratio.

Table 3.12. Mechanical properties of Chitosan based samples

Sample name	**Tensile Strength (MPa)**	**Young’s modulus (GPa)**
ChiPM-25	4.93±0.58	0.044±0.016
ChiPM-50	3.23±0.69	0.026±0.006
ChiPM-75	3.14±0.45	0.025±0.01

CHAPTER FOUR

CONCLUSIONS

For the first part of thesis, multilayer graphene (Gr)-reinforced cellulose composites were fabricated by dissolving of cellulose in 1-ethyl-3-methylimidazolium diethylphosphonate ionic liquid. The samples include different amount of graphene (Gr) (0.2, 0.4, and 0.6 wt.%).

The FTIR spectrum of cellulose exhibited some changes after the addition of [EMIM]DEP, DMAc, and graphene. The addition of these materials affected the cellulose chemical structure, and so the formation of new absorption peaks were observed at 1570, 1216, 944 and 794 cm^{-1}.

The crystallinity index of cellulose was calculated as 83%. The fabrication of cellulose based samples gave rise to changes in CI of cellulose. The decrease in CI and shifting for 2θ degree were observed for Cel-PO$_4$-Gr samples.
Maximum thermal decomposition temperature (T$_{max}$) was obtained to be 340 ^{o}C. T$_{max}$ of the Cel-PO4-Gr samples was observed at around 280 ^{o}C. Thermal stability of cellulose was decreased with the fabrication of Cel-PO$_4$-Gr samples while pyrolysis residue was increased.

The SEM micrographs of the samples are quite smooth. The smooth appearance can be due to the homogeneous distribution of graphene in the samples.
The increase in graphene concentration increased the tensile strength and the Young's modulus of the composites but decreased when 0.6 wt. % Gr was used. The decrease in mechanical mechanical properties is associated with aggregation of filler at higher graphene content.The decrease in the tensile strength of sample is probably due to poor dispersion of graphene.

The Cel-PO$_4$ exhibited max tip displacement for positive and negative voltages under 7V and -3V, respectively. The optimum values for Cel-PO$_4$-Gr0.2 were obtained to be 0.25 mm under 3V and 0.53 mm under -3V. The highest displacements for Cel-PO_4-Gr0.4 were obtained as 0.17 and 0.35 mm under DC voltages of 3V and -1V, respectively. The max tip displacements for Cel-PO_4-Gr0.6 were obtained as 0.12 and 0.07 mm under 7V and -7V, respectively. The maximum tip displacement for cellulose based actuators were obtained as 0.53mm for Cel-PO_4-Gr0.2 under -3V, 0.35mm for Cel-PO_4-Gr0.4 under -1V, and 0.12 mm for Cel-PO_4-Gr0.6 under 7V. The highest max tip displacement was exhibited by Cel-PO_4-Gr0.2 under -3V.

For the second part of thesis, chi-based IPMC actuators were fabricated by crosslinking chitosan with MBA. Besides in order to improve the displacement behavior, pDADMAC was added to crosslinked chitosan film. The fabricated films were coated with gold leaves. The effects of crosslinker concentration on the actuators were investigated.

The effect of crosslinker concentration on chemical functional groups of chitosan was investigated by FTIR analysis. FTIR spectra of the chitosan, ChiPM-1, ChiPM-2, ChiPM-3, and ChiM-2 were analyzed. In FTIR spectra of ChiPM-1, ChiPM-2, ChiPM-3, and ChiM-2, some changes were observed and the avaibility of MBA was noticed.

The XRD results show that CI decreased as the crosslinker concentration was increased. The decrease in CI is related with increasing amorphous regions. The decrease in the CI can be explained by the decrease in intermolecular and intramolecular hydrogen bonds which help the forming of crystalline structure.
TGA results of Chi film, ChiPM-1, ChiPM-2, ChiPM-3 and, ChiM-2 were compared and evaluated. Decomposition temperature of chi-based samples was lower than chitosan when the second decomposition stage was taken into consideration. Besides, pDADMAc addition gave rise to decrease in the maximum decomposition temperature in the third stage. It can be said that addition of pDADMAC led to decrease in the thermal stability of chitosan.

The SEM images were taken from surfaces and cross sections of the samples at different magnification sizes. SEM observations explained that the pore size of the structure decreased as the crosslinker concentration was increased.

According to the mechanical test results the increase in crosslinker concentration led to increase in Young's modulus. The decrease in tensile strength with the increasing crosslinking concentration was unusual.

The electroactive properties based on motion capability of chitosan based films were investigated under the DC voltages. The max tip displacements of ChiPM-1, ChiPM-2, and ChiPM-3 were determined to be 26.6 (15V), 19.6 (7V), and 1.2 (3V) mm, respectively. The ChiPM-3 film showed insufficient performance to be an actuator.

The resistances and electrical capacitances of chitosan based samples were evaluated. According to the results, the resistance of samples is directly proportion to amount of MBA. And also the capacitance of samples is inversely proportional to the amount of MBA.

The crosslinker which is used in the sample gave rise to decrease in storage modulus as the crossliker concentration was increased. The retention ratio gives the information about the mechanical properties of the samples with the temperature. The retention ratio decreased as the crosslinker concentration was decreased.

In the third part of the thesis, the effect of pDADMAc concentration on electroactive behaviors' and other properties of actuators were investigated. Four samples were prepared entitled ChiM, ChiPM-25, ChiPM-50, and ChiPM-75. While ChiM does not include pDADMAc, ChiPM-25, ChiPM-50, and ChiPM-75 contain 25, 50, and 75 µL pDADMAc, respectively. The results of the analysis are as follows:

The FTIR spectrum of chitosan exhibited characteristic bands. The intensity of the –OH vibration band of chitosan decreased with crosslinking and addition of other components. The existence of some vibrations shows the availability of MBA in films. Besides, some shifts were obtained in FTIR spectra.

The chitosan has an amorphous band at around $2\theta = 10°$ and has a main peak at around $2\theta = 20°$. The CI values of ChiPM-25, ChiPM-50, and ChiPM-75 were obtained to be 18.2, 9.9, and 9.1%, respectively. The presence of the pDADMAc inhibited the nucleation and the solution activity and so led to decrease in crystallinity index of samples.

The dynamic mechanical properties of the samples including different amount of pDADMAc ChiM, ChiPM-25, ChiPM-50, and ChiPM-75 were investigated via DMA. The loss and storage modulus of ChiPM-25, ChiPM-50, and ChiPM-75 approached to zero at about 200 °C. The E’ value of ChiM, ChiPM-25, ChiPM-50, and ChiPM-75 decreased from 4144, 1246, 375, and 304.3 MPa to 1932, 63.8, 11.68, and 11.67 MPa, respectively. The loss modulus is attributed to the relaxation processes *of* α and β. The α relaxation is related to the glass transition of the amorphous phase**.** The Tg value of ChiM was obtained to be 130 °C. β relaxations were seen at around 65, 66, and 73 °C for ChiPM-25, ChiPM-50, and ChiPM-75, respectively**.** For tan delta (δ), ChiPM-25, ChiPM-50, and ChiPM-75 samples exhibited two relaxation peaks**.** The β-relaxation, which originates from the motion of rigid segments in the chitosan molecules and reordering of hydrogen bonds, is seen at about 65 °C. The second α relaxation or Tg broad bands were observed at 166.7, 150, and 130.3°C for ChiPM-25, ChiPM-50, and ChiPM-75, respectively. Tg values decreased as the pDADMAC concentration was increased.

Thermal behavior of samples was determined by using TGA. Chi film has two mass loss stage. ChiM, ChiPM-25, ChiPM-50, and ChiPM-75 films exhibited three mass loss stages. The degradation temperature of samples decreased as the pDADMAc concentration was increased. It can be related with the decomposition of pDADMAc.

According to the SEM images, the pore sizes decreased as the pDADMAc concentration was increased in the samples. It can be explained that the added pDADMAC filled the pores of the membrane and so smaller pores were seen on the surface of the samples.

The maximum tensile strength and Young’s modulus values were obtained for ChiPM-25. With increasing the pDADMAc ratio, both the tensile strength and Young’s modulus of the chitosan based films decreased.

The electroactive properties based motion capability of samples were investigated under the DC voltages (3, 5, 7, 9, 11, 13, 17 V) with 500 s (0,002 Hz). The max tip displacements of samples are 12.8 mm for ChiPM-25 under 9V, 12.8 mm for ChiPM-50 under 5V, and 3.2 mm for ChiPM-75 under 5V. The tip displacement values of ChiPM-25 were initially increased up to 9V then the values decreased. The motion values of ChiPM-50 decreased as the voltage values were increased. ChiM has no motion under various voltages. pDADMAC can help the increase of ion mobility in polymer matrix. The increase in ion mobility enhances the bending of actuators up to critical limit. Above the critical limit the actuator performance of samples decreased. Importantly, chitosan gained electroactive properties with loading of PDADMAC. In addition to this, pDADMAc loaded samples work better under the low DC voltages.

REFERENCES

Abdu, Y. A., Hull, S. K., Fayek, M., & Hawthorne, F. C. (2011). The turquoise-chalcosiderite Cu (Al, Fe^{3+}) $6(PO_4)_4(OH)_8.4H_2O$ solid-solution series: A Mössbauer spectroscopy, XRD, EMPA, and FTIR study. *American Mineralogist*, *96*(10), 1433-1442.

Abe, Y., Mochizuki, A., Kawashima, T., Yamashita, S., Asaka, K., & Oguro, K. (1998). Effect on bending behavior of counter cation species in perfluorinated sulfonate membrane–platinum composite. *Polymers for Advanced Technologies*, *9*(8), 520-526.

Adeloju, S. B., Shaw, S. J., & Wallace, G. G. (1993). Polypyrrole-based potentiometric biosensor for urea part 1. Incorporation of urease. *Analytica Chimica Acta*, *281*(3), 611-620.

Ahn, S. K., Kasi, R. M., Kim, S. C., Sharma, N., & Zhou, Y. (2008). Stimuli-responsive polymer gels. *Soft Matter*, *4*(6), 1151-1157.

Akar, E., Seki, Y., Özdemir, O., Şen, İ., Sarıkanat, M., Gürses, Yılmaz, O, Cetin, L., & Sever, K. (2015). Electromechanical characterization of multilayer graphene-reinforced cellulose composite containing 1-ethyl-3-methylimidazolium diethylphosphonate ionic liquid. *Science and Engineering of Composite Materials*, 1-7.

Akle, B. J., Leo, D. J., Hickner, M. A., & McGrath, J. E. (2005). Correlation of capacitance and actuation in ionomeric polymer transducers. *Journal of Materials Science*, *40*(14), 3715-3724.

Alet, P. J., Palacin, S., Cabarrocas, P. R. I., Kalache, B., Firon, M., & De Bettignies, R. (2006). Hybrid solar cells based on thin-film silicon and P3HT.*The European Physical Journal Applied Physics*, *36*(03), 231-234.

Aliev, A. E., Oh, J., Kozlov, M. E., Kuznetsov, A. A., Fang, S., Fonseca, A. F. Ovalle, R., Lima, M., Haque, M., Garstein, Y., Zhang, M., Zakhidov, A., & Baughman, R. (2009). Giant-stroke, superelastic carbon nanotube aerogel muscles. *Science, 323*(5921), 1575-1578.

Alimohammadi, F., Gashti, M. P., & Shamei, A. (2012). A novel method for coating of carbon nanotube on cellulose fiber using 1, 2, 3, 4-butanetetracarboxylic acid as a cross-linking agent. *Progress in Organic Coatings*, *74*(3), 470-478.

Altınkaya, E., Seki, Y., Yılmaz, Ö. C., Çetin, L., Özdemir, O., Şen, İ., Sever, K., Gürses, B., & Sarıkanat, M. (2016). Electromechanical performance of chitosan-based composite electroactive actuators. *Composites Science and Technology*, *129*, 108-115.

Amiya, T., Hirokawa, Y., Hirose, Y., Li, Y., & Tanaka, T. (1987). Reentrant phase transition of N-isopropylacrylamide gels in mixed solvents. *The Journal of Chemical Physics*, *86*(4), 2375-2379.

Andreopoulos, F. M., Deible, C. R., Stauffer, M. T., Weber, S. G., Wagner, W. R., Beckman, & Russel, A. (1996). Photoscissable Hydrogel Synthesis via Rapid Photopolymerization of Novel PEG-Based Polymers in the Absence of Photoinitiators⊥. *Journal of the American Chemical Society*, *118*(26), 6235-6240.

Ansari, R. (2006). Polypyrrole conducting electroactive polymers: synthesis and stability studies. *Journal of Chemistry*, *3*(4), 186-201.

Antony, P., & De, S. K. (2001). Ionic thermoplastic elastomers: A review. *Journal of Macromolecular Science, Part C: Polymer Reviews*, *41*(1-2), 41-77.

Asaka, K., Mukai, K., Sugino, T., & Kiyohara, K. (2013). Ionic electroactive polymer actuators based on nano-carbon electrodes. *Polymer International*, *62*(9), 1263-1270.

Aureli, M., Kopman, V., & Porfiri, M. (2010). Free-locomotion of underwater vehicles actuated by ionic polymer metal composites. *Mechatronics, IEEE/ASME Transactions on*, *15*(4), 603-614.

Aviram, A. (1978). Mechanophotochemistry. *Macromolecules*, *11*(6), 1275-1280.

Ayre, M. (2003). *Biomimicry–A review, Work package report* (2nd ed.). Netherlands: European Space Research & Technology Centre (ESTEC).

Bahramzadeh, Y., & Shahinpoor, M. (2014). A review of ionic polymeric soft actuators and sensors. *Soft Robotics*, *1*(1), 38-52.

Bao, X., Bar-Cohen, Y., & Lih, S. S. (2002). Measurements and macro models of ionomeric polymer-metal composites (IPMC). In *SPIE's 9th Annual International Symposium on Smart Structures and Materials* (220-227). International Society for Optics and Photonics.

Bar-Cohen, Y. (2000*). Electroactive polymer (EAP) actuators as artificial muscles. Reality, potential and challenges* (2nd ed.). United States: American Society of Civil Engineers.

Baughman, R. H. (1996). Conducting polymer artificial muscles. *Synthetic metals*, *78*(3), 339-353.

Baughman, R. H., Cui, C., Zakhidov, A. A., Iqbal, Z., Barisci, J. N., Spinks, G. M., & Jaschinski, O. (1999). Carbon nanotube actuators. *Science*, *284*(5418), 1340-1344.

Behl, M., & Lendlein, A. (2007). Shape-memory polymers. *Materials Today*, *10*(4), 20-28.

Biddiss, E., & Chau, T. (2006). Electroactive polymeric sensors in hand prostheses: Bending response of an ionic polymer metal composite. *Medical Engineering & Physics*, *28*(6), 568-578.

Brufau-Penella, J., Puig-Vidal, M., Giannone, P., Graziani, S., & Strazzeri, S. (2007). Characterization of the harvesting capabilities of an ionic polymer metal composite device. *Smart Materials and Structures*, *17*(1), 015009.

Burn, P. L., Lo, S. C., & Samuel, I. D. (2007). The Development of Light-Emitting Dendrimers for Displays. *Advanced Materials*, *19*(13), 1675-1688.

Cai, Z., & Kim, J. (2008). Characterization and electromechanical performance of cellulose–chitosan blend electro-active paper. *Smart Materials and Structures*, *17*(3), 035028.

Cai, Z., Hou, C., & Yang, G. (2012). Characteristics and bending performance of electroactive polymer blend made with cellulose and poly (3-hydroxybutyrate). *Carbohydrate Polymers*, *87*(1), 650-657.

Cao, Y., Wu, J., Zhang, J., Li, H., Zhang, Y., & He, J. (2009). Room temperature ionic liquids (RTILs): A new and versatile platform for cellulose processing and derivatization. *Chemical Engineering Journal*, *147*(1), 13-21.

Castelaín, M., Martínez, G., Ellis, G., & Salavagione, H. J. (2013). A versatile chemical tool for the preparation of conductive graphene-based polymer nanocomposites. *Chemical Communications*, *49*(79), 8967-8969.

Charlesby, A. (2013). *Atomic Radiation and Polymers: International Series of Monographs on Radiation Effects in Materials* (1. Ed.). London: Elsevier.

Chen, L., Liu, C., Liu, K., Meng, C., Hu, C., Wang, J., & Fan, S. (2011). High-performance, low-voltage, and easy-operable bending actuator based on aligned carbon nanotube/polymer composites. *ACS Nano*, *5*(3), 1588-1593.

Chen, Z., Shatara, S., & Tan, X. (2010). Modeling of biomimetic robotic fish propelled by an ionic polymer–metal composite caudal fin. *Mechatronics, IEEE/ASME Transactions on*, *15*(3), 448-459.

Chen, Z., Shen, Y., Xi, N., & Tan, X. (2007). Integrated sensing for ionic polymer–metal composite actuators using PVDF thin films. *Smart Materials and Structures*, *16*(2), 262.

Chiono, V., Pulieri, E., Vozzi, G., Ciardelli, G., Ahluwalia, A., & Giusti, P. (2008). Genipin-crosslinked chitosan/gelatin blends for biomedical applications. *Journal of Materials Science: Materials in Medicine*, *19*(2), 889-898.

Choi, H. R., Jung, K., Ryew, S., Nam, J. D., Jeon, J., Koo, J. C., & Tanie, K. (2005). Biomimetic soft actuator: design, modeling, control, and applications. *Mechatronics, IEEE/ASME Transactions on, 10*(5), 581-593.

Chung, C. K., Fung, P. K., Hong, Y. Z., Ju, M. S., Lin, C. C. K., & Wu, T. C. (2006). A novel fabrication of ionic polymer-metal composites (IPMC) actuator with silver nano-powders. *Sensors and Actuators B: Chemical*, *117*(2), 367-375.

Colombani, O., Ruppel, M., Schubert, F., Zettl, H., Pergushov, D. V., & Müller, A. H. (2007). Synthesis of poly (n-butyl acrylate)-block-poly (acrylic acid) diblock copolymers by ATRP and their micellization in water. *Macromolecules*, *40*(12), 4338-4350.

Corazzari, I., Nisticò, R., Turci, F., Faga, M. G., Franzoso, F., Tabasso, S. Magnacca, G. (2015). Advanced physico-chemical characterization of chitosan by means of

TGA coupled on-line with FTIR and GCMS: Thermal degradation and water adsorption capacity. *Polymer Degradation and Stability*, *112*, 1-9.

De Britto, D., & Campana-Filho, S. P. (2007). Kinetics of the thermal degradation of chitosan. *Thermochimica Acta*, *465*(1), 73-82.

De Souza, S. (2007). Smart coating based on polyaniline acrylic blend for corrosion protection of different metals. *Surface and Coatings Technology*, *201*(16), 7574-7581.

Deetlefs, M., & Seddon, K. R. (2006). Ionic liquids: fact and fiction. *Chimica oggi*, *24*(2), 16-23.

Dhakate, S. R., Mathur, R. B., Sharma, S., Borah, M., & Dhami, T. L. (2009). Influence of expanded graphite particle size on the properties of composite bipolar plates for fuel cell application. *Energy & Fuels*, *23*(2), 934-941.

Dias, A. M. A., Cortez, A. R., Barsan, M. M., Santos, J. B., Brett, C. M. A., & De Sousa, H. C. (2013). Development of greener multi-responsive chitosan biomaterials doped with biocompatible ammonium ionic liquids. *ACS Sustainable Chemistry & Engineering*, *1*(11), 1480-1492.

Dietsch, B., & Tong, T. (2007). A review-: Features and benefits of shape memory polymers (smps). *Journal of Advanced Materials*, *39*(2), 3-12.

Dong, Y., Ruan, Y., Wang, H., Zhao, Y., & Bi, D. (2004). Studies on glass transition temperature of chitosan with four techniques. *Journal of Applied Polymer Science*, *93*(4), 1553-1558.

Duarte, M. L., Ferreira, M. C., Marvao, M. R., & Rocha, J. (2001). Determination of the degree of acetylation of chitin materials by 13 C CP/MAS NMR spectroscopy. *International Journal of Biological Macromolecules*, *28*(5), 359-363.

Duncan, A. J., Akle, B. J., Long, T. E., & Leo, D. J. (2009). Ionomer design for augmented charge transport in novel ionic polymer transducers. *Smart Materials and Structures*, *18*(10), 104005.

Dupont, J., de Souza, R. F., & Suarez, P. A. (2002). Ionic liquid (molten salt) phase organometallic catalysis. *Chemical Reviews*, *102*(10), 3667-3692.

Eberle, G., Schmidt, H., & Eisenmenger, W. (1996). Piezoelectric polymer electrets. *Dielectrics and Electrical Insulation, IEEE Transactions on*, *3*(5), 624-646.

Eichhorn, S. J., Baillie, C. A., Zafeiropoulos, N., Mwaikambo, L. Y., Ansell, M. P., & Dufresne, A. (2001). Review: Current international research into cellulosic fibres and composites. *Journal of Materials Science, 36*(9), 2107-2131.

Fan, H. J., Hu, J. L., & Ji, F. L. (2004). Environmental-benign thermal-sensitive polyurethane for textile finishing. In *World Textile Conference 4th AUTEX conference, 22,* Roubaix, France.

Fennimore, A. M., Yuzvinsky, T. D., Han, W. Q., Fuhrer, M. S., Cumings, J., & Zettl, A. (2003). Rotational actuators based on carbon nanotubes. *Nature*, *424*(6947), 408-410.

Finkelmann, H., & Rehage, G. (1980). Investigations on liquid crystalline polysiloxanes, 1. Synthesis and characterization of linear polymers. *Die Makromolekulare Chemie, Rapid* Communications, 1(1), 31-34.

Finkelmann, H., Kim, S. T., Munoz, A., Palffy-Muhoray, P., & Taheri, B. (2001). Tunable mirrorless lasing in cholesteric liquid crystalline elastomers. *Advanced Materials*, *13*(14), 1069-1072.

Finkenstadt, V. L. (2005). Natural polysaccharides as electroactive polymers. *Applied Microbiology and Biotechnology*, *67*(6), 735-745.

Finkenstadt, V., & Willett, J. L. (2005). Preparation and characterization of electroactive biopolymers. *In Macromolecular Symposia, 227*(1), 367-372.

Florence, A. T., & Attwood, D. (2011). Solids. *Physicochemical principles of pharmacy* (5th). London: Pharmaceutical Press.

Francis, S., Varshney, L., & Sabharwal, S. (2007). Thermal degradation behavior of radiation synthesized polydiallyldimethylammonium chloride. *European Polymer Journal*, *43*(6), 2525-2531.

Freidzon, Y. S., and Shibaev, V. (1993). *Liquid Crystal Polymers*. New York: Plenum Press.

Frohbergh, M. E., Katsman, A., Botta, G. P., Lazarovici, P., Schauer, C. L., Wegst, & Lelkes, P. (2012). Electrospun hydroxyapatite-containing chitosan nanofibers crosslinked with genipin for bone tissue engineering. *Biomaterials*, *33*(36), 9167-9178.

Frohbergh, M. E., Katsman, A., Botta, G. P., Lazarovici, P., Schauer, C. L., & Wegst, U. G. (2012). Electrospun hydroxyapatite-containing chitosan nanofibers crosslinked with genipin for bone tissue engineering. *Biomaterials*, *33*(36), 9167-9178.

Fukada, E. (1989). Introduction: Early studies in piezoelectricity, pyroelectricity, and ferroelectricity in polymers. *Phase Transitions: A Multinational Journal*, *18*(3-4), 135-141.

Galiński, M., Lewandowski, A., & Stępniak, I. (2006). Ionic liquids as electrolytes. *Electrochimica Acta*, *51*(26), 5567-5580.

Gall, K., Dunn, M. L., Liu, Y., Finch, D., Lake, M., & Munshi, N. A. (2002). Shape memory polymer nanocomposites. *Acta Materialia*, *50*(20), 5115-5126.

Ge, H., Teasdale, P. R., & Wallace, G. G. (1991). Electrochemical chromatography packings, hardware and mechanisms of interaction. *Journal of Chromatography A*, *544*, 305-316.

Gerard, M., Chaubey, A., & Malhotra, B. D. (2002). Application of conducting polymers to biosensors. *Biosensors and Bioelectronics*, *17*(5), 345-359.

Grabe, M., & Oster, G. (2001). Regulation of organelle acidity. *The Journal of General Physiology*, *117*(4), 329-344.

Grim, T. E., Iglesias, J. M., Speakes, K. M., Campos, M., & Pelote, S. T. (1999). *U.S. Patent No. 6,007,505*. Washington, DC: U.S. Patent and Trademark Office.

Grodzinsky, A. J., & Shoenfeld, N. A. (1977). Tensile forces induced in collagen by means of electromechanochemical transductive coupling. *Polymer*, *18*(5), 435-443.

Guo, D., Zeng, F., & Dkhil, B. (2014). Ferroelectric Polymer Nanostructures: Fabrication, Structural Characteristics and Performance Under Confinement. *Journal of Nanoscience and Nanotechnology*, *14*(2), 2086-2100.

Gurunathan, K., Murugan, A. V., Marimuthu, R., Mulik, U. P., & Amalnerkar, D. P. (1999). Electrochemically synthesised conducting polymeric materials for applications towards technology in electronics, optoelectronics and energy storage devices. *Materials Chemistry and Physics*, *61*(3), 173-191.

Hackl, C., Tang, H. Y., Lorenz, R. D., Turng, L. S., & Schröder, D. (2004). A multiphysics model of planar electro-active polymer actuators. *Industry Applications Conference, 39(*3), 2125-2130.

Hagen, R., Salmén, L., & Stenberg, B. (1996). Effects of the type of crosslink on viscoelastic properties of natural rubber. *Journal of Polymer Science Part B: Polymer Physics*, *34*(12), 1997-2006.

Han, D., Yan, L., Chen, W., & Li, W. (2011). Preparation of chitosan/graphene oxide composite film with enhanced mechanical strength in the wet state. *Carbohydrate Polymers*, *83*(2), 653-658.

Hayashi, S. H. U. N. I. C. H. I., Tasaka, Y. O. S. H. I. Y. U. K. I., Hayashi, N., & Akita, Y. A. S. U. H. I. R. O. (2004). Development of smart polymer materials and its various applications. *Mitsubishi Juko Giho*, *41*(1), 62-64.

Heinze, T., & Liebert, T. (2001). Unconventional methods in cellulose functionalization. *Progress in polymer science*, *26*(9), 1689-1762.

Hirokawa, Y., & Tanaka, T. (1984). Volume phase transition in a nonionic gel.*The Journal of Chemical Physics*, *81*(12), 6379-6380.

Hong, C. H., Ki, S. J., Jeon, J. H., Che, H. L., Park, I. K., Kee, C. D., & Oh, I. K. (2013). Electroactive bio-composite actuators based on cellulose acetate nanofibers with specially chopped polyaniline nanoparticles through electrospinning. *Composites Science and Technology*, *87*, 135-141.

Hsiue, G. H., Chen, J. K., & Liu, Y. L. (2000). Synthesis and characterization of nanocomposite of polyimide–silica hybrid from nonaqueous sol–gel process.*Journal of Applied Polymer Science*, *76*(11), 1609-1618.

Huang, F. Y. (2012). Thermal properties and thermal degradation of cellulose tri-stearate (CTs). *Polymers*, *4*(2), 1012-1024.

Huang, G., Liang, H., Wang, Y., Wang, X., Gao, J., & Fei, Z. (2012). Combination effect of melamine polyphosphate and graphene on flame retardant properties of poly (vinyl alcohol). *Materials Chemistry and Physics*, *132*(2), 520-528.

Idicula, M., Malhotra, S. K., Joseph, K., & Thomas, S. (2005). Dynamic mechanical analysis of randomly oriented intimately mixed short banana/sisal hybrid fibre reinforced polyester composites. *Composites Science and Technology*, *65*(7), 1077-1087.

Iijima, S. (1991). Helical microtubules of graphitic carbon. *nature*, *354*(6348), 56-58.

Iijima, S., & Ichihashi, T. (1993). Single-shell carbon nanotubes of 1-nm diameter. Nature, 363, 603 – 605.

Ikeda, T., Nakano, M., Yu, Y., Tsutsumi, O., & Kanazawa, A. (2003). Anisotropic Bending and Unbending Behavior of Azobenzene Liquid-Crystalline Gels by Light Exposure. *Advanced Materials*, *15*(3), 201-205.

Imaizumi, S., Ohtsuki, Y., Yasuda, T., Kokubo, H., & Watanabe, M. (2013). Printable polymer actuators from ionic liquid, soluble polyimide, and ubiquitous carbon materials. *ACS Applied Materials & Interfaces*, *5*(13), 6307-6315.

Jang, S. D., Kim, J. H., Zhijiang, C., & Kim, J. (2008). The effect of chitosan concentration on the electrical property of chitosan-blended cellulose electroactive paper. *Smart Materials and Structures*, *18*(1), 015003.

Jawaid, M., Khalil, H. A., Hassan, A., Dungani, R., & Hadiyane, A. (2013). Effect of jute fibre loading on tensile and dynamic mechanical properties of oil palm epoxy composites. *Composites Part B: Engineering*, *45*(1), 619-624.

Jeon, J. H., & Oh, I. K. (2009). Selective growth of platinum electrodes for MDOF IPMC actuators. *Thin Solid Films*, *517*(17), 5288-5292.

Jeon, J. H., Cheedarala, R. K., Kee, C. D., & Oh, I. K. (2013). Dry-type artificial muscles based on pendent sulfonated chitosan and functionalized graphene oxide for greatly enhanced ionic interactions and mechanical stiffness. *Advanced Functional Materials*, *23*(48), 6007-6018.

Jeon, J. H., Kang, S. P., Lee, S., & Oh, I. K. (2009). Novel biomimetic actuator based on SPEEK and PVDF. *Sensors and Actuators B: Chemical*, *143*(1), 357-364.

Jiang, H. Y., Kelch, S., & Lendlein, A. (2006). Polymers move in response to light. *Advanced Materials*, *18*(11), 1471-1475.

Jin, Z., Pramoda, K. P., Xu, G., & Goh, S. H. (2001). Dynamic mechanical behavior of melt-processed multi-walled carbon nanotube/poly (methyl methacrylate) composites. *Chemical Physics Letters*, *337*(1), 43-47.

Jing, R., & Hongfei, H. (2001). Study on interpenetrating polymer network hydrogel of diallyldimethylammonium chloride with kappa-carrageenan by UV irradiation. *European Polymer Journal*, *37*(12), 2413-2417.

Jing, R., Yanqun, Z., Jiuqiang, L., & Hongfei, H. (2001). Radiation synthesis and characteristic of IPN hydrogels composed of poly (diallyldimethylammonium chloride) and Kappa-Carrageenan. *Radiation Physics and Chemistry*, *62*(2), 277-281.

Jin-lian, H. U., Xue-mei, D. I. N. G., Xiao-ming, T. A. O., & Jian-ming, Y. (2002). Shape memory polymers and their applications to smart textile products. *Journal of Donghua University*, *19*(3).

Jung, J. H., Vadahanambi, S., & Oh, I. K. (2010). Electro-active nano-composite actuator based on fullerene-reinforced Nafion. *Composites Science and Technology*, *70*(4), 584-592.

Khan, A., Khan, R. A., Salmieri, S., Le Tien, C., Riedl, B., & Bouchard, J. (2012). Mechanical and barrier properties of nanocrystalline cellulose reinforced chitosan based nanocomposite films. *Carbohydrate Polymers*, *90*(4), 1601-1608.

Khonakdar, H. A., Morshedian, J., Wagenknecht, U., & Jafari, S. H. (2003). An investigation of chemical crosslinking effect on properties of high-density polyethylene. *Polymer*, *44*(15), 4301-4309.

Kim, B. K., Lee, S. Y., & Xu, M. (1996). Polyurethanes having shape memory effects. *Polymer*, *37*(26), 5781-5793.

Kim, J., Wang, N., & Chen, Y. (2007). Effect of chitosan and ions on actuation behavior of cellulose–chitosan laminated films as electro-active paper actuators. *Cellulose*, *14*(5), 439-445.

Kim, K. J., & Tadokoro, S. (2007). *Electroactive polymers for robotic applications. Artificial Muscles and Sensors* (291). London, United Kingdom: Springer.

Kim, K. J., Yim, W., Paquette, J. W., & Kim, D. (2007). Ionic polymer-metal composites for underwater operation. *Journal of Intelligent Material Systems and Structures*, *18*(2), 123-131.

Kim, S. H., Oh, K. W., & Choi, J. H. (2010). Preparation and self-assembly of polyaniline nanorods and their application as electroactive actuators. *Journal of Applied Polymer Science*, *116*(5), 2601-2609.

Kim, S. J., Dwiatmoko, A. A., Choi, J. W., Suh, Y. W., Suh, D. J., & Oh, M. (2010). Cellulose pretreatment with 1-n-butyl-3-methylimidazolium chloride for solid acid-catalyzed hydrolysis. *Bioresource Technology*, *101*(21), 8273-8279.

Kim, S. J., Yoon, S. G., Kim, I. Y., & Kim, S. I. (2004). Swelling characterization of the semiinterpenetrating polymer network hydrogels composed of chitosan and poly (diallyldimethylammonium chloride). *Journal of Applied Polymer Science*, *91*(5), 2876-2880.

Kim, S. J., Yoon, S. G., Lee, S. M., Lee, J. H., & Kim, S. I. (2003). Characteristics of electrical responsive alginate/poly (diallyldimethylammonium chloride) IPN hydrogel in HCl solutions. *Sensors and Actuators B: Chemical*, *96*(1), 1-5.

Klemm, D., Heublein, B., Fink, H. P., & Bohn, A. (2005). Cellulose: fascinating biopolymer and sustainable raw material. *Angewandte Chemie International Edition*, *44*(22), 3358-3393.

Koev, S. T., Dykstra, P. H., Luo, X., Rubloff, G. W., Bentley, W. E., & Payne, G. F. (2010). Chitosan: an integrative biomaterial for lab-on-a-chip devices. *Lab on a Chip*, *10*(22), 3026-3042.

Kondo, T. (1997). The assignment of IR absorption bands due to free hydroxyl groups in cellulose. *Cellulose, 4*(4), 281-292.

Kong, L., & Chen, W. (2014). Carbon Nanotube and Graphene-based Bioinspired Electrochemical Actuators. *Advanced Materials*, *26*(7), 1025-1043.

Kopeček, J. (2003). Smart and genetically engineered biomaterials and drug delivery systems. *European Journal of Pharmaceutical Sciences*, *20*(1), 1-16.

Kosmulski, M., Gustafsson, J., & Rosenholm, J. B. (2004). Thermal stability of low temperature ionic liquids revisited. *Thermochimica Acta*, *412*(1), 47-53.

Krings, L. H. M., Havinga, E. E., Donkers, J. J. T. M., & Vork, F. T. A. (1993). The application of polypyrrole as counterelectrode in electrolytic capacitors. *Synthetic Metals*, *54*(1-3), 453-460.

Kwon, H. J., Osada, Y., & Gong, J. P. (2006). Polyelectrolyte gels-fundamentals and applications. *Polymer Journal*, *38*(12), 1211-1219.

Kwon, T., Lee, J. W., Cho, H., Henkensmeier, D., Kang, Y., & Hong, S. M. (2015). Ionic polymer actuator based on anion-conducting methylated ether-linked polybenzimidazole. *Sensors and Actuators B: Chemical*, *214*, 43-49.

Lan, X., Huang, W. M., Liu, N., Phee, S. Y., Leng, J. S., & Du, S. Y. (2008). Improving the electrical conductivity by forming Ni powder chains in a shape-memory polymer filled with carbon black. *The 15th International Symposium on: Smart Structures and Materials & Nondestructive Evaluation and Health Monitoring*, *1*(15), 692717-692717.

Lee, J. W., Kim, J. H., Goo, N. S., Lee, J. Y., & Yoo, Y. T. (2010). Ion-conductive poly (vinyl alcohol)-based IPMCs. *Journal of Bionic Engineering*, *7*(1), 19-28.

Lee, J. Y., Wang, H. S., Yoon, B. R., Han, M. J., & Jho, J. Y. (2010). Radiation-Grafted Fluoropolymers Soaked with Imidazolium-Based Ionic Liquids for High-Performance Ionic Polymer–Metal Composite Actuators. *Macromolecular Rapid Communications*, *31*(21), 1897-1902.

Lee, M. J., Jung, S. H., Lee, S., Mun, M. S., & Moon, I. (2006). Control of IPMC-based artificial muscle for myoelectric hand prosthesis. *Biomedical Robotics and Biomechatronics.* The First IEEE/RAS-EMBS International Conference on, 1172-1177.

Lendlein, A., & Langer, R. (2002). Biodegradable, elastic shape-memory polymers for potential biomedical applications. *Science*, *296*(5573), 1673-1676.

Lendlein, A., & Langer, R. (2004). *U.S. Patent Application No. 10/546,092*.

Lendlein, A., Jiang, H., Jünger, O., & Langer, R. (2005). Light-induced shape-memory polymers. *Nature*, *434*(7035), 879-882.

Leng, J., Lu, H., Liu, Y., & Du, S. (2008). Conductive nanoparticles in electro activated shape memory polymer sensor and actuator. *The 15th International Symposium on: Smart Structures and Materials & Nondestructive Evaluation and Health Monitoring*, *1*(15), 693109-693109.

Li, Q., & Renneckar, S. (2011). Supramolecular structure characterization of molecularly thin cellulose I nanoparticles. *Biomacromolecules*, *12*(3), 650-659.

Li, Y., & Shimizu, H. (2008). Conductive PVDF/PA6/CNTs nanocomposites fabricated by dual formation of cocontinuous and nanodispersion structures. *Macromolecules*, *41*(14), 5339-5344.

Limam, Z., Selmi, S., Sadok, S., & El Abed, A. (2013). Extraction and characterization of chitin and chitosan from crustacean by-products: Biological and physicochemical properties. *African Journal of Biotechnology*, *10*(4), 640-647.

Liu, F., Li, F., Deng, G., Chen, Y., Zhang, B., Zhang, J., & Liu, C. Y. (2012). Rheological images of dynamic covalent polymer networks and mechanisms behind mechanical and self-healing properties. *Macromolecules*, *45*(3), 1636-1645.

Liu, Y. L., Su, Y. H., & Lai, J. Y. (2004). In situ crosslinking of chitosan and formation of chitosan–silica hybrid membranes with using γ-glycidoxypropyltrimethoxysilane as a crosslinking agent. *Polymer*, *45*(20), 6831-6837.

Liu, Y., Lv. H., Lan, X., Leng, J., & Du, S. (2009). Review of electro-active shape-memory polymer composite. *Composites Science and Technology*, *69*(13), 2064-2068.

Long, K. N., Scott, T. F., Qi, H. J., Bowman, C. N., & Dunn, M. L. (2009). Photomechanics of light-activated polymers. *Journal of the Mechanics and Physics of Solids*, *57*(7), 1103-1121.

Lu, J., Kim, S. G., Lee, S., & Oh, I. K. (2008). Fabrication and actuation of electro-active polymer actuator based on PSMI-incorporated PVDF. *Smart Materials and Structures*, *17*(4), 045002.

Lu, L., & Chen, W. (2010). Biocompatible composite actuator: a supramolecular structure consisting of the biopolymer chitosan, carbon nanotubes, and an ionic liquid. *Advanced Materials*, *22*(33), 3745-3748.

Luqman, M., Lee, J. W., Moon, K. K., & Yoo, Y. T. (2011). Sulfonated polystyrene-based ionic polymer–metal composite (IPMC) actuator. *Journal of Industrial and Engineering Chemistry*, *17*(1), 49-55.

Lv, H., Leng, J., Liu, Y., & Du, S. (2008). Shape-memory polymer in response to solution. *Advanced Engineering Materials*, *10*(6), 592-595.

Mahoney, J. J. D. (1967). *U.S. Patent No. 3,301,252*. Washington, DC: U.S. Patent and Trademark Office.

Mäki-Arvela, P., Anugwom, I., Virtanen, P., Sjöholm, R., & Mikkola, J. P. (2010). Dissolution of lignocellulosic materials and its constituents using ionic liquids—a review. *Industrial Crops and Products*, *32*(3), 175-201.

Mano, J. F., Koniarova, D., & Reis, R. L. (2003). Thermal properties of thermoplastic starch/synthetic polymer blends with potential biomedical applicability. *Journal of Materials Science: Materials in Medicine*, *14*(2), 127-135.

Markland, P., Zhang, Y., Amidon, G. L., & Yang, V. C. (1999). A pH-and ionic strength-responsive polypeptide hydrogel: synthesis, characterization, and preliminary protein release studies. *Journal of Biomedical Materials Research, 47*(4): 595-602.

May, P., Khan, U., O'Neill, A., & Coleman, J. N. (2012). Approaching the theoretical limit for reinforcing polymers with graphene. *Journal of Materials Chemistry, 22*(4), 1278-1282.

Meng, H., & Hu, J. (2010). A brief review of stimulus-active polymers responsive to thermal, light, magnetic, electric, and water/solvent stimuli. *Journal of Intelligent Material Systems and Structures*, *21*(9), 859-885.

Meng, Q., & Hu, J. (2009). A review of shape memory polymer composites and blends. *Composites Part A: Applied Science and Manufacturing*, *40*(11), 1661-1672.

Meng, Q., Heuzey, M. C., & Carreau, P. J. (2014). Hierarchical structure and physicochemical properties of plasticized chitosan. *Biomacromolecules*, *15*(4), 1216-1224.

Meng, Q., Hu, J., & Yeung, L. (2007). An electro-active shape memory fibre by incorporating multi-walled carbon nanotubes. *Smart Materials and Structures*, *16*(3), 830.

Meng, Q., Hu, J., Zhu, Y., Lu, J., & Liu, Y. (2007). Morphology, phase separation, thermal and mechanical property differences of shape memory fibres prepared by different spinning methods. *Smart Materials and Structures*, *16*(4), 1192.

Mermilliod, N., Tanguy, J., & Petiot, F. (1986). A study of chemically synthesized polypyrrole as electrode material for battery applications. *Journal of the Electrochemical Society*, *133*(6), 1073-1079.

Metcalfe, A., Desfaits, A. C., Salazkin, I., Yahia, L. H., Sokolowski, W. M., & Raymond, J. (2003). Cold hibernated elastic memory foams for endovascular interventions. *Biomaterials*, *24*(3), 491-497.

Mirfakhrai, T., Madden, J. D., & Baughman, R. H. (2007). Polymer artificial muscles. *Materials Today*, *10*(4), 30-38.

Mirmohseni, A., Price, W. E., Wallace, G. G., & Zhao, H. (1993). Adaptive membrane systems based on conductive electroactive polymers. *Journal of Intelligent Material Systems and Structures*, *4*(1), 43-49.

Mondal, S., & Hu, J. L. (2006). Thermal degradation study of functionalized MWNT reinforced segmented polyurethane membrane. *Journal of Elastomers and Plastics*, *38*(3), 261-271.

Mondal, S., Hu, J. L., & Yong, Z. (2006). Free volume and water vapor permeability of dense segmented polyurethane membrane. *Journal of Membrane Science*, *280*(1), 427-432.

Mucha, M., & Pawlak, A. (2005). Thermal analysis of chitosan and its blends. *Thermochimica Acta*, *427*(1), 69-76.

Naboka, O., Sanz-Velasco, A., Lundgren, P., Enoksson, P., & Gatenholm, P. (2012). Cobalt (II) chloride promoted formation of honeycomb patterned cellulose acetate films. *Journal of Colloid and Interface Science*, *367*(1), 485-493.

Nakashima, K., Yamaguchi, K., Taniguchi, N., Arai, S., Yamada, R., Katahira, & Kondo, A. (2011). Direct bioethanol production from cellulose by the combination of cellulase-displaying yeast and ionic liquid pretreatment. *Green Chemistry*, *13*(10), 2948-2953.

Nalwa, H. S. (1991). Recent developments in ferroelectric polymers. *Journal of Macromolecular Science, Part C: Polymer Reviews*, *31*(4), 341-432.

Nam, S., Jang, J., Kim, K., Yun, W. M., Chung, D. S., & Hwang, J. (2011). Solvent-free solution processed passivation layer for improved long-term stability of organic field-effect transistors. *Journal of Materials Chemistry*, *21*(3), 775-780.

Neto, C. D. T., Giacometti, J. A., Job, A. E., Ferreira, F. C., Fonseca, J. L. C., & Pereira, M. R. (2005). Thermal analysis of chitosan based networks. *Carbohydrate Polymers*, *62*(2), 97-103.

Newbury, K. M., & Leo, D. J. (2002). Electromechanical modeling and characterization of ionic polymer benders. *Journal of Intelligent Material Systems and Structures*, *13*(1), 51-60.

Nge, T. T., Yamaguchi, M., Hori, N., Takemura, A., & Ono, H. (2002). Synthesis and characterization of chitosan/poly (acrylic acid) polyelectrolyte complex. *Journal of Applied Polymer Science*, *83*(5), 1025-1035.

Nikonenko, N. A., Buslov, D. K., Sushko, N. I., & Zhbankov, R. G. (2000). Investigation of stretching vibrations of glycosidic linkages in disaccharides and polysaccarides with use of IR spectra deconvolution. *Biopolymers*, *57*(4), 257-262.

Nikonenko, N. A., Buslov, D. K., Sushko, N. I., & Zhbankov, R. G. (2005). Spectroscopic manifestation of stretching vibrations of glycosidic linkage in polysaccharides. *Journal of Molecular Structure*, *752*(1), 20-24.

O'Halloran, A., O'malley, F., & McHugh, P. (2008). A review on dielectric elastomer actuators, technology, applications, and challenges. *Journal of Applied Physics*, *104*(7), 071101.

Palmre, V., Hubbard, J. J., Fleming, M., Pugal, D., Kim, S., Kim, K. J., & Leang, K. (2012). An IPMC-enabled bio-inspired bending/twisting fin for underwater applications. *Smart Materials and Structures*, *22*(1), 014003.

Phillips, A. K., & Moore, R. B. (2005). Ionic actuators based on novel sulfonated ethylene vinyl alcohol copolymer membranes. *Polymer*, *46*(18), 7788-7802.

Pisarski, W. A., Żur, L., & Pisarska, J. (2011). Optical transitions of Eu 3+ and Dy 3+ ions in lead phosphate glasses. *Optics Letters*, *36*(6), 990-992.

Pookrod, P., Dungkaew, W., Un-Arn, P., & Haller, K. J. (2012). Polyelectrolyte-enhanced ultrafiltration (PEUF) process for low level arsenic removal: Recovery of polyelectrolyte from retentate stream. In *Advanced Materials Research*, *506*, 27-30.

Poon, L., Wilson, L. D., & Headley, J. V. (2014). Chitosan-glutaraldehyde copolymers and their sorption properties. *Carbohydrate Polymers*, *109*, 92-101.

Poulsen, M., & Ducharme, S. (2010). Why ferroelectric polyvinylidene fluoride is special. *IEEE Transactions on Dielectrics and Electrical Insulation*, *17*(4), 1028-1035.

Powell, H. M., & Boyce, S. T. (2006). EDC cross-linking improves skin substitute strength and stability. *Biomaterials*, *27*(34), 5821-5827.

Pugal, D., Jung, K., Aabloo, A., & Kim, K. J. (2010). Ionic polymer–metal composite mechanoelectrical transduction: review and perspectives. *Polymer International*, *59*(3), 279-289.

Qi, L., Xu, Z., Jiang, X., Hu, C., & Zou, X. (2004). Preparation and antibacterial activity of chitosan nanoparticles. *Carbohydrate Research*, *339*(16), 2693-2700.

Qiu, Y., & Park, K. (2012). Environment-sensitive hydrogels for drug delivery. *Advanced Drug Delivery Reviews*, *64*, 49-60.

Rajagopalan, M., & Oh, I. K. (2011). Fullerenol-based electroactive artificial muscles utilizing biocompatible polyetherimide. *ACS Nano*, *5*(3), 2248-2256.

Ravindra, R., Krovvidi, K. R., & Khan, A. A. (1998). Solubility parameter of chitin and chitosan. *Carbohydrate Polymers*, *36*(2), 121-127.

Rogers, R. D., & Seddon, K. R. (2003). Ionic liquids-solvents of the future. *Science*, *302*(5646), 792-793.

Rousseau, I. A., & Mather, P. T. (2003). Shape memory effect exhibited by smectic-C liquid crystalline elastomers. *Journal of the American Chemical Society*, *125*(50), 15300-15301.

Rowley, N. M., & Mortimer, R. J. (2002). New electrochromic materials. *Science Progress*, *85*(3), 243-262.

Rudra, R., Kumar, V., & Kundu, P. P. (2015). Acid catalysed cross-linking of poly vinyl alcohol (PVA) by glutaraldehyde: effect of crosslink density on the characteristics of PVA membranes used in single chambered microbial fuel cells. *RSC Advances*, *5*(101), 83436-83447.

Russel, D. A., Hayashi, S., & Yamada, T. (1999). The potential use of memory film in clothing. *Techtextil Symposium-New Protective Textiles (Through Textile Technology Index Database), 8*(8), 17-19.

Sasi, R., Rao, T. P., & Devaki, S. J. (2014). Bio-based ionic liquid crystalline quaternary ammonium salts: properties and applications. *ACS Applied Materials & Interfaces*, *6*(6), 4126-4133.

Schmaljohann, D. (2006). Thermo-and pH-responsive polymers in drug delivery. *Advanced Drug Delivery Reviews*, *58*(15), 1655-1670.

Seddon, K. R. (1997). Ionic liquids for clean technology. *Journal of Chemical Technology and Biotechnology*, *68*(4), 351-356.

Sen, I., Seki, Y., Sarikanat, M., Cetin, L., Gurses, B. O., Ozdemir, O., Yılmaz, O, Sever, K., Akar, E, & Mermer, O. (2015). Electroactive behavior of graphene nanoplatelets loaded cellulose composite actuators. *Composites Part B: Engineering*, *69*, 369-377.

Sencadas, V., Correia, D. M., Ribeiro, C., Moreira, S., Botelho, G., Ribelles, J. G., & Lanceros-Méndez, S. (2012). Physical-chemical properties of cross-linked chitosan electrospun fiber mats. *Polymer Testing*, *31*(8), 1062-1069.

Servant, A., Bussy, C., Al-Jamal, K., & Kostarelos, K. (2013). Design, engineering and structural integrity of electro-responsive carbon nanotube-based hydrogels for pulsatile drug release. *Journal of Materials Chemistry B, 1*(36), 4593-4600.

Setter, N., & Waser, R. (2000). Electroceramic materials. *Acta Materialia*, *48*(1), 151-178.

Shahinpoor, M. (2003). Ionic polymer–conductor composites as biomimetic sensors, robotic actuators and artificial muscles - a review. *Electrochimica Acta*, *48*(14), 2343-2353.

Shahinpoor, M., & Kim, K. J. (2000). Effects of counter-ions on the performance of IPMCs. In *SPIE's 7th Annual International Symposium on Smart Structures and Materials* (110-120). International Society for Optics and Photonics.

Shahinpoor, M., & Kim, K. J. (2001). Ionic polymer-metal composites: I. Fundamentals. *Smart Materials and Structures*, *10*(4), 819.

Shahinpoor, M., Bar-Cohen, Y., Simpson, J. O., & Smith, J. (1998). Ionic polymer-metal composites (IPMCs) as biomimetic sensors, actuators and artificial muscles-a review. *Smart Materials and Structures*, *7*(6), 15.

Shahinpoor, M., Kim, K. J., & Leo, D. J. (2003). Ionic polymer-metal composites as multifunctional materials. *Polymer Composites*, *24*(1), 24-33.

Shang, J., Shao, Z., & Chen, X. (2008). Chitosan-based electroactive hydrogel. *Polymer*, *49*(25), 5520-5525.

Sherrington, D. C. (1989). *Side Chain Liquid Crystal Polymers*. UK: Blackie Publishers.

Shiga, T., & Kurauchi, T. (1990). Deformation of polyelectrolyte gels under the influence of electric field. *Journal of Applied Polymer Science*, *39*(11-12), 2305-2320.

Siqueira, J. R., Gasparotto, L. H., Crespilho, F. N., Carvalho, A. J., Zucolotto, V., & Oliveira, O. N. (2006). Physicochemical properties and sensing ability of metallophthalocyanines/chitosan nanocomposites. *The Journal of Physical Chemistry B*, *110*(45), 22690-22694.

Slater, J. M., & Watt, E. J. (1989). Use of the conducting polymer, polypyrrole, as a sensor. In *Analytical Proceedings*, *26*(11), 397-399.

Sreedhar, B., Sairam, M., Chattopadhyay, D. K., Rathnam, P. A., & Rao, D. V. (2005). Thermal, mechanical, and surface characterization of starch–poly (vinyl alcohol) blends and borax-crosslinked films. *Journal of Applied Polymer Science*, *96*(4), 1313-1322.

Su, J., Ma, Z. Y., Scheinbeim, J. I., & Newman, B. A. (1995). Ferroelectric and piezoelectric properties of nylon 11/poly (vinylidene fluoride) bilaminate films. *Journal of Polymer Science Part B: Polymer Physics*, *33*(1), 85-91.

Su, Y., Wei, H., Gao, R., Yang, Z., Zhang, J., & Zhong, Z. (2012). Exceptional negative thermal expansion and viscoelastic properties of graphene oxide paper. *Carbon*, *50*(8), 2804-2809.

Sukeerthi, S., & Contractor, A. Q. (1994). Applications of conducting polymers as sensors. *Council Scientific Industrial Research*, *33*(6), 565-571.

Sullivan, A. L., & Ball, R. (2012). Thermal decomposition and combustion chemistry of cellulosic biomass. *Atmospheric Environment*, *47*, 133-141.

Suo, Z. (2010). Theory of dielectric elastomers. *Acta Mechanica Solida Sinica*, *23*(6), 549-578.

Swatloski, R. P., Spear, S. K., Holbrey, J. D., & Rogers, R. D. (2002). Dissolution of cellose with ionic liquids. *Journal of the American Chemical Society*, *124*(18), 4974-4975.

Takase, Y., Lee, J. W., Scheinbeim, J. I., & Newman, B. A. (1991). High-temperature characteristics of nylon-11 and nylon-7 piezoelectrics. *Macromolecules*, *24*(25), 6644-6652.

Talaie, A., Lee, J. Y., Lee, Y. K., Jang, J., Romagnoli, J. A., Taguchi, T., & Maeder, E. (2000). Dynamic sensing using intelligent composite: an investigation to development of new pH sensors and electrochromic devices. *Thin Solid Films, 363*(1), 163-166.

Tanaka, T. (1978). Collapse of gels and the critical endpoint. *Physical Review Letters*, *40*(12), 820.

Tanaka, T., Nishio, I., Sun, S. T., & Ueno-Nishio, S. (1982). Collapse of gels in an electric field. *Science*, *218*(4571), 467-469.

Terinte, N., Ibbett, R., & Schuster, K. C. (2011). Overview on native cellulose and microcrystalline cellulose I structure studied by X-ray diffraction (WAXD): comparison between measurement techniques. *Lenzinger Berichte*, *89,* 118-131.

Thomsen, D. L., Keller, P., Naciri, J., Pink, R., Jeon, H., Shenoy, D. & Ratna, B. R. (2001). Liquid crystal elastomers with mechanical properties of a muscle. *Macromolecules*, *34*(17), 5868-5875.

Tiwari, R., Kim, K. J., & Kim, S. M. (2008). Ionic polymer-metal composite as energy harvesters. *Smart Structures and Systems*, *4*(5), 549-563.

Tobushi, H., Hayashi, S., Hoshio, K., & Miwa, N. (2006). Influence of strain-holding conditions on shape recovery and secondary-shape forming in polyurethane-shape memory polymer. *Smart Materials and Structures*, *15*(4), 1033.

Tobushi, H., Matsui, R., Hayashi, S., & Shimada, D. (2004). The influence of shape-holding conditions on shape recovery of polyurethane-shape memory polymer foams. *Smart Materials and Structures*, *13*(4), 881.

Trchová, M., Šeděnková, I., Morávková, Z., & Stejskal, J. (2014). Conducting polymer and ionic liquid: Improved thermal stability of the material–A spectroscopic study. *Polymer Degradation and Stability*, *109*, 27-32.

Tripathi, S., Mehrotra, G. K., & Dutta, P. K. (2009). Physicochemical and bioactivity of cross-linked chitosan–PVA film for food packaging applications. *International Journal of Biological Macromolecules*, *45*(4), 372-376.

Tsuchida, T., & Yoshinaga, F. (1997). Production of bacterial cellulose by agitation culture systems. *Pure and Applied Chemistry*, *69*(11), 2453-2458.

Tundo, P., Perosa, A., & Zecchini, F. (2007). *Methods and Reagents for Green Chemistry,* (252). United States of America: Wiley.

Wache, H. M., Tartakowska, D. J., Hentrich, A., & Wagner, M. H. (2003). Development of a polymer stent with shape memory effect as a drug delivery system. *Journal of Materials Science: Materials in Medicine*, *14*(2), 109-112.

Wang, H., & Roman, M. (2011). Formation and properties of chitosan− cellulose nanocrystal polyelectrolyte− macroion complexes for drug delivery applications. *Biomacromolecules*, *12*(5), 1585-1593.

Wang, H., Gurau, G., & Rogers, R. D. (2012). Ionic liquid processing of cellulose. *Chemical Society Reviews*, *41*(4), 1519-1537.

Wang, N., Chen, Y., & Kim, J. (2007). Electroactive Paper Actuator Made with Chitosan-Cellulose Films: Effect of Acetic Acid. *Macromolecular Materials and Engineering*, *292*(6), 748-753.

Wang, X. L., Oh, I. K., Lu, J., Ju, J., & Lee, S. (2007). Biomimetic electro-active polymer based on sulfonated poly (styrene-b-ethylene-co-butylene-b-styrene). *Materials Letters*, *61*(29), 5117-5120.

Wang, Y., Sun, C., Zhou, E., & Su, J. (2004). Deformation mechanisms of electrostrictive graft elastomer. *Smart Materials and Structures*, *13*(6), 1407.

Warner, M., & Terentjev, E. M. (2003). *Liquid Crystal Elastomers* (3. Ed.). New York: OUP Oxford.

Watson, P., Jones, A. T., & Stephens, D. J. (2005). Intracellular trafficking pathways and drug delivery: fluorescence imaging of living and fixed cells. *Advanced Drug Delivery Reviews*, *57*(1), 43-61.

Welton, T. (1999). Room-temperature ionic liquids. Solvents for synthesis and catalysis. *Chemical Reviews*, *99*(8), 2071-2084.

Wu, J., Zhang, J., Zhang, H., He, J., Ren, Q., & Guo, M. (2004). Homogeneous acetylation of cellulose in a new ionic liquid. *Biomacromolecules*, *5*(2), 266-268.

Xie, X., Qu, L., Zhou, C., Li, Y., Zhu, J., Bai, H., & Dai, L. (2010). An asymmetrically surface-modified graphene film electrochemical actuator. *ACS Nano*, *4*(10), 6050-6054.

Xu, A., Wang, J., & Wang, H. (2010). Effects of anionic structure and lithium salts addition on the dissolution of cellulose in 1-butyl-3-methylimidazolium-based ionic liquid solvent systems. *Green Chemistry*, *12*(2), 268-275.

Xu, Y. X., Kim, K. M., Hanna, M. A., & Nag, D. (2005). Chitosan–starch composite film: preparation and characterization. *Industrial Crops and Products*, *21*(2), 185-192.

Yadav, M., Rhee, K. Y., Jung, I. H., & Park, S. J. (2013). Eco-friendly synthesis, characterization and properties of a sodium carboxymethyl cellulose/graphene oxide nanocomposite film. *Cellulose*, *20*(2), 687-698.

Yamaguchi, I., Tokuchi, K., Fukuzaki, H., Koyama, Y., Takakuda, K., & Monma, H. (2001). Preparation and microstructure analysis of chitosan/hydroxyapatite nanocomposites. *Journal of Biomedical Materials Research*, *55*(1), 20-27.

Yang, P., Wang, X., Fan, H., & Gu, Y. (2013). Effect of hydrogen bonds on the modulus of bulk polybenzoxazines in the glassy state. *Physical Chemistry Chemical Physics*, *15*(37), 15333-15338.

Yang, Y., Cui, J., Zheng, M., Hu, C., Tan, S., Xiao, Y. & Liu, Y. (2012). One-step synthesis of amino-functionalized fluorescent carbon nanoparticles by hydrothermal carbonization of chitosan. *Chemical Communications*, *48*(3), 380-382.

Yeng, C. M., Husseinsyah, S., & Ting, S. S. (2015). Effect of Cross-linking Agent on Tensile Properties of Chitosan/Corn Cob Biocomposite Films. *Polymer-Plastics Technology and Engineering*, *54*(3), 270-275.

Yeng, C. M., Husseinsyah, S., & Ting, S. S. (2015). Effect of Cross-linking Agent on Tensile Properties of Chitosan/Corn Cob Biocomposite Films. *Polymer-Plastics Technology and Engineering*, *54*(3), 270-275.

Yim, W., Lee, J., & Kim, K. J. (2007). An artificial muscle actuator for biomimetic underwater propulsors. *Bioinspiration & Biomimetics*, *2*(2), 31.

Yoon, W. J., Reinhall, P. G., & Seibel, E. J. (2007). Analysis of electro-active polymer bending: A component in a low cost ultrathin scanning endoscope. *Sensors and Actuators A: Physical*, *133*(2), 506-517.

Yoshida, R., Uchida, K., Kaneko, Y., Sakai, K., Kikuchi, A., & Sakurai, Y. (1995). Comb-type grafted hydrogels with rapid deswelling response to temperature changes. *Nature*, *374*(6519), 240-242.

Yu, Y., & Ikeda, T. (2005). Photodeformable polymers: A new kind of promising smart material for micro-and nano-applications. *Macromolecular Chemistry and Physics*, *206*(17), 1705-1708.

Yu, Y., Nakano, M., & Ikeda, T. (2004). Photoinduced bending and unbending behavior of liquid-crystalline gels and elastomers. *Pure and Applied Chemistry*, *76*(7-8), 1467-1477.

Zhang, H., Li, L., Feng, W., Zhou, Z., & Nie, J. (2014). Polymeric ionic liquids based on ether functionalized ammoniums and perfluorinated sulfonimides. *Polymer*, *55*(16), 3339-3348.

Zhang, H., Wu, J., Zhang, J., & He, J. (2005). 1-Allyl-3-methylimidazolium chloride room temperature ionic liquid: a new and powerful nonderivatizing solvent for cellulose. *Macromolecules*, *38*(20), 8272-8277.

Zhao, D., Li, H., Zhang, J., Fu, L., Liu, M., & Fu, J. (2012). Dissolution of cellulose in phosphate-based ionic liquids. *Carbohydrate Polymers*, *87*(2), 1490-1494.

Zhou, G. Y., & Li, J. R. (2003). Dynamic behavior of a magnetorheological elastomer under uniaxial deformation: I. Experiment. *Smart Materials and Structures*, *12*(6), 859.

Zhu, S., Wu, Y., Chen, Q., Yu, Z., Wang, C., Jin, S. Ding, Y., & Wu, G. (2006). Dissolution of cellulose with ionic liquids and its application: a mini-review. *Green Chemistry*, *8*(4), 325-327.

Zrinyi, M. (2000). Intelligent polymer gels controlled by magnetic fields. *Colloid and Polymer Science*, *278*(2), 98-103.

Zrínyi, M., Barsi, L., & Büki, A. (1996). Deformation of ferrogels induced by nonuniform magnetic fields. *The Journal of Chemical Physics*, *104*(21), 8750-8756.